universität wien

# DOCTORAL THESIS
# DISSERTATION

Title of the Doctoral Thesis
Titel der Dissertation

## Development of a micromechanical proof-of-principle experiment for measuring the gravitational force of milligram masses


submitted by
verfasst von

Jonas Schmöle, MSc


in partial fulfillment of the requirements for the degree of
angestrebter akademischer Grad

Doktor der Naturwissenschaften (Dr. rer. nat.)

Vienna, 2017

| | |
|---|---|
| **Degree programme code*** **(Studienkennzahl)** | A 796 605 411 |
| **Field of study*** **(Dissertationsgebiet)** | Physics |
| **Supervisor** **(Betreut von)** | Univ.-Prof. Dr. Markus Aspelmeyer |

*) as it appears on the student record sheet (laut Studienblatt)

"If you begin to wonder if your choices are actually meaningful, and whether you'll ever make a significant contribution to the world, just remember that in the vast infiniteness of space, your thoughts and problems are materially insignificant. And the feeling should subside."

---

The Stanley Parable
William Pugh

"Yeah, science, huh? Ain't it a thing? You know, I mean, like, old lady science. She's a real- you gotta hang on tight, because she bucks pretty hard!"

---

Rick and Morty
Justin Roiland, Dan Harmon

# Abstracts


## English abstract

This thesis is based on a simple question: how small can one make a gravitational source mass and still detect its gravitational coupling to a nearby test mass? We describe an experimental scheme based on micromechanical sensing to observe gravity between milligram-scale masses, thereby improving the current smallest source-mass values by three orders of magnitude and possibly even more.

Our discussion of the proposed experiment includes a theoretical treatment of the main physical effects and a range of auxiliary components. This spans the notion of spectral densities and the usage of harmonic oscillators as force transducers, with a discussion of the forces that come into play when attempting to measure gravity on small length scales. Further, we investigate a polarization based low-noise optical readout and develop a general framework to calculate transfer functions of passive vibration isolation systems.

The practical implementation of the proposed experiment is discussed from an engineering point of view, starting with a comparison of relevant effects for realistic parameters. We then split the technical assessment into four major engineering challenges: the fabrication of a high-quality test mass, the construction of a source-mass drive engine, the implementation of the optical readout scheme and the development of a suitable vibration isolation system.

Finally, we investigate the implications of experimentally accessing the gravitational source-mass character of small objects both for new precision measurements of Newton's constant and for a new generation of experiments at the interface between quantum physics and gravity.

## Deutsche Kurzfassung

Wie groß muss eine Quellmasse für ein Gravitationspotential sein, welches nachweislich an eine Testmasse koppelt? Diese simple Frage dient als Grundlage für die vorliegende Arbeit. Wir beschreiben ein experimentelles Schema basierend auf einem mikromechanischen Sensor, mit dem die Gravitation zwischen millimetergroßen Quellmassen gemessen werden kann und der aktuelle Größenrekord um mehrere Ordnungen verbessert wird.

Unsere Bearbeitung des vorgeschlagenen Experimentes beinhaltet eine theoretische Behandlung der wesentlichen physikalischen Effekte sowie der Hintergründe einer Reihe notwendiger Komponenten. Dies umfasst den Begriff der spektralen Dichte und die Verwendung von harmonischen Oszillatoren als Kraft-Transducer, gefolgt von einer Diskussion der relevanten Kräfte bei einer Messung von Gravitation auf kleinen Längenskalen. Ferner untersuchen wir ein polarisations-basiertes rauscharmes Setup für die optische Positionsmessung und entwickeln einen allgemeinen Formalismus für die Berechnung von Transferfunktionen von passiven Vibrationsisolierungs-Systemen.

Im angewandten Teil der Arbeit diskutieren wir die Herausforderungen einer praktischen Implementierung unter technischen Aspekten, anfangend mit einem Vergleich der Effektgrößen für realistische Parameter. Anschließend unterteilen wir die technische Behandlung in vier wesentliche Teilprojekte: die Fabrikation einer hochqualitativen Testmasse, die Konstruktion eines Quellmassenmotors, die Implementierung des optischen Ausleseschemas und die Entwicklung eines geeigneten Systems für die Vibrationsisolierung.

Abschließend beschäftigen wir uns mit den Implikationen des experimentellen Zugangs zum gravitativen Quellmassen-Character kleiner Objekte sowohl für neue Präzisionsmessungen von Newtons Gravitationskonstante, als auch für eine neue Generation von Experimenten an der Grenze zwischen Quantenphysik und Gravitation.

# Acknowledgements


## Editors

This thesis was supervised by *Markus Aspelmeyer*, who thoroughly worked through this document and provided a great amount of valuable comments and suggestions for improvements. Further main editing contributions were made by *Tobias Westphal*, who reviewed the entire thesis in-depth and hugely contributed to its scientific rigidity. Lastly, *Joshua Slater* helped with language and provided useful advice regarding the science and the accessibility of the early sections.

## Professional support

I want to thank Markus Aspelmeyer for his supervision during my time as a PhD student in his group, for his restless dedication and his passionate efforts to create the best possible scientific work environment. What started as a brief internship in Vienna became a Master's thesis and transitioned into a PhD, none of which would have happened without his enduring support.

Much of the work presented throughout this thesis could not have been accomplished without scientific support. Sebastian Hofer had solutions for most of my mathematica(l) problems and never hesitated to engage in long discussions about pressing issues. He also generously cross-checked the results presented in section 5.2. Ralf Riedinger was always glad to discuss and become engaged, sparking some valuable ideas and in particular contributing to the work presented in sections 9.3.2 and 11.2.3. Michael Vanner, while he was still in Vienna, served as my daily partner for scientific exchange and can not be valued enough for his optimistic and holistic views. Further, Jason Hoelscher provided some insight for sections 6.3.3 and 9.4, Garrett Cole served as the main advisor for the work mentioned in section 9.8.1 and Joshua Slater helped with the collection of the data shown in fig. 12.5.

As of early 2017, the *milliG* team includes three other members. Mathias Dragosits joined the project in 2014 to provide technical support and develop the drive engine for the source mass. Hans Hepach, who joined in 2015, is developing the detector electronics and performs some of the fabrication-related work that needs to be done in Vienna. After already investing many days during my visits in Hanover, Tobias Westphal recently joined the team and already contributes massively, especially with his deep knowledge of electronics and vibration isolation. Further, the test-mass development is currently carried out by Richard Norte, who performed most of the work presented in sections 9.8.2 to 9.8.4, and Simon Gröblacher from the Delft University of Technology.

I also want to thank Rana Adhikari, George Gillies, Harald Lück, Michael Martin, Fabrice Matichard, Conor Malcolm Mow-Lowry, Kevin Phelan and Michael Trupke for both technical and physical discussions. Lastly, I thank Petra Beckmannova, Christiane Maria Losert-Valiente Kroon, Alexandra Seiringer and the administrative team as well as Gerald Prager and Andreas Zink from the mechanical workshop, who are often not given enough credit for their efforts.

## Funding

The presented work is supported by the European Commission (*cQOM*), the European Research Council (*ERC CoG QLev4G*), and the Austrian Science Fund (*FWF*) under project F40 (*SFB FOQUS*). The author is supported by the FWF under project W1210 (*CoQuS*).

## Software

This document was created using the `Memoir` document class for LaTeX[1]. It was written with *TeXstudio*[2] and compiled with *MikTex*[3]. Data was prepared with *Wolfram Mathematica* and plotted using the `pgfplots` package[4] and the SRON colorblind- and print-friendly color scheme[5]. Figures were created using the open-source software *Blender*[6] and *Inkscape*[7] as well as *Adobe Photoshop* and *Illustrator*.

1) Wilson and Madsen 2001
2) Zander et al. 2009
3) Schenk 2006
4) Feuersänger 2008
5) Tol 2012
6) Blender Foundation 1995
7) Bah et al. 2003

# Short contents

Part I

# Introduction

The first part of this thesis serves as an introduction in multiple ways: In chapter 1 we lay out the concept and the basic structure of the thesis before motivating the proposed experiment in chapter 2. In the last chapter of this introduction we give an overview of related fields in physics and their current technological state (chapter 3).

"I'll be honest – we're throwing science
at the wall here to see what sticks."

---

Portal 2
Erik Wolpaw, Jay Pinkerton

Chapter 1

# About this thesis

In this thesis, we lay out an experimental design based on resonantly driving a micromechanical device by a gravitational force created by a small, oscillating source mass. As we will see, with current technology this scheme should allow the detection of Newtonian gravity of a millimeter-scale system and enable us to set a new size- and mass-record for the smallest object to have a measured gravitational field.

This thesis is divided into five parts with several chapters per part. After the current introductory part I, we cover the relevant theory for the components of the project in part II split into two major focuses. First, we derive the relevant signals in the measurement scheme, which are composed of the effects of both gravity and non-gravitational forces. Second, we explain the fundamentals regarding the major experimental components such as vibration isolation and optical readout. This will lead into the derivation of the technical requirements for the implementation of the experiment. In part III we propose a concrete experimental design based on the results from the previous part, including the relevant auxiliary components, and detail the technical challenges. In the last part of the main text (part IV) we give an outlook of both short- and long-term goals for the proposed experiment and conclude with a summary and some remarks on the current state on the project. Part V includes a technical appendix and the relevant indexes.

At several instances throughout this thesis, it will become evident that the proposed experiment poses a significant challenge in precision measurement and engineering. Therefore, a large part of the presented work is concerned with foreseeable problems and potential solutions. In essence, this thesis should be seen as a comprehensive blueprint that spans over the entire development, from the abstract theoretical basis to the design of individual components.

Note that some parts of the presented thesis are directly related to a recently published, comparably compact summary of the proposed experiment

(Schmöle et al. 2016). As the author of this thesis authored said paper, we do not cite it at every instance of reference as some overlap of content is to be expected.

Chapter 2

# Motivation

The measurement of gravitational forces has been a benchmark for high-precision metrology for hundreds of years.[1] While the gravitational forces between celestial bodies are sufficiently large to dominate their dynamics, thus allowing for measurements with striking precision, laboratory-scale gravitational effects are comparably minuscule. This poses a significant challenge for detection of gravitational forces in laboratory experiments. Nevertheless, ground-based laboratory experiments have been able to achieve high-precision tests of gravity involving laboratory-scale source masses, i.e. objects generating a gravitational field. These are are typically on the order of several kilograms and heavier.[2] To the author's knowledge, the smallest source masses that have ever been used in a direct measurement of gravity were two 20 mm-diameter DyFe-cylinders in a torsional pendulum configuration, which added up to a total mass of 90 g.[3]

[1] Will 2006

[2] Gillies and Unnikrishnan 2014; Speake and Quinn 2014

[3] Ritter et al. 1990

The search for gravitational sources smaller than the aforementioned mass requires high-sensitivity force sensors, which naturally leads into the vast field of micromechanical devices. Thanks to the development of modern fabrication processes, such devices have been subject to increasing scientific interest over the last decade, resulting in sensors with unprecedented sensitivity. Examples include mechanical measurements of single electron spins[4], of superconducting persistent currents[5] and of mechanical displacement noise caused by the backaction of quantum-mechanical photon fluctuations (shot noise) in a laser beam[6]. The basic principle behind these measurements is the use of driven harmonic oscillators as transducers for small forces. The main limitation on the sensing performance of such devices is due to thermally induced amplitude fluctuations (*thermal noise*), which over a certain measurement time $T$ accumulate to a Brownian force noise $N_{\mathrm{th}}$ of equivalent amplitude $F_{N_{\mathrm{th}}} = (4\pi m\gamma)^{1/2}(T\beta)^{-1/2}$ on resonance. Here, $\beta = (k_{\mathrm{B}}\Theta)^{-1}$ denotes the thermodynamic beta (*coldness*) of the thermal bath that the oscillator is coupled to, $m$ denotes the effective mass of the device and $\gamma = \omega_0/Q$ denotes

[4] Kolkowitz et al. 2012; Rugar, Budakian, et al. 2004

[5] Bleszynski-Jayich et al. 2009

[6] Purdy, Peterson, and Regal 2013

the mechanical bandwidth that is given as the ratio of mechanical eigenfrequency $\omega_0$ and mechanical quality $Q$.[7] This sets a lower limit for the detection of external forces, even if they can be arbitrarily modulated (e.g. completely switched off in certain time intervals). As a consequence, high-$Q$ nanomechanical oscillators at low temperatures have already reported force sensitivities on the zeptonewton scale.[8] Our goal is to utilize these sensitivities as a means to the measurement of small gravitational forces.

As an introductory example, we consider a spherical lead mass of 1 mm-radius ($m \approx 40\,\mathrm{mg}$), mounted on a cantilever to yield an effective frequency of $\omega_0/(2\pi) = 100\,\mathrm{Hz}$ with a quality factor of $Q = 10^4$ at room temperature ($\theta = 297\,\mathrm{K}$). After 60 minutes of integration time, this results in a thermal noise limit of $F_{N_{\mathrm{th}}} \approx 6 \cdot 10^{-15}\,\mathrm{N}$, which corresponds to the gravitational force exerted by a mass of the same size separated by 3 mm in center-of-mass distance. That being said, such a simple estimate neglects the fact that for practical reasons the external gravitational force would have to be modulated in time, which in turn decreases the response of the sensor because of the finite modulation depth. As an order of magnitude estimate, however, it suggests that in principle it should be possible to exploit the sensitivity of state-of-the-art micromechanical devices to measure gravity between millimeter-sized objects of milligram-scale mass and possibly even below that.

As a concluding remark to this brief chapter, we emphasize that this proposal is different from experiments that probe possible deviations from Newtonian gravity at short distances, which also involve small source masses.[9] Their sensitivities and experimental configurations are targeted to put bounds on a modified force term (cf. section 3.2.3 on p. 12), while our proposal is seeking to detect the signal generated by Newtonian gravity alone. Compared to the current experimental bounds on these deviations in the regime corresponding to the dimensions of maximum sensitivity the proposed experiment, the effect of Newtonian gravity is much weaker.

7) Mamin and Rugar 2001

8) Biercuk et al. 2010; Moser et al. 2013; Schreppler et al. 2014

9) Geraci, Smullin, et al. 2008; Hamilton et al. 2015

Chapter 3

# Related topics

The proposed experiment is located at the interface of micromechanical sensing and laboratory-scale gravitation. These topics are briefly covered in this chapter. In section 3.1 we investigate micromechanical systems in the context of force-sensing and the field of cavity optomechanics. The vast field of experimental gravity is covered in section 3.2, divided into the topics of gravitational wave detection, measurements of Newton's constant $G$ as well as probings of the inverse-square law. Lastly, in section 3.3 we mention some of the models beyond present-day physics that are relevant in the context of experiments at the interface of gravity and quantum systems.

## Chapter contents



## 3.1 Micromechanics

In the last years, significant experimental progress has been made in the field of micromechanics, with a focus on the interaction between electromagnetic radiation and micromechanical motion.[a] These systems exhibit a potential for high sensitivity, making them prime candidates for a span of applications.

On the one hand, being susceptible to weak fields allows for demonstrations of fundamental effects of quantum physics. Strong coupling, an important

[a] For extensive reviews of the field of (quantum) cavity optomechanics, see e.g. the articles by Aspelmeyer, Kippenberg, and Marquardt (2014), Aspelmeyer, Meystre, and Schwab (2012), and Kippenberg and Vahala (2008).

requirement for the manipulation of micromechanical systems, has been observed in the interaction with superconducting qubits[1], electro[2]- and optomechanical[3] systems. Further noteworthy demonstrations include quantum-limited state preparation of micromechanical cantilevers in pulsed schemes[4], mechanical mode thermometry via sideband-asymmetry[5] and non-classical correlations between single photons and single mechanical phonons[6]. High-frequency oscillators have been prepared in the quantum ground state of motion in cryogenic environments with sideband-cooling by means of electromechanical[7] and optomechanical[8] interaction and without additional manipulation[9]. Further, we find entangled states of macroscopic oscillators[10] between vibrational states of spatially separate diamonds[11] and between micromechanical oscillators and microwave fields[12]. More recently, squeezed quantum states have been achieved in several micromechanical systems.[13]

1) O'Connell et al. 2010
2) Teufel, Li, et al. 2011
3) Gröblacher et al. 2009; Verhagen et al. 2012
4) Vanner et al. 2013
5) Safavi-Naeini et al. 2012
6) Riedinger et al. 2016
7) Teufel, Donner, et al. 2011
8) Chan, Alegre, et al. 2011
9) O'Connell et al. 2010
10) Müller-Ebhardt et al. 2008; Wipf et al. 2008
11) Lee et al. 2011
12) Palomaki et al. 2013
13) Lecocq et al. 2015; Pirkkalainen et al. 2015; Wollman et al. 2015

On the other hand, due to their high sensitivity, micromechanical systems can serve as sensors/transducers for extremely small forces or displacements. Examples include large-bandwidth accelerometers with n$g$ Hz$^{-1/2}$ sensitivity based on cavity-enhanced position readout[14], and zeptonewton force detection with cryogenic cantilevers[15] and carbon nanotubes[16]. Furthermore, it has been shown that the combination of a cavity-optomechanical structure with a MEMS sensing plattform allows for electrically tunable optomechanical coupling and mechanical transfer functions.[17]

14) Guzmán Cervantes et al. 2014
15) Mamin and Rugar 2001; Stowe et al. 1997
16) Moser et al. 2013
17) Miao, Srinivasan, and Aksyuk 2012

While all of the systems listed above are mechanically supported by their respective environments, there also has been increasing interest in levitated schemes. Potential realizations of levitated micromechanics include optically trapped dielectric silica spheres[18] and diamagnetically levitated superconductors[19]. While so far cooling to the ground state of motion has not been demonstrated for such systems, first instances of cavity-cooling have been achieved[20] and cooled silica nanospheres in an optical lattice were shown to exhibit zeptonewton force sensitivity at room temperature.[21]

18) Romero-Isart, Pflanzer, et al. 2011
19) Cirio, Brennen, and Twamley 2012; Romero-Isart, Clemente, et al. 2012; Schmöle 2011
20) Asenbaum et al. 2013; Kiesel et al. 2013
21) Ranjit et al. 2016

In addition to these rather new technologies, we also want to point to the extremes on the mass scale. On the side of very small and light oscillators, atom interferometry provides a method for local acceleration measurements with high precision. Acceleration noise below $3 \cdot 10^{-9}$ $g$ Hz$^{-1/2}$ has been obtained in atom-fountain experiments[22], and yoctonewton force sensitivity was demonstrated in an resonantly driven ultracold gas[23], which is just slightly above the standard quantum limit (section 6.2 on p. 56). On the very large side, gravitational wave detectors (section 3.2.1) involve huge mechanical oscillators (kilograms and more) that undergo continuous position-measurement with noise in the sub-attometer regime.

22) Sorrentino et al. 2014
23) Schreppler et al. 2014

## 3.2 Experimental gravity

Measurements of gravity have a rich history. They started with with the pioneering experiments by Maskelyne (1775), who used a pendulum to measure the gravitational attraction of a mountain and test Newton's conjecture about the value for the density of the earth. Two decades later, the torsion balance experiment by Cavendish (1798) allowed a direct measurement of Newton's gravitational constant $G$ and consequently the total mass $M_\oplus$ of the earth (as the $GM_\oplus$ product is known from astronomical observations). Now, more than two hundred years later, there is a vast range of experimental tests of gravity.[24] In addition to astronomical observations[25], there is a range of significant earth-based experiments, each sparking a number of successors that improved on sensitivity. This includes the well-known tests of the gravitational redshift with resonance spectroscopy by Pound and Rebka (1959, 1960) and the observation of gravitationally induced quantum interference in a neutron interferometer by Colella, Overhauser, and Werner (1975). Further, the atomic fountain experiments pioneered by Kasevich and Chu (1991), in which a gravity-gradient-induced phase shift is probed in a light-atom-interferometer with high accuracy, laid a significant milestone for precision measurements.[26] Other noteworthy measurements include the verification of the time dilation induced by the Earth's mass between atomic clocks that are just 0.5 m apart[27] and quantum states of ultra-cold neutrons that are bound in the gravitational field of the Earth[28]. Note that one feature these experiments have in common is that they use genuine quantum effects for precision measurement on a fixed gravitational background and therefore their full description requires the frameworks of both gravity and quantum mechanics, but not as a combined, coherent theory (cf. section 3.3).

[24] Will 2006
[25] Keith 2015
[26] Biedermann et al. 2015
[27] Chou et al. 2010
[28] Jenke, Geltenbort, et al. 2011; Nesvizhevsky et al. 2002

In the following we treat three special sub-fields (gravitational wave detectors, measurements of the gravitational constant and tests of the equivalence principle) as they are of direct relevance for the proposed experiment that is the main focus of this thesis.

### 3.2.1 Gravitational wave detectors

The existence of gravitational waves is a direct consequence of Einstein's theory of general relativity.[29] For many years gravitational waves were considered inaccessible to experimental observation due to their small amplitude. However, the discovery of super-massive astronomical objects, like neutron stars and black holes, eventually led to the notion that gravitational waves caused by these objects could indeed be discovered in earth-based observatories.[30]

[29] Einstein and Rosen 1937
[30] Cutler and Thorne 2002

The first indirect observation of gravitational waves was performed by Hulse and Taylor (1975), who measured a decrease in rotational kinetic energy

of a binary pulsar that agreed with the predicted rate of energy dissipation through gravitational waves.[31] However, as this observation of gravitational waves was indirect, a more direct confirmation remained an outstanding challenge. After several decades of development and generations of detectors[32], the first direct detection of gravitational waves was achieved in early 2016 by the advanced LIGO (aLIGO) collaboration.[33] The data is consistent with the expected signal from a merging binary black hole event that occurred 1.3 billion years ago and caused a (space-time) distortion of aLIGO's interferometer arms on the order of $10^{-21}$. The possibility to directly detect gravitational waves opens up a new field of observational astrophysics in which an entire realm of astronomical objects become accessible to our observation. As of 2017, aLIGO is ramping up towards its full performance and even more advanced gravitational wave observatories are nearing their commencement of operation: the advanced Virgo detector in Italy[34], the cryogenic KAGRA detector in Japan[35] and potentially another LIGO detector in India[36] (IndIGO). The combined signals of a network of multiple detectors not only serve as a consistency check and a measure to exclude false signals, but also allow for triangulation of the origin of the gravitational wave in space, making it a unique tool to gather knowledge about the universe[37] and thereby providing complementary data to the existing observations in the electromagnetic domain.

Gravitational wave detectors also serve as benchmark systems for state-of-the-art technology in optical sensing and vibration isolation. Advanced LIGO[38] reaches strain-noise levels of beyond $10^{-23}\,\mathrm{Hz}^{-1/2}$, corresponding to less than $4 \cdot 10^{-20}\,\mathrm{m\,Hz}^{-1/2}$ given its arm length of 4 km. This is achieved via a three-level passive and active isolation system (with each level having multiple sub-stages)[39] and opto-interferometric detection by means of an elaborate laser source[40] yielding 165 W of continuous power. To a large extent, the remaining noise is given by the intrinsic photon quantum noise and the thermal noise of the mirror suspensions and coatings.

Future generations of gravitational wave detectors, like the ground-based Einstein Telescope[41] and the space-based eLISA observatory[42] are approaching final stages of design development. These instruments could again yield vastly improved sensitivities as well as access to additional frequency bands, thereby allowing detections on a daily basis with precise determination of the physical parameters of the cosmological sources for gravitational waves.

### 3.2.2 Measurements of the gravitational constant

Surprisingly, little progress in the precise determination of Newton's constant $G$ has been made since the first measurement by Cavendish (1798). Due to the minuscule gravitational interaction between non-celestial bodies, the measurement of $G$ in laboratory-scale experiments remains a significant challenge.

31) Taylor and Weisberg 1982

32) Blair et al. 2012

33) Abbott, Abbott, Abbott, et al. 2016

34) Acernese et al. 2015

35) Flaminio and KAGRA collaboration 2016

36) Souradeep 2016

37) Klimenko et al. 2011

38) The LIGO Scientific Collaboration et al. 2015

39) Matichard et al. 2015

40) Mueller et al. 2016

41) Punturo et al. 2010

42) Amaro-Seoane et al. 2012

While astronomical observations can be done with astonishing precision, they can only yield the $GM$ product of celestial bodies. Therefore, separate measurements of $G$ are required for astronomers to determine the mass of these bodies. Current laboratory methods to measure $G$ can be divided roughly into three different classes: torsion balance-, pendulum- and differential acceleration-measurements.[43]

[43] Quinn 2000; Rothleitner and Schlamminger 2015

In the category of torsion-balance experiments we find not only the first, but also the (as of early 2017) most precise measurement of $G$ with $\Delta G/G \approx 1.4 \cdot 10^{-5}$.[44]. Here, a fiber torsion-balance setup with dynamic compensation was used with a suspended cuboid rod serving as the oscillator and spherical 8 kg source masses. Instead of the typical measurement of the oscillation period of the pendulum, the pendulum support was rotated with a constant angular velocity. Due to the gravitational force of the source masses, the pendulum was subject to a periodic modulation in deflection, which was compensated by rotation of the pendulum's support in real-time using active feedback. In this way, the deflection of the pendulum could be reduced to the equivalent noise of the deflection readout and thus, many systematic errors typically associated with the nonlinear restoring force of the fibers used for the test-mass suspension could be avoided. In addition, the entire experimental setup could be rotated with respect to the laboratory frame, therefore enabling control over systematic errors from external sources of gravitational attraction. The main remaining sources of error stem from separation measurements of the source masses, temperature variations and uncertainties in thickness and flatness of the cuboid test mass[45]. Conceptually similar torsion balance tests have been performed in other institutions, though none of them stated a higher precision[46] (see also fig. 13.1 on p. 176).

[44] Gundlach and Merkowitz 2000

[45] Mohr, Taylor, and Newell 2012

[46] Armstrong and Fitzgerald 2003; Hu, Guo, and Luo 2005; Luo et al. 2009; Newman et al. 2014; Quinn, Parks, et al. 2013; Tu et al. 2010

Another technique conceptually different from torsion pendulums is to modulate the position of fiber-suspended test masses along a linear axis by heavy sources masses in varied positions. If the test masses are equipped with mirrors and aligned such that an optical cavity is formed, the distance of the test masses can be determined with high precision. While the first iteration of the scheme was done with microwaves and yielded mediocre sensitivity compared to state-of-the-art $G$-measurements[47], the same scheme realized in the optical wavelength regime allowed to resolve the change of a few nanometers in cavity length caused by the 125 kg source masses with competitive precision[48] ($\Delta G/G \approx 2.1 \cdot 10^{-5}$). However, the latter resulted in a stated value of $G$ with a huge (seemingly systematic) offset from the average value obtained in torsion-balance experiments (cf. section 13.1 on p. 175).

[47] Kleinevoß 2002

[48] Parks and Faller 2010

In a third class of experiments $G$ is measured through changes in the local gravitational acceleration caused by massive source masses. This technique was demonstrated by measuring the change in weight of a test mass caused by

repositioning of a 6.5 ton source mass with a high-precision scale[49] ($\Delta G/G \approx 1.6 \cdot 10^{-5}$). In a conceptionally similar experiment, a double vertically-stacked atom fountain was used to measure the change in acceleration caused by varying the position of 516 kg of tungsten.[50] For an overview of source masses used throughout measurements of $G$, see e.g. Gillies and Unnikrishnan (2014).

The current recommended value for $G$ is a weighted average of the results of several different experiments[51] and has a relative precision of around $10^{-4}$. While individually published results have much higher precision (see fig. 13.1 on p. 176), comparing results of separate groups shows a spread in the absolute values that corresponds to many standard deviations.[52] One possible explanation for this phenomenon is the huge susceptibility of most of the above measurements to systematic errors that are caused by the necessarily large dimensions of the systems. The known errors include imprecision in the determination of the length scales, in the homogeneities of materials, total masses, temperature effects, distortion by external gravitational gradients and nonlinearities and suspension noise in the fiber suspensions that are used in most of the experiments – with the latter even causing significant deviations for the measured value of $G$ with different fiber types used *within the same experimental apparatus*.[53]

Today, the importance of a precise measurement of $G$ maintains a certain level of interest, though due to the well-known $GM$ product of celestial bodies, it is not required for cosmology or space engineering. From the perspective of fundamental physics, there are some attempts to derive $G$ from other, supposedly more fundamental values. However, those attempts deviate in relative predictions of the value of $G$ by more than $10^{-3}$ and therefore no determination of $G$ with higher relative precision is required to test these theories.[54] Nevertheless, the situation is certainly unpleasant on an intellectual level and hence it remains a serious experimental challenge to repeat or improve current experiments[55] or come up with entirely new schemes, e.g. deep space satellite missions[56].

### 3.2.3 Deviations from standard gravitation

As a third sub-class of laboratory-scale measurements of gravity the search for modifications of standard Newtonian gravitation on certain scales is gaining increasing interest. In essence, as a consequence of some non-standard physical theories, the typical Newtonian $r^{-1}$-potential could be modified on an (unknown) length scale $\lambda_Y$.[57] These deviations from Newtonian gravity can arise from predictions of exotic particles[58] (where $\lambda_Y$ is related to the Compton wavelength) or theories of extra dimensions[59] (where $\lambda_Y$ is be related to the radius of compactification). Other concepts of new physical models with similar consequences for Newtonian gravity include violations of the weak

[49] Schlamminger et al. 2006

[50] Rosi et al. 2014; Sorrentino et al. 2014

[51] Mohr, Newell, and Taylor 2016

[52] Speake and Quinn 2014

[53] Newman et al. 2014

[54] Gillies 1997

[55] Quinn 2016

[56] Feldman et al. 2016

[57] Geraci, Smullin, et al. 2008

[58] Brax et al. 2008; Dimopoulos and Giudice 1996

[59] Antoniadis, Dimopoulos, and Dvali 1998; Antoniadis 2005; Arkani-Hamed, Dimopoulos, and Dvali 1999; Kehagias and Sfetsos 2000

equivalence or the Lorentz-invariance principle on certain scales. In addition to yielding high-precision measurements of $G$, torsion balances also turned out to be a suitable tool for the measurements of the proposed short-range forces[60], as their basic geometry can be compacted into centimeter-scale experiments that allow for measurements of micrometer-scale effects.[61] However, some groups have also proposed and successfully used typical micromechanical systems for probes of gravity. This includes driven cantilever systems[62], optically levitated microspheres[63] and free-falling Bose-Einstein condensates[64]. Another possibility for probing Newtonian gravity is realized using precision spectroscopy of the confining potential of gravitationally bound states of neutrons.[65]

[60] Adelberger et al. 2009; Terrano 2015; Wagner et al. 2012

[61] Kapner et al. 2007

[62] Geraci, Smullin, et al. 2008; Long et al. 2003

[63] Geraci, Papp, and Kitching 2010; Rider et al. 2016

[64] Aguilera et al. 2014; Hamilton et al. 2015

[65] Jenke, Cronenberg, et al. 2014; Jenke, Geltenbort, et al. 2011

To the author's knowledge, so far no significant deviation from the standard Newtonian $r^{-1}$ potential has been discovered. In addition, even though one might intuitively believe the contrary, most of these experiments do actually not directly confirm standard gravity. This is because most experiments that probe the $r^{-1}$ potential are either specifically designed to be sensitive to all potentials *except* for $r^{-1}$, or they put an upper bound to the strength of the additional interaction that is significantly higher than the strength of actual Newtonian gravity (at a specific length scale). This means that these experiments had *zero*-outcomes and did not see any signature of gravity, so even though their sources masses are small, they can not be considered as (Newtonian) gravitational detectors. One noteworthy exception is the torsion pendulum test of the equivalence principle using polarized masses.[66] This experiment has already been mentioned in chapter 2 as the non-zero experiment with the hitherto smallest gravitational source mass. Here, a measurement of the gravitational constant with $\Delta G/G = 2.3 \cdot 10^{-2}$ could be achieved as a side result.

[66] Ritter et al. 1990

We also briefly note that short-range deviations from the gravitational $1/r$ potential are not the only prediction of non-standard physical theories that can be subject to experimental investigation. It has been proposed that higher-order corrections of the quantum commutator, that may arise from a minimal length scale through spacetime quantization, could be measured in a pulsed readout scheme of an optomechanical system.[67] A similar scheme based on residual angular-frequency modulations has already been experimentally demonstrated.[68].

[67] Kwon and Hogan 2016; Pikovski, Vanner, et al. 2012

[68] Bawaj et al. 2015

## 3.3 Non-standard physics

The development of a coherent theory that includes both the effects of general relativity and quantum mechanics in their "most extreme" cases, e.g. black holes rotating near the speed of light and massive spatial quantum superpositions, has been a major concern of modern physics and remains an outstanding challenge.[69] The first reason as to why this theory would be so interesting is, at the same time, the reason as to why it is so conceptually hard: There are funda-

[69] Kiefer 2007; Kiefer 2012; Rovelli 2007

mental discrepancies between the theories when it comes to the treatment of space and time, making it impossible to answer even simple questions, such as "What is the curvature due to gravity in a spatial superposition of mass?". The second reason is that mathematically, the respective frameworks of quantum mechanics and general relativity (i.e. Lie algebra and differential geometry) are somewhat incompatible. Perturbative approaches to a quantum theory of gravity are non-renormalizable and are therefore not considered consistent[70], while non-perturvative approaches (such as string theory) face other mathematical difficulties or are simply too underdeveloped to be considered underlying theories of quantum mechanics and relativity[71].[b]

[70] Bern 2002

[71] Manoukian 2016

One major aspect of the mechanism behind the emergence of the classical world from an underlying quantum theory could potentially be linked to the question about the validity of the superposition principle at any length scale: "Does it hold true at macroscopic scales or does it break down due to some kind of collapse or decoherence due to unknown physical effects?" Some approaches deduce the existence of collapse mechanisms from dynamical quantum effects[72] or by introducing new physical models that include microscopic and macroscopic systems as limiting cases[73] and forbid the occurrence of spatial superpositions with large separation.

[72] Ghirardi, Pearle, and Rimini 1990; Pearle 2015

[73] Ghirardi, Rimini, and Weber 1985; Ghirardi, Rimini, and Weber 1986

Another set of ideas, however, regard gravity as a driving mechanism of collapse or decoherence. These involve arguments based on, e.g., a universal gravity-induced mechanism that leads to classical trajectories and the destruction of macroscopic superpositions on short time-scales[74], the ill-definition of the quantum time on relativistic space-time leading to finite lifetimes of superpositions of energetic eigenstates and thereby to state reduction[75] and gravity as a mechanism causing the bundling of world lines in a path-integral formalism of quantum theory[76]. Further, we find predictions of decoherence through gravity as an environment in perturbative quantizations of relativity[77], through gravity as a classical communication channel between quantum systems[78], or through dephasing due to eigentime divergence[79]. We note that these approaches are not consistent in their assumption of whether gravity is classical or quantized, and that most, but not all models rely on some unknown phenomenological parameters that define the respective collapse rates for given sizes and complexities of quantum superpositions. For a more detailed overview, see e.g. Bahrami, Smirne, and Bassi (2014).

[74] Diósi 1989

[75] Penrose 1996

[76] Stamp 2012; Stamp 2015

[77] Blencowe 2013

[78] Kafri, Taylor, and Milburn 2014

[79] Pikovski, Zych, et al. 2015

Following the developments in proposals for gravity-induced collapse mechanisms is not made easier by the rising number of proposals to experimentally probe such models in novel laboratory tests. Of special interest in the context of micromechanical systems are those ideas that suggest using

[b] Note that it is possible to write down effective quantum field theories of gravity for the low-energy regime, which should yield the the correct limit for small space-time curvatures if quantum gravity exists (Blencowe 2013; Donoghue 1994).

quantum harmonic oscillators, e.g. as probes for the quantum properties of massive superpositions through gravity-induced position fluctuations[80] or for Newtonian Schrödinger-cat-states[81] and to search for squeezing signatures caused by a modified Schrödinger-evolution in the nonrelativistic limit[82]. At the same time there has been rising interest in using magnetomechanical systems to test collapse models.[83] For overviews of the current developments of experimental systems and their viability for testing the limits of macroscopic quantum states see e.g. Arndt and Hornberger (2014), Leggett (2002), and Romero-Isart (2011), as well as Howl et al. (2016) for a more general view on laboratory-scale experiments combining gravity and quantum measurements.

[80] Bahrami, Bassi, et al. 2015

[81] Anastopoulos and Hu 2015; Derakhshani, Anastopoulos, and Hu 2016

[82] Belenchia et al. 2016

[83] Pino et al. 2016

Part II

# Theory

In this part we develop the theory and perform some necessary calculations for the proposed experiment. We start by introducing a fundamental quantity of signal and noise processing, the spectral density (chapter 4). Based on this notion we investigate how a harmonic oscillator can be used as a force transducer device and derive the response to various forces (chapter 5). In the next chapter (chapter 6) we analyze the output of a specific implementation of a position-readout interferometer and show the validity of this approach. In the last chapter of this part (chapter 7) we derive the basic concepts of passive vibration isolation and develop a framework to estimate the performance of multiple chained vibration isolation stages with coupled degrees of freedom.

"You are in a maze of twisty
little passages, all alike."

---

Colossal Cave Adventure
Will Crowther

"Numbers, numbers, math math math."

---

Borderlands 2
Anthony Burch

Chapter 4

# Spectral density

In this chapter we introduce the spectral density, one of the standard tools in the analysis of signals or noise.[a] Through the notion of variance distributions (section 4.1) we motivate the definition of power (section 4.2) and energy (section 4.3) spectral densities and their relation (section 4.4). The concept is then generalized to random processes (section 4.5) and linked to autocorrelations via the Wiener-Khinchin theorem (section 4.6). In the last section we explain how the finiteness and discreteness of actual measurements impacts these concepts (section 4.7). The relevant conventions of definitions used throughout this chapter are given in appendix A.1 on p. 189.

## Chapter contents



## 4.1 Variance distributions and spectral variance density

The notion of a spectral density can be motivated by first defining the *spectral (variance) distribution* $\mathcal{S}_x(\omega)$ of the physical quantity $x(t)$ as the variance of $x(t)$ contributed by frequencies between 0 and $\omega$.[1] Throughout this thesis we will associate $t$ with time, but the concept remains unchanged for any combination of physical quantities. Naturally, $\omega$ is the angular frequency related to the

[1] Davenport and Root 1987

[a] This is by no means a complete introduction to spectral densities, but it represents the fundamental aspects that went into the calculations in this part.

parameter $t$. As, by definition, $\mathcal{S}_x$ has the same units as $x^2$, it is often referred to as a *power distribution*, even though it does not necessarily have a direct relation to physical power. In fact, this name can be somewhat misleading.

Following the above definition of $\mathcal{S}_x$ the contribution of variance within an interval $[\omega_1, \omega_2)$ will be $\mathcal{S}_x(\omega_2) - \mathcal{S}_x(\omega_1)$. We may write this as

$$\mathcal{S}_x(\omega_2) - \mathcal{S}_x(\omega_1) = \int_{\omega_1}^{\omega_2} S_x(\omega)\,\mathrm{d}\omega$$

by defining a *spectral density* (technically spectral variance density) $S_x(\omega) := \mathrm{d}\mathcal{S}_x(\omega)/\mathrm{d}\omega$. Since it has the same units as $x^2/\omega$, it can be interpreted as a density of variance distributions in frequency-space. More specifically, it is the amount of variance contributed by frequencies in the neighborhood of $\omega$ to the variance of $x$.

At this point we can introduce a useful distinction of signals. We categorize signals $x(t)$ in either continuous (e.g. periodic signals or noise) or transient. The latter one has finite support or at least converges to zero outside of a certain interval in time $t$. In mathematical terms, the continuous signals are not within the set $L_2$ of square-integrable functions, while the pulse-like signals are square-integrable.

## 4.2 Power spectral density

Approaching a measurement of a quantity $x(t)$ from a practical perspective, we find that in many cases a data point is gathered by integrating the power at a resistor dropped by a detector-generated voltage that scales linearly with the quantity of interest, e.g. the number of photons in a light field or electrons in a conductor. Since by Ohm's law the power drop at a resistor scales quadratically with the Voltage, it is very common to focus on the square of the physically interesting quantity, which gives a somewhat natural intuition for the importance of the variance distributions. Another, separate motivation comes from the fact that some rapidly-oscillating field amplitudes, such as that of light, can often not be measured directly, but only in terms of their power.[2]

[2] Goulielmakis et al. 2004

Going back to the distinction we made at the end of the previous section, for time-continuous signals, $x(t) \notin L_2$, the physical situation resembles a signal with infinite total energy. This would correspond to an experiment that is running forever, without ever being switched on or off, while the signal is recorded continuously. Instead of working with the notion of total energy, it therefore makes sense to consider energy per time, or power, which is finite for most physical situations. For such signals $x(t)$, one commonly defines the *power spectral density*[3] (PSD)

[3] Miller and Childers 2004

$$S_x(\omega) := \lim_{T\to\infty} \frac{1}{2T} \left| \int_{-T}^{T} x(t) e^{i\omega t} \, \mathrm{d}t \right|^2 ,$$

which is often written in terms of the *windowed Fourier transform* ${}_T\tilde{x}(\omega)$,

$$S_x(\omega) = \lim_{T\to\infty} |{}_T\tilde{x}(\omega)|^2 \quad \text{with} \quad {}_T\tilde{x}(\omega) = \frac{1}{\sqrt{2T}} \int_{-T}^{T} x(t) e^{i\omega t} \, \mathrm{d}t. \tag{4.1}$$

Note that this definition does not properly account for random signals. We will consider the general case in section 4.5 along with the proper definition of the PSD. If one were to omit the limit in eq. (4.1), the definition would resemble a *truncated* PSD. Note that in any real experiment, measurements can not be infinite in time. Therefore, the truncated PSD will be the physical quantity that is actually extracted, while the PSD itself is just a hypothetical construction.

We emphasize that due to the absolute square, the PSD does not entail any phase information of the signal, making the calculation of noise PSDs more convenient (see e.g. the calculation of Brownian thermal noise in section 5.7.1 on p. 45). However, especially in the context of measurements that are subject to random noise, the phase information might actually simplify signal processing. We investigate this topic in appendix B.4 on p. 200.

As we mentioned above, the PSD is suitable for signals $x(t)$ with $x(t) \notin L_2$, which means that the Fourier transform $\tilde{x}(\omega)$ of these signals will generally not exist as a function. However, it might still exist in the sense of distributions. We can use this to simplify the computation of $S_x$. Consider rewriting the finite integral of the windowed Fourier transform ${}_T\tilde{x}(\omega)$ as an infinite integral using a rectangular window function ${}_Th(t)$ as

$${}_T\tilde{x}(\omega) = \frac{1}{\sqrt{2T}} \int_{-\infty}^{\infty} {}_Th(t)x(t)e^{\mathrm{i}\omega t} \, \mathrm{d}t \quad \text{with} \quad {}_Th(t) = \begin{cases} 1 & \text{for } t \in [-T;T] \\ 0 & \text{else,} \end{cases},$$

which can be rewritten using the convolution theorem, eq. (A.2), as

$${}_T\tilde{x}(\omega) = \frac{1}{\sqrt{2T}} \frac{1}{2\pi} \left[ {}_T\tilde{h} \cdot \tilde{x} \right](\omega) \quad \text{with} \quad {}_T\tilde{h}(\omega) = 2T \, \mathrm{sinc}(\omega T). \tag{4.2}$$

This allows us to calculate the windowed Fourier transform from an infinite Fourier transform. We also note that due to the linearity in $\tilde{x}$, if $\tilde{x}$ is composed as a sum of individual terms $\tilde{x}_i$, we may compute the total ${}_T\tilde{x}$ as the sum of the individual window functions ${}_T\tilde{x}_i$,

$$\tilde{x}(\omega) = \sum_i \tilde{x}_i(\omega) \quad \Rightarrow \quad {}_T\tilde{x}(\omega) = \sum_i {}_T\tilde{x}_i(\omega) = \sum_i \frac{1}{\sqrt{2T}} \frac{1}{2\pi} \left[ {}_T\tilde{h} \cdot \tilde{x}_i \right](\omega). \tag{4.3}$$

## 4.3 Energy spectral density

As the proposed experiment and therefore all measured quantities are continuous, we will only briefly investigate the notion of the energy spectral density, which is defined for pulse-like signals. Given that $x(t) \in L_2$, the total integral of $x^2(t)$ exists and we can use Parseval's theorem (eq. (A.3)) and write

$$\int_{-\infty}^{+\infty} x(t)^2 \,\mathrm{d}t = \frac{1}{2\pi} \int_{-\infty}^{+\infty} |\tilde{x}(\omega)|^2 \,\mathrm{d}\omega.$$

In this equation, the left-hand side can be associated with total energy in $x(t)$ in the broad sense of signal processing (i.e. not necessarily physical energy).[4] With this interpretation the meaning of an *spectral energy density* can be assigned to $|\tilde{x}(\omega)|^2$. It will have the units of signal energy per frequency and for a physical scenario will usually be related to physical energy per frequency by some constants. Therefore, we define

[4] Corinthios 2009

$$S_{E,x} = \left| \int_{-\infty}^{\infty} x(t) \mathrm{e}^{i\omega t} \,\mathrm{d}t \right|^2 = |\tilde{x}(\omega)|^2$$

as the *energy spectral density*.

## 4.4 Relation between power and energy spectral density

From the above definitions, we may quickly convince ourselves that both types of spectral densities cannot be relevant physical quantities at the same time. If the limit in eq. (4.1) exists and is non-zero,

$$0 < \lim_{T\to\infty} \frac{1}{2T} \left| \int_{-T}^{T} x(t) \mathrm{e}^{i\omega t} \,\mathrm{d}t \right|^2 < \infty,$$

then clearly the energy spectral density $\left| \int_{-\infty}^{+\infty} x(t) \mathrm{e}^{i\omega t} \,\mathrm{d}t \right|^2$ has to be infinite, which is expected from the physical motivation of the definitions above. Similarly, if

$$\left| \int_{-\infty}^{+\infty} x(t) \mathrm{e}^{i\omega t} \,\mathrm{d}t \right|^2 < \infty,$$

then the limit $\lim_{T\to\infty} (2T)^{-1} \left| \int_{-T}^{T} x(t) \mathrm{e}^{i\omega t} \,\mathrm{d}t \right|^2$ has to be zero. The choice of the useful physical quantity therefore depends on the type of signal. For a transient signal, e.g. a pulse, the energy spectral density will be relevant, whereas for an infinitely lasting (e.g. periodic) signal, the power spectral density is the formally correct choice. Also, it is important to keep in mind that as both quantities require infinite measurement times, they are technically not physical.

## 4.5 Spectral density of random processes

So far, we have implicitly assumed that the considered signals are completely deterministic, i.e. $\langle x(t) \rangle = x(t)$ (where $\langle\,\rangle$ denotes the mean or expectation value). For signals that have a noisy component or are entirely composed of noise, a straightforward Fourier transform will usually be very noisy as well[5], which can render finding certain frequency peaks of interest impossible in actual measurements. Therefore, for practical scenarios, where noise is almost always an issue, it makes sense to include ensemble averages in the definitions of both spectral densities, yielding

[5] Smith 2010

$$S_x = \lim_{T\to\infty} \langle |_T\tilde{x}(\omega)|^2 \rangle\,, \quad \text{and} \quad S_{E,x} = \langle |\tilde{x}(\omega)|^2 \rangle\,. \tag{4.4}$$

These are the standard definitions of power and energy spectral density. In fact, they can also directly be applied to quantum observables, where the ensemble average is replaced by the quantum expectation value.[6] In many real-world experiments in which just a single system is available to measure, the ensemble average has to be replaced by an average over repeated measurements.[b]

[6] Clerk et al. 2010

In section 4.1 we introduced the spectral density as a *variance*. However, an ensemble or a time average of a noisy signal can only reproduce the true value of the PSD for an infinite number of samples or repeated measurements. Therefore, it makes sense to ask about the expected deviation of the measured PSD from the actual hypothetical PSD, given a finite number of samples. In other words, we have to ask about the variance of a variance. We analyze the convergence behavior for the case of *Gaussian white noise*, which is the one of main interest (section 5.7 on p. 45), in appendix A.3.1 on p. 191. There, we show that the variance $\sigma^2_{\langle x^2\rangle_M} := \langle \big(\langle x^2\rangle_M - \langle\langle x^2\rangle_M\rangle\big)^2\rangle$ of $x^2$ for a finite number $M$ of samples is given by

$$\sigma^2_{\langle x^2\rangle_M} = \frac{2}{M}\sigma_x^4.$$

It follows that the standard deviation of $S_x$ scales with $M^{-1/2}$, so *halving* the uncertainty on noise power requires to *quadruple* the measurement time.

## 4.6 Wiener-Khinchin theorem

For a special class of random processes as described below, there is a more convenient (and in many cases the only feasible) way to calculate a PSD. If the

[b] In technical data sheets, it is common to find noise power values given as root-mean-square values with physical units resembling those of $x^2$ or $x$ instead of $x^2/\omega$ or $x/\sqrt{\omega}$. This is discussed in more detail in appendix B.3 on p. 200.

autocorrelation function

$$r_x(\tau) := \langle x(t)\bar{x}(t-\tau)\rangle$$

(with the complex conjugate $\bar{x}(t)$) of the signal $x(t)$ is known, the PSD can be calculated as its Fourier transform since

$$S_x(\omega) = \int_{-\infty}^{\infty} r_x(\tau)\mathrm{e}^{i\omega\tau}\,\mathrm{d}\tau. \tag{4.5}$$

The proof for this relation can be found in appendix A.3.2 on p. 192. It is important to note that in the definition of $r_x$ we implicitly assumed that the autocorrelation will not depend on the absolute time $t$, but only on the relative time difference $\tau$.[c] A physical situation that yields such an $x(t)$ is usually referred to as *wide sense stationary random process* (*stationäre Zufallsprozesse im weiteren Sinn*), and the Wiener-Khinchin theorem will in general *not* be valid for a process that does not fulfill this criterion. As the adjective *random* implies, there are hardly any deterministic functions $x(t)$ that the Wiener-Khinchin theorem can be applied to and therefore, in the case of a deterministic drive (like a force modulation), the general Wiener-Khinchin theorem can not be used. For some cases, the notion above can be varied to allow the direct computation of power spectral densities from autocorrelation functions (see e.g. Behunin et al. (2014)), though an investigation of this method was not performed within the scope of this thesis.

## 4.7 Finite times, discrete sampling and window functions

The concepts of infinite measurement times and continuous sampling are mere hypothetical constructions and do not represent practical experimental situations. We can technically implement finite measurement times by omitting the limit out of the definition of the PSD (eq. (4.4)). As shown in appendix B.2.2, the impact of finite sampling intervals can be modeled by introducing the discrete Fourier transform of a finitely sampled window function, $\tilde{h}_f(\omega) := \sum_{n=-\infty}^{\infty} {}_T h(n\Delta t)\mathrm{e}^{\mathrm{i}\omega n\Delta t}\Delta t$. Here, $\Delta t$ denotes the sampling time step and ${}_T h(t)$ does not necessarily need to be a rectangular window function. The windowed Fourier transform of $x(t)$ is then calculated as

$${}_T\tilde{x}(\omega) = \frac{1}{\sqrt{2T}}\frac{1}{2\pi}\left[\tilde{h}_f \cdot \tilde{x}\right](\omega). \tag{4.6}$$

For the simple case of a rectangular window function, ${}_T h(t) = \begin{cases} 1 & \text{for } t\in[-T;T], \\ 0 & \text{else} \end{cases}$, we find that

$$\tilde{h}_f(\omega) = 2T\,\mathrm{sinc}(\omega T)\frac{\exp(-\mathrm{i}\omega\Delta t/2)}{\mathrm{sinc}(\omega\Delta t/2)},$$

[c] Note that this in particular means that $\langle|x(t)|^2\rangle$ is constant in time $t$, i.e. stationary.

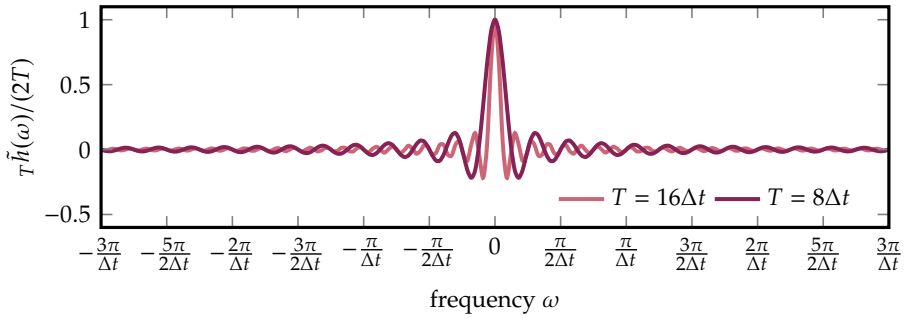


(a) Continuously sampled $_T\tilde{h}(\omega) = 2T\,\mathrm{sinc}(\omega T)$.

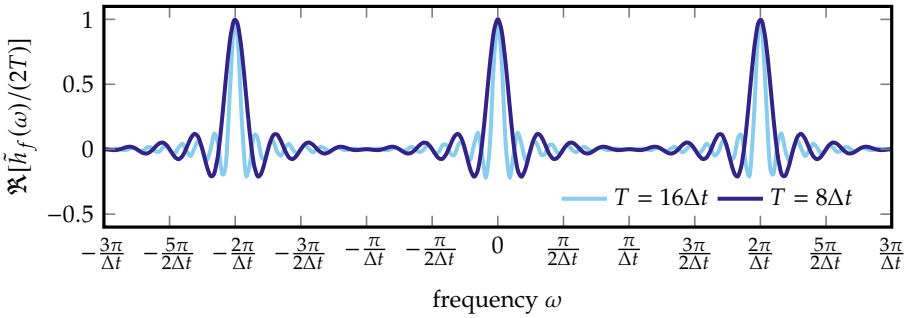


(b) Real part of discretely sampled $\tilde{h}_f(\omega) = 2T\,\mathrm{sinc}(\omega T)\exp(-\mathrm{i}\omega\Delta t/2)\,\mathrm{sinc}^{-1}(\omega\Delta t/2)$.

**Figure 4.1:** Convolution functions for the hypothetical case of continuous sampling and the real case of discrete sampling, given a rectangular window function $_Th(t)$ as defined above.

while the general case is shown in eq. (B.3) on p. 198. This function is periodic in frequency $\omega$ with period $\omega_p = 2\pi/\Delta t$ and modulated with rate $\omega_m = 2\pi/T$, which is visualized in fig. 4.1. We see that frequency contributions are smoothly "binned" into intervals of width $\omega_m$ due to the finite measurement time, and higher-frequency contributions (above $\omega_p$) are shifted back and added to lower ones due to the finite sampling (a more general formulation of this effect is referred to as the *Nyquist–Shannon sampling theorem*[7]). The simple choice of a rectangular window $_Th(t)$ is usually called a *periodogram* in the context of PSD estimation methods, and it represents the most basic estimation method for a PSD. For an in-depth analysis of spectrum estimation methods, see e.g. Boashash (2015) and Brown and Hwang (2012). The role of window functions is investigated further in appendix B.2.2 on p. 198.

[7] Luke 1999

Equation (4.6) reveals a fundamental problem for any measurement in which high-frequency contributions have non-negligible size. If those contributions are not resolved by sufficiently short measurement timesteps $\Delta t$, they will contribute to the estimated spectrum at lower frequencies, an effect

called *aliasing*. The only way to circumvent this effect is to implement physical low-pass filters that dissipate the power of high-frequency contributions into a bath.

Chapter 5

# Harmonic oscillators for force measurements

In this chapter we introduce a one-dimensional system with a linear restoring force, the harmonic oscillator, as a device for force measurements. For this, a purely classical description is convenient and therefore we will remain in a classical framework unless we explicitly need to consider quantum effects.

The aim of the analysis is to understand a system composed of a spherical harmonic oscillator (*test mass*) that is driven in multiple ways: By a spherical driving mass (*source mass*), by motion of its support (both deterministic and stochastic), by various deterministic forces $F_i$ that depend on the total distance between the center-of-mass (COM) of the oscillator and the driving system, and by zero-mean stochastic noise terms. We start by deriving the equation of motion in section 5.1 before considering the explicit effects of a sinusoidal force excitation by a source-mass motion (section 5.2) and additional noise (section 5.3). This will lead to expressions for the total power spectral density and power spectrum in section 5.4 and, equivalently, the driven amplitude of the harmonic oscillator in section 5.5. We then consider a range of actual forces (section 5.6), sources of noise (section 5.7) and non-standard corrections (section 5.8). A specific drive amplitude yields an optimal signal, which we investigate in section 5.9. We close this chapter with technical remarks on the effective mass of oscillator modes (section 5.10) and optimal mass shapes (section 5.11).

## Chapter contents

## 5.1 Equation of motion

We refer to a physical system as a harmonic oscillator if the most significant force $F$ acting on it is linear and restoring (i.e. opposing deflections with spring constant $k$) in the position coordinate $x$,

$$m\ddot{x} = F, \qquad F = -kx + \dots .$$

This is Newton's second law, where $m$ denotes the mass of the system. Without additional force contributions, once excited the restoring force $F$ will cause the system to oscillate with the eigenfrequency $\omega_0^2 = k/m$. We now generalize this system to include a variety of additional forces, including damping, as

$$\begin{aligned} \ddot{x}' + \omega_0'^2(x' - x_{\text{sup}}) = & -\gamma'_{\text{int}}\dot{x}' - \gamma'_{\text{sup}}(\dot{x}' - \dot{x}_{\text{sup}}) \\ & + m^{-1}\left(\sum_i F'_i(d_{\text{tot}}, \dot{d}_{\text{tot}}) + \sum_i N_i\right). \end{aligned} \tag{5.1}$$

Here, we rename the position coordinate to $x'$ and the eigenfrequency to $\omega'_0$ as we will later define a new, shifted coordinate $x$ and effective eigenfrequency $\omega_0$. We introduce the coordinate of the support $x_{\text{sup}}$ of the spring that is causing the restoring force, an intrinsicn (viscous) damping rate $\gamma_{\text{int}}$ of the oscillator and a spring damping rate $\gamma_{\text{sup}}$.[a] The system is driven by various (not

[a] An example for an intrinsic damping rate, i.e. one that does not depend on the relative support deflection, is damping through drag by gas molecules. A counter-example is the spring damping caused by internal material losses, which depends on the relative deflection $x' - x_{\text{sup}}$.

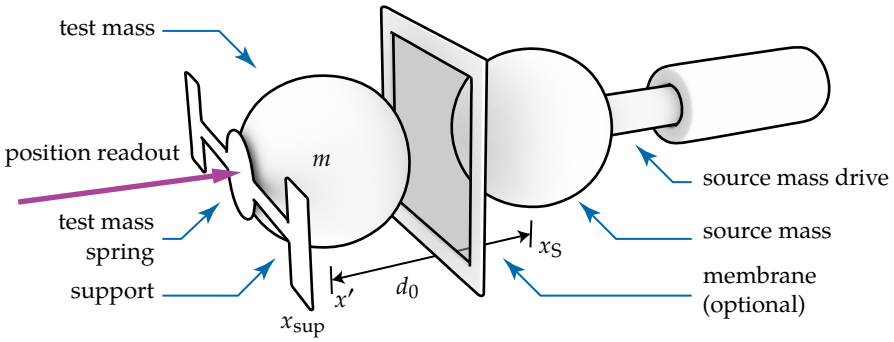


**Figure 5.1:** Basic system composed of the test mass and the source mass. Also shown is the mechanism that moves the source mass (*source-mass drive*), an optional shielding membrane and the optical beam for position readout we treat in chapter 6.

necessarily deterministic) forces $F_i'$ that depend only on the total distance $d_{\mathrm{tot}}$ (and its derivatives) between the center-of-mass (COM) of the oscillator and the driving system. Practically this means that the forces we consider are static and will only become time-dependent through the action of the motion of the driving system. Lastly, we added zero-mean stochastic force noise terms $N_i$. Implicitly we have to assume that the physical dynamics of this system are fully described by the COM coordinates (and therefore do not depend on the shape of the masses), which, as we see in section 5.11 on p. 51, is not necessarily true. From here on, we refer to the oscillator as the *test mass* and to the driving system as the *source mass*.

In order to obtain linearized force terms and derive a solution to eq. (5.1), we write the time-dependent distance as $d_{\mathrm{tot}} = d_0 + x_{\mathrm{S}} - x'$ (see fig. 5.1), where $d_0$ is the (static) COM distance with both masses being non-deflected and $x_{\mathrm{S}}(t)$ is the drive displacement. We can then expand the force terms as

$$\begin{aligned}
&\sum_i F_i'(d_0 + x_{\mathrm{S}} - x', \dot{x}_{\mathrm{S}} - \dot{x}') \\
&\quad\approx \sum_i \underbrace{F_i'(d_0 + x_{\mathrm{S}}, \dot{x}_{\mathrm{S}})}_{=:F_i(x_{\mathrm{S}}, \dot{x}_{\mathrm{S}})} + \underbrace{\sum_i \partial_{x'} F_i'\big|_{d_0,0}}_{=:-m\xi}\, x' + \underbrace{\sum_i \partial_{\dot{x}'} F_i'\big|_{d_0,0}}_{=:-m\zeta}\, \dot{x}' \\
&\qquad + \text{higher orders of } x',\, \dot{x}' + \text{mixed terms with } x_{\mathrm{S}},\, \dot{x}_{\mathrm{S}},
\end{aligned} \tag{5.2}$$

with $|_{d_0,0}$ being used as *evaluated at* $d_{\mathrm{tot}}{=}d_0$ *and* $\dot{d}_{\mathrm{tot}}{=}0$. We define $\xi$ and $\zeta$ as the relevant displacement and velocity gradient amplitudes. The newly defined force term $F_i(x_{\mathrm{S}}, \dot{x}_{\mathrm{S}})$ now describes the dynamic (i.e. non-static) effects. It can

be expanded as

$$\sum_i F_i(x_\mathrm{S}, \dot{x}_\mathrm{S}) = \underbrace{\sum_i F_i(0,0)}_{=:m\varsigma} + \underbrace{\sum_i \partial_{x_\mathrm{S}} F_i\big|_{0,0}}_{=m\xi} x_\mathrm{S} + \underbrace{\sum_i \partial_{\dot{x}_\mathrm{S}} F_i\big|_{0,0}}_{=m\zeta} \dot{x}_\mathrm{S} + \sum_{n_1,n_2=1}^{\infty} \underbrace{\sum_i \frac{1}{n_1! n_2!} \frac{\partial^{n_1+n_2}}{\partial x_\mathrm{S}^{n_1} \partial \dot{x}_\mathrm{S}^{n_2}} F_i(x_\mathrm{S}, \dot{x}_\mathrm{S})\Big|_{0,0}}_{=:m\Xi(n_1,n_2)} x_\mathrm{S}^{n_1} \dot{x}_\mathrm{S}^{n_2}. \tag{5.3}$$

In the first term we introduce a new definition $\varsigma$, which sums up the absolute amplitude of forces at the point of the test mass. The associations of the second and third term with $m\xi$ and $m\zeta$ follow from eq. (5.2). The last term of the sum includes all the second- and higher-order force terms. Inserting eq. (5.3) into eq. (5.1) yields the simplified oscillator equation of motion,

$$\ddot{x} + \gamma\dot{x} + \omega_0^2 x = \omega_0'^2 x_\mathrm{sup} + \gamma'_\mathrm{sup}\dot{x}_\mathrm{sup} + \xi x_\mathrm{S} + \zeta\dot{x}_\mathrm{S} + \sum_{n_1,n_2=1}^{\infty} \Xi(n_1,n_2) x_\mathrm{S}^{n_1}\dot{x}_\mathrm{S}^{n_2} + m^{-1}\sum_j N_j. \tag{5.4}$$

Here, we defined

$$\omega_0^2 := \omega_0'^2 + \xi, \quad \gamma := \gamma'_\mathrm{int} + \gamma'_\mathrm{sup} + \zeta, \quad \text{and} \quad x := x' - \varsigma\omega_0^{-2} \tag{5.5}$$

as the new effective frequency $\omega_0$, damping rate $\gamma$ and position $x$ due to the presence of forces with non-zero static components, respectively. We see that while the shift of position $x$ scales with the 0th-order amplitude of the forces (related to $\varsigma$), frequency $\omega_0$ and damping rate $\gamma$ are only affected by the spatial displacement and velocity *gradients* and higher derivatives expressed through $\xi$ and $\zeta$. The magnitude of the change in position and frequency for the specific case of gravity is investigated in section 8.3 on p. 86.

### 5.1.1 Homogeneous solution

For later reference we briefly mention the homogeneous solution of eq. (5.4). Dropping all external force and driving terms, the equation becomes

$$\ddot{x} + \gamma\dot{x} + \omega_0^2 x = 0.$$

With the ansatz $x(t) = \exp(\omega_\mathrm{hom} t)$ we can quickly see that

$$\omega_\mathrm{hom} = -\frac{\gamma}{2} \pm \frac{\mathrm{i}}{2}\sqrt{4\omega_0^2 - \gamma^2}$$

is a solution to the equation. The general homogeneous solution will be the sum of both solutions to $x_{\mathrm{hom}}(t)$, with arbitrary complex amplitudes, which we choose such that $x_{\mathrm{hom}}$ is real as

$$x_{\mathrm{hom}}(t) = \mathrm{e}^{-\gamma t/2}\left[A_1 \cos\left(t\sqrt{\omega_0^2 - \gamma^2/4}\right) + A_2 \sin\left(t\sqrt{\omega_0^2 - \gamma^2/4}\right)\right], \tag{5.6}$$

where $A_1$ and $A_2$ are real-valued amplitudes that depend on the boundary conditions. Due to the common prefactor $\exp(-\gamma t/2)$ this solution will decay to a fraction $1/\mathrm{e}$ of the original amplitude after a time $\tau = 2/\gamma$.

### 5.1.2 Frequency-space representation

Most linear differential equations can be drastically simplified by converting them into Fourier space. Applying the conventions listed in appendix A.1, the oscillator equation of motion, eq. (5.4), can be rewritten as

$$\begin{aligned}\underbrace{\left(\omega_0^2 - \omega^2 - \mathrm{i}\gamma\omega\right)}_{=:\chi(\omega)^{-1}}\tilde{x} = {} & \underbrace{\left(\omega_0'^2 - \mathrm{i}\gamma'_{\mathrm{sup}}\omega\right)T_{\mathrm{E}}(\omega)}_{=:A_{\mathrm{E}}(\omega)}\tilde{x}_{\mathrm{E}} \\ & + \underbrace{\left[\left(\omega_0'^2 - \mathrm{i}\gamma'_{\mathrm{sup}}\omega\right)T_{\mathrm{S}}(\omega) + \xi - \mathrm{i}\omega\zeta\right]}_{=:A_{\mathrm{S}}(\omega)}\tilde{x}_{\mathrm{S}} \\ & + \sum_{n_1,n_2=1}^{\infty}\Xi(n_1,n_2)\mathcal{F}[x_{\mathrm{S}}^{n_1}\dot{x}_{\mathrm{S}}^{n_2}] + m^{-1}\sum_j \tilde{N}_j.\end{aligned} \tag{5.7}$$

Here, $\chi(\omega) = (\omega_0^2 - \omega^2 - \mathrm{i}\gamma\omega)^{-1}$ is the *susceptibility*[b], $A_{\mathrm{S}}(\omega)$ is the Fourier amplitude component of the system that is caused by the linearized forces, and $A_{\mathrm{E}}(\omega)$ is the amplitude component caused by environmental displacements. This form of eq. (5.7) is achieved by splitting up the support motion into an environmental statistical noise and a drive contribution with their respective *transmissibilities*, $\tilde{x}_{\mathrm{sup}} = T_{\mathrm{E}}(\omega)\tilde{x}_{\mathrm{E}} + T_{\mathrm{S}}(\omega)\tilde{x}_{\mathrm{S}}$. $T_{\mathrm{E}}$ and $T_{\mathrm{S}}$ are the frequency-dependent functions that describe how a finite amplitude excitation is modulated after progressing from the point of deflection to the test-mass oscillator.[c] These definitions slightly simplify eq. (5.7) as

$$\tilde{x}(\omega) = \tilde{X}_{\mathrm{S}}(\omega) + \tilde{X}_{\mathrm{E}}(\omega) + \tilde{X}_N(\omega) + \tilde{X}_\Xi(\omega), \tag{5.8a}$$

[b] A definition that varies from the one used here by a factor of $m^{-1}$ is commonly encountered in the standard literature and also commonly referred to as *compliance* (as it converts physical force to displacement units). We use this definition as it allows to directly see how mass ratios of coupled oscillators affect the dynamics, which becomes useful in chapter 7, and because it slightly simplifies many expressions throughout this thesis.

[c] The assumption that such functions exist is an implicit simplification, as it neglects the backaction within coupled oscillator systems. We review these effects in section 7.4 on p. 78.

where we defined the individual Fourier contributions

$$\tilde{X}_{\mathrm{S}}(\omega) := \chi(\omega) A_{\mathrm{S}}(\omega) \tilde{x}_{\mathrm{S}}, \tag{5.8b}$$

$$\tilde{X}_{\mathrm{E}}(\omega) := \chi(\omega) A_{\mathrm{E}}(\omega) \tilde{x}_{\mathrm{E}}, \tag{5.8c}$$

$$\tilde{X}_{N}(\omega) := \chi(\omega) m^{-1} \sum_{i} \tilde{N}_{i}, \tag{5.8d}$$

$$\tilde{X}_{\Xi}(\omega) := \chi(\omega) \sum_{n_1, n_2 = 1}^{\infty} \Xi(n_1, n_2) \mathcal{F}[x_{\mathrm{S}}^{n_1} \dot{x}_{\mathrm{S}}^{n_2}]. \tag{5.8e}$$

Here, $\tilde{X}_{\mathrm{S}}(\omega)$ includes all the linear contributions that depend on the dynamics of the source mass, while $\tilde{X}_{\Xi}(\omega)$ has all the second- and higher-order contributions. $\tilde{X}_{\mathrm{E}}(\omega)$ represents the environmental displacement noise and $\tilde{X}_{N}(\omega)$ is statistic noise that does not depend on the source-mass position.

In the following, we make a few simplifications. The first one is to drop the nonlinear contributions $\tilde{X}_{\Xi}(\omega)$ for now. Even though they are important for the evaluation of actual signal data, at this point we will start our analysis by being mainly interested in slightly better than order-of-magnitude estimations.[d] Some straightforward arguments can be made that would say that while including $\tilde{X}_{\Xi}(\omega)$ does not change the mathematical nature of the problem, it greatly increases the computational complexity, which is investigated in appendix A.3.6. The second simplification is that we will assume that all force terms that depend on the source-mass dynamics are deterministic, i.e. free of statistic noise. This is trivially true for forces in the classical limit, such as gravity and the Coulomb force. However, some forces, such as those caused by electromagnetic patch-potentials (section 5.6), do in principle have distance-dependent statistical components too. Within this framework, there is essentially no problem with including these effects; however, the necessary calculations have not been performed within the scope of this thesis.

As pointed out when previously defining the PSD (eq. (4.4) on p. 23), it will eventually be necessary to compute an ensemble average over the absolute square of the total windowed Fourier transform. Using the above two simplifications, we may carry out these calculations individually for $\tilde{X}_{\mathrm{S}}(\omega)$, $\tilde{X}_{\mathrm{E}}(\omega)$ and $\tilde{X}_{N}(\omega)$, which greatly simplifies the computation. The justification for doing so comes from the fact that the expectation value of statistically uncorrelated effects vanishes from the total PSD. The technical form of this argument is presented in appendix A.3.5 on p. 193.

[d] It is important to be conscious about the degree of expected deviations of this approximation from an exact solution depending on the nonlinearity of the force that is approximated. For example, while a force that scales with inverse-square distance (such as gravity) can be reasonably approximated by a linearizion even in the near field, forces with much higher orders in distance-dependency, such as the London-vd. Waals force (section 5.6.4), are poorly approximated by such a simplification.

## 5.2 Effect of a sinusoidal source drive

To further process the previous results, we assume an explicit form of the source-mass motion. The simplest case is a sinusoidal modulation

$$x_S(t) := d_S \cos(\omega_S t) \tag{5.9}$$

with amplitude $d_S$ and driving frequency $\omega_S$. In appendix B.5 on p. 203 we demonstrate that to first order of the modulated displacements, this case is equivalent to a source mass rotating in a circular motion. The Fourier transform of $x_S(t)$ is a distribution,

$$\tilde{x}_S(\omega) = d_S \pi \left(\delta(\omega - \omega_S) + \delta(\omega + \omega_S)\right).$$

Inserting this expression into eq. (5.8b) yields

$$\tilde{X}_S(\omega) = \chi(\omega) A_S(\omega) d_S \pi \left(\delta(\omega - \omega_S) + \delta(\omega + \omega_S)\right). \tag{5.10}$$

As becomes clear from eq. (4.3) on p. 21, due to the linearity of the windowed Fourier transform we may proceed by calculating the individual windowed Fourier transform for the drive contribution. Inserting eq. (5.10) into eq. (4.2) on p. 21 allows us to compute the windowed Fourier transform through a convolution of the infinite Fourier transform with a rectangular window function ${}_T\tilde{h}(\omega) = \begin{cases} 1 & \text{for } t \in [-T;T], \\ 0 & \text{else} \end{cases}$. This is trivial as $\tilde{X}_S(\omega)$ is composed of Dirac $\delta$ functions, so

$$\begin{aligned} {}_T\tilde{x}_S(\omega) &= \frac{1}{\sqrt{2T}} \frac{1}{2\pi} \left[{}_T\tilde{h} \cdot \tilde{X}_S\right](\omega) \\ &= \frac{d_S}{2\sqrt{2T}} \left[{}_T\tilde{h}(\omega - \omega_S)\chi(\omega_S)A_S(\omega_S) + {}_T\tilde{h}(\omega + \omega_S)\chi(-\omega_S)A_S(-\omega_S)\right], \end{aligned}$$

and using the explicit form of ${}_T\tilde{h}(\omega)$ from eq. (4.2) on p. 21,

$$\begin{aligned} \ldots = \frac{d_S\sqrt{2T}}{2} &\left[\operatorname{sinc}\left((\omega - \omega_S)T\right)\chi(\omega_S)A_S(\omega_S)\right. \\ &\left. + \operatorname{sinc}\left((\omega + \omega_S)T\right)\chi(-\omega_S)A_S(-\omega_S)\right]. \end{aligned}$$

For the calculating the PSD, we require the absolute square of this quantity. Given the simplifications made at the end of section 5.1, and the argument in appendix A.3.5 on p. 193, we may neglect the other contributions of the total windowed Fourier transform ${}_T\tilde{x}(\omega)$ for now and focus on the source contribution ${}_T\tilde{x}_S(\omega)$. As $x(t)$ is real-valued, we can use eq. (A.1) on p. 190 and

calculate the absolute square of ${}_T\tilde{x}_S(\omega)$ as

$$\begin{aligned}
|{}_T\tilde{x}_S(\omega)|^2 &= {}_T\tilde{x}_S(\omega)\,{}_T\tilde{x}_S(-\omega) \\
&= \frac{d_S^2 T}{2}\Big\{|\chi(\omega_S)|^2\,|A_S(\omega_S)|^2 \\
&\qquad \cdot \left[\mathrm{sinc}^2\left((\omega-\omega_S)T\right)+\mathrm{sinc}^2\left((\omega+\omega_S)T\right)\right] \\
&\quad + \left[\chi(\omega_S)^2 A_S(\omega_S)^2 + \chi(-\omega_S)^2 A_S(-\omega_S)^2\right] \\
&\qquad \cdot \mathrm{sinc}\left((\omega-\omega_S)T\right)\mathrm{sinc}\left((\omega+\omega_S)T\right)\Big\}\,.
\end{aligned} \tag{5.11}$$

The PSD will then be given by the limit of this expression for $T \to \infty$. Due to the asymptotic behavior of the sinc function, in this limit the second contribution of eq. (5.11) will vanish at every point where $\omega \neq \pm\omega_D$. However, at the two resonances the function will not converge, but will instead be bounded by a finite sinusoidal oscillation. In a naive physicist notation we write this as

$$\mathrm{sinc}\left((\omega-\omega_D)T\right)\mathrm{sinc}\left((\omega+\omega_D)T\right)T \xrightarrow{T\to\infty} \delta_{\omega,\pm\omega_D} I_{[-1;+1]},$$

where $\delta_{a,b}$ denotes the Kronecker delta function and $I_{[-1;+1]}$ is a symbolic expression for values in the intervall between $-1$ and 1. This contribution has zero support and is finitely bounded. Since the spectral density only has a physical meaning when integrated over a certain bandwidth (see eq. (5.16) on p. 37), we can omit the second part of eq. (5.11) completely.[e] For the first contribution of eq. (5.11), we use that $\lim_{T\to\infty} T\,\mathrm{sinc}^2(\omega T) = \pi\delta(\omega)$, which is proven in appendix A.3.3. This allows us to calculate

$$\begin{aligned}
S_{xS} &= \lim_{T\to\infty}\langle|{}_T\tilde{x}_S(\omega)|^2\rangle \\
&= d_S^2\frac{\pi}{2}\,|\chi(\omega_S)|^2\,\langle|A_S(\omega_S)|^2\rangle\left[\delta(\omega-\omega_S)+\delta(\omega+\omega_S)\right].
\end{aligned} \tag{5.12}$$

Here, we made use of the fact that the ensemble average needs to, if at all, only be applied to $A_S(\omega_S)$ as only this term can contain statistical force contributions, while $\chi(\omega)$ and $\delta(\omega)$ are deterministic. Recalling that we defined $A_S$ such that

$$A_S(\omega_S) = \left(\omega_0'^2 - \mathrm{i}\gamma'_{\mathrm{sup}}\omega\right)T_S(\omega) + m^{-1}\sum_i \partial_{x_S}F_i\big|_{0,0} + \mathrm{i}\omega m^{-1}\sum_i \partial_{\dot{x}_S}F_i\big|_{0,0}\,,$$

another problem of working with PSDs becomes evident. Due to the absolute square, the deterministic force contributions in $A(\omega_S)$, which are necessarily correlated as they originate from the same source mass, will create cross terms

[e] As we pointed out in section 4.7 on p. 24 and explain more detailed in appendix B.2.2 on p. 198, the most physical representation of the PSD is actually one where the limit $T \to \infty$ is never performed. Therefore, for increased precision measurement, one might indeed need to properly incorporate the term we just argued to be omitted.

between separate forces. This is critical if a certain force, here gravity, is supposed to dominate all other contributions by a certain margin, as there will be mixed terms between gravity and non-gravitational forces in the signal. As all forces drive the test mass with the same frequency $\omega_S$, they will be impossible to distinguish. This problem can in principle be resolved by taking the square root of the measured PSD, but this is again causing other difficulties if the PSD also includes contributes without square cross terms. Therefore, it is important to know the non-gravitational force terms well, and it might be necessary to take extra-care with respect to shielding them properly from the test mass or even choosing a favorable distance regime.

As another important observation we see that every force or noise acting on the test mass is modulated with the mechanical susceptibility. This means that improving the mechanical properties of the test mass (especially the damping rate) might not necessarily improve the measurement if other effects dominate the gravitational contribution. Also, we note that switching from the PSD to a evaluation quantity that entails phase information can yield a possible improvement when separating deterministically driven signals from noise-driven contributions (see appendix B.4 on p. 200), but it does not help with the distinction of deterministic signals caused by different forces.

## 5.3 Effect of noise terms

We proceed in computing the PSD terms by processing the statistical noise terms. Inserting the previous expression for the noise contributions, eq. (5.8d) on p. 32, into the rewritten windowed Fourier transform, eq. (4.2) on p. 21, yields

$$ {}_T\tilde{x}_N(\omega) = \frac{1}{\sqrt{2T}} \frac{1}{2\pi} \left[ {}_T\tilde{h} \cdot \left( \chi m^{-1} \sum_i \tilde{N}_i \right) \right] (\omega) \quad \text{with} \quad {}_T\tilde{h}(\omega) = 2T \operatorname{sinc}(\omega T), $$

which enables us to calculate the PSD using the standard definition (eq. (4.4) on p. 23) as

$$ \begin{aligned} m^2 S_{xN} &= \lim_{T\to\infty} \langle |{}_T\tilde{x}_N(\omega)|^2 \rangle \\ &= \lim_{T\to\infty} \frac{1}{(2\pi)^2} \iint_{-\infty}^{+\infty} \mathrm{d}\omega' \mathrm{d}\omega'' \Bigg[ 2T \operatorname{sinc}((\omega-\omega')T) \operatorname{sinc}((\omega-\omega'')T) \\ &\qquad \cdot \chi(\omega')\chi(-\omega'') \sum_{i,j} \langle \tilde{N}_i(\omega') \tilde{N}_j(-\omega'') \rangle \Bigg], \end{aligned} $$

where we used that $\bar{\chi}(\omega) = \chi(-\omega)$, $\bar{\tilde{N}}_i(\omega) = \tilde{N}_i(-\omega)$. To further process this expression, we assume that all noise terms $N_i(t)$ are uncorrelated and white

(see also appendix A.3.5 on p. 193), i.e.

$$\langle \tilde{N}_i(\omega)\tilde{N}_j(\omega')\rangle = 2\pi\delta_{i,j}S_{N_i}(\omega)\delta(\omega+\omega').$$

This simplifies the above to

$$m^2 S_{xN} = \frac{1}{2\pi}\int_{-\infty}^{+\infty} \mathrm{d}\omega' \left[\left(\lim_{T\to\infty} 2T\,\mathrm{sinc}^2((\omega-\omega')T)\right)|\chi(\omega')|^2 \sum_i S_{N_i}(\omega')\right].$$

Again, we can make use of knowing the limit derived in appendix A.3.3 on p. 192, which yields

$$\begin{aligned}\ldots &= \frac{1}{2\pi}\int_{-\infty}^{+\infty} \mathrm{d}\omega' \left[2\pi\delta(\omega-\omega')\,|\chi(\omega')|^2 \sum_i S_{N_i}(\omega')\right] \\ &= |\chi(\omega)|^2 \sum_i S_{N_i}(\omega).\end{aligned}$$

Therefore, the final result is

$$S_{xN} = m^{-2}\,|\chi(\omega)|^2 \sum_i S_{N_i}(\omega). \tag{5.13}$$

In analogue fashion, we can compute the contribution of environmental vibrations $S_{x_\mathrm{E}}$ via eq. (5.8c). The expression is

$$S_{x\mathrm{E}} = |\chi(\omega)|^2\,|A_\mathrm{E}(\omega)|^2\,S_{x_\mathrm{E}}(\omega). \tag{5.14}$$

## 5.4 Total power spectral density and power spectrum

We combine the previous results in order to derive an expression for the total power spectral density. It is given by the sum of the individual contributions of source drive (S), further noise terms (N) and environmental vibrations (E), eqs. (5.12) to (5.14), as

$$\begin{aligned}S_x(\omega) &= S_{x\mathrm{S}}(\omega) + S_{x\mathrm{N}}(\omega) + S_{x\mathrm{E}}(\omega) \\ &\quad + \text{nonlinear source motion terms and cross terms}\end{aligned} \tag{5.15a}$$

with

$$S_{x\mathrm{S}}(\omega) = d_\mathrm{S}^2\frac{\pi}{2}\,|\chi(\omega_\mathrm{S})|^2\,\langle|A_\mathrm{S}(\omega_\mathrm{S})|^2\rangle\,[\delta(\omega-\omega_\mathrm{S})+\delta(\omega+\omega_\mathrm{S})]\,, \tag{5.15b}$$

$$S_{xN}(\omega) = m^{-2}\,|\chi(\omega)|^2 \sum_i S_{N_i}(\omega), \tag{5.15c}$$

$$S_{x\mathrm{E}}(\omega) = |\chi(\omega)|^2\,|A_\mathrm{E}(\omega)|^2\,S_{x_\mathrm{E}}(\omega), \tag{5.15d}$$

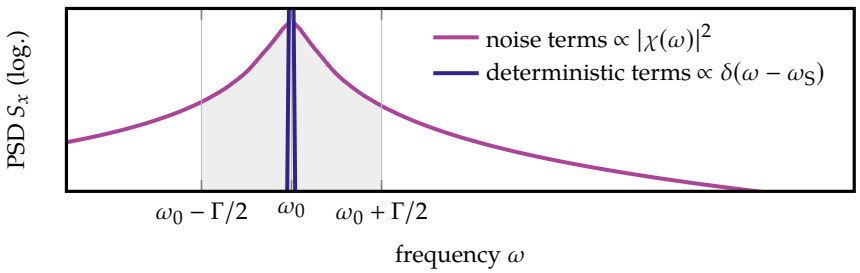


**Figure 5.2:** Visualization of eq. (5.16) for the resonant drive $\omega_S = \omega_0$. The gray area under the purple curve equals the (displacement) power spectrum $P_x$ of the noise terms, while the power of the deterministic terms lies entirely within the blue delta peak, which for the purpose of demonstration was replaced by a peak with non-zero width.

where

$$\chi(\omega) = \left(\omega_0^2 - \omega^2 - \mathrm{i}\gamma\omega\right)^{-1}, \tag{5.15e}$$

$$A_S(\omega) = \left(\omega_0'^2 - \mathrm{i}\gamma'_{\mathrm{sup}}\omega\right) T_S(\omega) + \xi + \mathrm{i}\omega\zeta, \tag{5.15f}$$

$$A_E(\omega) = \left(\omega_0'^2 - \mathrm{i}\gamma'_{\mathrm{sup}}\omega\right) T_E(\omega), \tag{5.15g}$$

$$\xi = m^{-1} \sum_i \partial_{x_S} F_i\big|_{0,0} \quad \text{and} \quad \zeta = m^{-1} \sum_i \partial_{\dot{x}_S} F_i\big|_{0,0}\,. \tag{5.15h}$$

From eq. (5.15f) we immediately see that the magnitude of wanted force contributions in $\xi$ can easily be dominated by the mechanical displacement due to the drive, $(\omega_0'^2 - \mathrm{i}\gamma'_{\mathrm{sup}}\omega)T_S(\omega)$, when the drive displacement attenuation (described by the transfer function $T_S(\omega_0)$) is not high enough.

In order to find the *power spectrum* contributions $P_x$ in an actual measurement with finite measurement time $\tau$, we have to integrate the PSD $S_x$ over a finite bandwidth $\Gamma = 2\pi/\tau$ around the (driven) frequency of interest $\omega_S$. Here, that can be the resonance frequency $\omega_0$ of the harmonic oscillator for a *resonant* measurement, or, alternatively, a lower frequency for an *off-resonant* measurement,

$$P_x(\omega_S) = \int_{\omega_S - \Gamma/2}^{\omega_S + \Gamma/2} S_x(\omega)\,\mathrm{d}\omega. \tag{5.16}$$

The integration is visualized in fig. 5.2. It can be performed numerically, but in order to come up with analytical estimations for the resonant case, we assume that the measurement bandwidth $\Gamma$ is much smaller than the mechanical width $\gamma$.[f] For the finite-width PSD contributions, the power is

[f] Technically, we also have to assume that it is much broader than the width of the sinusoidal

then approximated by the product of the contribution at $\omega_0$ and the width of the measurement band $\Gamma$,

$$\begin{aligned} P_x(\omega_S) &= P_{xS}(\omega_S) + P_{xN}(\omega_S) + P_{xE}(\omega_S) \\ &\quad + \text{nonlinear source motion terms and cross terms,} \end{aligned} \tag{5.17a}$$

where the contributions in the resonant ($\omega_S = \omega_0$) and off-resonant ($\omega_S = \omega_{off} < \omega_0 -$ some $\gamma$) are

$$P_{xS}(\omega_0) = \frac{\pi}{2}\frac{d_S^2}{(\gamma\omega_0)^2}\left\langle |A_S(\omega_0)|^2 \right\rangle, \qquad P_{xS}(\omega_{off}) \approx \frac{\pi}{2}\frac{d_S^2}{\omega_0^4}\left\langle |A_S(\omega_{off})|^2 \right\rangle, \tag{5.17b}$$

$$P_{xN}(\omega_0) \approx \frac{\Gamma}{(m\gamma\omega_0)^2}\sum_i S_{N_i}(\omega_0), \qquad P_{xN}(\omega_{off}) \approx \frac{\Gamma}{m^2\omega_0^4}\sum_i S_{N_i}(\omega_{off}), \tag{5.17c}$$

$$P_{xE}(\omega_0) \approx \frac{\Gamma}{(\gamma\omega_0)^2}|A_E(\omega_0)|^2 S_{x_E}(\omega_0), \quad P_{xE}(\omega_{off}) \approx \frac{\Gamma}{\omega_0^4}|A_E(\omega_{off})|^2 S_{x_E}(\omega_{off}), \tag{5.17d}$$

where we used that $\chi(\omega)$ is approximately constant for all frequencies from zero up to a few $\gamma$ below the resonance frequency $\omega_0$, so $|\chi(\omega_{off})|^2 \approx \omega_0^{-4}$, as well as $|\chi(\omega_0)|^2 = (\gamma\omega_0)^{-2}$. These are the main results of this chapter and will serve as a reference for many of the following discussions. In the next section we take a short detour and establish the relation between the PSD or the power spectrum and the actual amplitude of the driven harmonic oscillator.

## 5.5 Driven amplitude

The actual time-domain displacement amplitude of the driven mechanical oscillator, $X_S$, is of relevance for the optical readout (chapters 6 and 11) in terms of range and discretization. We start the calculation with the Fourier representation of the deterministically driven amplitude contribution, eq. (5.10) on p. 33, and apply the inverse Fourier transform (with the convention given in appendix A.1 on p. 189),

$$\begin{aligned} X_S(t) &= \frac{1}{2\pi}\int_{-\infty}^{+\infty} \chi(\omega)A_S(\omega)d_S\pi\left(\delta(\omega-\omega_S)+\delta(\omega+\omega_S)\right)e^{-i\omega t}d\omega \\ &= d_S\left\{\Re\left[\chi(\omega_S)A_S(\omega_S)\right]\cos(\omega_S t) + \Im\left[\chi(\omega_S)A_S(\omega_S)\right]\sin(\omega_S t)\right\}. \end{aligned} \tag{5.18}$$

drive. Here, we set the drive to have zero width, however, in an actual experiment with very long measurement times (and therefore small $\Gamma$), it might be necessary to take care when selecting the reference signal for the driven motion (see also section 10.1.2 on p. 121).

The second line holds as $\bar{\chi}(\omega) = \chi(-\omega)$ and identically for $A_S(\omega)$. Using the definitions of $\chi$ and $A_S$ from eq. (5.7) on p. 31, we find

$$\Re\left[\chi(\omega_S)A_S(\omega_S)\right] = \frac{(\omega_0^2 - \omega_S^2)(\omega_0'^2 T_S(\omega_S) + \xi) + \gamma\omega_S^2(\gamma'_{sup}T_S(\omega_S) + \zeta)}{(\omega_0^2 - \omega_S^2)^2 + \gamma^2\omega_S^2},$$
$$\Im\left[\chi(\omega_S)A_S(\omega_S)\right] = \frac{\gamma\omega_S(\omega_0'^2 T_S(\omega_S) + \xi) - \omega_S(\omega_0^2 - \omega_S^2)(\gamma'_{sup}T_S(\omega_S) + \zeta)}{(\omega_0^2 - \omega_S^2)^2 + \gamma^2\omega_S^2}.$$

On resonance, i.e. $\omega_S = \omega_0$, and in the weak-force limit $\omega_0' \approx \omega_0$, the expressions simplify to

$$\Re\left[\chi(\omega_0)A_S(\omega_0)\right] = \gamma^{-1}\left(\gamma'_{sup}T_S(\omega_0) + \zeta\right), \tag{5.19a}$$
$$\Im\left[\chi(\omega_0)A_S(\omega_0)\right] = \gamma^{-1}\left(\omega_0 T_S(\omega_0) + \omega_0^{-1}\xi\right). \tag{5.19b}$$

Inserting eqs. (5.19a) and (5.19b) back into eq. (5.18) yields the resonantly driven amplitude

$$X_{S,res}(t) := d_S\gamma^{-1}\left[\left(\gamma'_{sup}T_S(\omega_0) + \zeta\right)\cos(\omega_0 t) + \left(\omega_0 T_S(\omega_0) + \omega_0^{-1}\xi\right)\sin(\omega_0 t)\right]. \tag{5.20}$$

These results have a straightforward interpretation. Setting the source-mass transfer function to zero, $T_S = 0$, the amplitude is $X_{S,res}(t) = d_S\gamma^{-1}[\zeta\cos(\omega_0 t) + \omega_0^{-1}\xi\sin(\omega_0 t)]$. Recalling that the original drive motion was defined as a cosine function without a phase shift (eq. (5.9) on p. 33), we should expect that the resonantly driven motion will pick up a $\pi/2$ phase shift and behave as $\cos(\omega_0 t - \pi/2) = \sin(\omega_0 t)$. Indeed, since

$$\xi = m^{-1}\sum_i \partial_{x_S}F_i\big|_{0,0} \quad \text{and} \quad \zeta = m^{-1}\sum_i \partial_{\dot{x}_S}F_i\big|_{0,0},$$

the sine term in eq. (5.20) contains the effects of deterministic forces that depend on relative position, while the cosine term contains the velocity-dependent effects.[g] The transfer function $T_S$ appears in both terms of eq. (5.20), however, in the sine contribution they are larger by a factor of $\omega_0/\gamma_{sup}$, which corresponds to the mechanical quality $Q_{sup}$ of the test-mass support.

We may at this point also ask how the integrated power spectral density, the power spectrum, relates to the actual amplitude. Comparing the time-domain amplitude of the resonant drive, eq. (5.20), to the deterministic power spectrum contribution, eq. (5.17b), and recalling that the PSD does not entail phase information, we realize that the amplitude in the power spectrum is

[g] Also, recall that $\gamma = \gamma'_{int} + \gamma'_{sup} + \zeta$ and therefore the velocity-dependent force contributions $\zeta$ will also indirectly appear in the sin terms.

given by the sum of squared amplitudes of the cosine and sine contributions in eq. (5.20).

Another way to quickly relate the actual driven amplitude to the PSD is to repeat the computation done in section 5.2 on p. 33, but start by specifically setting the motion of the test mass to be sinusoidal instead. Doing so one quickly finds that

$$x(t) := d_A \cos(\omega_T t) \quad \Rightarrow \quad S_x = d_A^2 \pi \left(\delta(\omega - \omega_T) + \delta(\omega + \omega_T)\right),$$

so an amplitude $d_A$ of actual sinusoidal motion results in a Dirac delta function PSD with amplitude $d_A^2 \pi$.

## 5.6 Deterministic force contributions

The main purpose of the proposed experiment is to measure gravity. Gravity is known to dominate all other forces at large distances, however, at microscopic distances, gravity can be dwarfed by other effects. In this section we discuss a number of forces that potentially come into play. We divide them into deterministic forces and noise, where the latter is treated in section 5.7.

Since most of the forces analyzed below depend on the geometry of the source and test masses, we have to make specific assumptions about their density-distributions. Thus far we have treated both masses as being point-like. For the case of a $1/r$ potential, such as gravity, this is equivalent to rotationally symmetric masses[1] (*shell theorem*). To simplify the treatment of the system, we assume that both masses are homogeneous and spherical with radii $r_T$, $r_S$. The shortest distance between the surfaces of the spheres is then given by $d_{tot} - r_T - r_S$, which will be a common expression in the analysis below.

[1] Newton 1726

### 5.6.1 Newtonian gravity

For rotationally symmetric masses, classical (instantaneous) Newtonian gravity outside the surface does not depend on the radial density distribution but only on the total mass. It takes the well-known form

$$F_G = -G\frac{mM}{d_{tot}^2}. \tag{5.21}$$

To simplify the discussion, we assume that the effective mass of the oscillator mode (see section 5.10 on p. 50) is identical to the gravitational mass.[h]

[h] As we lay out in section 9.1 on p. 94, at least in the first iterations of the proposed experiment, the test mass will likely be a compound system consisting of a micromechanical cantilever or trampoline, which provides the restoring force for the harmonic oscillator, and an added,

As we will later need to calculate the optimal value of the drive amplitude (section 5.9 on p. 49), we calculate the power spectral contribution of the gravitational forces. Using the expression for the deterministic power spectrum terms, eq. (5.17b), and reducing the deterministic amplitude to the gravitational contribution, $A_{SG} := m^{-1} \sum_i \partial_{x_S} F_G\big|_{0,0}$, we write down the "pure" gravitational power spectrum

$$P_{x\mathrm{G}}(\omega) = |\chi(\omega)|^2 \frac{\pi}{2} d_S^2 \langle |A_{SG}(\omega_S)|^2 \rangle = |\chi(\omega)|^2 2\pi (GM)^2 \frac{d_S^2}{d_0^6}, \tag{5.22a}$$

$$P_{x\mathrm{G}}(\omega_0) = 2\pi \left(\frac{GM}{\gamma\omega_0}\right)^2 \frac{d_S^2}{d_0^6}, \quad P_{x\mathrm{G}}(\omega_{\mathrm{off}}) = 2\pi \left(\frac{GM}{\omega_0^2}\right)^2 \frac{d_S^2}{d_0^6}. \tag{5.22b}$$

Similarly, we can write down the harmonic amplitude that is induced by the gravitational drive. Reducing eq. (5.20) to the gravitational contribution, we write

$$X_{S,\mathrm{res}_G}(t) = \frac{\xi_G d_S}{\gamma\omega_0} \sin(\omega_0 t) = \frac{2GM}{\gamma\omega_0} \frac{d_S}{d_0^3} \sin(\omega_0 t). \tag{5.23}$$

### 5.6.2 Coulomb force

For the Coulomb force we consider the (worst) case in which all free additional charges are located at the closest possible positions on the sphere surfaces (see fig. 5.3(a)). This means that the distance of the attracting/repulsive centers is not given by the COM distance $d_{\mathrm{tot}}$, but by the surface distance $d_{\mathrm{tot}} - r_T - r_S$, as

$$F_q = \frac{1}{4\pi\epsilon_0} \frac{q_1 q_2}{(d_{\mathrm{tot}} - r_T - r_S)^2}, \tag{5.24}$$

with the charges $q_1$ and $q_2$ on the test and source mass.

### 5.6.3 Electrostatic force due to a fixed potential difference

If both spheres are conductors with a relative potential difference $V_0$, one can give expressions for the two limiting cases of close approach and widely separated spheres (Lekner 2012a,b). They are

$$F_{\mathrm{estat}} = \begin{cases} -\frac{1}{4} V_0^2 \frac{r_T r_S}{r_T + r_S} (d_{\mathrm{tot}} - r_T - r_S)^{-1}, & (d_{\mathrm{tot}} - r_T - r_S)/d_{\mathrm{tot}} \ll 1 \\ -V_0^2 \left(\frac{r_T r_S}{r_T + r_S}\right)^2 d_{\mathrm{tot}}^{-2}, & d_{\mathrm{tot}} \gg r_T + r_S. \end{cases}$$

comparably heavy mass. Neglecting the mass of the micromechanical device is reasonable as the gravitational dynamics of the compound test-mass device should be dominated by the added mass. However, once the proposed experiment progresses to the stage of a quantitative precision measurement, this simplification may have to be reinvestigated.


(a) Dimensions $d_{tot}$, $r_T$ and $r_S$ and worst-case positions of charges (red and blue).

(b) The gas molecules are scattered off the big sphere equally in all directions while a fraction $\pi r_s^2/(4\pi d_{tot}^3)$ hits the small sphere.

**Figure 5.3:** Vizualisations of dimensions for the location of charges and effects of residual gas molecules.

This situation does not necessary relate to the proposed experiment. However, setting both masses on a fixed potential difference yields and artificial, tunable force that might serve for, e.g., calibration purposes.

### 5.6.4 London-Van der Waals force

The surface separation in the proposed setup is much larger than typical interaction distances of forces emerging from dipole fluctuations (i.e. London-vd. Waals, Casimir-Polder and Casimir forces)[i]. However, we want to be convinced that any of the aforementioned effects do not contribute significantly to the signal.

We can extract an expression for the London-vd. Waals force by calculating the spatial derivative $\mathrm{d}E_y/\mathrm{d}x$ of the sphere-sphere potential expression given by Hamaker (1937, eq. (13)), which we find to be

$$F_{\mathrm{VDW}} = A_{\mathrm{VDW}} \frac{32 r_{\mathrm{T}}^3 r_{\mathrm{S}}^3 d_{\mathrm{tot}}}{3(d_{\mathrm{tot}} - r_{\mathrm{T}} - r_{\mathrm{S}})^2 (d_{\mathrm{tot}} - r_{\mathrm{T}} + r_{\mathrm{S}})^2 (d_{\mathrm{tot}} + r_{\mathrm{T}} - r_{\mathrm{S}})^2 (d_{\mathrm{tot}} + r_{\mathrm{T}} + r_{\mathrm{S}})^2}. \tag{5.25}$$

Here, $A = \pi^2 Q_1 Q_2 \lambda_{1-2}(d_{\mathrm{tot}})$ is the (distance-dependent) Hamaker coefficient, with $Q_{1,2}$ denoting the atom number per cubic centimeter of both materials and $\lambda_{1-2}(d_{\mathrm{tot}})$ being the material- and distance-dependent London-vd. Waals constant.

### 5.6.5 Casimir force

For the effect of the Casimir force between two spherical surfaces we find two different expressions in Teo (2012), which hold in near- and far-field

[i] Insights into how these forces are related are given for example by Genet et al. (2003) and Rodriguez, Capasso, and Johnson (2011).

approximations, respectively:

$$F_{\text{Cas}} = \begin{cases} F_{\text{Cas,near}} & \text{for } d_{\text{tot}}(\beta\hbar c)^{-1} \ll 1 \\ F_{\text{Cas,far}} & \text{for } d_{\text{tot}}(\beta\hbar c)^{-1} \gg 1 \end{cases}, \tag{5.26}$$

with

$$\begin{aligned} F_{\text{Cas,near}} &= \frac{7\pi^3}{5760}\hbar c \frac{r_{\text{T}} r_{\text{S}}}{r_{\text{T}} + r_{\text{S}}}(d_{\text{tot}} - r_{\text{T}} - r_{\text{S}})^{-3} + \frac{\pi}{45}\frac{1}{\beta^4\hbar^3 c^3}\frac{r_{\text{T}} r_{\text{S}}}{r_{\text{T}} + r_{\text{S}}}(d_{\text{tot}} - r_{\text{T}} - r_{\text{S}}), \\ F_{\text{Cas,far}} &= \frac{3}{32\beta}\frac{r_{\text{T}} r_{\text{S}}}{r_{\text{T}} + r_{\text{S}}}(d_{\text{tot}} - r_{\text{T}} - r_{\text{S}})^{-2}\zeta(3), \end{aligned} \tag{5.27}$$

with the Riemann zeta function $\zeta(z)$ and thermodynamic beta $\beta$. As we will see when physically evaluating the expressions in chapter 8, only the far field region is of interest in the proposed experiment.

### 5.6.6 Patch potentials

Another possible signal contribution is due to non-contact friction caused by time-dependent electric fields (patch potentials), which is a known effect for conducting surfaces.[2] For the effect of patch potentials, an expression for the interaction energy per unit area in the isotropic-material case was originally presented by Speake and Trenkel (2003) and can be found with a slightly more rigorous derivation in Kim et al. (2010, eq. (11)). Note that the relevant expression in the latter publication has been adjusted by removing the contribution at infinite separation. Adding it back, we arrive at

[2] Burnham, Colton, and Pollock 1992; Stipe et al. 2001

$$U_{\text{patch}}/A = \frac{\epsilon_0}{2}\int_{k_{\text{min}}}^{k_{\text{max}}} k^2 \coth\left[k(d_{\text{tot}} - r_{\text{T}} - r_{\text{S}})\right] S(k)\,\mathrm{d}k,$$

where $k$ denotes the wave number of the interacting electromagnetic wave and $k_{\text{min}}$, $k_{\text{max}}$ denote the boundaries of the relevant wave number range. $S(k)$ is the PSD of patch distributions in spatial frequency space. Following Kim et al. (2010, eq. (19)) we may estimate the latter as

$$S(k) \approx \frac{2V_{\text{rms}}^2}{k_{\text{max}}^2 - k_{\text{min}}^2},$$

with the RMS potential fluctuations $V_{\text{rms}}$. The underlying assumption for this expression is that the surface patch-potential correlations are constant in a certain wave number range $k_{\text{min}} < k < k_{\text{max}}$. Taking the derivative $\frac{\partial}{\partial d_{\text{tot}}}$ of the patch potential per unit area and multiplication by the effective area $A_{\text{eff}}$ yields the expression for a static force due to patch effects,

$$|F_{\text{patch}}| \approx A_{\text{eff}}\frac{\epsilon_0 V_{\text{rms}}^2}{k_{\text{max}}^2 - k_{\text{min}}^2}\frac{\partial}{\partial d_{\text{tot}}}\int_{k_{\text{min}}}^{k_{\text{max}}} \frac{k^2 \exp(-k(d_{\text{tot}} - r_{\text{T}} - r_{\text{S}}))}{\sinh(k(d_{\text{tot}} - r_{\text{T}} - r_{\text{S}}))}\,\mathrm{d}k. \tag{5.28}$$

We emphasize that by this notion we have reduced the effect of patch effects to a static, distance-dependent force between two spheres. The effects of both random fluctuations and velocity-dependence (friction) have been neglected but could be included for a more precise evaluation. However, we can assume that the effect of the statistic contributions will at most have a magnitude on the same order as the averaged fluctuations above, and it can be further suppressed with increased measurement times.

### 5.6.7 Transfer of momentum kicks through gas molecules

Residual gas molecules can not only cause friction (cf. section 9.3.1 on p. 100 on damping by residual gas molecules), but also facilitate an effective momentum transfer between moving bodies. In our specific situation, the moving source mass will add momentum onto each molecule that is reflected off its surface. This momentum can then be transfered onto the test mass and in effect cause an extra force. In the following, we derive an upper bound on the force resulting from this effect. We assume that the pressure is sufficiently low for both masses to be in the molecular regime (see section 9.3.1), i.e. we can completely neglect the interactions between individual gas molecules. Then the rate $R_{\mathrm{coll}}$ at which air molecules will hit the source mass is[3]

[3] Chang et al. 2010

$$R_{\mathrm{coll}} = \pi\beta P v_{\mathrm{air}} r_{\mathrm{S}}^2,$$

where $v_{\mathrm{air}} = (\beta m_{\mathrm{air}})^{-1/2}$ is the average velocity of air molecules. The fraction of these air molecules that is scattered towards the spherical test mass can be estimated by comparing the cross-sectional area of the test mass, $\pi r_{\mathrm{T}}^2$, to the virtual surface area $4\pi r^3$ of a sphere that is defined by sharing its origin with the source mass and radius equal to the COM distance between the two masses as the radius, $r = d_{\mathrm{tot}}$ (fig. 5.3(b)). Therefore, the rate $R_{\mathrm{S}\to\mathrm{T}}$ at which air molecules that were previously scattered off the source mass hit the test mass is given by

$$R_{\mathrm{S}\to\mathrm{T}} = \frac{r_{\mathrm{T}}^2}{4d_{\mathrm{tot}}^2} R_{\mathrm{coll}}.$$

Compared to a gas molecule, the test and source masses are large. This implies that every scattered molecule will carry twice the source-mass velocity as additional velocity after elastically colliding with the source mass. By the same notion, twice the molecule's momentum is transfered onto the test mass in direct hits. We may assume that, apart from the additional velocity contribution due to the source-mass modulation, the equally distributed kicks from all directions cancel out, so only the momentum difference caused through the motion of the source mass is relevant. The effective force can then be expressed

in terms of rate of momentum transfers, or

$$|F_{\text{kick}}(t)| \lesssim 4 m_{\text{air}} \dot{d}_{\text{tot}} R_{\text{B}\to\text{S}} = \frac{r_{\text{T}}^2}{d_{\text{tot}}^2} R_{\text{coll}} m_{\text{air}} \dot{d}_{\text{tot}}. \tag{5.29}$$

Of course, the direct correspondence between the sphere velocity and the force will only work if the momentum transfer by air molecules is quasi-instantaneous compared to the typical time scales of the system.

## 5.7 Noise contributions

Without diving deeply into the theory of (quantum) noise, below we analyze major contributors to noise in the proposed experiment. Following Clerk et al. (2010), we assume that the noise processes are *wide-sense stationary*, i.e. the autocorrelation function of the noise terms only depends on the time difference, not on absolute time (cf. section 4.6 on p. 23). Then, by the central limit theorem[4], due to the large number of involved independent and identically distributed instances (such as photons in a laser beam), the distribution of the average will be Gaussian, independent of the underlying distribution. This is why in systems composed of many particles, one often assumes *Gaussian noise*, which conveniently is completely specified by its mean and autocorrelation function.

[4] Billingsley 2012

Recalling the Wiener-Khinchin theorem, eq. (4.5), the autocorrelation function $r_x$ is related to the PSD via

$$r_x(t) = \frac{1}{2\pi} \int_{-\infty}^{\infty} S_x(\omega) \mathrm{e}^{-i\omega t} \, \mathrm{d}\omega. \tag{5.30}$$

It is evident that autocorrelations with short timescales imply spectral densities which are non-zero over a large band of frequencies. The most extreme case of this is *white noise*, which has a flat (i.e. frequency independent) PSD and a delta-like autocorrelation,

$$r_x(t) = S_x \delta(t) \quad \Leftrightarrow \quad S_x \text{ is constant,}$$

which will be of relevance in the next section.

### 5.7.1 Brownian force noise

From the equipartition theorem we know that for a system in thermal equilibrium, every contribution to its total energy has mean value equal to $(2\beta)^{-1}$, where $\beta = (k_{\text{B}}\Theta)^{-1}$ is the thermodynamic beta with the Boltzmann constant $k_{\text{B}}$ and temperature $\Theta$.[5] The thermal noise, in this case Brownian force noise, poses a true fundamental limit on the minimal detectable force using mechanical systems. Here, we perform a rough derivation of Brownian noise for

[5] Butt and Jaschke 1995

a single-mode oscillator. For a more in-depth derivation, see e.g. Clerk et al. (2010, appendix A.1).

We assume that the thermal force noise $N_{\mathrm{th}}(t)$ is white and Gaussian, i.e.

$$r_{N_{\mathrm{th}}}(t-t') = \langle N_{\mathrm{th}}(t) N_{\mathrm{th}}(t') \rangle = S_{N_{\mathrm{th}}} \delta(t-t').$$

Following eq. (5.13), we write down the displacement PSD contribution caused by thermal force noise as

$$S_{x\,\mathrm{th}} = m^{-2} \left|\chi(\omega)\right|^2 S_{N_{\mathrm{th}}},$$

which, as $S_{N_{\mathrm{th}}}$ is constant, we may easily integrate over the entire spectral width once knowing the required integral of $|\chi(\omega)|^2$, which we give in eq. (A.7) on p. 193:

$$\int_{-\infty}^{+\infty} S_{x\,\mathrm{th}}\, \mathrm{d}\omega = \pi \frac{1}{m^2} \frac{1}{\gamma \omega_0^2} S_{N_{\mathrm{th}}}. \tag{5.31}$$

From the identity eq. (A.4) on p. 190 we also know that

$$\int_{-\infty}^{+\infty} S_{x\,\mathrm{th}}\, \mathrm{d}\omega = 2\pi \lim_{T\to\infty} \frac{1}{2T} \int_{-T}^{+T} \langle x(t)^2 \rangle \, \mathrm{d}t = 2\pi \left\langle x(t)^2 \right\rangle, \tag{5.32}$$

where the second equality has to hold as white noise is stationary, and therefore $\langle x(t)^2 \rangle$ is constant in time. Now we may make use of the relation between the variance $\langle x(t)^2 \rangle$ and the thermal and mechanical properties of the system using the equipartition theorem[6]

[6] Pathria and Beale 2011

$$m\omega_0^2 \langle x^2 \rangle = \beta^{-1}. \tag{5.33}$$

Combining eqs. (5.31) to (5.33) yields

$$S_{N_{\mathrm{th}}} = 2\frac{m\gamma}{\beta} \quad \text{and} \quad S_{x\,\mathrm{th}} = \left|\chi(\omega)\right|^2 \frac{2\gamma}{m\beta}. \tag{5.34}$$

Of course, real devices rarely have just a single mechanical mode, and therefore the effective thermal PSD will be given by the sum of individual thermal noise PSDs for each mechanical mode, where the mass $m$ is then given by the effective mass of the individual modes for a given readout position (see section 5.10).

It is sometimes said (see e.g. Stowe et al. (1997)) that thermal noise poses a fundamental limit for the detection of forces, "$F_{\mathrm{min}} = \sqrt{2m\gamma\Gamma/\beta}$", where $\Gamma = 2\pi/T$ is the bandwidth of the measurement. This expression is derived by integrating $S_{N_{\mathrm{th}}}$ in eq. (5.34) over a bandwidth $\Gamma$ and taking the square root of the result. Even though this quantity has the physical units of force, it is

only equivalent to the smallest detectable force in a limiting case. Specifically, in order to reach this limit, the measurement would have to either be taken at $\omega = 0$ ($DC$), which implies infinite $1/\omega$ noise (cf. section 5.7.3), or the force of magnitude $A$ needs to be modulated over the entire range from $-A$ to $+A$, at a certain signal frequency. The latter is possible in some cases, e.g. if the forces are caused by externally generated fields with direct modulation of the field amplitude. In our case, however, we create the force modulation by motion of an external mass. Therefore, without the masses being able to pass through each other, it is difficult to achieve this kind of modulation.[j] However, we can rephrase the expression above and state that $\Delta F_{\mathrm{min}} = \sqrt{2m\gamma\Gamma/\beta}$ is a lower limit for the resolvable force *modulation*, i.e. the difference between both extrema of the force (in the case of harmonic modulation). The fact that one has to implicitly assume some kind of optimal modulation between said points is closely related to the existence of a finite optimal driving amplitude, which we investigate in section 5.9 on p. 49.

### 5.7.2 Photon backaction

The use of light for the readout of mechanical motion implies some kind of interaction, as every photon carries momentum that is partially transfered onto the system at the moment of reflection. The net action of these momentum kicks can carry a signature of the readout-photon distribution. Here, we differentiate between two effects. The first one is the direct impact of photon momentum, which, similar to the Heisenberg microscope[7], physically changes the state of the mechanical system (photon *backaction*). We investigate this below. The second effect is the statistical uncertainty, or measurement imprecision, in the detection of a photon readout beam due to the photon statistics (photon *shot noise*), which we investigate in section 6.1 as part of the optical readout scheme.

[7] Heisenberg 1930

We start with the momentum $\hbar k$ carried by a single photon. A perfect reflection of this photon will cause a transfer of a total momentum $2\hbar k$. The force PSD of photon impacts is given by

$$S_{N_{\mathrm{ph}}} = (2\hbar k)^2 S_{R_{\mathrm{ph}}},$$

where $R_{\mathrm{ph}}$ denotes the rate of photon impacts per unit time. Assuming a coherent state of light, we can follow Clerk et al. 2010, appendix G to calculate the PSD of the photon rate $R_{\mathrm{ph}}$, which for the special case of a normally distributed rate turns out to be

$$S_{R_{\mathrm{ph}}} = \langle R_{\mathrm{ph}} \rangle .$$

[j] In one dimension, this kind of modulation is simply impossible. However, one might envision a two-dimensional scheme with a source mass moving along an elliptical path that effectively causes such a modulation to a test mass that is constraint to one axis.

The power $P$ of a light beam is given by the single photon energy times the photon rate, $P = \hbar\omega_{\mathrm{ph}} \langle R_{\mathrm{ph}} \rangle = \hbar c k \langle R_{\mathrm{ph}} \rangle$. With the wave number $k = 2\pi/\lambda$, we find that

$$S_{N_{\mathrm{ph}}} = 8\pi\hbar \frac{P}{\lambda c}.$$

Relating this to a displacement PSD using eq. (5.13) on p. 36, the effect of photon backaction is

$$S_{x\,\mathrm{ph}} = m^{-2} \left|\chi(\omega)\right|^2 8\pi\hbar \frac{P}{\lambda c}. \tag{5.35}$$

The notion that a measurement of a system may impact the system itself is of course a well established concept in the realm of quantum systems. However, it also plays a role in vastly macroscopic setups.[8] As an interesting side remark, comparing the expression to those by Clerk et al. (2010) (who are using the same conventions for the PSD) yields that reflection off a single mirror is mathematically equivalent to a (appropriately tuned) cavity with finesse $F = \pi/2$.

[8] Murch et al. 2008; Purdy, Peterson, and Regal 2013

### 5.7.3 Environmental noise

Due to the limited knowledge about the general laboratory environment, achieving an analytic derivation of the environmental noise PSD $S_{x_{\mathrm{E}}}(\omega)$ in eq. (5.17d) on p. 38 is unfeasible. However, we may expect a noise background that roughly follows a common $1/f$ curve[9]. There is some uncertainty as to why exactly $1/f$ noise is so common in both natural and urban environments, but the consensus seems to be that is a general manifestation of complex systems.[10] Even though the effect of deterministic forces in eq. (5.17b) scales very favorably when transitioning to lower frequencies $\omega_0$, due to $1/f$ noise there can be practical limitations in the form of minimal feasible frequencies for any given physical experiment, depending on the specific laboratory environment.

[9] Westphal 2016, p. 33

[10] Bak and Sneppen 1993; Mandelbrot 1999; Milotti 2002

## 5.8 Contributions from non-Newtonian gravity

There are two qualitatively different types of corrections to Newtonian gravity we might consider in the context of the proposed experiment. First, a Yukawa-Newtonian potential, which we motivated in section 3.2.3 on p. 12. It takes the form

$$\Phi_{G,\mathrm{Yukawa}} = -G\frac{mM}{d_{\mathrm{tot}}}\left(1 + \alpha_{\mathrm{Y}} \mathrm{e}^{-d_{\mathrm{tot}}/\lambda_{\mathrm{Y}}}\right),$$

where $\lambda_Y$ is the characteristic length scale and $\alpha_Y$ an unknown parameter corresponding to the amplitude of the modification. We can derive the corresponding force as

$$F_{G,\text{Yukawa}} = -\frac{\mathrm{d}}{\mathrm{d}d_{\text{tot}}}\Phi_{G,\text{Yukawa}} = F_G\left[1 + \left(1 + \frac{d_{\text{tot}}}{\lambda_Y}\right)\alpha_Y \mathrm{e}^{-d_{\text{tot}}/\lambda_Y}\right], \tag{5.36}$$

where we used the Newtonian gravitational force $F_G$ from eq. (5.21) on p. 40.

Second, we can also consider corrections from modified Newtonian dynamics[11] (MOND). However, finding a similar expression for a modified gravitational potential is not straight-forward. The basic assumption of MOND is not that the laws of gravity are changed, but that the *inertial* mass $m$ is modified by a function $\mu$ depending on acceleration $\ddot{x}$,

[11] Milgrom 1983

$$m \to m\mu(\ddot{x}/a_0) \quad \text{with} \quad \mu(\ddot{x}/a_0 \gg 1) \approx 1, \quad \mu(\ddot{x}/a_0 \ll 1) \approx x.$$

Here, $a_0$ is some typical acceleration scale where the corrections from MOND become significant. As Newton's law now reads $F = m\mu(\ddot{x}/a_0)\ddot{x}$, the equation of motion is necessarily nonlinear, and, in order to be properly evaluated, requires a new solution. This has not been attempted within the scope of this thesis.

## 5.9 Optimal drive amplitude

Intuitively, we can expect that the effect of a gravitational drive will be maximized for a certain optimal source-mass amplitude $d_{S\text{opt}}$. If $d_S$ is too small, the modulation will be small too and if $d_S$ is too large, the source mass will only be in the regime of a relevant strength of force for a short amount of time per cycle of movement. We can quickly derive this optimum by first setting the *minimal distance* $\epsilon$ between the test mass and source-mass surfaces to a fixed value, which we take as a technical requirement in a practical experiment. As a purely geometric consideration, both sphere's radii, $r_T$ for the test mass and $r_S$ for the source mass, the minimal distance $\epsilon$ and the driving amplitude $d_S$ need to add up to the COM distance $d_0$; $d_0 = d_S + r_T + r_S + \epsilon$. From eq. (5.22b) on p. 41 we know that the Newtonian contribution to the measurement signal scales with $d_S^2 d_0^{-6}$. Setting $\mathrm{d}(d_S^2 d_0^{-6})/\mathrm{d}d_0 \stackrel{!}{=} 0$ yields the optimum COM distance and drive amplitude,

$$d_{0\text{opt}} = \frac{3}{2}(r_T + r_S + \epsilon), \quad d_{S\text{opt}} = \frac{1}{2}(r_T + r_S + \epsilon). \tag{5.37}$$

We note that (in our case of linearized forces) these optima hold *independently of frequency*, and specifically for the case of the gravitational force (due to its characteristic distance-scaling). The latter implies that the optima are likely

different for forces that follow other power laws. Therefore, when deviating too much from these optimal parameters in practical experiments, it is well possible that non-gravitational forces gain in power contribution while gravity loses.

## 5.10 Effective mass of oscillator modes

So far we have considered just one mechanical mode of the harmonic oscillator. However, most physical harmonic oscillators are continuous expanded bodies and therefore possess many eigenmodes. Each mode has a specific eigenfrequency $\omega_{0i}$, a specific damping rate $\gamma_i$ and a specific effective mass $m_{\text{eff}}$ that depend on the shape of the mode, the point of measured deflection and the relative internal stress that it is causing.[k]

The effective mass is the point-mass equivalent of a modal mass. We can derive it by comparing the potential energy of an expanded oscillator (in a deflected stage) to the potential energy of a single point-like particle.[12] The former is given by

[12] Pinard, Hadjar, and Heidmann 1999; Vanner et al. 2013

$$U = \omega_0^2/2 \int_V \left[u^2(\vec{x}) + v^2(\vec{x}) + w^2(\vec{x})\right] \rho \, \mathrm{d}x^3,$$

where $u$, $v$ and $w$ are the entries of the displacement vector field, and the integration is carried out over the volume $V$ of the oscillator. In order to compare this expression to the potential energy of a point mass $U = \omega_0^2 m_{\text{eff}} D^2/2$, we need to factor in the mode overlap $D$ between the mechanical mode and the geometric representation of the readout. For the case of a Gaussian probing beam with width $r_0$, this is

$$D = (2\pi r_0^2)^{-1} \int_{x,y} w(x, y, z = 0) \exp[-(x^2 + y^2)/(2r_0^2)] \, \mathrm{d}x \, \mathrm{d}y,$$

but the mode overlap can also represent a change in arm length when the same concept is applied to a vibrating interferometer, as presented in section 6.4 on p. 66. Comparing both terms yields the effective modal mass

$$m_{\text{eff}} = D^{-2} \int_V \left[u^2(\vec{x}) + v^2(\vec{x}) + w^2(\vec{x})\right] \rho \, \mathrm{d}x^3. \tag{5.38}$$

This expression can be used, e.g., in a finite element approach to the description of an actual test-mass system, as we demonstrate in section 9.2 on p. 97.

[k] Depending on the community (see e.g. Gatscher and Kawiecki (1996)), there is a second definition of effective mass, namely the frequency-dependent mass $m_{\text{comp}}(\omega)$ that relates the force $\vec{F}_{\text{in}}$ applied at a certain point of a mechanical system to the acceleration amplitude $\vec{a}_{\text{out}}$ at another point via Newton's second law, $m_{\text{comp}}(\omega) = |\vec{F}_{\text{in}}|/|\vec{a}_{\text{out}}|$. This quantity is usually important in the context of vibration isolation and specifically compliance. We treat it in section 7.1 on p. 68.

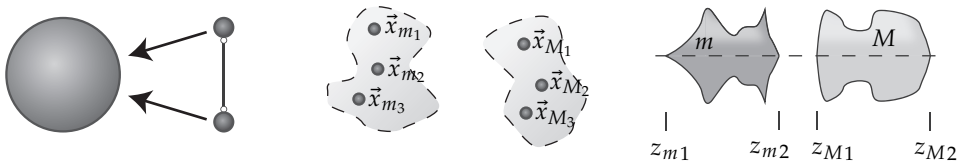


(a) An expanded object (rod to the right) will not be accelerated as expected from a point-like object.

(b) The gravitational potential of two point-like mass distributions has to include all pairs of mass points.

(c) Integration boundaries for the cylindrical-symmetry case.

**Figure 5.4:** Conceptual figures to illustrate steps for the optimization of test and source-mass shapes.

## 5.11 Mass shape optimization

In this section we ask if we can vary the distribution of the masses in a way that optimizes the effect of the gravitational drive. One might intuitively think that the gravitational pull should be independent of the masses' density distribution and only affect the COM coordinates. However, this is an approximation that breaks down when the size of the masses is on the order of their separation. Specifically, with the exception of rotationally symmetric mass distributions, the weak equivalence principle does only hold for point-like objects and is invalid for expanded objects. A simple example for this effect is a mass rod that falls down towards a singular (or rotationally symmetric) center of gravitation (fig. 5.4(a)) and, compared to perfect free fall, will experience local deceleration due to partially canceling force components, leading to a slower fall than expected from a point mass. In order to find the mass distribution which maximizes the effect of gravity in the proposed scheme, we first write down the potential between two sets of mass points that form rigid bodies (fig. 5.4(b)). It is

$$U_G = -G \sum_{i=1}^{N_m} \sum_{i=1}^{N_M} \frac{m_i M_j}{|\vec{x}_{m_i} - \vec{x}_{M_j}|},$$

which in the continuum limit becomes

$$\ldots \to \quad -G \int_{V_m} \int_{V_M} \frac{\mathrm{d}m(\vec{x}_m)\,\mathrm{d}M(\vec{x}_M)}{|\vec{x}_m - \vec{x}_M|}.$$

Assuming constant densities for both bodies we may write $\mathrm{d}m(\vec{x}) = \rho\,\mathrm{d}\vec{x}^3$, so

$$\ldots = -G\rho_m\rho_M \int_{V_m} \int_{V_M} \frac{\mathrm{d}x_m^3\,\mathrm{d}x_M^3}{|\vec{x}_m - \vec{x}_M|}.$$

For clarity we now rename the previously used test- and source-mass coordinates from $x$ and $x_S$ to $z$ and $z_S$, as below we will switch to cylinder coordinates. The force $F_G$ of the above potential on the test mass is then given by

$$F_G = -\frac{\partial U}{\partial z}. \tag{5.39}$$

As we saw in section 5.1, the driving strength of the source mass is not determined by the absolute force (0th-order), but by the gradient of the force with respect to the source-mass position. Therefore, the quantity $\iota$ that needs to be maximized is

$$\iota := \frac{\partial F}{\partial z_S} = G\rho_m\rho_M \frac{\partial^2}{\partial z \partial z_S} \int_{V_m}\int_{V_M} \frac{\mathrm{d}x_m^3\,\mathrm{d}x_M^3}{|\vec{x}_m - \vec{x}_M|}. \tag{5.40}$$

This equation alone does not make sense without specifying appropriate constraints. In our case, we are interested in keeping both total masses fixed, which, given the constant density, is equivalent to fixed volumes. Therefore, the constraints for the equation above are

$$\frac{m}{\rho_m} = \int_{V_m} \mathrm{d}x_m^3, \quad \frac{M}{\rho_M} = \int_{V_M} \mathrm{d}x_M^3. \tag{5.41}$$

A third constraint arises from the condition that at the point of closest separation the minimal distance between both masses has to be $\epsilon$ (see section 5.9 on p. 49), the mathematical implementation of which depends on the choice of coordinates. Finally, one likely has to account for the possibility that the optimal drive amplitude will change as well with differently shaped masses.

### 5.11.1 Cylinder coordinates and two specific cases

Analytically processing eq. (5.40) with the given constraints is a challenging undertaking. In order to compare some specific examples, we assume cylindric symmetry of both masses and transfer the equation to cylinder coordinates, i.e.

$$\begin{aligned}\iota = G\rho_m\rho_M \frac{\partial^2}{\partial z \partial z_S} \int_{z_{m1}}^{z_{m2}} \int_{z_{M1}}^{z_{M2}} \int_0^{2\pi} \int_0^{2\pi} \int_0^{r(z_m)} \int_0^{r_S(z_M)} \\ \cdot r_m r_M \left((d_0 + z_S + z_M - z - z_m)^2 + r_M^2 + r_m^2 - r_M r_m \cos(\theta_M - \theta_m)\right)^{-1/2} \\ \cdot \mathrm{d}r_m\,\mathrm{d}r_M\,\mathrm{d}\phi_m\,\mathrm{d}\phi_M\,\mathrm{d}z_m\,\mathrm{d}z_M.\end{aligned} \tag{5.42}$$

The integration boundaries are visualized in fig. 5.4(c). Let us now treat two special cases. In the first case, both masses are cylinders of height $h_{\mathrm{cyl}}$ with

the test- and source-mass coordinate positioned at the closest points within both masses (see also fig. 9.8(b)). The constraints (eq. (5.41)) then read

$$\frac{m}{\rho_m} = 2\pi \int_{-h_{\mathrm{cyl}}}^{0} \int_{0}^{r_{\mathrm{cyl}}} r_m \, \mathrm{d}r_m \, \mathrm{d}z_m \quad \Rightarrow \quad r_{\mathrm{cyl}} = \sqrt{\frac{m}{\pi \rho_m h_{\mathrm{cyl}}}}.$$

In the second case both masses are cones with height $h_{\mathrm{con}}$ with the flat sides facing the respective other mass, such that the radius is given by $r(z) = \alpha(z - h_{\mathrm{con}})$ with some inclination $\alpha$ (see also fig. 9.8(c)). The constraints then read

$$\frac{m}{\rho_m} = 2\pi \int_{-h_{\mathrm{con}}}^{0} \int_{0}^{\alpha(z_m + h_{\mathrm{con}})} r_m \, \mathrm{d}r_m \, \mathrm{d}z_m \quad \Rightarrow \quad \alpha = \sqrt{\frac{3m}{\pi \rho_m h_{\mathrm{con}}^3}}.$$

For the case of two spheres with diameter $h_{\mathrm{sph}}$ where the coordinates refer to the closest position, we refer to eq. (5.21) on p. 40 and write

$$\iota = GmM \frac{\partial F}{\partial z_{\mathrm{S}}} (d_0 + h_{\mathrm{sph}} + z_{\mathrm{S}} - z)^{-2}. \tag{5.43}$$

After establishing some key parameters and dimensions in chapter 8, in section 9.7 on p. 113 we perform a brief numerical estimation of eq. (5.42) to get a qualitative idea as to whether non-spherical mass distributions yield a significant advantage for the potential signal amplitude.

### 5.11.2 Semi-optimal case with a point-like test mass

If we make the specific assumption that the test mass behaves point-like, we may write $\mathrm{d}m = m\delta(x_m)\delta(y_m)\delta(z_m - z)\,\mathrm{d}^3 x_m$, and eq. (5.39) becomes

$$F_G = Gm\rho_M \frac{\partial^2}{\partial z \partial z_{\mathrm{S}}} \int_{V_M} \frac{\mathrm{d}x_M^3}{|\vec{x}_m - \vec{x}_M|},$$

which we may further process by using cylinder coordinates and assuming cylinder symmetry, i.e.

$$F_G = 2\pi Gm\rho_M \frac{\partial^2}{\partial z \partial z_{\mathrm{S}}} \int_{z_1}^{z_2} \int_{0}^{r(z_M)} \frac{r_M \mathrm{d}r_M \mathrm{d}z_M}{\sqrt{(d_0 + z_{\mathrm{S}} + z_M - z)^2 + r_M^2}},$$

where we reintroduced the distance $d_0$ (which now acts as a COM-to-surface distance). This expression can be used instead of eq. (5.21) on p. 40, as a semi-improved approach to improve the validity of the current formalism for non-spherical mass shapes.

Chapter 6

# Optical-interferometric position measurement

In this chapter we describe the relevant theoretical background of optical-interferometric position-sensing of a micromechanial device. We will first discuss the effect of photon shot noise (section 6.1), which combined with the aforementioned backaction noise yields the standard quantum limit for continuous measurements (SQL, section 6.2). We then motivate optical interferometry and homodyning as the means for high precision readout of motion before developing the relevant relations for one specific implementation of a Mach-Zehnder interferometer (section 6.3). In the last section (section 6.4) we develop the means to estimate the mechanical effective masses of practical homodyne setups, which is relevant for thermal noise considerations.

## Chapter contents



## 6.1 Photon shot noise

On a fundamental level, the method of using light for the determination of mechanical displacement is subject to the statistics of photon ensembles. The simple notion that the photon rates underly statistic distributions implies additional photon-distribution dependent noise for the measurement. In our

case, we use a single-frequency, single-spatial-mode laser beam and therefore assume the light to be in a coherent state. Using the input-ouput formalism for homodyne detection, we can follow Clerk et al. (2010, (G20)) to derive the contribution to the phase spectral density of a light field that is entirely caused by photon statistics of a coherent state. It is

$$S_{\phi\mathrm{sh}} = \frac{1}{4\,\langle R_{\mathrm{ph}}\rangle},$$

where $R_{\mathrm{ph}}$ denotes the rate of photons, as we already saw in the derivation of back-action noise (section 5.7.2). Since we consider the simple case without an optical cavity, a phase shift $\mathrm{d}\phi$ can directly be expressed as a position shift $\mathrm{d}x$ via

$$\mathrm{d}\phi = 2k\,\mathrm{d}x$$

with the wavenumber $k$. We may then use the (same) relations between power and photon number that we already employed in section 5.7.2 and arrive at an expression for the additional position noise through readout-photon statistics,

$$S_{x\mathrm{sh}} = \frac{S_{\phi\mathrm{sh}}}{4k^2} = \frac{\hbar}{32\pi}\frac{\lambda c}{P}. \tag{6.1}$$

Remember that even though this effect is expressed as a displacement PSD, the mechanical displacement $x$ is not actually affected. The conversion above yields a displacement PSD *equivalent* to the photon noise seen at a detector (see also section 11.3.1 on p. 139).

## 6.2 The standard quantum limit

The effect of photon shot noise, eq. (6.1), is often treated combined with photon back action noise, eq. (5.35), to form the *standard quantum limit*[1] for continuous measurements,

[1] Braginsky, Khalili, et al. 1995; Caves 1980; Clerk et al. 2010

$$S_{x\mathrm{SQL}} = S_{x\mathrm{sh}} + S_{x\mathrm{ph}} = \frac{\hbar}{32\pi}\frac{\lambda c}{P} + m^{-2}\,|\chi(\omega)|^2\,8\pi\hbar\frac{P}{\lambda c}. \tag{6.2}$$

While the shot noise contribution scales with inverse power, the backaction contribution scales linearly with power. It is clear that an optimal value for the power $P$ has to exist that minimizes the sum of both PSDs, $S_{x\mathrm{SQL}}$. This turns out to be

$$P_{\mathrm{opt,SQL}} = \frac{\lambda c m}{16\pi\,|\chi(\omega)|}. \tag{6.3}$$

However, in most practical cases, thermal noise or other noise sources, e.g. classical amplitude noise (and, in consequence, classical backaction), will pose

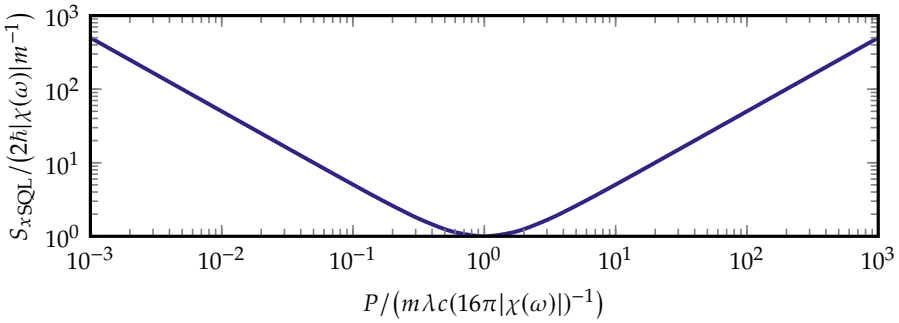


**Figure 6.1:** The standard quantum limit, eq. (6.2), in normalized units for the no-cavity case. We directly see that the minimal noise of $S_{x\mathrm{SQL}} = 2\hbar|\chi(\omega)|m^{-1}$ is achieved if $P/\left(m\lambda c(16\pi|\chi(\omega)|)^{-1}\right) = 1$.

a major noise limitation before the SQL *with optimal power* can be reached. Nevertheless, measurements close to the SQL have recently become available, e.g. as demonstrated by LaHaye (2004) and Schreppler et al. (2014). It is important to stress that both terms in eq. (6.2) have the same physical origin, namely the statistics of photons, but are also fundamentally different in one aspect: Photon backaction noise affects the actual position of the mechanics (and could therefore also be detected if one would apply an additional position readout scheme that does not rely on the detection of the same photons) while the photon shot noise is an effect that is part of the detection of the light quanta and does not affect the mechanics. Lastly, we also note that eq. (6.2) only holds for the case of coherent (i.e. Poisson-distributed) light, which is likely not the optimal choice for a given measurement and might well be improved using non-classical states of light, e.g. squeezed light, which is a well-explored topic in the context of gravitational wave detectors.[2] The typical standard quantum limit curve is shown in fig. 6.1.

[2] McKenzie 2002; Stefszky 2012; Vahlbruch 2008

## 6.3 Balanced optical homodyning of a classical phase

Generally, one speaks of homodyning when a (phase-)modulated signal (*SI*) is mixed with a reference signal of the same optical frequency, the local oscillator (*LO*), in order to convert the otherwise non-measurable phase modulations of light into well-measurable amplitude modulations. To achieve a fixed phase relation of optical input fields, both SI and LO usually have the same original source, which is then split into the SI and LO pathways and later recombined. Usually, one output port of the recombination already entails the required phase information, which is at the heart of interferometry. However, as we will see below, it can be advantageous to use both outputs and measure the difference signal, which is sometimes called *balanced* homodyne detection. This

allows to cancel the offset and noise of the light amplitude and in consequence become more sensitive to its phase.

In the experimental part of this thesis, specifically in section 11.2.3 on p. 132, we present a specific interferometric readout configuration for the proposed experiment. Here, we focus on its core elements and employ a quantum treatment using the input-output-operator matrix formalism[3] (also *Jones calculus*) in order to analyze how an input operator is propagated through the chain of optical elements.

[3] Gerry and Knight 2005; Loudon 2000

### 6.3.1 Transfer matrix of a polarizer-based Mach-Zehner interferometer

We treat the light in the basis of horizontal and vertical polarization (with respect to the optical table) and denote the polarization of operators with the subscripts $H$ and $V$. The three basic optical elements we will use are a polarizing beam splitter (*PBS*), a half-wave plate with fast axis at angle $\varphi$ and an arbitrary-phase retarder (*APR*) rotated to have no off-diagonal entries. These will propagate input states as

$$\begin{pmatrix}\hat{a}_H\\ \hat{a}_V\\ \hat{b}_H\\ \hat{b}_V\end{pmatrix} \xrightarrow{\text{PBS}} \begin{pmatrix}1 & & & \mathrm{i}\\ & & 1 & \\ & 1 & & \\ \mathrm{i} & & & \end{pmatrix}\begin{pmatrix}\hat{a}_H\\ \hat{a}_V\\ \hat{b}_H\\ \hat{b}_V\end{pmatrix}, \tag{6.4a}$$

$$\begin{pmatrix}\hat{a}_H\\ \hat{a}_V\end{pmatrix} \xrightarrow{\lambda/2} \begin{pmatrix}\cos 2\varphi & \sin 2\varphi\\ \sin 2\varphi & -\cos 2\varphi\end{pmatrix}\begin{pmatrix}\hat{a}_H\\ \hat{a}_V\end{pmatrix}, \tag{6.4b}$$

$$\begin{pmatrix}\hat{a}_H\\ \hat{a}_V\end{pmatrix} \xrightarrow{\text{APR}} \begin{pmatrix}\mathrm{e}^{-\mathrm{i}\theta} & 0\\ 0 & 1\end{pmatrix}\begin{pmatrix}\hat{a}_H\\ \hat{a}_V\end{pmatrix}, \tag{6.4c}$$

where $\hat{a}$ and $\hat{b}$ are used to distinguish spatially distinct modes and for later convenience we dropped a common phase from the typical APR matrix. Figure 6.2(a) shows the chains of optical elements, where the input and output ports of each element are individually labeled. A variation of this scheme, fig. 6.2(b), is be analyzed in section 6.3.6.

In order to derive the relation between the output ports $\hat{c}$ and $\hat{d}$ and all interferometer input ports, we first write down the transformation for each optical element using the relations above. The input state vector $(\,\hat{a}_H\ \hat{a}_V\ \hat{v}_H\ \hat{v}_V\,)$ is transformed by the first PBS as

$$\begin{pmatrix}\hat{a}_H^{\mathrm{I}} & \hat{a}_V^{\mathrm{I}} & \hat{b}_H & \hat{b}_V\end{pmatrix}^T = \begin{pmatrix}\hat{a}_H & \mathrm{i}\hat{v}_V & \hat{v}_H & \mathrm{i}\hat{a}_V\end{pmatrix}^T.$$

The half-wave plate at angle $\varphi_1$ and the APR oriented to cause a phase shift $\theta$ between horizontal and vertical polarization act as

$$\begin{pmatrix}\hat{a}_H^{\mathrm{II}}\\ \hat{a}_V^{\mathrm{II}}\end{pmatrix} = \begin{pmatrix}\cos(2\varphi_1)\hat{a}_H^{\mathrm{I}} + \sin(2\varphi_1)\hat{a}_V^{\mathrm{I}}\\ \sin(2\varphi_1)\hat{a}_H^{\mathrm{I}} - \cos(2\varphi_1)\hat{a}_V^{\mathrm{I}}\end{pmatrix}, \quad \begin{pmatrix}\hat{a}_H^{\mathrm{III}}\\ \hat{a}_V^{\mathrm{III}}\end{pmatrix} = \begin{pmatrix}\mathrm{e}^{-\mathrm{i}\theta}\hat{a}_H^{\mathrm{II}}\\ \hat{a}_V^{\mathrm{II}}\end{pmatrix}.$$

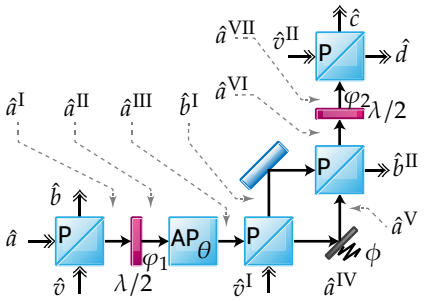


(a) Angled-reflection scheme where, in principle, all power can be used for detection. This scheme is analyzed in sections 6.3.1 to 6.3.5.

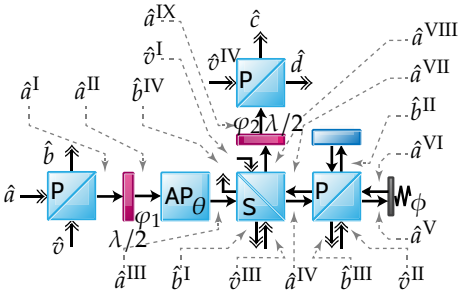


(b) Direct reflection scheme. Compared to the first scheme, it sacrifices power for practicality. This scheme is analyzed in section 6.3.6.

**Figure 6.2:** Two slightly different realizations of optical homodyning schemes where SI and LO are implemented via orthogonal polarizations. Both figures include all relevant optical elements (P for polarizing beam splitter, AP for arbitrary phase retarder, S for beam splitter) and the corresponding operators. The operators are indexed by ascending roman numerals according to their appearance in the propagation chain, and operators that correspond to vacuum input ports are denoted by $\hat{v}$.

As one can quickly see, the choice of $\varphi_1$ determines the splitting of power into the spatially separated part of the interferometer at the next PBS, which acts similar to the first one as

$$\begin{pmatrix} \hat{a}_H^{\mathrm{IV}} & \hat{a}_V^{\mathrm{IV}} & \hat{b}_H^{\mathrm{I}} & \hat{b}_V^{\mathrm{I}} \end{pmatrix}^T = \begin{pmatrix} \hat{a}_H^{\mathrm{III}} & \mathrm{i}\hat{v}_V^{\mathrm{I}} & \hat{v}_H^{\mathrm{I}} & \mathrm{i}\hat{a}_V^{\mathrm{III}} \end{pmatrix}^T .$$

One of the output ports of the second PBS will now be modulated by a time-dependent mechanical phase, which simply means that

$$\begin{pmatrix} \hat{a}_H^{\mathrm{V}} & \hat{a}_V^{\mathrm{V}} \end{pmatrix}^T = \mathrm{e}^{-\mathrm{i}\phi} \begin{pmatrix} \hat{a}_H^{\mathrm{IV}} & \hat{a}_V^{\mathrm{IV}} \end{pmatrix}^T .$$

This is followed by a third polarizer,

$$\begin{pmatrix} \hat{a}_H^{\mathrm{VI}} & \hat{a}_V^{\mathrm{VI}} & \hat{b}_H^{\mathrm{II}} & \hat{b}_V^{\mathrm{II}} \end{pmatrix}^T = \begin{pmatrix} \hat{a}_H^{\mathrm{V}} & \mathrm{i}\hat{b}_V^{\mathrm{I}} & \hat{b}_H^{\mathrm{I}} & \mathrm{i}\hat{a}_V^{\mathrm{V}} \end{pmatrix}^T ,$$

and a second half-wave plate with angle $\varphi_2$,

$$\begin{pmatrix} \hat{a}_H^{\mathrm{VII}} \\ \hat{a}_V^{\mathrm{VII}} \end{pmatrix} = \begin{pmatrix} \cos(2\varphi_2)\hat{a}_H^{\mathrm{VI}} + \sin(2\varphi_2)\hat{a}_V^{\mathrm{VI}} \\ \sin(2\varphi_2)\hat{a}_H^{\mathrm{VI}} - \cos(2\varphi_2)\hat{a}_V^{\mathrm{VI}} \end{pmatrix} .$$

The last step is to spatially separate both polarizations with another PBS, yielding the output

$$\begin{pmatrix} \hat{c}_H & \hat{c}_V & \hat{d}_H & \hat{d}_V \end{pmatrix}^T = \begin{pmatrix} \hat{a}_H^{\mathrm{VII}} & \mathrm{i}\hat{v}_V^{\mathrm{II}} & \hat{v}_H^{\mathrm{II}} & \mathrm{i}\hat{a}_V^{\mathrm{VII}} \end{pmatrix}^T .$$

We may now simply perform the necessary algebra and arrive at the total transformation matrix of the interferometer, which splits into two parts. First, the relevant output ports are given by

$$\begin{pmatrix}\hat{c}_H\\ \hat{d}_V\end{pmatrix} = \begin{pmatrix}M_{1,1} & M_{1,2}\\ M_{2,1} & M_{2,2}\end{pmatrix}\begin{pmatrix}\hat{a}_H\\ \hat{v}_V\end{pmatrix},$$

with the matrix elements

$$\begin{aligned}
M_{1,1} &= \mathrm{e}^{-\mathrm{i}(\phi+\theta)}\cos(2\varphi_1)\cos(2\varphi_2) - \sin(2\varphi_1)\sin(2\varphi_2),\\
M_{1,2} &= \mathrm{i}\mathrm{e}^{-\mathrm{i}(\phi+\theta)}\sin(2\varphi_1)\cos(2\varphi_2) + \mathrm{i}\cos(2\varphi_1)\sin(2\varphi_2),\\
M_{2,1} &= \mathrm{i}\mathrm{e}^{-\mathrm{i}(\phi+\theta)}\cos(2\varphi_1)\sin(2\varphi_2) + \mathrm{i}\sin(2\varphi_1)\cos(2\varphi_2),\\
M_{2,2} &= -\mathrm{e}^{-\mathrm{i}(\phi+\theta)}\sin(2\varphi_1)\sin(2\varphi_2) + \cos(2\varphi_1)\cos(2\varphi_2).
\end{aligned}$$

Second, the transformation matrix of the auxiliary operators reads

$$\begin{pmatrix}\hat{c}_V\\ \hat{d}_H\\ \hat{b}_H\\ \hat{b}_V\\ \hat{b}_H^{\mathrm{II}}\\ \hat{b}_V^{\mathrm{II}}\end{pmatrix} = \begin{pmatrix}\mathrm{i} & & & & & \\ & 1 & & & & \\ & & 1 & & & \\ & & & \mathrm{i} & & \\ & & & & 1 & \\ & & & & & -\mathrm{e}^{-\mathrm{i}\phi}\end{pmatrix}\begin{pmatrix}\hat{v}_V^{\mathrm{II}}\\ \hat{v}_H^{\mathrm{II}}\\ \hat{v}_H\\ \hat{a}_V\\ \hat{v}_H^{\mathrm{I}}\\ \hat{v}_V^{\mathrm{I}}\end{pmatrix},$$

implying that all of these modes leave the interferometer unaffected (up to some phase). This makes clear that the output $\hat{c}_H$, $\hat{d}_V$ is completely determined by the original input $\hat{a}_H$ and one vacuum port $\hat{v}_V$, with all other vacuum contributions disappearing in the final result.

### 6.3.2 Homodyne signals

The number operators of the two outputs of the interferometer are $\hat{c}_H^\dagger\hat{c}_H$ and $\hat{d}_V^\dagger\hat{d}_V$. Straight-forward multiplication yields

$$\begin{aligned}
\left.\begin{matrix}\hat{c}_H^\dagger\hat{c}_H, & \text{“+”,“+”,“−”,}\\ \hat{d}_V^\dagger\hat{d}_V, & \text{“−”,“−”,“+”}\end{matrix}\right\} &= \frac{1}{2}\left(\hat{a}_H^\dagger\hat{a}_H + \hat{v}_V^\dagger\hat{v}_V\right)\\
&\pm \overbrace{\frac{1}{4}\left[(1-\cos(\phi+\theta))\cos(4\varphi_1-4\varphi_2) + (1+\cos(\phi+\theta))\cos(4\varphi_1+4\varphi_2)\right]}^{=:A_{\mathrm{diff}}(\phi,\theta,\varphi_1,\varphi_2)/2}\\
&\quad\cdot\left(\hat{a}_H^\dagger\hat{a}_H - \hat{v}_V^\dagger\hat{v}_V\right)
\end{aligned}$$

$$
\begin{aligned}
&\overbrace{\pm \frac{\mathrm{i}}{4}\left[(1-\cos(\phi+\theta))\sin(4\varphi_1-4\varphi_2)+(1+\cos(\phi+\theta))\sin(4\varphi_1+4\varphi_2)\right]}^{=:B_{\mathrm{diff}}(\phi,\theta,\varphi_1,\varphi_2)/2} \\
&\quad\cdot\left(\hat{a}_H^\dagger\hat{v}_V-\hat{a}_H\hat{v}_V^\dagger\right) \\
&\mp\cos 2\varphi_2\sin 2\varphi_2\sin(\phi+\theta)\left(\hat{a}_H^\dagger\hat{v}_V+\hat{a}_H\hat{v}_V^\dagger\right).
\end{aligned}
\tag{6.5}
$$

The sum and difference of the number operators of both arms are given by

$$
\hat{c}_H^\dagger\hat{c}_H+\hat{d}_V^\dagger\hat{d}_V=\hat{a}_H^\dagger\hat{a}_H+\hat{v}_V^\dagger\hat{v}_V, \tag{6.6a}
$$

$$
\begin{aligned}
\hat{c}_H^\dagger\hat{c}_H-\hat{d}_V^\dagger\hat{d}_V &= A_{\mathrm{diff}}(\phi,\theta,\varphi_1,\varphi_2)\left(\hat{a}_H^\dagger\hat{a}_H-\hat{v}_V^\dagger\hat{v}_V\right) \\
&\quad+B_{\mathrm{diff}}(\phi,\theta,\varphi_1,\varphi_2)\left(\hat{a}_H^\dagger\hat{v}_V-\hat{a}_H\hat{v}_V^\dagger\right) \\
&\quad-2\cos 2\varphi_2\sin 2\varphi_2\sin(\phi+\theta)\left(\hat{a}_H^\dagger\hat{v}_V+\hat{a}_H\hat{v}_V^\dagger\right).
\end{aligned}
\tag{6.6b}
$$

At this point we can assume a coherent input state $|\alpha_{\mathrm{coh}}\rangle$ for the $\hat{a}_H$ port and a vacuum state $|0\rangle$ at the vacuum entry port $\hat{v}_V$. Since $\langle\hat{v}_V\rangle_0=\langle\hat{v}_V^\dagger\rangle_0=\langle\hat{v}_V^\dagger\hat{v}_V\rangle_0=0$, eqs. (6.5) and (6.6b) yield

$$
\begin{aligned}
\langle\hat{c}_H^\dagger\hat{c}_H\rangle &= \frac{1}{2}\left[1+A_{\mathrm{diff}}(\phi,\theta,\varphi_1,\varphi_2)\right]|\alpha_{\mathrm{coh}}|^2, \\
\langle\hat{d}_V^\dagger\hat{d}_V\rangle &= \frac{1}{2}\left[1-A_{\mathrm{diff}}(\phi,\theta,\varphi_1,\varphi_2)\right]|\alpha_{\mathrm{coh}}|^2
\end{aligned}
\tag{6.7}
$$

and

$$
\langle\hat{c}_H^\dagger\hat{c}_H+\hat{d}_V^\dagger\hat{d}_V\rangle=|\alpha_{\mathrm{coh}}|^2, \tag{6.8a}
$$

$$
\langle\hat{c}_H^\dagger\hat{c}_H-\hat{d}_V^\dagger\hat{d}_V\rangle=A_{\mathrm{diff}}(\phi,\theta,\varphi_1,\varphi_2)|\alpha_{\mathrm{coh}}|^2. \tag{6.8b}
$$

Now, we can identify $A_{\mathrm{diff}}$ as the amplitude modulation of the difference signal, which depends on the mechanical phase $\phi$, the APR phase shift $\theta$ and the half-wave plate angles $\varphi_1$ and $\varphi_2$.

### 6.3.3 Shot noise scaling

Before we analyze the behavior of $A_{\mathrm{diff}}$ for different choices of wave plate angles $\varphi_1$, $\varphi_2$ in the next section, we briefly check how photon shot noise appears in the output signal. This can be done by computing the variance of $\hat{c}_H^\dagger\hat{c}_H-\hat{d}_V^\dagger\hat{d}_V$,

$$
\sigma^2_{\hat{c}_H^\dagger\hat{c}_H-\hat{d}_V^\dagger\hat{d}_V}=\langle\left(\hat{c}_H^\dagger\hat{c}_H-\hat{d}_V^\dagger\hat{d}_V\right)^2\rangle-\left(\langle\hat{c}_H^\dagger\hat{c}_H-\hat{d}_V^\dagger\hat{d}_V\rangle\right)^2. \tag{6.9}
$$

We already know the second summand from eq. (6.8b). For the first summand we expand the expression, yielding new terms of fourth order in $\hat{c}_H$ and $\hat{d}_V$. Using the expectation values from eq. (6.7) and applying the commutation relations for creation/annihilation operators, $[\hat{c}_H, \hat{c}_H^\dagger] = [\hat{d}_V, \hat{d}_V^\dagger] = 1$, yields

$$\begin{aligned}
\langle c_H^\dagger c_H c_H^\dagger c_H \rangle &= \frac{1}{2}\left(1 + A_{\mathrm{diff}}\right)|\alpha_{\mathrm{coh}}|^2 \langle c_H c_H^\dagger \rangle \\
&= \frac{1}{2}\left(1 + A_{\mathrm{diff}}\right)|\alpha_{\mathrm{coh}}|^2 \left(1 + \langle c_H^\dagger c_H \rangle\right) \\
&= \frac{1}{2}\left(1 + A_{\mathrm{diff}}\right)|\alpha_{\mathrm{coh}}|^2 + \frac{1}{4}\left(1 + A_{\mathrm{diff}}\right)^2 |\alpha_{\mathrm{coh}}|^4, \\
\langle d_V^\dagger d_V d_V^\dagger d_V \rangle &= \frac{1}{2}\left(1 - A_{\mathrm{diff}}\right)|\alpha_{\mathrm{coh}}|^2 + \frac{1}{4}\left(1 - A_{\mathrm{diff}}\right)^2 |\alpha_{\mathrm{coh}}|^4, \\
\langle c_H^\dagger c_H d_V^\dagger d_V \rangle &= \frac{1}{4}\left(1 - A_{\mathrm{diff}}^2\right)|\alpha_{\mathrm{coh}}|^4.
\end{aligned}$$

Combining these results with eq. (6.8b) and inserting them into eq. (6.9) yields

$$\sigma^2_{\hat{c}_H^\dagger \hat{c}_H - \hat{d}_V^\dagger \hat{d}_V} = |\alpha_{\mathrm{coh}}|^2.$$

Therefore, the ratio of the homodyne amplitude over its shot-noise dominated standard deviation, or quantum-limited signal-to-noise ratio, will depend on the mechanical phase $\phi$ and on the choice of $\varphi_1$, $\varphi_2$ and $\theta$ as

$$\frac{\langle \hat{c}_H^\dagger \hat{c}_H - \hat{d}_V^\dagger \hat{d}_V \rangle}{\sqrt{\sigma^2_{\langle \hat{c}_H^\dagger \hat{c}_H - \hat{d}_V^\dagger \hat{d}_V \rangle}}} = A_{\mathrm{diff}}(\phi, \theta, \varphi_1, \varphi_2)|\alpha_{\mathrm{coh}}|.$$

We can interpret this in the following way: choosing $\varphi_1$, $\varphi_2$ and $\theta$ in order to make eq. (6.8b) extremal will also maximize the signal-to-noise ratio in the case of dominating shot noise (i.e. the sum of all other noise sources being lower than the shot noise contribution).

### 6.3.4 Optimal power distribution

We can further process the modulation amplitude $A_{\mathrm{diff}}$ as defined in eq. (6.5) on p. 61. To this end we write the mechanical phase $\phi$ as a sum of a constant phase $\phi_0$ and a small modulation $\phi_{\mathrm{mod}}$. With a series expansion we may therefore write $\cos(\phi + \theta) \approx \cos(\phi_0 + \theta) - \sin(\phi_0 + \theta)\phi_{\mathrm{mod}}$ and

$$\begin{aligned}
A_{\mathrm{diff}}|\alpha_{\mathrm{coh}}|^2 = \frac{1}{2}\Big[&(1 - \cos(\phi + \theta))\cos(4\varphi_1 - 4\varphi_2) \\
&+ (1 + \cos(\phi + \theta))\cos(4\varphi_1 + 4\varphi_2)\Big]\,|\alpha_{\mathrm{coh}}|^2
\end{aligned}$$

$$\begin{aligned} &\approx A_+(\varphi_1,\varphi_2)|\alpha_{\mathrm{coh}}|^2 \\ &\quad + A_-(\varphi_1,\varphi_2)|\alpha_{\mathrm{coh}}|^2\left[\cos(\phi_0+\theta)-\sin(\phi_0+\theta)\phi_{\mathrm{mod}}\right], \end{aligned} \tag{6.10}$$

$$\text{with}\quad A_\pm(\varphi_1,\varphi_2) := \frac{1}{2}\left[\cos(4\varphi_1+4\varphi_2)\pm\cos(4\varphi_1-4\varphi_2)\right].$$

From this expression we can directly see that tuning $\theta$ will allow us to make the output signal proportional to any (normalized) superposition of $\phi_{\mathrm{mod}}$ and 1 (plus some constant term), where the extreme cases are commonly referred to as measuring the *phase quadrature* or the *amplitude quadrature*[4].[a] Of the two summands just the latter, which scales with $A_-(\varphi_1,\varphi_2)$, also scales with the mechanical phase modulation $\phi_{\mathrm{mod}}$. Therefore, this part should be made extremal by the choice of $\varphi_1$, $\varphi_2$. Figure 6.3 shows plots for this expression as well as the first term of eq. (6.10), which causes an offset (i.e. a contribution with no dependency on $\phi_{\mathrm{mod}}$) and scales with $A_+(\varphi_1,\varphi_2)$. The smallest values yielding extremal values of $A_-(\varphi_1,\varphi_2)$ can be found for $\varphi_1$, $\varphi_2 = \pm\pi/8$. Conveniently, for these values we find that $A_+(\varphi_1,\varphi_2) = 0$, so the offset vanishes and $\theta$ can be chosen such that there is no signal contribution that is not directly proportional to $\phi_{\mathrm{mod}}$.

[4] Welsch, Vogel, and Opatrny 2009

Going back to eq. (6.4b), we see that the transfer matrix of a half wave-plate for $\varphi = \pm\pi/8$ yields a symmetric power-distribution into both outputs,

$$\begin{pmatrix}\hat{a}_H^{\mathrm{II}}\\ \hat{a}_V^{\mathrm{II}}\end{pmatrix} = \frac{1}{\sqrt{2}}\begin{pmatrix}1 & \pm1\\ \pm1 & -1\end{pmatrix}\begin{pmatrix}\hat{a}_H^{\mathrm{I}}\\ \hat{a}_V^{\mathrm{I}}\end{pmatrix},$$

i.e. a polarization rotation by 45°.The fact that a symmetric power-distribution yields optimal performance may seem unintuitive, given that in many practical experiments much more power is put into the LO than into the SI, but the situation at hand is slightly different from these scenarios. First, many experiments employ an optical cavity in the SI path, which is shifting the optimal power-distribution towards the LO (as a cavity-based readout yields increased mechanical-phase sensitivity per power). Second, there often is a restriction on the maximal power that can be tolerated at a mechanical sample, which we did not consider here. Third, in some cases, one also wants to measure amplitude fluctuations, which is different from our assumptions. For our case, however, the total power is limited by either the available input power or the

[a] In the context of these results, this terminology might appear to be somewhat confusing, as the amplitude $|\alpha_{\mathrm{coh}}|^2$ enters proportionally in both cases. However, this expression already contains an expectation value, which means that it averages over quantum noise in the quadratures. It turns out that when performing the same calculation without expectations, the amplitude quantum noise will enter the phase quadrature only in second order, and vice-versa. Therefore, in the context of quantum noise, it makes sense to speak of phase and amplitude quadratures.

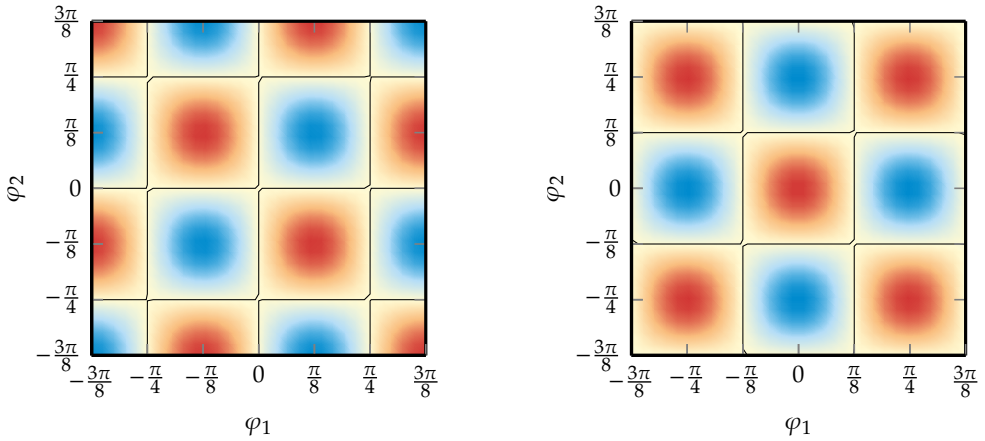


(a) $A_-(\varphi_1, \varphi_2)$, which determines the amplitude of the phase modulation $\phi_{\mathrm{mod}}$.

(b) $A_+(\varphi_1, \varphi_2)$, which determines the constant offset to the difference signal.

**Figure 6.3:** Colourmap plots of signal contributions for the homodyne output depending on the angle settings of the half-wave plates. The plot ranges from −1 to 1, with negative values drawn blue, positive values drawn red and lines indicating 0.

power at the optical detectors, and a mechanical-phase modulation is the main quantity of interest. In this scenario the ideal choice of power splitting is to put equal power into both arms.

### 6.3.5 Mismatched photodetectors

We briefly estimate the effect of a mismatch in the detection efficiency of the optical detectors. Imperfect detectors are properly modeled by placing conceptual beam splitters in front of ideal detectors[5], but for simplicity, here we just replace the matched number difference $\hat{c}_H^\dagger \hat{c}_H - \hat{d}_V^\dagger \hat{d}_V$ by an unmatched one $\hat{c}_H^\dagger \hat{c}_H - (1-2\kappa)\hat{d}_V^\dagger \hat{d}_V$, where $0 < \kappa < 1/2$. The expectation value of this operator is then

[5] Leonhardt and Paul 1995

$$\begin{aligned}
&\langle \hat{c}_H^\dagger \hat{c}_H - (1-2\kappa)\hat{d}_V^\dagger \hat{d}_V \rangle = \kappa |\alpha_{\mathrm{coh}}|^2 + (1-\kappa) A_{\mathrm{diff}}(\phi, \theta, \varphi_1, \varphi_2) |\alpha_{\mathrm{coh}}|^2 \\
\approx\ & \left[\kappa + (1-\kappa) A_+(\varphi_1, \varphi_2)\right] |\alpha_{\mathrm{coh}}|^2 \\
&+ (1-\kappa) A_-(\varphi_1, \varphi_2) |\alpha_{\mathrm{coh}}|^2 \left[\cos(\phi_0 + \theta) - \sin(\phi_0 + \theta)\phi_{\mathrm{mod}}\right].
\end{aligned}$$

In order for the non-$\phi_{\mathrm{mod}}$-dependent contribution to vanish, we require that

$$A_+(\varphi_1, \varphi_2) |\alpha_{\mathrm{coh}}|^2 \stackrel{!}{=} -\frac{\kappa}{1-\kappa} \approx -\kappa,$$

where the approximation is valid if $\kappa \ll 1/2$, corresponding to the case of closely matched detectors. Looking at fig. 6.3(b) it becomes clear that this can

be achieved with the proper setting of $\varphi_1$ and $\varphi_2$, but forces a less-than-optimal limit on the signal amplitude proportional to $A_-(\varphi_1, \varphi_2)$ in fig. 6.3(a).

### 6.3.6 Beamsplitter variation

We can vary the interferometer as shown in fig. 6.2(b) on p. 59 by using the second PBS in both directions and adding a 50/50 beam splitter

$$\begin{pmatrix}\hat{a}\\ \hat{b}\end{pmatrix} \overset{\text{BS}}{\to} \frac{1}{\sqrt{2}}\begin{pmatrix}1 & \mathrm{i}\\ \mathrm{i} & 1\end{pmatrix}\begin{pmatrix}\hat{a}\\ \hat{b}\end{pmatrix}$$

to separate the ingoing from the outgoing beam. Up to a global phase, the relevant output operators of this system are given by

$$\begin{pmatrix}\hat{c}_H\\ \hat{d}_V\end{pmatrix} = \begin{pmatrix} M_{1,1} & M_{2,1}\\ M_{1,2} & M_{2,2}\\ \frac{\mathrm{i}}{2}\mathrm{e}^{-\mathrm{i}\phi}\cos(2\varphi_2) & -\frac{1}{2}\mathrm{e}^{-\mathrm{i}\phi}\sin(2\varphi_2)\\ -\frac{\mathrm{i}}{2}\sin(2\varphi_2) & -\frac{1}{2}\cos(2\varphi_2)\\ -\frac{\mathrm{i}}{\sqrt{2}}\cos(2\varphi_2) & \frac{1}{\sqrt{2}}\sin(2\varphi_2)\\ -\frac{\mathrm{i}}{\sqrt{2}}\sin(2\varphi_2) & -\frac{1}{\sqrt{2}}\cos(2\varphi_2)\end{pmatrix}^T \begin{pmatrix}\hat{a}_H\\ \hat{v}_V\\ \hat{v}_H^{\mathrm{I}}\\ \hat{v}_V^{\mathrm{I}}\\ \hat{v}_H^{\mathrm{III}}\\ \hat{v}_H^{\mathrm{III}}\end{pmatrix},$$

with

$$\begin{aligned}
M_{1,1} &= \frac{1}{2}\left(\mathrm{e}^{-\mathrm{i}(\phi+\theta)}\cos(2\varphi_1)\cos(2\varphi_2) - \sin(2\varphi_1)\sin(2\varphi_2)\right),\\
M_{1,2} &= \frac{\mathrm{i}}{2}\left(\mathrm{e}^{-\mathrm{i}(\phi+\theta)}\sin(2\varphi_1)\cos(2\varphi_2) + \cos(2\varphi_1)\sin(2\varphi_2)\right),\\
M_{2,1} &= \frac{\mathrm{i}}{2}\left(\mathrm{e}^{-\mathrm{i}(\phi+\theta)}\cos(2\varphi_1)\sin(2\varphi_2) + \sin(2\varphi_1)\cos(2\varphi_2)\right),\\
M_{2,2} &= -\frac{1}{2}\left(\mathrm{e}^{-\mathrm{i}(\phi+\theta)}\sin(2\varphi_1)\sin(2\varphi_2) - \cos(2\varphi_1)\cos(2\varphi_2)\right),
\end{aligned}$$

where the remaining contributions necessary to make this transformation unitary are contained within $\hat{b}^{\mathrm{I}}$ and $\hat{b}^{\mathrm{IV}}$. The expressions relating $\hat{c}_H$, $\hat{d}_V$ with $\hat{a}_H$, $\hat{v}_V$ differ from those derived for the first interferometer (section 6.3.1) by a factor of 1/2, so we can reuse previous results to shorten the calculation, yielding

$$\begin{aligned}
\langle \hat{c}_H^\dagger \hat{c}_H + \hat{d}_V^\dagger \hat{d}_V\rangle &= \frac{1}{4}|\alpha_{\text{coh}}|^2,\\
\langle \hat{c}_H^\dagger \hat{c}_H - \hat{d}_V^\dagger \hat{d}_V\rangle &= \frac{1}{4}A_{\text{diff}}(\phi, \theta, \varphi_1, \varphi_2)|\alpha_{\text{coh}}|^2,
\end{aligned}$$

and the variance and signal-to-noise

$$\sigma^2_{\hat{c}_H^\dagger \hat{c}_H - \hat{d}_V^\dagger \hat{d}_V} = \frac{1}{4}|\alpha_{\text{coh}}|^2,$$

$$\frac{\langle \hat{c}_H^\dagger \hat{c}_H - \hat{d}_V^\dagger \hat{d}_V \rangle}{\sqrt{\sigma^2_{\langle \hat{c}_H^\dagger \hat{c}_H - \hat{d}_V^\dagger \hat{d}_V \rangle}}} = \frac{1}{2} A_{\text{diff}}(\phi, \theta, \varphi_1, \varphi_2) |\alpha_{\text{coh}}|.$$

Comparing these results to the previous case (section 6.3.2) we see that, as we would naturally expect, the configuration involving a beam splitter yields a quarter of the original absolute signal and halves the quantum limited signal-to-noise ratio.

## 6.4 Mechanical noise of homodyne implementations

Generally, the difference signal of a balanced homodyne detection will be sensitive to every relative phase change between the SI and LO pathways. Apart from a mechanical phase caused by a moving mirror, a relative change of path lengths can also be induced by other elements in the beam path, or by a change of refractive indexes of the optical components. On the time scales of seconds to hours or even days, one usually speaks of drifts, which are typically induced by the environment, e.g. through changes in temperature or humidity. But the practical implementation of any interferometer will also have a variety of mechanical modes, which can be excited acoustically or thermally (see section 5.7.1 on p. 45).[b]

As seen in section 5.10 on p. 50, we might assign an effective mass $m_{\text{eff}}$ to a mechanical mode by normalizing the total integrated stress,

$$\int_V \left[ u^2(\vec{x}) + v^2(\vec{x}) + w^2(\vec{x}) \right] \rho \, \mathrm{d}x^3,$$

with the mode overlap, which in many cases can be simplified to the change in position $z_0$ at the spot of probing. Transferring this concept to an interferometer, the change in position can be replaced by a change in arm length difference $\Delta z = \Delta L_1 - \Delta L_2$, where $L_1, L_2$ are the lengths of the interferometer arms and $\Delta L_1$, $\Delta L_2$ are their mode-induced changes. The effective mass of an interferometer mode is then

$$m_{\text{eff}} = \Delta z^{-2} \int_V \left[ u^2(\vec{x}) + v^2(\vec{x}) + w^2(\vec{x}) \right] \rho \, \mathrm{d}x^3. \tag{6.11}$$

in analogy to eq. (5.38).

[b] Similar effects arise in the context of laser stabilization, where one commonly speaks of *residual amplitude modulations* (RAM). For an overview of this topic, see e.g. Zhang et al. (2014) and the references therein.

Chapter 7

# Vibration isolation at low frequencies

The field of vibration isolation is vast, ranging from high-force applications in aerospace and vehicle design[1], where acceleration magnitudes above $g$ need to be compensated for, to gravitational wave detectors in space[2] that can tolerate only a microscopic fraction of typical accelerations on earth. Here, we will focus mainly on the working principle of isolation systems that are used for gravitational wave detection on earth. This is because the proposed experiment has requirements similar to gravitational wave detectors – with respect to achieving very low displacement background noise within a laboratory environment.

[1] Keane 1995

[2] Amaro-Seoane et al. 2012

We start this chapter by explaining how a harmonic oscillator can be used as a motion attenuator in section 7.1 (as opposed to a amplification, which we treated in chapter 5). We then derive the attenuation properties of general one-dimensional (section 7.2) as well as a specific class of three-dimensional (section 7.3) spring mass systems. As we will ultimately have to estimate the performance of a compound vibration-isolation system, we briefly look into the topic of chaining multiple attenuation systems in section 7.4. We close this chapter with a few remarks on active vibration isolation in section 7.5.

## Chapter contents

## 7.1 Harmonic oscillators as motion attenuators

The main principle of passive vibration-isolation revolves around employing low-frequency harmonic oscillators as elements of force or displacement suppression between the environment and the system that needs to be at rest. The underlying mechanism can be derived in a straightforward fashion. We start by writing down the equation of a harmonic oscillator, which in this case is driven by both movement of the support $x_{\text{sup}}$ as well as an external force $F$:

$$F/m = \ddot{x} + \gamma(\dot{x} - \dot{x}_{\text{sup}}) + \omega_0^2(x - x_{\text{sup}}), \tag{7.1}$$

which in Fourier space reads[a]

$$\Leftrightarrow \quad \tilde{x} = \left(\omega_0^2 - \omega^2 - \mathrm{i}\gamma\omega\right)^{-1} \left(\tilde{F}/m + (\omega_0^2 - \mathrm{i}\gamma\omega)\tilde{x}_{\text{sup}}\right),$$

or, expressed through the acceleration spectrum,

$$\Leftrightarrow \quad \tilde{\ddot{x}} = \left(1 + \mathrm{i}\frac{\gamma}{\omega} - \frac{\omega_0^2}{\omega^2}\right)^{-1} \left(\frac{\tilde{F}}{m} - \left(\frac{\omega_0^2}{\omega^2} + \mathrm{i}\frac{\gamma}{\omega}\right)\tilde{\ddot{x}}_{\text{sup}}\right),$$

where we neglected inherent damping of $x$ that does not depend on $x_{\text{sup}}$.[b] With this, we may write the response of $x$ to an input motion $x_{\text{sup}}$ or force $F$ as

$$\frac{\tilde{x}}{\tilde{x}_{\text{sup}}} = \frac{\omega_0^2 - \mathrm{i}\gamma\omega}{\omega_0^2 - \omega^2 - \mathrm{i}\gamma\omega} \qquad \text{transmissibility,} \tag{7.2a}$$

$$\frac{\tilde{x}}{\tilde{F}} = \frac{1}{m}(\omega_0^2 - \omega^2 - \mathrm{i}\gamma\omega)^{-1} \qquad \text{compliance, or} \tag{7.2b}$$

$$\frac{\tilde{\ddot{x}}}{\tilde{F}} = \frac{1}{m}\left(1 + \mathrm{i}\frac{\gamma}{\omega} - \frac{\omega_0^2}{\omega^2}\right)^{-1} =: m_{\text{comp}}^{-1}(\omega) \qquad \text{effective mass.} \tag{7.2c}$$

The first expression $\tilde{x}/\tilde{x}_{\text{sup}}$ is the conversion from ingoing displacement to outgoing displacement, or *transmissibility*. The second expression $\tilde{x}/\tilde{F}$ is the conversion from force to displacement, or *compliance*. The third expression is the conversion from force to acceleration, which in this context is often called effective mass[3] (or *apparent weight*), though it should not be confused with the effective modal mass introduced in section 5.10 on p. 50. The first two expressions are plotted in fig. 7.1. We note that below resonance, the transmissibility

[3] Gatscher and Kawiecki 1996

[a] In the context of vibration isolation, the Laplace transform is commonly used instead of the Fourier transform (Matichard et al. 2015). In essence, both methods are mathematically equivalent.

[b] Technically, damping that directly affects a single degree of freedom can only be achieved by damping its motion with respect to an *inertial reference*, i.e. a system that is completely at rest. Therefore, neglecting this type of damping in the context of vibration isolation is justified.

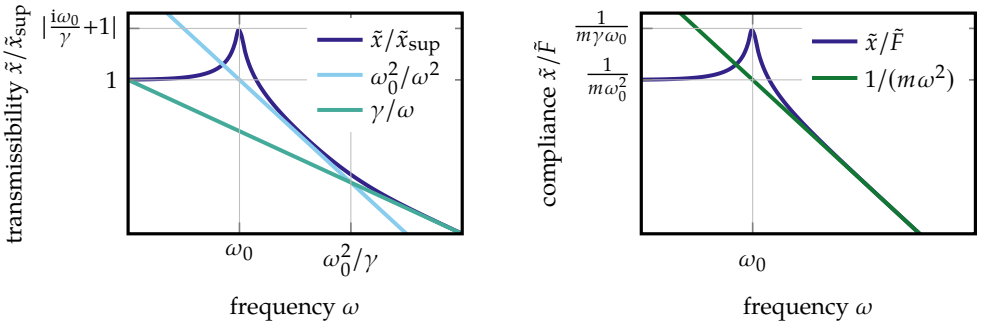


(a) Qualitative transmissibility curve.

(b) Qualitative compliance curve.

**Figure 7.1:** Transmissibility and compliance as functions of frequency $\omega$. All axes are scaled logarithmically.

is essentially unity, so no attenuation of motion can be achieved, while the compliance scales with inverse mass and inverse squared frequency (i.e. with inverse spring constant). Above resonance, the transmissibility goes with $1/\omega^2$ up to $\omega_0^2/\gamma$ and then changes into a less steep $1/\omega$ falloff, while the compliance follows a $1/\omega^2$ curve. Note however that the difference in qualitative behavior is due to the $\gamma\dot{x}_{\mathrm{sup}}$ term in eq. (7.1), which effectively provides a vibrational shortcut above the transition frequency $\omega_0^2/\gamma$. If the dominant damping force in the system was only proportional to $x$ (internal mass damping) or negligible, the transmissibility would go as $\omega_0^2/\omega^2$ above resonance, similar to the compliance. We also note that in terms of motion/force isolation, it is highly advantageous for the transmissibility to have low eigenfrequencies $\omega_0$ and for the compliance to have large masses $m$, while the respective other quantity is not affected by these choices.

Both quantities are highly relevant for passive isolation systems. The transmissibility allows to estimate the passive *seismic* isolation and similar scenarios where the mass of the driving system is very large compared to the isolated system, from the motion of tectonic plates to the residual noise of a (heavy) pre-isolation platform, and therefore completely dictates the input motion (i.e. negligible backaction). In contrast, the compliance is needed in the context of active vibration compensation (section 7.5 on p. 80), as it yields a frequency-dependent value for the force required to achieve a certain displacement.

## 7.2 Transfer functions of one-dimensional compound systems

We derive the response of a vertical one-dimensional mass chain with positions $x_i$ and masses $m_i$ ($i \leq n$) that is connected by springs $k_{ij}$ and excited by

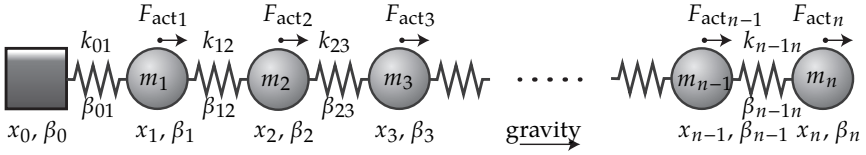


**Figure 7.2:** One-dimensional mass chain with actuation forces, gravity and full set of damping.

displacement $x_0$ of its zeroth element as well as forces $F_{\text{act}i}$ acting on its $i$th element (fig. 7.2), where the latter is necessary to model active actuation. With $\boldsymbol{x} = (x_1, \ldots, x_n)$, the equation of motion for this system is

$$M_m \ddot{\boldsymbol{x}} + B\dot{\boldsymbol{x}} + K\boldsymbol{x} = gM_m \begin{pmatrix} 1 \\ \vdots \\ 1 \end{pmatrix} + \boldsymbol{F}_{\text{act}} + \boldsymbol{F}_{\text{in}} \quad \text{with} \quad \boldsymbol{F}_{\text{in}} = \begin{pmatrix} k_{01}x_0 + \beta_{01}\dot{x}_0 \\ 0 \\ \vdots \\ 0 \end{pmatrix},$$

where $B = B_s + B_k$, with

$$M_m = \text{diag}(m_1, \ldots, m_n) \quad \text{and} \quad B_s = \text{diag}(\beta_1, \ldots, \beta_n)$$

being diagonal matrices for mass elements and self-damping and

$$K = \begin{pmatrix} k_{01} + k_{12} & -k_{12} & & & & \\ -k_{12} & k_{12} + k_{23} & -k_{23} & & & \\ & \ddots & \ddots & \ddots & & \\ & & -k_{n-2n-1} & k_{n-2n-1} + k_{n-1n} & k_{n-1n} & \\ & & & -k_{n-1n} & k_{n-1n} \end{pmatrix},$$

$$B_k = \begin{pmatrix} \beta_{01} + \beta_{12} & -\beta_{12} & & & & \\ -\beta_{12} & \beta_{12} + \beta_{23} & -\beta_{23} & & & \\ & \ddots & \ddots & \ddots & & \\ & & -\beta_{n-2n-1} & \beta_{n-2n-1} + \beta_{n-1n} & \beta_{n-1n} & \\ & & & -\beta_{n-1n} & \beta_{n-1n} \end{pmatrix}.$$

The term caused by gravity will cause a constant offset in the system without affecting the dynamics. This can be seen by defining

$$\boldsymbol{x}' = \boldsymbol{x} + \Delta\boldsymbol{x}$$

and requiring that the gravitational term is vanishing,

$$M_m \ddot{\boldsymbol{x}}' + B\dot{\boldsymbol{x}}' + K\boldsymbol{x}' - \boldsymbol{F}_{\text{act}} - \boldsymbol{F}_{\text{in}} = gM_m \begin{pmatrix} 1 \\ \vdots \\ 1 \end{pmatrix} + K\Delta\boldsymbol{x} \stackrel{!}{=} 0$$

$$\Leftrightarrow \quad \Delta\boldsymbol{x} = gK^{-1}M_m \begin{pmatrix} 1 \\ \vdots \\ 1 \end{pmatrix}.$$

The remaining system can be re-written using the Fourier transform, i.e.

$$\begin{aligned} &\left(-\omega^2 M_m - \mathrm{i}\omega B + K\right)\tilde{\boldsymbol{x}}' - \tilde{\boldsymbol{F}}_{\text{in}} - \tilde{\boldsymbol{F}}_{\text{act}} = 0 \\ \Leftrightarrow \quad &\tilde{\boldsymbol{x}}' = \left(-\omega^2 M_m - \mathrm{i}\omega B + K\right)^{-1}\left[\begin{pmatrix} (k_{01}+\mathrm{i}\omega\beta_{01})\tilde{x}_0 \\ 0 \\ \vdots \\ 0 \end{pmatrix} + \tilde{\boldsymbol{F}}_{\text{act}}\right]. \end{aligned} \tag{7.3}$$

Using this expression we may compute the response of any element in the chain to an ingoing displacement of $x_0$ (transmissibility) or a force acting on any element (compliance). Specifically, we are usually interested in the response of the last chain element to ingoing displacement, as well as the response to an actuation force acting on the first stage.[c]

## 7.3 Transfer function of a compound system in three spatial dimensions

Of course, actual isolation systems are three-dimensional and exhibit specific transfer functions in all Euclidean directions. As these directions are orthogonal, it seems logical to treat them separately as three uncoupled one-dimensional isolation chains. However, this can only yield a rough approximation of the absolute performance of an isolation system, and will likely be too optimistic. We can understand this as follows: Intuitively, as soon as rotation of the rigid bodies forming individual isolation stages is allowed, orthogonal Euclidean DOFs are effectively related via rotation DOFs (see fig. 7.3(a)). This implies that the total transfer in any spatial coordinate involves non-trivial modes (i.e. modes that can not be represented by a one-dimensional system) of typically lower isolation performance.[4]

[4] Hua 2005

There are some tools available to estimate the performance of complex isolation systems[5]; however, they seem either too specific (and likely not suitable for our application of estimating the isolation between an actuated source mass and a test-mass platform), or outdated or not publicly documented. Here, we develop a framework for the performance estimation of isolation systems based on elastic springs in both horizontal and vertical directions. We assume that the horizontal springs are realized with *wire pendulums* (see section 12.2.2), and from here on refer to the vertical springs as *blade flexures* (see section 12.2.1). In order to correctly account for advanced isolation element developments such as inverted pendulums and geometric anti-springs (see section 12.2.3), the scheme presented would have to be slightly modified but is in principle still applicable.

[5] Barton 2004; Husman et al. 2000; Plissi, Torrie, Husman, et al. 2000; Torrie 2001

[c] In order to utilize the passive stages for the filtering of noise from active vibration compensation, one usually places the actuators early in the isolation chain (Robertson, Cagnoli, et al. 2002).


(a) Orthogonal displacement degrees of freedom can be coupled through tilt motion.

(b) Displacement $\vec{x}$, spring attachment $\vec{p}$ and rotation angle $\vec{\phi}$.

**Figure 7.3:** Conceptual figures to illustrate the effect of stage rotations and the relevant labels.

### 7.3.1 Total spring potential formalism

We search for the total spring forces acting on the various DOFs of the isolation system, similar to the basic concept used by Coyne et al. (2007). The latter describes a system composed of a single stage with six DOFs (three for displacement and three for rotation), which makes it possible to write down all spring-forces without too much complication. We want to generalize this method to systems composed of multiple chained platforms with six DOFs per platform. With the added complexity, finding the forces on each individual DOF can be a challenging undertaking. We approach this task by constructing a total spring potential of the coupled system. This allows us to compute the restoring forces on each individual DOF by the means of taking partial derivatives of the total potential with respect to the specific DOFs. Given some support by computer algebra, this method drastically simplifies the search for the desired force expressions.

The potential can be constructed as follows: For every spring, we refer to an upper (*up*) and a lower (*lo*) stage. At both stages we find points of spring attachment $\vec{p}_{\mathrm{up}}$, $\vec{p}_{\mathrm{lo}}$ relative to the COM of that stage (fig. 7.3(b)). Both stages are parametrized by two times three degrees of freedom; for displacement $\vec{x}_{\mathrm{up}}$, $\vec{x}_{\mathrm{low}}$ and rotation $\vec{\phi}_{\mathrm{up}}$, $\vec{\phi}_{\mathrm{low}}$ with

$$\vec{x}_i = (x_i, y_i, z_i) \quad \text{and} \quad \vec{\phi}_i = (\phi_i, \theta_i, \psi_i),$$

where each angle vector entry donates the rotation angle around the respective axis. At first, we need a general expression for the displacement caused by non-zero deflections of the two stages. In the approximation of small angles, this is given by

$$\vec{\Delta}(\vec{p}_{\mathrm{up}}, \vec{p}_{\mathrm{lo}}) \approx \left(R_{\mathrm{up}}\vec{p}_{\mathrm{up}} + \vec{x}_{\mathrm{up}}\right) - \left(R_{\mathrm{lo}}\vec{p}_{\mathrm{lo}} + \vec{x}_{\mathrm{lo}}\right) - (\vec{p}_{\mathrm{up}} - \vec{p}_{\mathrm{lo}}),$$

$$\text{with the linearized rotation matrix} \quad R_i = \begin{pmatrix} 1 & -\psi_i & \theta_i \\ \psi_i & 1 & -\phi_i \\ -\theta_i & \phi_i & 1 \end{pmatrix}.$$

Due to the nature of a typical blade pendulum system (see e.g. Aston et al. (2012) and Torrie (2001)), we have to deal with two kinds of flexible mechanical elements causing spring potentials:

1. A wire is suspended between two attachment points on two platforms. In a first approximation, the potential of this wire is composed of two individual potentials. First, an elongation/compression potential proportional to $k_{\asymp}$ in the direction parallel to the wire (fig. 7.4(b)), where the deflection $\vec{\Delta}_{\parallel}$ is given by

$$\vec{\Delta}_{\parallel} = \left(\vec{\Delta}(\vec{p}_{\text{up}}, \vec{p}_{\text{lo}}) \cdot \vec{e}_{\langle\rangle}\right) \vec{e}_{\langle\rangle},$$

   and second, a restoring contribution proportional to $k_{\langle\rangle}$ within the plane orthogonal to the wire direction[d] (fig. 7.4(a)), onto which the projection of the deflection $\vec{\Delta}_{\perp}$ can be written as

$$\vec{\Delta}_{\perp} = \vec{\Delta}(\vec{p}_{\text{up}}, \vec{p}_{\text{lo}}) - \vec{\Delta}_{\parallel}.$$

2. A blade flexure is causing a soft spring with stiffness $k_{\triangleright}$ that effectively adds an additional small mass which can move orthogonal to the upper stage plane, the degree of which we call $\mathfrak{z}$, and has the wire attached to it (fig. 7.4(c)). We also incorporate a lateral blade mode with stiffness $k_{\trianglerighteq}$, which we associate with a coordinate $\mathfrak{x}$ and a blade direction $\vec{e}_{\triangleright}$. Similar to the case above, we have

$$\begin{aligned} \vec{\Delta}_{\parallel} &= \left(\vec{\Delta}(\vec{p}_{\text{up}} + \mathfrak{z}\vec{e}_z + \mathfrak{x}\vec{e}_{\triangleright}, \vec{p}_{\text{lo}}) \cdot \vec{e}_{\langle\rangle}\right) \vec{e}_{\langle\rangle}, \\ \vec{\Delta}_{\perp} &= \vec{\Delta}(\vec{p}_{\text{up}} + \mathfrak{z}\vec{e}_z + \mathfrak{x}\vec{e}_{\triangleright}, \vec{p}_{\text{lo}}) - \vec{\Delta}_{\parallel}. \end{aligned}$$

Therefore, a connection between an upper and a lower stage can yield two kinds of potentials;

$$\begin{aligned} V_{\text{wire}} &= \frac{1}{2} k_{\langle\rangle} \vec{\Delta}_{\perp}^2 + \frac{1}{2} k_{\asymp} \vec{\Delta}_{\parallel}^2 \\ &= \frac{1}{2} k_{\langle\rangle} \left[\vec{\Delta}(\vec{p}_{\text{up}}, \vec{p}_{\text{lo}}) - \left(\vec{\Delta}(\vec{p}_{\text{up}}, \vec{p}_{\text{lo}}) \cdot \vec{e}_{\langle\rangle}\right) \vec{e}_{\langle\rangle}\right]^2 \\ &\quad + \frac{1}{2} k_{\asymp} \left(\vec{\Delta}(\vec{p}_{\text{up}}, \vec{p}_{\text{lo}}) \cdot \vec{e}_{\langle\rangle}\right)^2, \end{aligned}$$

[d] Contrary to intuition, the restoring force of an angled wire suspension is not dictated by the absolute gravitational potential, but by the load along the wire axis. Therefore the relevant plane is orthogonal to the wire, not orthogonal to gravity.

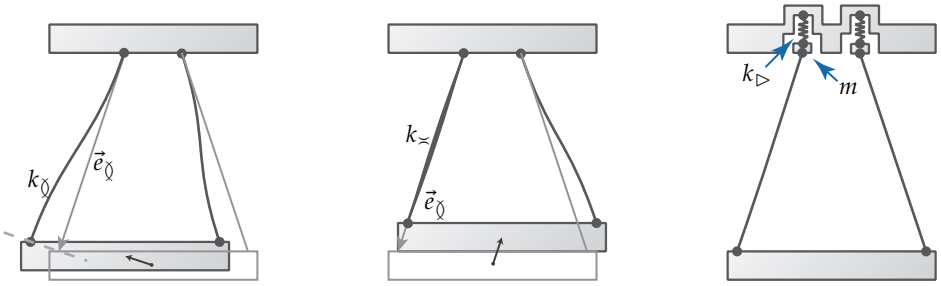


(a) Deflection orthogonal to wire, with restoring force proportional to $k_{\langle}$.

(b) Deflection in wire direction (bounce), with restoring force proportional to $k_{\asymp}$

(c) Vertical spring with stiffness $k_{\rhd}$ incorporated via a point mass $m$ with two attachments.

**Figure 7.4:** Basic wire deflection illustrations. For an analysis of the physical pendulums and springs/blade flexures, see sections 12.2.1 and 12.2.2 on p. 149 and on p. 152.

for a single wire, as well as

$$\begin{aligned} V_{\text{wire/blade}} &= \frac{1}{2}k_{\rhd}\mathfrak{z}^2 + \frac{1}{2}k_{\trianglerighteq}\mathfrak{x}^2 + \frac{1}{2}k_{\langle}\vec{\Delta}_{\perp}^2 + \frac{1}{2}k_{\asymp}\vec{\Delta}_{\parallel}^2 \\ &= \frac{1}{2}k_{\rhd}\mathfrak{z}^2 + \frac{1}{2}k_{\trianglerighteq}\mathfrak{x}^2 + \frac{1}{2}k_{\langle}\left[\vec{\Delta}(\vec{p}_{\text{up}} + \mathfrak{z}\vec{e}_3 + \mathfrak{x}\vec{e}_{\rhd}, \vec{p}_{\text{lo}})\right. \\ &\quad \left. - \left(\vec{\Delta}(\vec{p}_{\text{up}} + \mathfrak{z}\vec{e}_3 + \mathfrak{x}\vec{e}_{\rhd}, \vec{p}_{\text{lo}}) \cdot \vec{e}_{\langle}\right)\vec{e}_{\langle}\right]^2 \\ &\quad + \frac{1}{2}k_{\asymp}\left(\vec{\Delta}(\vec{p}_{\text{up}} + \mathfrak{z}\vec{e}_3 + \mathfrak{x}\vec{e}_{\rhd}, \vec{p}_{\text{lo}}) \cdot \vec{e}_{\langle}\right)^2, \end{aligned}$$

for a combined blade and wire suspension. In addition to the small-angle approximation mentioned before, we made two major simplifications here: First, we ignored any twist-motion or internal modes of the blade flexures. They act as perfect vertical/horizontal springs with respect to their attachment plane. Second, we completely ignored all violin-modes of the wires.[e]

The total potential will be given by the combination of all individual potentials as well as gravity,

$$V_{\text{total}} = \sum_{\text{springs}} V + \sum_{\text{stages}} mgz.$$

Due to the rotation matrix $R$ acting on $\mathfrak{z}$ and $\mathfrak{x}$, this potential will include terms that have a fourth power in some combinations of DOFs and therefore

[e] The advanced LIGO suspension Mathematica model (Barton 2004) includes these modes; but it seems like the model is not maintained anymore and as far as the author can tell, running the Mathematica notebooks available online with current versions of the software would require considerable effort.

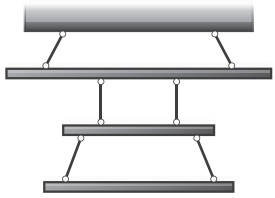

(a) Symmetric wire suspension.

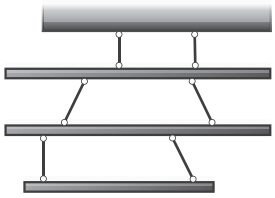

(b) Asymmetric wire suspension (not desired).

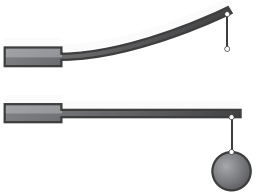

(c) Pre-bent blade-spring that reaches the intended pseudo "non-deflected" state when the payload is attached.

**Figure 7.5:** Conceptual figures to illustrate the proper design of wire suspensions and of vertical springs.

it will not be possible to achieve linear equations of motion without further simplification. In the following, we will derive force terms from the potential that can then be linearized. This method is most precise if the springs and wires have been placed such that the steady state of the system has already been reached. For this, the wires should to be symmetric with respect to a centered vertical plane (figs. 7.5(a) and 7.5(b)), and the vertical springs have to be designed such that the linearization point is reached when the payload is attached (fig. 7.5(c)).

### 7.3.2 Construction of the spring matrix

We can now use the total potential to calculate the resulting force on a specific degree of freedom $\alpha_i$, which can be any displacement or angle coordinate of a stage or a blade tip. This force is given by

$$F_i = -\frac{\partial V_{\text{total}}}{\partial \alpha_i}.$$

The goal of this analysis is to achieve linear equations of motion. The proper point of linearization should be the point of equilibrium, i.e. the set of coordinate values that put the system at rest. Mathematically, we request that all time derivatives of all coordinates vanish, which is equivalent to the condition that the static force on each coordinate is vanishing, $F_i = 0 \ \forall \alpha_i$. This leads to an equation system of six equations and unknowns per stage and two per blade. As some equations of this system are nonlinear, finding a (numerical) solution can be time-consuming. Therefore, we further simplify the problem for computation by making use of the previous assumption that the entire system is symmetric (figs. 7.5(a) and 7.5(b)). In this case, the forces on all angles and non-vertical coordinates must naturally vanish at the non-deflected (i.e.

0-) position of said coordinates, leading to a remaining system of one equation and unknown vertical coordinate $z$ per stage and $\mathfrak{z}$ per blade. This system can then be solved to gather said coordinates and fully define the linearization point for the force terms. Further, we can then shift the vertical coordinates $z$ and $\mathfrak{z}$ for the stages and blades in order to compensate for the static offset due to gravity, as seen in section 7.2. This means that if we approximate the force terms to first order in any coordinate,

$$F_i = -\frac{\partial V_{\text{total}}}{\partial \alpha_i} \approx -\sum_j K_{ij}\alpha_j + F_{\text{const}},$$

there will be no static offset, or $F_{\text{const}} = 0$. This implies that the system of equations of motion we aim to construct can be solved via Fourier transform, as seen before.

We may write the above relation in matrix form as

$$-\boldsymbol{F}_K = K\boldsymbol{\alpha}$$
$$\text{with } \boldsymbol{\alpha} = (\vec{x}_0, \vec{\phi}_0, \vec{x}_1, \vec{\phi}_1, \ldots, \vec{x}_{n_{\text{stages}}}, \vec{\phi}_{n_{\text{stages}}}, \mathfrak{z}_1, \mathfrak{x}_1, \mathfrak{z}_2, \mathfrak{x}_2, \ldots, \mathfrak{z}_{n_{\text{blades}}}, \mathfrak{x}_{n_{\text{blades}}})^T,$$

where $\boldsymbol{\alpha}$ now has $6(n_{\text{stages}}+1)+2n_{\text{blades}}$ entires, with $n_{\text{stages}}$ and $n_{\text{blades}}$ denoting the total number of stages and blades, respectively. Now, as $\vec{x}_0$, $\vec{\phi}_0$ serve as input for the system of coupled oscillator and are not part of the dynamics itself, the matrix $K$ will have dimensions $(6n_{\text{stages}}+2n_{\text{blades}})\times(6(n_{\text{stages}}+1)+2n_{\text{blades}})$. We may therefore write

$$-\boldsymbol{F}_K = \underset{(n_{\text{DOF}}\times 6)}{(\ K_0\ }\Big|\ \underset{(n_{\text{DOF}}\times n_{\text{DOF}})}{K_{\text{dyn}}\ )} \begin{pmatrix} \boldsymbol{\alpha}_0 \\ \hline \boldsymbol{\alpha}_{\text{dyn}} \end{pmatrix}_{(n_{\text{DOF}}\times 1)}^{(6\times 1)} = \underset{(n_{\text{DOF}}\times 1)}{K_0\boldsymbol{\alpha}_0 + K_{\text{dyn}}\boldsymbol{\alpha}_{\text{dyn}}}, \tag{7.4}$$

where we split up the dynamic part and the input part of the DOF vector $\boldsymbol{\alpha}$ and defined $n_{\text{DOF}} := 6n_{\text{stages}} + 2n_{\text{blades}}$ as the total number of dynamic DOFs.

### 7.3.3 Construction of the damping matrix

The damping matrix $B$ can be constructed in a similar fashion, where, in analogy to the one dimensional chain (section 7.2) , $B = B_s + B_k$ consists of a self-damping part proportional to a DOF's velocity and a spring-damping part proportional to the velocity difference of several DOF's that are linked via springs. Due to the similarity to spring forces, we can construct it in the same way as the spring force matrix $K$, i.e. by writing down an effective total "damping potential" and then calculating $B_k$ by derivation with respect to the dynamic DOFs. This will lead to the damping force

$$-\boldsymbol{F}_B = B_0\dot{\boldsymbol{\alpha}}_0 + B_{\text{dyn}}\dot{\boldsymbol{\alpha}}_{\text{dyn}}. \tag{7.5}$$

### 7.3.4 Construction of the mass matrix

In order to equate the sum of these forces to the total force $\boldsymbol{F} = M\ddot{\boldsymbol{\alpha}}$, a mass matrix $M$ is required. For every DOF in $\boldsymbol{\alpha}$, we need to find the effective inertial mass. This is straight-forward for the translational DOFs, $\vec{x}_i$, and the rotational DOFs, $\vec{\phi}_i$, of the stages. For $n = 1, \ldots, n_{\text{stages}}$, we write

$$\vec{F}_{\vec{x}_i} = m_i \ddot{\vec{x}}_i \quad \text{and} \vec{F}_{\vec{\phi}_i} = J_i \ddot{\vec{\phi}}_i,$$

where $m_i$ is the mass of the stage and $J_i$ is the moment-of-inertia tensor with respect to the rotation axes. As the DOFs of the blade tips are coordinates in the relative frames of the stages the blades are attached to, we have to factor in the stage motion when determining the blade-tip forces. For $n = 1, \ldots, n_{\text{blades}}$, the force on the vertical DOF $\mathfrak{z}_i$ of a blade tip is given by

$$F_{\mathfrak{z}_i} = m_{\mathfrak{z}i} \frac{\mathrm{d}^2}{\mathrm{d}t^2} \left[ R_{i'} \left( \vec{p}_i + \mathfrak{z}\vec{e}_3 + \mathfrak{x}\vec{e}_\triangleright \right) + \vec{x}_{i'} \right] \cdot \vec{e}_3,$$

where $i'$ denotes the index of the stage that hosts the blade and $m_{\mathfrak{z}i}$ is the effective mass of the blade mode. Since we neglect second-order terms in DOFs, and further $\vec{e}_3 \perp \vec{e}_\triangleright$, we can approximate this as

$$\approx m_{\mathfrak{z}i} \left[ \left( \ddot{R}_{i'} \vec{p}_i \right) \cdot \vec{e}_3 + \ddot{\mathfrak{z}} + \ddot{z}_{i'} \right].$$

Similarly, for a blade tip deflection DOF $\mathfrak{x}_i$,

$$F_{\mathfrak{x}_i} \approx m_{\mathfrak{x}i} \left[ \left( \ddot{R}_{i'} \vec{p}_i \right) \cdot \vec{e}_\triangleright + \ddot{\mathfrak{x}} + \ddot{\vec{x}}_{i'} \cdot \vec{e}_\triangleright \right].$$

Combining all forces into a single vector,

$$\boldsymbol{F} = \Big( \vec{F}_{\vec{x}_1}, \vec{F}_{\vec{\phi}_1}, \vec{F}_{\vec{x}_2}, \vec{F}_{\vec{\phi}_2}, \ldots, \vec{F}_{\vec{x}_{n_{\text{stages}}}}, \vec{F}_{\vec{\phi}_{n_{\text{stages}}}}, F_{\mathfrak{z}1}, F_{\mathfrak{x}_1}, F_{\mathfrak{z}2}, F_{\mathfrak{x}_2}, \ldots, F_{\mathfrak{z}n_{\text{blades}}}, F_{\mathfrak{x}_{n_{\text{blades}}}} \Big)^T,$$

we can make use of the previous linearizion and write

$$\boldsymbol{F} = M\ddot{\boldsymbol{\alpha}} = M_0 \ddot{\boldsymbol{\alpha}}_0 + M_{\text{dyn}} \ddot{\boldsymbol{\alpha}}_{\text{dyn}} \tag{7.6}$$

in analogy to eqs. (7.4) and (7.5).

### 7.3.5 Total equation of motion and solution

Comparing the terms in eqs. (7.4) to (7.6), we may now write

$$\begin{aligned} & \boldsymbol{F} = \boldsymbol{F}_B + \boldsymbol{F}_K \\ \Leftrightarrow \quad & M_m \ddot{\boldsymbol{\alpha}}_{\text{dyn}} + B_{\text{dyn}} \dot{\boldsymbol{\alpha}}_{\text{dyn}} + K_{\text{dyn}} \boldsymbol{\alpha}_{\text{dyn}} = -M_0 \ddot{\boldsymbol{\alpha}}_0 - B_0 \dot{\boldsymbol{\alpha}}_0 - K_0 \boldsymbol{\alpha}_0 \\ \Leftrightarrow \quad & (-\omega^2 M_m - \mathrm{i}\omega B_{\text{dyn}} + K_{\text{dyn}}) \tilde{\boldsymbol{\alpha}}_{\text{dyn}} = (-\omega^2 M_0 + \mathrm{i}\omega B_0 - K_0) \tilde{\boldsymbol{\alpha}}_0. \end{aligned}$$

This allows us to compute the frequency-dependent transmissibility of any DOF $\tilde{\alpha}_{\mathrm{dyn}_i}$ for any input excitation $\tilde{\alpha}_{0_j}$. By construction of the matrices, the equation above does always have an analytic exact solution. In practice, finding this solution is difficult due to the large number of individual equations that form the matrix equation. Instead, one can quickly solve the equations numerically for a discrete number of frequencies $\omega_j$ with built-in functionality of most computational software, such as Mathematica's `LinearSolve[]` command. We apply this framework in section 12.3 on p. 157 to estimate the transmissibility of a proposed test-mass suspension system.

## 7.4 Effective transfer of chained systems with all degrees of freedom

In order to model the effective transmissibility of a system composed of multiple isolation stages, it is necessary to combine the individual systems in a coherent manner. In the case of the sophisticated vibration-isolation systems of gravitational wave detectors, this is simple: There is a clear mass hierarchy between the stages, which effectively allows to regard the next higher element in the hierarchy-chain as having infinite mass and thereby excludes the notion of backaction between chain elements (fig. 7.6(a)). For example, for the Advanced LIGO core optics[6], the first (active, hydraulic) isolation stage, HEPI, receives seismic (i.e. earth-) motion as input, where the effective mass of the ground is obviously many times heavier than the mass of the stage. The second (mechanical, passive and active) isolation stage, BSC-ISI, is again much lighter than the effective mass of HEPI, which allows to consider the input of HEPI onto BSC-ISI without accounting for backaction. The third-stage, the quadruple pendulum system, is again much lighter than BSC-ISI, so the same logic applies. This means that the effective transfer function of the system can simply be gathered by multiplying the individual transfer function matrices. For a displacement/rotation vector $(\vec{x}|\vec{\phi})^T$ and transfer matrices $T''$, $T'$ and $T$, we may calculate the output of such systems as

[6] Matichard et al. 2015

$$\begin{pmatrix}\vec{x}\\ \vec{\phi}\end{pmatrix}''_{\mathrm{out}} = T'' \begin{pmatrix}\vec{x}\\ \vec{\phi}\end{pmatrix}''_{\mathrm{in}} = T'' \begin{pmatrix}\vec{x}\\ \vec{\phi}\end{pmatrix}'_{\mathrm{out}} = \ldots = T''T'T \begin{pmatrix}\vec{x}\\ \vec{\phi}\end{pmatrix}_{\mathrm{in}}.$$

The task becomes significantly more challenging when the simplification of infinite masses can not be made, i.e. if the masses or excitations of the individual systems are similar or less than a few orders of magnitude apart. To the author's knowledge, there is no general procedure to couple the individual transfer functions of complex systems into a total transfer function. The problem arises from the circumstance that in a coupled system where the involved masses are not vastly different, every spring will cause an effect of backaction between the masses that it couples. Therefore it is not possible to deduce the total dynamics by knowing the response curves of all compound spring

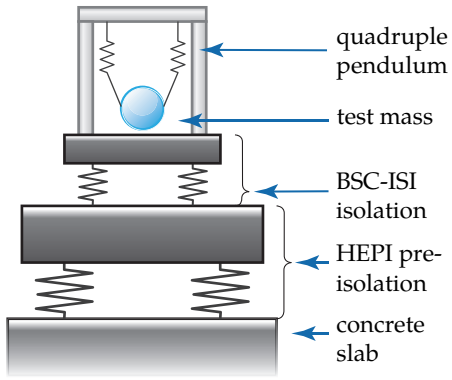


(a) Advanced LIGO isolation schematic (not representative of the actual isolation system geometry). Each isolation stage has practically infinite weight compared to the next in the chain, making it possible to calculate the total transmissibility function by multiplication of sub-system transfers.

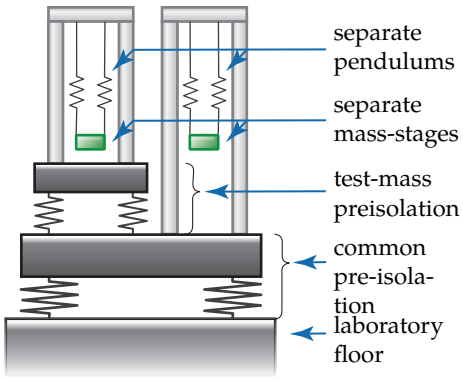


(b) Isolation schematic for the proposed experiment (disregarding the circumstance that both mass stages need to be very close). The mass stages have comparable weight, therefore backaction plays a role in the transmissibility between the stages and a full model needs to be calculated

**Figure 7.6:** Comparison of a typical gravitational wave detector isolation system and the system required for the proposed experiment.

systems individually, and an exact result can only be achieved when the entire calculation is performed from scratch for the complete system. This becomes even harder if some parts of the system can not be easily separated into springs and masses, i.e. if the system has extended soft bodies (like rubber feet). It turns out that even for the most simple system of just two coupled springs (e.g. in the context of mounted accelerometers), sophisticated methods are required in order to estimate approximate transfer functions[7].

[7] Gatscher and Kawiecki 1996

As sketched in fig. 7.6, the proposed experiment will necessarily involve a mechanical coupling between test and source mass as both are in some way mounted to a shared environment (e.g. the walls of a vacuum system). This implies that we have to require motion attenuation between the platforms that host the driving source mass and the test mass, the two of which have very comparable sizes and necessarily need to be coupled through isolation systems that at some points will have comparable masses as well. Therefore, an extended theory for the estimation of the error caused by neglecting backaction would be desirable and poses a logical progression of the work presented in this chapter.

## 7.5 Active vibration isolation and damping

Given its massive scope, we can only superficially touch upon the vast topic of active isolation and damping here. For a proper introduction into the topic of active isolation in gravitational wave detectors, see e.g. Matichard et al. (2015).

Fundamentally, any kind of active isolation will require inertial *sensors* that measure acceleration, and *actuators*. To counteract vibrational displacement, the signal from the sensors can be fed into the corresponding actuators. Naturally, even in the optimal case the residual vibration with active compensation is dictated by the sensor sensitivity, and can only be reached with sufficient gain in the control scheme. Additionally, both sensors and actuators introduce additional noise, which is the reason why usually additional passive isolation in later stages is needed to reach the high performance levels required in gravitational wave detection.[8]

[8] Robertson, Cagnoli, et al. 2002

The requirement of active damping arises from the necessity to neutralize internal modes of passive suspensions that lie within the frequency band of interest. Given a proper set of filters, it is possible to compensate for these modes with high selectivity, without significantly affecting the isolation performance in the neighboring frequencies.

The actuation force required for active control of certain DOFs can be inferred from the framework presented above. This is essentially compliance, though it is important to always specify where the force is acting and which displacement should be compensated. For the one-dimensional isolation chain discussed in section 7.2, we can simply derive the required actuation force per incoming displacement. For example, when setting the feedback to act exclusively on the first stage, $\tilde{\boldsymbol{F}}_{\mathrm{act}} = (\tilde{F}_{\mathrm{act1}}, 0, \ldots, 0)^T$, and requiring that the displacement of the final stage is vanishing, $\tilde{x}_n \stackrel{!}{=} 0$, solving eq. (7.3) allows us to find a frequency-dependent $\tilde{F}_{\mathrm{act1}}/\tilde{x}_0$. This method can easily be expanded to the three-dimensional system analyzed in section 7.3.

Part III

# Experimental design

In this part we will use the theoretical framework above and present a concrete experimental design based on driving of a mechanical oscillator that will allow to observe the gravitational field of a mm-sized object. We first present our choice of parameters in chapter 8 and argue that the proposed experiment is feasible as long as technical noise sources are not dominated over the actual gravitational signal. In order to tackle the former, we then dive into the technical aspects of the test mass in chapter 9, review some current design possibilities and investigate potential show-stoppers. Chapter 10 follows a similar structure, where we discuss possible implementations of the source-mass drive and trade-off considerations. As for outside noise sources, in chapter 11 we propose a compact optical readout scheme that should allow for thermal noise limited readout of the test mass position. Lastly, in chapter 12 we develop a multi-stage seismic isolation system that will shield the test mass from both the environment and the source-mass drive to a degree that will prohibit mechanical excitation through anything else then fundmental physical forces.

"Restless souls wander
where they don't belong."

---

The Legend of Zelda: Ocarina of Time
Shigeru Miyamoto

"Oh Christ, who walks up to a
switch marked 'LASERS' and thinks
'This. This is the one for me!'?"

---

Dr. Langeskov, The Tiger, and The Terribly
Cursed Emerald: A Whirlwind Heist
William Pugh

Chapter 8

# Parameters and effect size

We start the experimental part with a chapter on the parameters for the proposed measurement. Given the expressions derived in chapter 5, the aim is to find a set of conservative quantities that should ultimately allow us to observe the gravitational attraction of a pinhead-sized source mass. Here, we are primarily interested in the scenario where the limitations are dominated by fundamental physical effects, such as thermal noise, as opposed to technical hurdles. The latter will be the main concern of the remainder of part III.

After choosing the parameters for the test mass in section 8.1, in section 8.2 we motivate our choices for the quantities appearing in the force terms investigated in chapter 5 (sections 5.6 and 5.7). We check if the magnitude of gravity-induced frequency- and position-shifts of a micromechanical harmonic oscillator can be resolved in section 8.3 before demonstrating that a scheme based on resonant detection should indeed yield observable effects in section 8.4. We briefly investigate if the observation of non-Newtonian gravity is feasible with our current choices of parameters in section 8.5 before concluding with an overview of noise sources in section 8.6.

## Chapter contents

## 8.1 Test-mass parameters

In the first iteration of this experiment we select spherical masses. The simple reason for this choice is that by the shell theorem, Newtonian gravity of objects with spherical symmetry can be reduced to point masses, which heavily simplified our calculations in chapter 5. Furthermore, we were able to find exact expressions for most other forces in the common literature. This reduces the computational effort required to weight the effect of gravity compared to its potential rivals.

As the goal is to find the smallest feasible *source mass* for a micromechanical measurement of gravity, we can in principle chose our *test mass* size freely. Larger test masses are advantageous for the proposed measurement due to their lower thermal noise (see eq. (5.34) on p. 46). However, for this proof-of-principle demonstration, having a test mass significantly larger than the source mass would defeat the purpose of demonstrating gravitation between as-small-as-possible objects. Here, we will fix the test mass to have a diameter of $2r_\mathrm{T} = 2\,\mathrm{mm}$. As we will see below, this should allow to see the effect of a gravitational force with a similarly sized source mass, which is significantly smaller than source masses in previous measurements of gravity.[1]

[1] Gillies and Unnikrishnan 2014

For the resonance frequency of the test-mass device, there are two major considerations. The desired effect scales favorably with lower frequencies (see eq. (5.17b) on p. 38), which is the reason why typical torsion balance experiments (section 3.2.2 on p. 10) have oscillation periods up to tens of minutes. However, overcoming environmental noise (section 5.7.3 on p. 48) and electronic noise poses a significant challenge at low frequencies. This sets some limit to the lowest frequencies that can be reasonably used without the need for excessive additional effort in vibration isolation and the development of the electronic circuits. We chose a frequency of $\omega_0/(2\pi) \approx 50\,\mathrm{Hz}$, as we should be able to reach the required levels of electronic noise given state-of-the-art detectors (section 11.4 on p. 143) and environmental-vibration isolation that can fall short by some orders of magnitude compared to the highly sophisticated systems used in modern gravitational wave detectors (section 12.1 on p. 146). Another reason for this choice of frequency is that the gravitational pull of the earth may impede achieving comparably low frequencies in a micromechanical test-mass system (see section 9.2.2 on p. 98). Lastly, we assume a very conservative quality factor $Q = 2 \cdot 10^4$ which should be reasonable to achieve with a variety of current micromechanial systems (see section 9.8 on p. 114).

## 8.2 Force parameters

Here, we list the relevant choices of parameters for all deterministic force contributions analyzed in section 5.6 on p. 40. The values are summarized in

table 8.1 on p. 88.

**Newtonian Gravity.** In the following we will consider gold as the material of choice ($\rho_{\mathrm{Au}} = 19.3 \cdot 10^3\,\mathrm{kg\,m^{-3}}$) for the Newtonian force, eq. (5.21). The reasoning is provided in section 9.1.2 on p. 95.

**Coulomb force.** For the Coulomb force, eq. (5.24), we assume 200 surface charges on each mass with opposing charges and located at the closest position on each sphere. The magnitude of charging effects is investigated in section 9.5 on p. 109.

**London-Van der Waals.** From Hamaker (1937) we extract the largest measured London-vd. Waals constant of $\lambda_{1-2} = 400 \cdot 10^{-60}\,\mathrm{erg\,cm^6} = 400 \cdot 10^{-67}\,\mathrm{N\,m\,cm^6}$ (for alkalihalides), whereas an average value for other materials will be roughly a third of that. Using gold (197 amu per molecule and a density of $19.3\,\mathrm{g\,cm^{-3}}$) the atom number density of both masses is $Q_{1,2} = 5.7 \cdot 10^{22}\,\mathrm{cm^{-3}}$. This results in

$$A_{\mathrm{VDW}} < 1.4 \cdot 10^{-18}\,\mathrm{N\,m},$$

which yields as an upper boundary in the London-vd. Waals force, eq. (5.25).

**Casimir force.** With the exception of temperature, this force depends entirely on geometric parameters. For our consideration we choose room temperature $\Theta = 293\,\mathrm{K}$. At this temperature, eq. (5.26) indicates that we can consider the far-field approximation, eq. (5.27), as long as $d_{\mathrm{tot}} \gg 7.4\,\mu\mathrm{m}$.

**Patch potentials.** Speake and Trenkel (2003) chose the central wave number for eq. (5.28) such that the integrand is maximal for the given distance, and a width of one decade around that band is chosen to set the integration boundaries. For our system that number would correspond to a wavelength larger than the source mass, which is an unphysical assumption. Therefore we take the source-mass size to be the maximum wavelength and the smallest wavelength to be one decade smaller. We apply a theoretical value[2] for polished gold surfaces of $V_{\mathrm{rms}} \approx 45\,\mathrm{mV}$[a] and choose the cross section of the smaller of both spheres as the effective area. This is a very rough approximation of the situation as the above expression is only valid for the geometry of two planes. However, since the effective interaction area is necessarily bounded by the smaller of both cross-sections, this approximation is unlikely to cause an underestimation of the effect's strength.[b]

[2] Singh-Miller and Marzari 2009

[a] Note that for contaminated gold surfaces, the value of $V_{\mathrm{rms}}$ is significantly lower (Behunin et al. 2014).

[b] A potential flaw of this estimation is that we only considered the effect of a static deterministic patch potential force, while in fact the patch potentials also behave in a dynamic noise-like

**Gas molecule momentum kicks.** For eq. (5.29) we choose a background pressure of $10^{-8}$ hPa, which is a reasonable quantity for a non-baked UHV system that is opened on a regular basis (see section 12.3.6 on p. 166 for an overview of the proposed vacuum system). This yields a mean air molecule velocity $v_{\text{air}} \approx 500\,\text{m}\,\text{s}^{-1}$, which is much higher than the velocities expected from a drive modulation at 50 Hz. This confirms the validity of the approximations performed in section 5.6.7.

## 8.3 Magnitude of frequency and position shift

As shown in section 5.1 on p. 28, splitting the time-dependent distance into a static part $d_0$ and a zero-mean contribution of the displacement of both masses allows us to linearize the force terms around the non-deflected position of the test mass. Furthermore it was shown that the test-mass position coordinate and frequency are shifted due to the presence of the force terms.

We calculate the magnitude of parameter shifts due to the gravitational interaction of source and test mass, which are typically the observables of torsional-balance experiments. The explicit terms are given in eq. (5.5) on p. 30. Inserting gravity, eq. (5.21) on p. 40, yields

$$\Delta\omega_0 = \omega_0' - \omega_0, \quad \text{with} \quad \omega_0 = \sqrt{\omega_0'^2 + \xi} \quad \text{and} \quad \xi = -2\frac{GM}{d_0^3},$$
$$\Delta x = \varsigma\omega_0^{-2}, \qquad \text{with} \qquad \varsigma = \frac{GM}{d_0^2}.$$

With the source mass $M = 4\pi\rho_S r_S^3/3$ (where $r_S$ is the source-mass radius) we assume the extremal case where the surfaces of the test mass and the source-mass sphere are touching, i.e. $d_0 = r_T + r_S$. If now the test mass is selected to be extremely small compared to the source mass, $r_S \gg r_T$,[c] the shifts should be maximized as $d_0 \approx r_S$, leading to $\xi \approx -8\pi G\rho_S/3$ and $\varsigma \approx 4\pi G\rho_S r_S/3$. The resulting values are plotted in fig. 8.1 as a function of source-mass size. For typical Cavendish-type experiments with centimeter to decimeter-size source masses and a torsional pendulum operating at a resonance frequency of some millihertz, one can expect frequency shifts up to some hundreds of microhertz and displacements up to millimeters, both of which can be resolved reasonably in precision measurements.[d] One way of reducing the

manner (Speake and Trenkel 2003). The investigation of this effect was not performed within the scope of this thesis, but as explained in section 5.6.6, we expect it to be smaller than the averaged patch potential effect considered here.

[c] Note that an infinitely small mass has infinite thermal noise.

[d] The frequency shifts in actual measurements of $G$ are typically one order of magnitude higher, as the geometry of a torsion balance pendulum is only vaguely approximated by our one-dimensional, linear model.

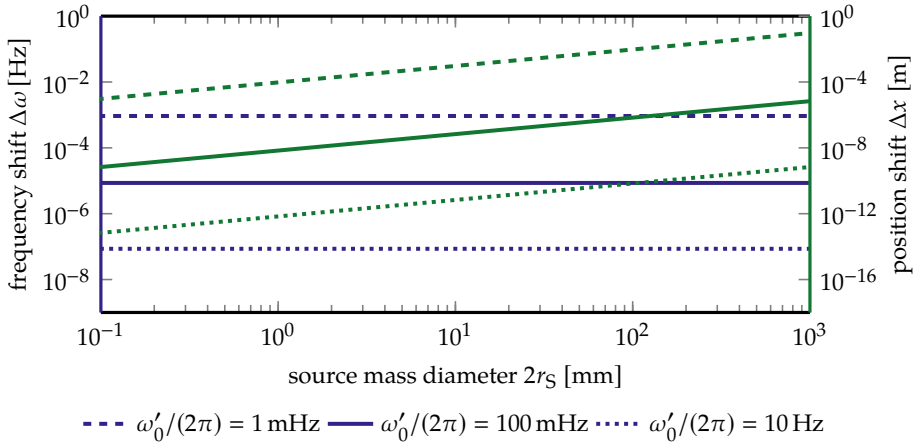


**Figure 8.1:** Gravitationally induced frequency and position shifts of a harmonic oscillator with frequency $\omega_0$.

mass further would be to reduce the experimental dimension $d_0$, which is however accompanied by an increase in resonance frequency $w_0$ (if we assume an unaltered spring constant). This results in a highly unfavorable scaling of the observable effects, since $\Delta\omega_0 \propto 1/\omega_0'$ and $\Delta x \propto (d_0\omega_0)^{-2}$. In particular, using $d_S = 2\,\mathrm{mm}$ and $\omega_0' = 10\,\mathrm{Hz}$ yields effective frequency and position shifts of tens of nanohertz and picometers, respectively, which is significantly more challenging to measure. For this reason, simply scaling down a Cavendish experiment is not sufficient to measure the gravitational effects of small source masses.[e]

## 8.4 Actual amplitude

We now consider the size of the individual force contributions to the integrated PSD, or the power spectrum, from eq. (5.17a) on p. 38. As was already pointed out there, this spectrum will entail cross-terms of various forces listed in sections 5.6 and 5.7 on p. 40 and on p. 45, which can be neglected as long as one force (here gravity) is dominating over all other contributions. For now, we

[e] The high precision of time measurements, with the definition of the second being down to one part in $10^{15}$, leads to the general consensus that frequency measurements are desirable in experimental physics. This was explicitly pointed out by Inguscio, Stringari, and Wieman (1999) writing "A precision measurement is almost always a frequency measurement.", which might well be absolutely correct for the Bose-Einstein condensates considered in the book, that typically oscillate at frequencies of hundreds of kilohertz and higher. However, low frequencies become tedious to measure, and the experimental environment may actually change (e.g. through drifts) during the measurement time. More precisely, the quote above should therefore read "A precision measurement is almost always a *high* frequency measurement (except for the cases where the effect scales with inverse frequency)."

| symbol | meaning | value |
|---|---|---|
| $\omega_0/(2\pi)$ | test-mass frequency | 50 Hz |
| $r_\mathrm{T}$ | test-mass radius | 1 mm |
| $Q$ | test-mass quality factor | $2 \cdot 10^4$ |
| $m$ | test-mass | 80.9 mg |
| $r_\mathrm{S}$ | source-mass radius | 1 mm |
| $M$ | source mass | 80.9 mg |
| $\epsilon$ | minimal surface-distance | 0.5 mm |
| $\Theta$ | temperature | 293 K |
| $\Gamma/2\pi$ | integration bandwidth | $1/3600\,\mathrm{s}^{-1}$ |
| $\rho$ | density | $19.3 \cdot 10^3\,\mathrm{kg\,m}^{-3}$ |
| $q_1, q_2$ | charges | 200 e |
| $Q_1, Q_2$ | atom density | $5.7 \cdot 10^{22}\,\mathrm{cm}^{-3}$ |
| $\lambda_{1-2}$ | London-vd. Waals constant | $4 \cdot 10^{-65}\,\mathrm{N\,m\,cm}^6$ |
| $V_\mathrm{rms}$ | RMS potential-fluctuations | 45 mV |
| $P$ | pressure | $10^{-8}$ hPa |

**Table 8.1:** Parameters of masses and experimental settings for the comparison of driving forces.

also ignore the effects of the readout noise and environmental noise, as they are separately treated in chapters 11 and 12. In this section we purely want to demonstrate that we can find a parameter regime within a millimeter-scale system where the effect of gravity dominates not only thermal noise, but also all other deterministic noise contributions.

In order to maximize the effect of the gravitational drive, we chose an optimal drive amplitude (see section 5.9 on p. 49; non-optimal amplitudes are investigated in section 10.1.1 on p. 120), a minimal surface distance $\epsilon = 0.5\,\mathrm{mm}$ and an integration time of 1 h. All parameters are summarized in table 8.1. Figure 8.2 shows the signal contribution of thermal noise and gravity as well as the other deterministic forces as a function of the source-mass radius. For these (conservative) settings, a signal to noise ratio of 1 is reached for a source-mass radius of 500 $\mu$m, which in case of gold corresponds to a source-mass weight of about 10 mg. For the parameters used (table 8.1), the main limitation of the measurement is posed by thermal noise. For our further considerations we want to leave some overhead for unaccounted experimental noise sources and hence choose a source-mass radius of 1 mm, where the gravitational contribution is about six times higher than the thermal noise. A gold sphere of this size has a volume of $4.2\,\mathrm{mm}^3$ and a mass of 80.9 mg, which is still

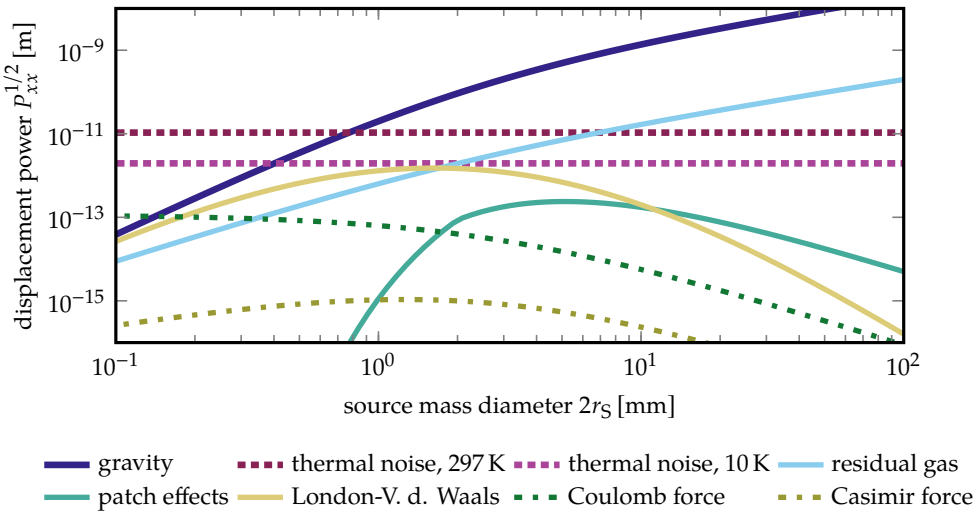


**Figure 8.2:** Signal contribution of gravity, thermal noise and various forces as a function of source mass diameter $2r_S$ at $\Theta = 293\,\mathrm{K}$ and $\Gamma/2\pi = 1/3600\,\mathrm{s}^{-1}$. The parameters for the various forces are explained in section 8.2 and summarized in table 8.1. The plot assumes a minimal surface distance of $\epsilon = 0.5\,\mathrm{mm}$ and an optimal modulation amplitude.

three orders of magnitude smaller than the smallest reported attractor masses in any experiment.[3] Using eq. (5.23) on p. 41, we find the actual harmonic amplitude (0-to-peak) for this configuration to be $5.2 \cdot 10^{-11}\,\mathrm{m}$. As here we only investigated fundamental physical effects, the main remaining challenge will now be to reach the requirements for the test- and source-mass in terms of frequency, mechanical quality, charges and drive amplitude (chapters 9 and 10), and to suppress environmental- and readout-related noise to below the thermal noise limit (chapters 11 and 12).

[3] Gillies and Unnikrishnan 2014; Ritter et al. 1990

We note that due to the relatively large distance $\epsilon = 500\,\mu\mathrm{m}$ between the test- and source-mass surfaces, some unwanted fields as well as the effect of residual-gas momentum transfers can be shielded by putting a thin membrane between the two masses.[4] The effect of additional Brownian damping through a membrane in proximity to the test mass is investigated in section 9.3.1 on p. 100.

[4] Weld 2007

## 8.5 Effect of non-Newtonian gravity

We briefly explore whether the proposed selection of parameters can in principle yield any improvement on the current bounds of conjectured extensions to Newtonian gravity. Recalling eq. (5.36) on p. 49, for a typical length scale $\lambda_Y$

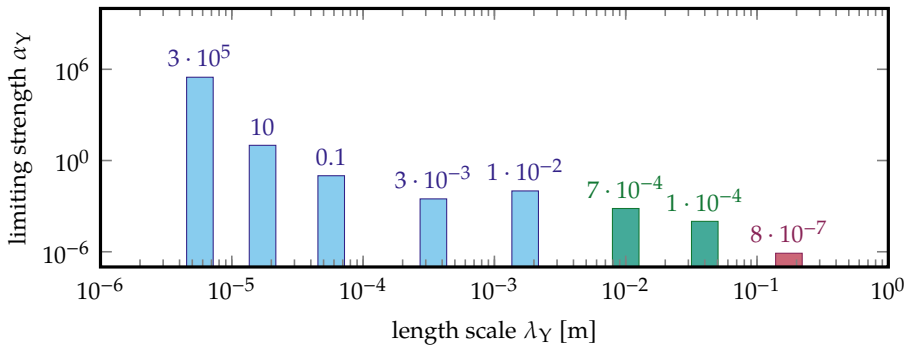


**Figure 8.3:** Current upper bounds of the correction strength $\alpha_Y$ for given values of the length scale $\lambda_Y$. Data was taken from Kapner et al. (2007) (blue), Hoskins et al. (1985) (green) and Wagner et al. (2012) (red).

the Yukawa potential is defined by a strength $\alpha_Y$. The upper bounds for $\alpha_Y$ from previous measurements are summarized in fig. 8.3 for the relevant range of length scales in the context of the proposed experiment. For each pair of length scale $\lambda_Y$ and Yukawa strength $\alpha_Y$, we checked if the Yukawa correction could yield a significant deviation from classical Newtonian gravity in the proposed experiment. Of the listed values, this is only the case for $\alpha_Y < 10^{-2}$ at $\lambda_Y = 3 \cdot 10^{-3}$ m, which yields a difference in the expected signals of about 1 % for a source-mass diameter below 2 mm. In the scope of the linearized theory used here, this value is not drastically improved by decreasing the minimal distance $\epsilon$ between both masses to 10 $\mu$m. These numbers might change with other choices of mass geometries and an advanced theory which incorporates higher-order force-terms, but with the current linear model of two spherical masses, detecting deviations from Newtonian gravity is likely not a worthwhile investigation until the relative precision of the experiment reaches the low-percentage regime.

As mentioned in section 5.8 on p. 48, accounting for MOND effects would require a new equation of motion with non-trivial changes to the current solutions. However, we note the that the typical low acceleration scale for which these forces are expected to become relevant lies around $a_0 \approx 10^{-10}\,\mathrm{m\,s^{-2}}$.[5] For the parameters set in table 8.1, the acceleration caused by Newtonian gravity, $F_G/m$, is located at around $3.9 \cdot 10^{-10}\,\mathrm{m\,s^{-2}}$. This means that the accelerations in our experiment are actually on a scale where deviations from standard gravity through MOND could potentially be tested.

[5] Milgrom 1983

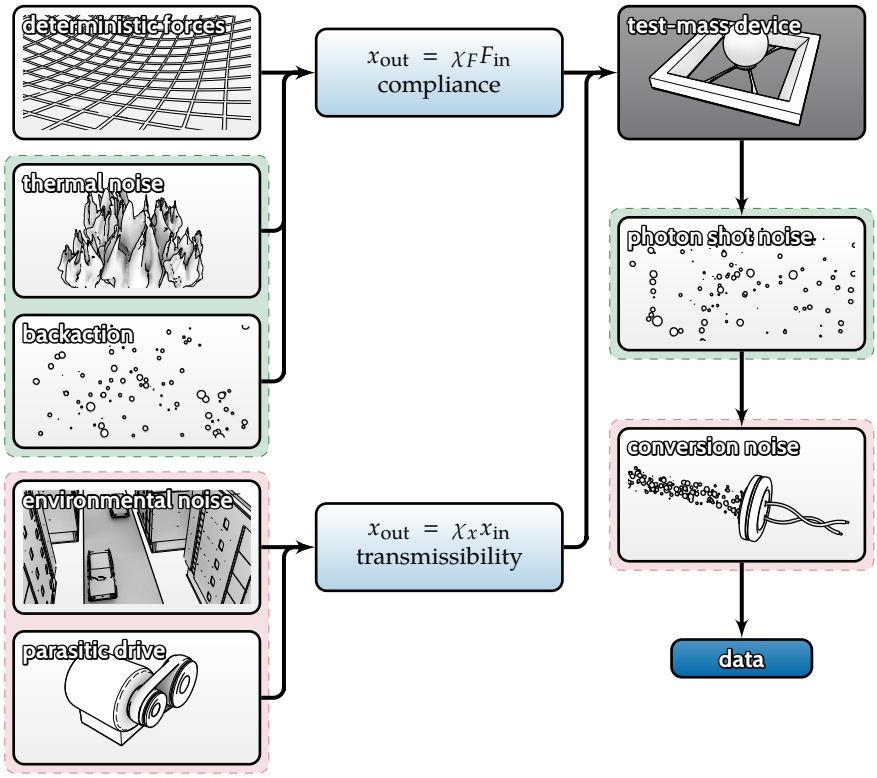


**Figure 8.4:** Individual signal contributions we account for. Deterministic forces as well as white thermal noise and backaction noise act on the test-mass device via the (symbolic) compliance $\chi_F$, while environmental vibrations and the parasitic drive act on the test mass via the transmissibility $\chi_x$. The readout of the test-mass motion is affected by photon shot noise and noise from the conversion from photons to current and digitization. Fundamental effects are highlighted in light green, while technical hurdles are highlighted in light red.

## 8.6 Summary of foreseeable sources of noise

In order to motivate the remaining chapters of the experimental part, we briefly categorize the sources of noise that need to be considered. We divide these sources into two major categories, depending on whether they cause actual physical displacement noise of the test mass or emerge from the measurement. The effects are illustrated in fig. 8.4.

In the first category of noise we find the sources that act directly on the mechanical harmonic oscillator and cause a displacement noise that is intrinsic to the system. The thermal noise (section 5.7.1 on p. 45) and the photon backaction (section 5.7.2 on p. 47) have flat force-noise spectra, which are converted to displacement by the mechanical compliance (eq. (7.2b) on p. 68). The environmental laboratory noise (section 5.7.3 on p. 48) (typically with a

$1/f$ displacement spectrum) and the mechanically coupled effect of the source-mass drive (*parasitic drive*) with a delta-like peak at the drive frequency. These forces act on the test mass support and are converted to oscillator displacement by the mechanical transmissibility (eq. (7.2a) on p. 68).

The second category has the noise sources that are part of the readout conversion from actual displacement to some electric signal corresponding to an *equivalent* displacement noise. Photon shot noise (sections 6.1 and 11.3.1 on p. 55 and on p. 139) adds flat, uncorrelated equivalent displacement noise to the system. Electronic noise (section 11.4 on p. 143) usually consists of $1/f$-type noise from electronic components. Finally, we include some additional effects from the discretization of the continuous voltage values.

Chapter 9

# Test mass

The last two decades have seen dramatic improvements in the fabrication and performance of micro- and nanomechanical devices[1]. In this chapter we investigate the feasibility of mass-loading high-$Q$ micromechanical devices with up to a 100 mg test mass.

[1] Imboden and Mohanty 2014; Zwickl et al. 2008

We start in section 9.1 with a brief overview on mass-loading of micromechanical devices, an argument for our choice of test-mass material and some considerations for the chip design. In section 9.2 we explain how we can set up FEM simulations of test-mass device geometries in order to calculate thermal spectra and gravitational effects. In section 9.3 we explain test-mass damping mechanisms beyond internal losses and in section 9.4 we investigate the effects of device heating from the optical readout. The accumulation of charges on the test mass is investigated in section 9.5 and in section 9.6 we comment on the effects of a slowed-down oscillator amplitude response due to the oscillator's small bandwidth. We conclude with a section on the optimization of the test-mass shape (section 9.7) and a list of the current candidates for devices (section 9.8).

## Chapter contents

## 9.1 Test-mass design

Here, we introduce some general considerations for the design of a micromechanical device loaded with a comparably heavy additional mass.

### 9.1.1 Mass-loading of devices

For our experiment, we are considering a micromechanical system that is mass-loaded with an 80 mg gold sphere, where the dimensions are chosen such that a test-mass cantilever at the target frequency $\omega_0$ of 50 Hz is formed. An open question is if there is a limit to the achievable mechanical quality for such a structure. For the measurement of Casimir forces[2] as well as in the context of biological applications of atomic force microscopy (AFM) with colloidal probes, microbeads of glass, polystyrene, polyethylene and other materials have been successfully attached to micromechanical cantilevers while maintaining typical AFM cantilever quality factors in the ten-thousands to millions[3]. However, if the added masses are much larger (tens to hundreds of grams), it remains an outstanding question whether the desired high quality factors can still be achieved in this extreme case. Here, a number of new challenges arise, e.g. increased damping by residual gas molecules (see section 9.3.1 on p. 100) and losses through clamping of the cantilever-chip to the environment, which become non-negligible when a huge mass is attached to the cantilever (see section 9.3.2 on p. 102). We also note that as an alternative to loading the out-of-plane COM mode of a typical cantilever one might consider loading a torsion-mode, which has been shown to yield comparably low stiffness while maintaining high mechanical quality factors in a measurement of Casimir forces[4].

For the stable attachment of a massive sphere to a fragile mechanical membrane or cantilever there are currently three different approaches. The first method is the application of an adhesive. As the mechanical loss rates of

[2] Chan, Aksyuk, et al. 2001; Mohideen and Roy 1998

[3] Butt, Cappella, and Kappl 2005; Owen and Müller 2014; Plodinec, Loparic, and Aebi 2010

[4] Chan, Aksyuk, et al. 2001

most adhesives are high, this method will almost certainly limit the overall $Q$ of the devices, unless special high-$Q$ adhesives are used (cf. section 9.3.3 on p. 104). A second method is welding by direct melting of the test-mass sphere. Given the low melting point of lead, we were able to demonstrate clean attachment points of lead to SiC (see section 9.8.3 on p. 117), but it is unclear if this technique can be used for higher-density metals with higher melting points (such as gold and tungsten) due to the limited thermal resistivity of possible substrate materials. As a third approach one might consider bonding techniques, i.e. thermal compression bonding[5] or wire bonding[6].

[5] Ang et al. 2006

[6] Corti, Holliday, and World Gold Council 2010, ch. 13

### 9.1.2 Test-mass material

We chose gold as the material for both the source and the test mass due to its high density ($\rho_{\mathrm{AU}} = 19.3\,\mathrm{g\,m^{-3}}$), purity (there is just a single stable isotope of gold) and homogeneity[7]. Though possessing comparable density, we chose gold over tungsten. In addition to a much higher melting point[8] and the existence of four stable isotopes, the latter has higher surface hardness[9], which potentially increases the mechanical quality but makes the manufacturing process of the test mass more challenging. Using electropolishing techniques, high surface qualities can be achieved.[10] For testing purposes we acquired sample gold masses in both spherical and cylindric shape (both with a diameter of 2 mm) from a local goldsmith[11]. We measured the deviation of weight to be within 1 % for a sample size of ten masses.

[7] Montgomery 2011

[8] Haynes 2014

[9] Issler, Ruoß, and Häfele 2003

[10] Wolf 1977

[11] Kub 2017

Since a thin layer of gold can easily be deposited on clean surfaces[12], this leaves the possibility to create lower-density test- and source masses with identical surface properties to the actual devices in order to perform consistency- and background measurements. Note that in the context of AFM cantilevers, gold coatings have been associated with significant reduction in mechanical quality.[13]

[12] Corti, Holliday, and World Gold Council 2010

[13] Churnside et al. 2012

### 9.1.3 Chip design considerations

The are some geometric considerations when designing the chip that hosts the mass-loaded device. We naturally require some kind of access from both sides of the chip. On the mass-loaded side, we require enough space to bring the source mass sufficiently close (down to $\epsilon = 0.5\,\mathrm{mm}$) and potentially to fit a shielding membrane. We should also account for some tolerance here as the test and source mass will be mounted on individual free-swinging vibration isolation stages. Ideally, a cylinder above the test mass of at least 3 mm to 4 mm in diameter should be kept clear. The other side of the chip will be used for optical readout. This means that we require a certain minimal reflectivity to keep test-mass heating low (see section 9.4 on p. 106) and enough space to

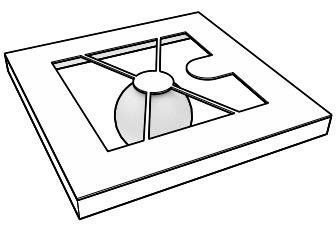

(a) Cantilever design where a high-frequency reflective "tongue" is added to the substrate in order to provide the reflective point for the local oscillator beam.

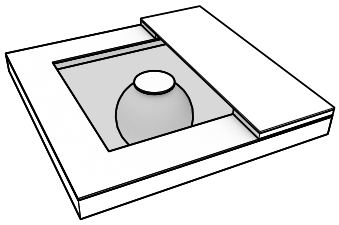

(b) Membrane design where a separate layer needs to be added for the local oscillator reflective point, such that the motion of the membrane is not affected.

**Figure 9.1:** Chip designs that provide additional mirror surface for local oscillator beams.

fit the (possibly angled) beams for the interferometric position probe.[a] These geometric constraints of clearance above and below the test-mass device seem trivial to achieve when thinking of a flat chip design, however, as explained in section 9.3.2 on p. 102, it will likely be required to have a stiff bond between the chip and a large high-$Q$ mass, which makes it more challenging to achieve the necessary clearances.

There is a another geometric requirement arising from our specific choice of optical readout geometry. As is argued for in section 11.2.3 on p. 132, it is advantageous to reflect not only the signal beam, but also the local oscillator beam off the device chip. This interferometer design puts the beam separation of signal and local oscillator at about 2 mm, so an additional mirror surface needs to be placed close to the test-mass mirror to reflect the local oscillator. In the case of a tethered structure, this can be done easily by adding a tongue shape to the tether cutout (fig. 9.1(a)), while for a membrane structure it might require an additional fabrication layer (fig. 9.1(b)). A similar scheme was demonstrated by Paolino, Sandoval, and Bellon (2013) with a much smaller beam separation by reflecting the local oscillator beam off a device arm (instead of the substrate). We note that this method will naturally lead to decreased sensitivity for the fundamental mode, where the mode shape spans the whole space from the point of maximal deflection to the substrate monotonously.

Due to the "floppy" nature of the proposed device, handling might pose an additional challenge. As shown in section 9.2.2, the effect of the gravitational pull alone will cause a significant deflection of the device. With impacts from transportation potentially exerting enough force to break devices, one might

[a] Depending on the readout scheme (see fig. 11.2 on p. 134), this can either be a cylindric clearance for the less-efficient scheme (fig. 11.2(a)), or a prism-like clearance for the more efficient scheme with an angled reflection (fig. 11.2(b)).

therefore consider specially damped transport boxes that provide some degree of vibration isolation.

## 9.2 Test-mass finite element simulations

We are interested in eigenmodes and -frequencies of specific device geometries, mechanical qualities of modes, thermal-conduction behavior and the effects of external forces. These questions can be efficiently investigated with finite element solvers. Specifically, we use the COMSOL suite and its built-in functionality (such as the **Eigenfrequency** solver for **Solid Mechanics**) that is tailored to typical applications in physics research (opposed to engineering-focused applications).

Tuning the dimensions of a given device such that an out-of-plane COM mode has the desired shape and frequency can be achieved in multiple ways. Trial-and-error iterations yield reasonable results after a few attempts. As a more systematic approach, one may vary the parameters in a **parametric sweep** with COMSOL's onboard tools, or connect COMSOL to MatLab via the LiveLink interface and write an optimizer program to find the ideal geometry.

### 9.2.1 Total thermal power spectral density

So far, we have considered just one mechanical mode. An actual mechanical oscillator will not have a single eigenmode, but a spectrum of higher-order modes. Reading out the position of a thermally driven oscillator will show a spectrum of all of those modes combined. The results of the **Eigenfrequency** study can be processed into such a thermal mode spectrum by using the effective modal mass as defined in eq. (5.38) on p. 50. In order to extract the quantities needed to calculate this expression, we require two probes. A **Domain Probe** is used to integrate the total squared local displacement times the local mass density `(u^2+v^2+w^2)*solid.rho` over the entire volume of the device for each mode. This is normalized using a **Boundary Probe** that integrates the mode overlap, namely the product of the local deflection in the beam's direction and the Gaussian beam profile of the readout beam, `w*exp(-(x^2+y^2)/(2r0)^2)`, over the reflective surface of the device. For every individual mode $i$, both expressions are then combined as shown in eq. (5.38), yielding the effective modal masses $m_{\mathrm{eff}\,i}$.

As seen in eq. (5.34) on p. 46, the thermal PSD of a single mode is given by $S_{x\,\mathrm{th}} = |\chi(\omega)|^2\, 2\gamma/(m_{\mathrm{eff}}\beta)$. Using eq. (5.15c) on p. 36, we may utilize the orthogonality of mechanical modes and generalize this expression to a sum of individual modal contributions as[14]

[14] Gillespie and Raab 1995; Levin 1998; Saulson 1990

$$S_{x\,\mathrm{th,tot}} = \sum_i |\chi_i(\omega)|^2 \frac{2\gamma_i}{m_{\mathrm{eff}\,i}\beta} \quad \text{with} \quad \chi_i(\omega) = (\omega_{0i}^2 - \omega^2 - \mathrm{i}\gamma_i\omega)^{-1}, \tag{9.1}$$

where for every mode $i$, $\omega_{0i}$ denotes the eigenfrequency, $\gamma_i$ denotes the specific damping rate and $m_{\mathrm{eff}\,i}$ is the specific mass we have just calculated.[b] In fig. 9.2(d) below we show such a total spectrum for a specific example geometry.

### 9.2.2 Effect of gravitational pull

We estimate the deflection caused by the Earth's gravitational pull acting on the test mass. We also evaluate the added stress-induced effect on the model frequency. With a spring in vertical direction, the analytic expression for the static deflection follows directly from the harmonic oscillator equations of motion. It is

$$\Delta x = gm/k = g/\omega_0^2, \tag{9.2}$$

which is about 100 $\mu$m for the selected frequency of 50 Hz. In a perfect harmonic oscillator (i.e. with a linear restoring force), no gravitationally-induced frequency shift should occur in this scenario, as the gravitational background field has negligible position dependence. However, as seismic isolation is significantly easier in horizontal direction (see chapter 12), it would be preferable to drive the test mass horizontally. With gravity then pulling the sample in some in-plane direction, which might have less stiffness, even stronger deflections could be encountered (see figs. 9.2(a) to 9.2(c)). It therefore makes sense to incorporate the gravitational pull into the FEM model. In COMSOL, we can perform a **`Prestressed Analysis`**, which is a **`Study`** that consists of two steps. In the **`Stationary`** step the solver is searching for the steady-state of the device given the forces caused by a high-stress membrane layer and the gravitational pull on a relatively huge mass, which is implemented by adding a **`Gravity`** domain force. The result of the first step is then taken as the linearization point for the **`Eigenfrequency`** step, which finds the mechanical modes and eigenfrequencies of the model while neglecting external forces (this makes the first step necessary). If the model and the computational power allows it, it is advantageous to set both study steps to **`Include geometric nonlinearity`**, as the expected deflection due to the actual test mass are significant and therefore may change the qualitative behavior of the system.

We performed the above analysis for a four-arm tethered AlGaAs structure (cf. section 9.8.1) for the case of no gravitational pull, a gravitational pull within

[b] As is pointed out by Levin (1998) and Neben et al. (2012), we have to implicitly assume that the dissipation of the individual modes is uniformly distributed over the test-mass interior for the above expression to be correct, and more general methods to estimate the PSD are required for genuinely precise estimations.

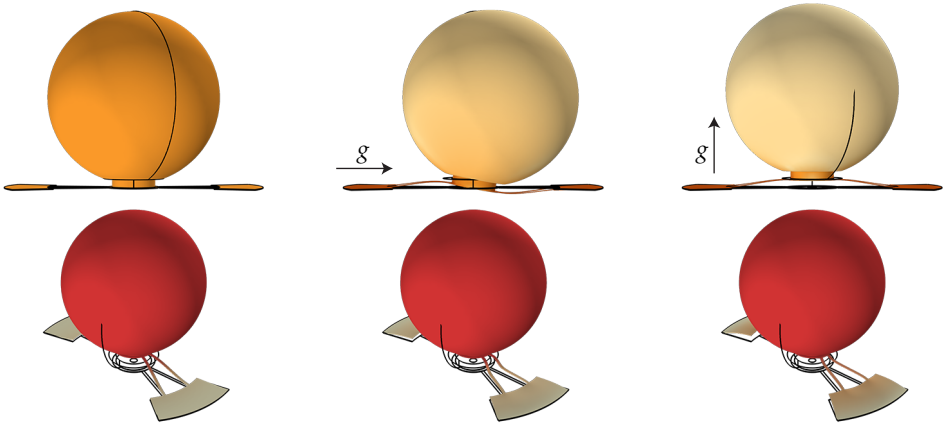

(a) No gravitational pull yields a clean mode at $\omega_0/(2\pi) = 52.2\,\text{Hz}$.




(b) An in-plane gravitational pull yields a distorted mode at $\omega_0/(2\pi) = 543\,\text{Hz}$.




(c) An out-of-plane pull yields a distorted mode at $\omega_0/(2\pi) = 677\,\text{Hz}$.

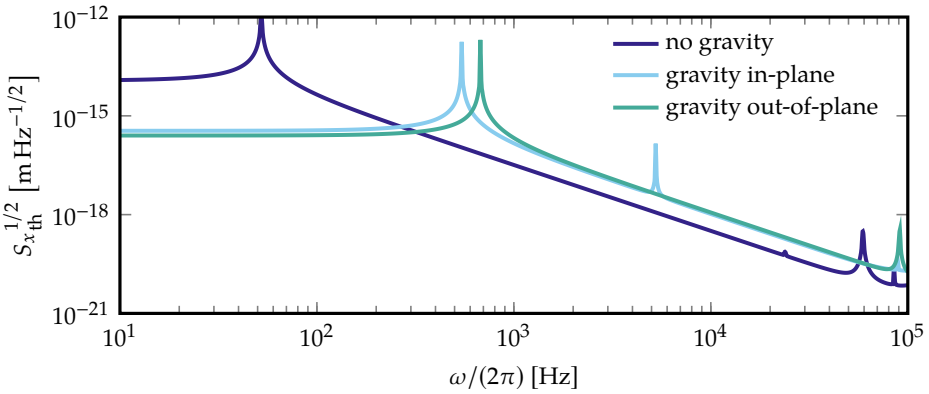


(d) Thermal PSD for the same structure and three different cases of gravitational pull, generated from the first 40 modes.

**Figure 9.2:** Effect of gravitational pull for a test mass based on a tethered AlGaAs structure with a thickness of 7 $\mu$m, a mirror pad with diameter 600 $\mu$m (tether length 700 $\mu$m and width 40 $\mu$m) and a readout beam spot radius $r_0 = 100\,\mu$m. In (a), (b) and (c) the top pictures show the to-scale static deflections, while the bottom pictures show the normalized COM out-of-plane modes (all of which have an effective mass $m_{\text{eff}} = 83\,\text{mg}$).

the plane of the device and an out-of-plane pull. The results are shown in fig. 9.2, along with the thermal PSD as explained in section 9.2.1. The frequency shift induced by the change of the linearization point is massive, yielding an increase by more than one order of magnitude. This is very surprising as in a simple harmonic oscillator analytic model, no such shift should occur. A potential reason for the change in eigenfrequency could be a drastic increase in

stress due to the gravitational pull. Initially no pre-stress (typical for AlGaAs) was assumed for the simulation, so we should also expect a different behavior for (inherently) pre-stressed devices from e.g. silicon nitride or silicon carbide (section 9.8). It will be necessary to compare these results to spectra obtained from actual devices in order to reach a final conclusion.[c]

## 9.3 Damping

In this section we investigate the magnitude of additional damping effect, i.e. effects that ore not directly related to geometry or internal material losses, as the goal is to ultimately be limited only by the internal losses of the substrate material.

### 9.3.1 Brownian force noise damping

We estimate the effect of additional Brownian force noise from residual air molecule impacts. For optically levitated nano-particles, an expression for the damping rate is provided by Li, Kheifets, and Raizen (2011) that holds for both the viscous as well as the molecular regime,

$$\begin{aligned} \gamma_{\text{nano}} &= \frac{6\pi\eta r_{\text{T}}}{m}\frac{0.619}{0.619+\text{Kn}(P)}(1+c_K(P)), \\ \text{with}\quad c_K(P) &= \frac{0.31\text{Kn(P)}}{0.785+1.152\text{Kn}(P)+\text{Kn}^2(P)}, \\ \text{Kn(P)} &= \frac{s(P)}{r_{\text{T}}} \quad \text{and} \quad s(P) = \left(\sqrt{2}\pi d_{\text{mol}}^2 \beta P\right)^{-1}, \end{aligned}$$

where $\eta$ is the viscosity of air, $P$ is the pressure, $r_{\text{T}}$ is the test-mass radius, Kn(P) is the Knudsen number and $d_{\text{mol}}$ is the molecular diameter of air. As our test mass is significantly larger than nano-particles, it is not clear whether this estimation holds. Therefore, we compare this to an expression for macroscopic bodies in the molecular regime.[d] For spheres and cylinders, we find[15]

$$\gamma_{\text{sphere}} = \frac{P}{m v_{\text{air}}} r_{\text{T}}^2 \left(\frac{128\pi}{9}\right)^{1/2}\left(1+\frac{\pi}{8}\right)$$

[15] Cavalleri, Ciani, Dolesi, Hueller, et al. 2010

[c] Note that lowering the frequency of gravitational pull-free devices further in order to compensate for the shifts will likely not yield devices that exhibit the desired frequencies under gravitational load. The additional stress through gravitational pull causes an *additional* stiffness that simply dominates in the total stiffness. In the worst case, one then has to transition to an experimental parameter regime that incorporates higher test-mass frequencies.

[d] At the transition from the viscous to the molecular regime the mean free path length $s(P)$ of gas molecules is on the order of the scale of the object. As this quantity exceeds significant scales of the experiment already below $10^{-3}$ hPa, we can safely assume to be in the molecular regime.

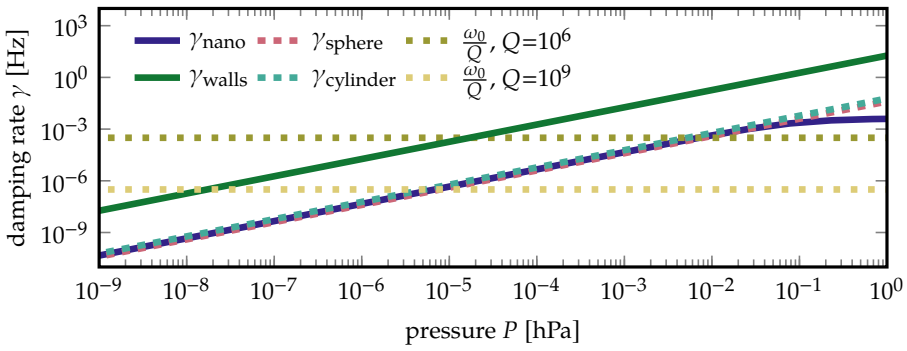


**Figure 9.3:** Gas-molecule induced damping rates as a function of background pressure. The dashed lines mark the quality factor $Q$ equivalent values for a frequency $\omega_0/(2\pi) = 50\,\text{Hz}$.

$$\gamma_{\text{cylinder}} = \frac{P}{m v_{\text{air}}} r_{\text{T}}^2 \sqrt{8\pi} \left( \frac{h_{\text{T}}}{2r_{\text{T}}} + \frac{\pi}{4} + 1 \right),$$

where $v_{\text{air}} = (\beta m_{\text{air}})^{-1/2}$ is the average velocity of air molecules and $h_{\text{T}}$ is the test-mass cylinder height. We also take into account the additional damping due to a membrane that is placed between the test mass and the source mass, since significant increases in residual-gas damping rates have been observed for larger test masses in constraint volumes.[16] As we will potentially deploy a membrane close to the test mass, we need to take these effects into account. An analytic expression for the additional losses in a cylinder close to a wall in the low-frequency limit is given by Dolesi et al. (2011) as

[16] Cavalleri, Ciani, Dolesi, Heptonstall, et al. 2009

$$\gamma_{\text{walls}} = \frac{P}{m v_{\text{air}}} r_{\text{T}}^2 \frac{\pi^{3/2} r_{\text{T}}^2}{\sqrt{2} d_{\text{mem}}^2 \ln\left(r_{\text{T}}^2 / d_{\text{mem}}^2 + 1\right)},$$

with a separation length $d_{\text{mem}}$ between the cylinder face and the surface. This is essentially a worst-case estimate for the proposed spherical test-mass design, as a cylinder face close to a flat surface can trap significantly more gas molecules.

We choose $r_{\text{T}} = 1\,\text{mm}$ and $h_{\text{T}} = 2\,\text{mm}$, and, for the estimation of $\gamma_{\text{walls}}$, $d_{\text{mem}} = 10\,\mu\text{m}$. All resulting damping rates are shown in fig. 9.3 as functions of the background pressure $P$. For the chosen parameters and at a fixed background pressure of $P = 10^{-8}\,\text{hPa}$, the damping from residual air molecules, $\gamma_{\text{air}}$, can only limit the mechanical quality $Q$ if it approaches values above $10^7$. In order to achieve higher values of $Q$, one would have to decrease the background pressure or increase the distance $d_{\text{mem}} = 10\,\mu\text{m}$ between test mass and membrane; both of which can easily be done as our assumed parameters are conservative.

We see that air damping should not pose an issue in vacuum systems that are continuously pumped; however, from our experience, in a system without

a running pump UHV components will be necessary to keep the pressure below $10^{-3}$ hPa.

### 9.3.2 Clamping losses

Typical chip-scale support structures that carry the micromechanical structure are on the order of a few centimeters in size and a few milligrams in weight. For example, the chips used by Vanner et al. (2013) have a weight of about 1 mg. This has to be contrasted with the 80 mg test mass selected for the proposed experiment. Thinking in terms of the eigenmodes of an *unconstrained* device, it is clear that the mode shapes feature much higher displacement amplitudes in the light chip than in the heavy test mass, as the total COM needs to be conserved. In consequence, if the chip motion is constrained by clamping it to a heavy environment, the mechanical quality of the clamp will ultimately limit the effective $Q$ of the device. This effect also occurs in the context of suspensions for the mirrors of gravitational wave detectors, where it is referred to as *recoil damping*.[17] The theory is consistent with the observation that the clamping losses scale extremely favorably with temperatures approaching cryogenic regimes[18], due to increased hardness and therefore increased mechanical quality of a relatively soft clamping material.

[17] Willems et al. 2002

[18] Yuan, Cohen, and Steele 2015

In order to estimate the effect of a low-$Q$ clamping, we can set up a simple mechanical model (fig. 9.4(a)). As before (cf. chapter 7), the test mass has coordinate $x$ and mass $m$ and is connected to the chip substrate with a spring of spring constant $k$ and damping $\beta$ (with $k/m = \omega_0^2$, $\beta/m = \gamma$). The chip has the coordinate $x_C$ and mass $m_C$ and is connected to the (infinitely heavy) environment with a spring of stiffness $k_C = m_C\omega_C^2$ and damping $\beta_C = m_C\gamma_C$. This system is described by the equations of motion

$$\begin{aligned} 0 &= m\ddot{x} + \beta(\dot{x} - \dot{x}_C) + k(x - x_C), \\ 0 &= m_C\ddot{x}_C + \beta(\dot{x}_C - \dot{x}) + k(x_C - x) + \beta_C\dot{x}_C + k_C x_C. \end{aligned}$$

We are interested in the damping rates of the effective modes of the compound system. Therefore we make the ansatz $x = x_0 \exp(st)$, $x_C = x_{C0} \exp(st)$, where the real and imaginary part of $s$ correspond to the modal damping rate and frequency, respectively. We may then rewrite the above equations as

$$\begin{pmatrix} s^2 + \gamma s + \omega_0^2 & -\gamma s - \omega_0^2 \\ -\gamma s - \omega_0^2 & \mu^{-1}(s^2 + \gamma_C s + \omega_C^2) + \gamma s + \omega_0^2 \end{pmatrix} \begin{pmatrix} x_0 \\ x_{C0} \end{pmatrix} = 0, \tag{9.3}$$

where we substituted the individual damping rates and frequencies for the damping coefficients and spring constants and introduced the mass ratio $\mu = m/m_C$. This equation has four complex solutions for $s$, which are obtained by requiring the determinant of the left-hand matrix to vanish. The four

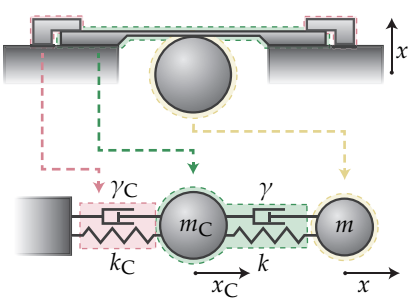


(a) Schematic illustration of test-mass chip system (top) and equivalent mass-spring-model (bottom).

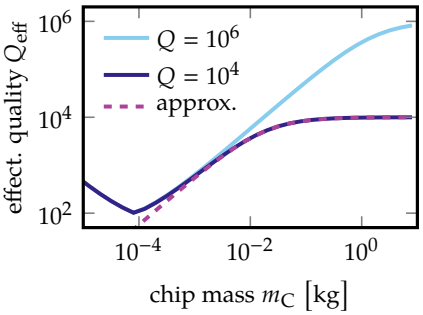


(b) Exact solution of eq. (9.3) and approximation eq. (9.4) for the relevant test-mass mode.

**Figure 9.4:** Effective mechanical quality for a clamped system where we assumed $Q_C = 10$, $\omega_C/(2\pi) = 10\,\mathrm{Hz}$ and the standard test-mass parameters (table 8.1 on p. 88).

solutions correspond to the two mechanical eigenmodes with damping rate $\gamma_{\mathrm{eff}} = -2\Re(s)$ and two opposing-sign frequencies per mode $\omega_{\mathrm{eff}} = \pm\Im(s)$. A full exact expression for these terms is quickly derived with computer algebra; however, it fills multiple pages. Fortunately, a formally identical model has been analyzed by Saulson (1990) to estimate the thermal noise of mirror suspensions. There, a simple approximation for the relevant mode in the regime of the support mass being much higher than the test mass ($\mu \gg 1$) has been derived as

$$\gamma_{\mathrm{eff}} \approx \gamma + \gamma_C \mu \frac{\omega_0^4}{(\omega_0^2 - \omega_C^2)^2}. \tag{9.4}$$

This expression as well as the exact solution above are plotted in fig. 9.4(b). It is immediately clear that similar frequencies of the test-mass mode and the clamp mode should be avoided, as this will massively increase the effective damping rate. This is consistent with the observation that the frequency of the exact solution, $\Im(s)$, will jump non-continuously in the regime of similar frequencies due to the degeneracy of the effective modes.

Demanding that recoil damping will only increase the effective damping by a small fraction $\kappa$, i.e. $\gamma_{\mathrm{eff}} < (1+\kappa)\gamma$, we can rewrite the above equation as

$$\kappa m_C \overset{!}{>} m \frac{Q}{Q_C} \frac{\omega_0^3 \omega_C}{(\omega_0^2 - \omega_C^2)^2}.$$

Typical clamps are compact and made from soft materials, such as polytetrafluoroethylene. We roughly estimate a clamping frequency of $\omega_C/(2\pi) = 10\,\mathrm{Hz}$ and quality $Q_C \approx 10$. Demanding a maximum relative damping increase

$\kappa = 10\,\%$, this yields a minimum chip mass of 35 g for a test mass $Q = 2 \cdot 10^4$ and 3.5 kg for $Q = 2 \cdot 10^6$.

We can think of two ways to effectively increase the chip mass. The first solution is to either directly bond, or to rigidly glue the chip to an appropriately shaped slab of a high-$Q$ material, such as quarz or aluminum, using a very thin layer of a high-$Q$ glue (see also section 9.3.3). The second solution is to extend the chip such that it reaches the desired mass, either by bonding it to a bulk piece of the same material in the microfabrication process, or by actually fabricating the structures on massive wafers (which can be made up to 40 mm thickness, where other restrictions of the fabrication process will likely limit the size).

### 9.3.3 Bonding interface and adhesive

Compared to the masses that are used in biological applications and established force-sensing techniques (section 9.1.1), our experiment deals with significantly more massive objects. From the need of a relatively large contact-area follows a comparably large deformation of the test mass as part of the relevant oscillator mode. This means that the bulk mechanical quality $Q_{\text{mass}}$ of the test mass becomes relevant for the overall loss rate of the device. Since we could not find a convincing value for the mechanical quality of the high-density metals gold and lead, we performed a forward transmission measurement[19] (also referred to as measuring the $S_{21}$ matrix element of a two-port network) of a 2 mm gold sphere (fig. 9.5(a)). This was implemented by piezomechanical excitation and readout, and the desired transmission parameter is the ratio of generated readout-voltage and applied excitation-voltage.[e] With the half-maximum width $\Delta\omega/(2\pi) = \gamma/\pi \approx 1.6\,\text{Hz}$ and central frequency $\omega_0/(2\pi) \approx 360.5\,\text{Hz}$, we can estimate the mechanical quality as $Q_{\text{mass}} = \omega_0/\gamma \approx 456$. However, we do not expect more than order-of-magnitude precision out of this measurement, as the piezo heads were large compared to the test mass. Instead of the measured value, we use a safer value of $Q_{\text{mass}} = 100$ for the computation.

[19] Orfanidis 2016

With such low mechanial quality it is important to avoid deformation of the test mass as a mode-shape contribution of the relevant COM mode. This requires a careful design of the cantilever geometry. FEM methods provide the means to analyze mode shapes and to estimate effective $Q$-values of compound cantilever systems. The results can be used to optimize geometries with regard to test-mass deformation.

For devices that are limited in mechanical quality not geometrically but by internal losses, one obtains the overall dissipation by adding up the loss

[e] These initial $Q$ measurements where performed in collaboration with Stephan Puchegger (Faculty Center for Nanostructure Research, University of Vienna), who also supported us with $Q$ measurements of commercial adhesives.

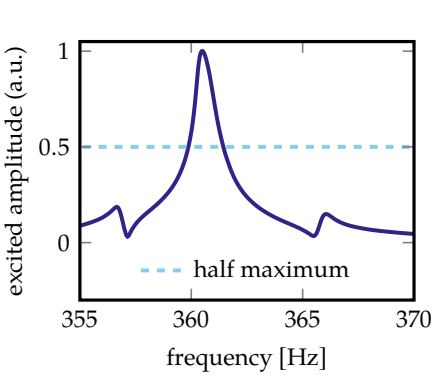


(a) Spectral forward transmission (S21 gain/loss) of a 2mm gold sphere mounted on opposite poles.

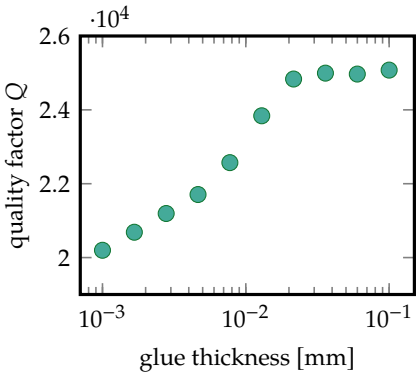


(b) Mechanical qualify factor as a function of the thickness of the adhesive layer as obtained by the FEM simulation.

**Figure 9.5:** Relevant plots for the estimation of $Q$ for a compound system of AlGaAs cantilever, adhesive layer and test mass.

angles while scaling their contribution with the mode stress derived from FEM simulations. The effective $Q$ value of a compound system can therefore be computed as[20]

[20] Harry et al. 2002

$$Q^{-1} = U^{-1} \sum_i Q_i^{-1} U_i .$$

Here, $U$ is the total elastic energy of the excited mode, $U_i$ is the part of the energy stored in the $i$th component and $Q_i$ is its quality factor. In our case,

$$Q = U \left( \frac{U_{\text{substrate}}}{Q_{\text{substrate}}} + \frac{U_{\text{adhesive}}}{Q_{\text{adhesive}}} + \frac{U_{\text{mass}}}{Q_{\text{mass}}} \right)^{-1} , \tag{9.5}$$

where *substrate* denotes the cantilever material. For completeness we added an (optional) adhesive layer to our model.

With COMSOL eigenmode simulations we can tune a cantilever geometry to roughly oscillate at 50 Hz with the out-of-plane COM mode. We then integrate the energy density in the deflected state by means of **`solid.Ws`** for all individual components of the system for any given mode using **`Domain Probe`**s. This allows us to calculate $Q$ using the above expression. The individual $Q$-values were gathered as follows: For the adhesive, a $Q_{\text{adhesive}}$ value of "more than 300" at room temperature was reported by Schediwy et al. (2005). As a substrate we assume AlGaAs (section 9.8.1), similar to the devices used by Cole (2012), with a room temperature $Q_{\text{substrate}} \approx 30\,000$. The geometry we chose for the FEM simulation is a 4-arm-cantilever with a central mirror pad (fig. 9.2) with

a thickness of 7 $\mu$m, an arm length of roughly 1 mm and a resulting center of mass out-of-plane mode frequency of roughly 53 Hz. Applying eq. (9.5) to the results obtained from the FEM simulations we estimate the effective mechanical quality of the compound system as a function of the adhesive thickness. The results are shown in fig. 9.5(b). Since the mechanical quality decreases when the adhesive layer thickness is smaller than 20 $\mu$m, it will be necessary to apply a suitable minimal amount when assembling the actual structures. Note that this unintuitive scaling is an effect of the adhesive having a *larger* mechanical quality than the test mass. Assuming that our assumptions are valid (i.e. specifically that the device is not $Q$-limited by geometric losses), mass-loaded structures with quality factors of at least $Q \approx 24\,000$ should be feasible.

## 9.4 Absorptive heating

The readout of the test mass motion will be achieved via optical interferometry as described in chapter 11. Even for the most advanced mirror-coatings, a fraction of the probing light will not be reflected or scattered and necessarily absorbed by the test-mass substrate. Significant heating of the test mass would not only shift the mechanical resonance, but may also raise the thermal noise and could potentially render the proposed experiment unfeasible. Therefore, we estimate the heating effect from absorbed light both with an analytic approximation as well as a finite element model.

### 9.4.1 Analytic estimation of heating

Assuming a fraction $\kappa$ of the probing light $P$ is absorbed by the test-mass mirror, we consider two major dissipation mechanisms for heat. First, dissipation through the cantilever arms or the membrane. Integrating Fourier's law[21] over the total cross section $A_{\text{cross}}$ of all cantilever arms yields

[21] Lienhard and Lienhard 2011

$$P_{\text{transfer}} = -k_{\text{heat}} A_{\text{cross}} \Delta\Theta / l \quad \text{with} \quad \Delta\Theta = \Theta - \Theta_0,$$

where $k_{\text{heat}}$ is the material's heat conductivity, $l$ is the length of the cantilever arms, $\Theta$ is the temperature of the test mass and $\Theta_0$ is the temperature of the environment. The expression will be slightly more complex for the case of a membrane, but conceptually indifferent. The second mechanism is black body radiation of the test-mass surface $A_{\text{surf}}$, where the dissipated power is given by the Stefan-Boltzmann law,

$$P_{\text{radiation}} = -A_{\text{surf}} \sigma \epsilon \left[ (\Theta_0 + \Delta\Theta)^4 - \Theta_0^4 \right],$$

with the material- and wavelength dependent emissivity $\epsilon \leq 1$ and the Stefan-Boltzmann constant $\sigma = \pi^2 k_B^4 (60 \hbar^3 c^2)^{-1} \approx 5.67 \cdot 10^{-8}\,\text{W}\,\text{m}^{-2}\,\text{K}^{-4}$. Both functions are shown in fig. 9.6(b) for the specific case of a 4-arm AlGaAs cantilever

test mass (fig. 9.6(a)). In a thermal steady state, the sum of both dissipation terms has to be equal to the absorbed power $\kappa P_{\text{light}}$, where $\kappa$ is the absorption coefficient. Selecting the physical (i.e. real and positive) solution for $\Delta\Theta(\kappa)$ from all solutions of

$$\kappa P_{\text{light}} = P_{\text{transfer}} + P_{\text{radiation}}$$

yields the curve shown in fig. 9.6(c).

### 9.4.2 Finite element modeling of heating

Using the **`Heat Transfer in Solid`** module of `COMSOL`, we can perform a similar estimation numerically with finite elements. The absorbed laser power can be implemented with a **`Heat Source`** domain; while a **`diffuse surface`** boundary node marks the parts of the system that emit black body radiation. The results of an exemplary study are shown in fig. 9.6(c). From the results it is safe to say that for AlGaAs structures test-mass heating through light absorption will likely not pose an issue for thermal noise, as the increase in temperature is at most 1 K even for an absorption coefficient as high as $\kappa \approx 10\,\%$.[f] Obviously, once the designs for SiN (section 9.8.2) are finalized, this study has to be repeated with the new geometry and material properties.

### 9.4.3 Temperature-induced frequency shift

We suspect that a heating-induced eigenfrequency shift of the desired COM mode could bring it out of the resonant driving range (for a delta-like driving peak). Therefore, we process the last result further by analyzing the frequency dependence of the out-of-plane COM mode on temperature. In `COMSOL`, this can be done with a **`Prestressed Analysis`**, where the resulting stress from the thermal study above is used as the linearization point for an **`Eigenfrequency`** study. Figure 9.6(d) shows the frequency shift as a function of the heating-induced shift of the average test-mass temperature $\Theta$. Also shown is the mechanical width $\gamma = \omega_0/Q$ for the given set of parameters. We see that already a minor increase of $\Delta\Theta \approx 10^{-2}\,\text{K}$ is enough to shift the resonant peak by more than one mechanical bandwidth. Therefore, in a resonant detection scheme it will likely be necessary to drive the test mass with a drive width broader than $\gamma$.[g] Alternatively, the problem of consistently driving the test

[f] Typical absorption coefficients are much lower. For example, $\kappa < 10^{-6}$ has recently been demonstrated for GaAs/AlGaAs multilayer mirrors (Cole, Zhang, et al. 2016).

[g] In the signal derivation starting from section 5.2 on p. 33 we assumed a delta-like source drive. In order to derive the correct signal contributions for a broadened drive, this treatment will have to be expanded to a more general case incorporating finite-width drive modulations. Note that due to the small bandwidth of the test mass, the amount of power that effectively drives the test mass will not drastically change with a broader drive, and hence we do not expect significant changes in signal contributions.

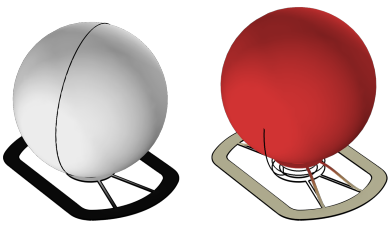

(a) 4-arm AlGaAs cantilever design with a heat source at the bottom circular mirror pad, qualitative temperature distribution when the outer edge of the chip is defined as a heat bath (left). Shape of the relevant COM displacement mode with $\omega/(2\pi) \approx 60\,\mathrm{Hz}$ (right).

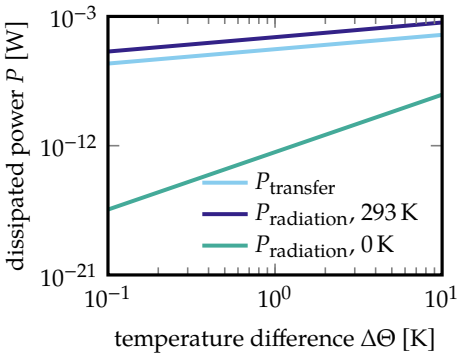


(b) Power dissipated through the cantilever arms and black body radiation as a function of temperature difference. As $P_{\mathrm{transfer}}$ depends directly on $\Delta\theta$, it is independent of $\Theta_0$. However, $P_{\mathrm{radiation}}$ is negligible at $\Theta_0 \to 0\,\mathrm{K}$ while it dominates at room temperature.

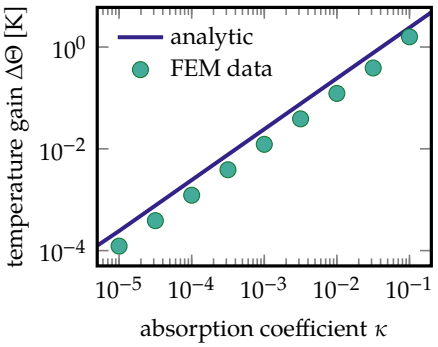


(c) Relative increase in temperature depending on absorption coefficient $\kappa$ for 1 mW of reflected power. The FEM estimation is slightly lower, likely because it includes thermal radiation off the chip surface in addition to the test-mass surface.

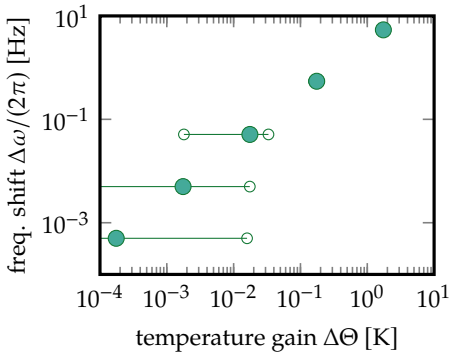


(d) Relative frequency shift of the COM mode depending on test-mass temperature. Horizontal bars indicate the mechanical bandwidth of the test mass, which for the rightmost two points are too narrow to be visible given the logarithmic scaling.

**Figure 9.6:** Relevant plots for the dissipation of heat in a 4-arm AlGaAs cantilever design (see also fig. 9.2). The parameters are $P_{\mathrm{light}} = 1\,\mathrm{mW}$, $k_{\mathrm{heat}} = 14\,\mathrm{Wm^{-1}K^{-1}}$ ($Al_{0.92}Ga_{0.08}As$), $A_{\mathrm{cross}} = 4 \cdot 20\,\mu\mathrm{m} \cdot 7\,\mu\mathrm{m}$, $l = 1.5\,\mathrm{mm}$, $\Theta_0 = 293.15\,\mathrm{K}$, $A_{\mathrm{surf}} = 4\pi(1\,\mathrm{mm})^2$, $\epsilon = 0.5$.

mass on resonance could be completely avoided by transitioning to an off-resonant driving scheme. We investigate this in section 9.6.

As a side remark, we note that with this specific cantilever geometry, for temperature changes higher than a few Kelvin the COM mode disappears, likely due to the additional internal stress. This emphasizes again that temperature

stability plays a crucial role in the proposed experiment, and heating/cooling effects need to properly be accounted for.

## 9.5 Accumulation of charges

Charge accumulation on suspended test masses has been studied extensively in the context of gravitational wave detectors. For the case of large (cm-scale) fused-silica mirrors, surface charge densities up to $10^6\,\mathrm{C\,cm^{-2}}$ have been observed directly after evacuation, probably due to friction-related effects during the pumping process.[22] For our geometry (spherical masses of 2 mm diameter) this would result in approx. 30 000 charges per mass. However, static charging of this type can be removed through various ways, either by discharging through electrical contact or by UV light illumination[23].

[22] Hewitson et al. 2007; Mitrofanov, Prokhorov, and Tokmakov 2002

[23] Hewitson et al. 2007; Shaul et al. 2008

Further potential charging-mechanisms arise from cosmic radiation.[24] Following Buchman et al. (1995) we can use the Bethe-Bloch formula to calculate the energy range of protons and electrons that would, after penetrating the laboratory walls and the vacuum tank, come to stop in the test mass and potentially charge it. We start by writing down the penetration depth $\Delta x$ of a particle by

[24] Braginsky, Ryazhskaya, and Vyatchanin 2006

$$\Delta x = \int_{T_\mathrm{in}}^{T_\mathrm{out}} \frac{\mathrm{d}x}{\mathrm{d}T}\mathrm{d}E,$$

where $T_\mathrm{in}$ and $T_\mathrm{out}$ denote the kinetic energy of the proton entering and exiting the absorber. Through substitution we may rewrite this in terms of velocity as

$$\ldots = \int_{v_\mathrm{in}}^{v_\mathrm{out}} \left(\frac{\mathrm{d}T}{\mathrm{d}x}\right)^{-1} \frac{\mathrm{d}T}{\mathrm{d}v}\mathrm{d}v. \tag{9.6}$$

As the kinetic energy of a particle of mass $m_\mathrm{p}$ is given by $T = m_\mathrm{p}c^2(\gamma - 1)$, where $\gamma = (1-\beta^2)^{1/2}$ with $\beta = v/c$ is the relativistic factor, we see that

$$\frac{\mathrm{d}T}{\mathrm{d}v} = m_\mathrm{p} v \gamma^3.$$

Now, for $\mathrm{d}x/\mathrm{d}T$, we use the Bethe-Bloch formula in SI units,

$$-\frac{\mathrm{d}T}{\mathrm{d}x} = \frac{K}{A}\rho z^2 Z \frac{1}{\beta^2}\left[\frac{1}{2}\ln\left(\frac{2m_e e^2\beta^2\gamma^2 T_\mathrm{max}}{I^2} - \beta^2\right)\right] \quad \text{with} \quad K = 4\pi r_e^2 m_e c^2,$$

and the maximal transferable energy for a single collision,

$$T_\mathrm{max} = \frac{2m_e c^2\beta^2\gamma^2}{1 + 2\gamma m_e/m_\mathrm{p} + (m_e/m_\mathrm{p})^2}.$$

This gives us the mean rate of energy loss, or stopping power, of a particle with charge factor $z$ in an absorber with atomic mass $A$, density $\rho$, atomic number $Z$ and mean ionization potential $I \approx 10\,\mathrm{eV} \cdot Z$. We may now use eq. (9.6) to estimate a penetration depth depending on the in- and outgoing velocities of the particle.

To arrive at an energy range that we can compare to that of incoming cosmic protons, we start "from the end", i.e. from the last absorber, which is the gold mass of depth 2 mm. Then, we work backwards to the chamber and a concrete wall. For gold we have $Z = 79$, $A = 197\,\mathrm{amu}$ and $\rho = 19\,300\,\mathrm{kg\,m^{-3}}$. Obviously every incoming proton with velocity $v_{\mathrm{gold,lo}} > 0$ will penetrate the particle, but we also need to know the highest velocity of a particle that will still come to rest within the gold mass. We can not solve eq. (9.6) analytically, but numerically we find that for $\Delta x = 2\,\mathrm{mm}$ all particles up to a velocity $v_{\mathrm{gold,hi}} \approx 1.11 \cdot 10^8\,\mathrm{m\,s^{-1}}$ will stop within that range (see fig. 9.7(a)). For the next layer, a 3 mm thick steel vacuum tank, the highest relevant incoming velocity $v_{\mathrm{steel,hi}}$ will be one that results in outgoing velocity $v_{\mathrm{gold,hi}}$ after penetrating the steel, as higher velocities will not come to rest within the gold mass.[h] Correspondingly, the lowest relevant incoming velocity $v_{\mathrm{steel,low}}$ will be the one that results in a velocity of $0 = v_{\mathrm{gold,low}}$ after penetrating the steel, as those particles with lower velocity will not be able to penetrate the gold mass. Approximating steel with iron, we have $Z \approx 26$, $A \approx 56\,\mathrm{amu}$ and $\rho \approx 7874\,\mathrm{kg\,m^{-3}}$ and with the same numeric method used before, we find that that for $\Delta x = 3\,\mathrm{mm}$ we have $v_{\mathrm{steel,low}} \approx 1.02 \cdot 10^8\,\mathrm{m\,s^{-1}}$, $v_{\mathrm{steel,hi}} \approx 1.23 \cdot 10^8\,\mathrm{m\,s^{-1}}$. Finally, we repeat the same step for a concrete wall with $Z \approx 13$, $A = 27\,\mathrm{amu}$, $\rho \approx 1500\,\mathrm{kg\,m^{-3}}$ and $\Delta x = 0.3\,\mathrm{m}$ and find that the relevant velocity band for incoming protons is $v_{\mathrm{concrete,lo}} < v < v_{\mathrm{concrete,hi}}$ with

$$\begin{aligned} v_{\mathrm{concrete,lo}} &\approx 1.858 \cdot 10^8\,\mathrm{m\,s^{-1}} \quad \text{or} \quad T_{\mathrm{concrete,lo}} \approx 268\,\mathrm{MeV}, \\ v_{\mathrm{concrete,hi}} &\approx 1.884 \cdot 10^8\,\mathrm{m\,s^{-1}} \quad \text{or} \quad T_{\mathrm{concrete,hi}} \approx 257\,\mathrm{MeV}. \end{aligned}$$

Now, we may simply take some proton-flux data at sea level, e.g. by Diggory et al. (1974) or Grieder (2001, ch. 3), and integrate the flux over this energy band at the relevant energies well below 1 GeV (i.e. close to the material critical energy). The data is shown in fig. 9.7(b). The integration yields a proton absorption rate of roughly $0.1\,\mathrm{m^{-2}\,s^{-1}\,sr^{-1}}$. For a sphere with 2 mm diameter and a half sphere of incoming particles with $2\pi$ sr, this sums up to about $10^{-5}$ scattering events per second, or on the order of one ionizing scattering event per five to fifty hours. This estimate is consistent with long-term measurements on silica test masses in high vacuum, which report a monotonic charging rate of up to $10^5$ charges per $\mathrm{cm^2}$ per month.[25]

[25] Mitrofanov, Prokhorov, and Tokmakov 2002

[h] Obviously, the above procedure would not work if the solution to the Bethe formula was not strongly monotonic.

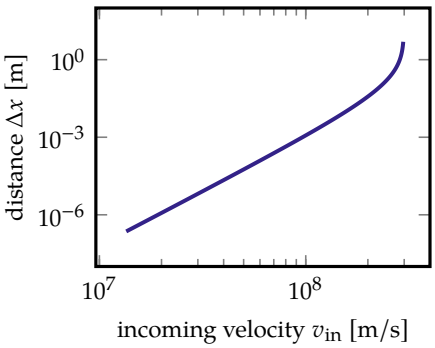


(a) Typical penetration depth (terminal velocity zero) as a function of incoming proton velocity from eq. (9.6). The curve is shown for gold but looks similar for most materials.

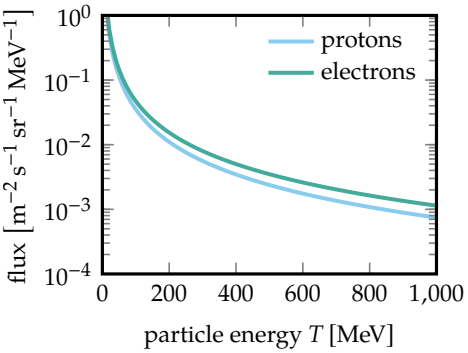


(b) Proton (directly taken from Diggory et al. (1974)) and electron (through derivation of integrated flux from Olive (2014)) flux densities.

**Figure 9.7:** Relevant plots for the accumulation of charges through absorption of cosmic radiation.

For the flux of electrons, values for integrated spectra are given by Olive (2014, ch. 28), which we need to numerically derive in order to find the flux densities which are plotted in fig. 9.7(b). When we repeat the process from above for electrons, we find that within standard machine precision, there are no scattering events from electrons at all. In addition, we know that for electrons *Bremsstrahlung*[26] provides a loss mechanism even stronger than collisional losses, implying that we can safely assume that the charging rate by electrons is negligible. The relevant charging mechanism is therefore dominated by protons.

[26] Jackson 1998

Lastly we note that even though in our estimation of signal contributions (fig. 8.2 on p. 89) we assumed 200 charges per mass, up to 5000 opposing charges could be tolerated without increasing the Coulomb force above the thermal contribution.

## 9.6 Ring-down and ring-in

As seen from eq. (5.6) on p. 31, the homogeneous solution of the harmonic oscillator decays on a time scale of $\tau = 2/\gamma$, which for the given parameters is on the order of a few minutes. As this time is proportional to the mechanical quality, it will easily increase to above one hour for higher values of $Q$. This leads to two closely related potential problems: Ring-down and ring-in times. The steady-state of a driven harmonic oscillation will be reached when the non-driven component of the motion, or in mathematical terms the homogeneous

solution, has decayed. Therefore, the waiting times before time traces of the driven test mass or the dark noise of the non-driven test mass can be taken will potentially be intolerable.

The requirement for a decrease of ring-in times is similar to those found in the AFM community, where it is necessary to collect data of many points in short concussion. In the *slope detection* method, the AFM cantilever is driven slightly off-resonant and gets pulled onto resonance by a force gradient $\mathrm{d}F/\mathrm{d}z$ (cf. eq. (5.5) on p. 30), where its amplitude is amplified. The clear downside of this method, apart from the small bandwidth, is the requirement for a ring-in at every point of measurement. And while large mechanical qualities $Q$ of the cantilever increase the sensitivity per point, they also increase the ring-in times. Here, the solution comes in form of the *FM method*, where the cantilever is always driven on resonance, with a carefully deployed feedback circuit (accounting for the correct phase) that corrects for force gradient induced frequency shifts.[27] Unfortunately, the expected frequency shifts in the proposed experiment are much smaller than those in typical AFM systems, and therefore cannot be resolved in reasonable time, independent of the detection scheme. However, it would still be feasible to modulate the test-mass oscillator such that its amplitude corresponds to the *expected* signal. This requires a feed back/feed forward scheme that takes into account both the current motion of the device as well as the motion of the gravitational source mass.[i]

[27] Albrecht et al. 1991; Giessibl 2003; Poggio and Degen 2010

An alternative to such a scheme would be to artificially dampen the test-mass oscillator during the ring-ins, effectively lowering the mechanical $Q$ and thereby making the amplitude changes happen on a much shorter time scale.[28] The technical implementation of this would be not trivial in the proposed experiment. Because of the relatively large test mass, optical feedback would require around 100 W of optical circulating power (cf. eq. (11.2) on p. 140), which is simply unfeasible due to the lack of appropriate laser source and the absurd heating rates imposed on the test mass. Instead, one might think of modulating the base of the test mass using a mechanical actuator. The potential issue with this approach is that such an actuator, i.e. most likely a piezoactuator, would require electrical power, which puts an actuating broad-band antenna directly at the base of the test mass – where it is most critical when it comes to unwanted excitations. In addition, the backaction of an actuator would act on the center of mass of the test-mass stage, thereby moving it and potentially exciting modes of the vibration isolation, which would then have to be actively damped as well.

[28] Arcizet et al. 2006; Giessibl 2003

In summary, if the test-mass quality factors approach a regime where ring-in times become excessive, dampening techniques will be required. However,

[i] Similar techniques have been used to suppress residual motion to a fraction of the standard quantum limit in ion trap experiments (Bushev et al. 2013).

one must expect to spend considerable engineering effort into not introducing additional low frequency noise when using them.

One approach to completely circumvent this problem could be to transition from a resonant detection-scheme to an off-resonant scheme, where the system is driven close to, but not directly on resonance. As all forces acting on the test-mass scale with the susceptibility $\chi(\omega)$ (see eqs. (5.15a) to (5.15h) on pages 36–37), this would not change the fundamental signal to noise limits and not only annihilate the problem of resonant ring-in, but also of thermal frequency drifts analyzed in section 9.4.3 on p. 107. However, an off-resonant detection scheme necessarily requires thermal-noise limited optical readout off the resonance without a cavity, which, as we describe in section 11.4 on p. 143, is at the edge of current technology.

## 9.7 Shape optimization

In section 5.11 on p. 51 we derived a general expression for the gravitational potential between two rigid bodies (eq. (5.42)). We now perform a rough numeric estimation on the potential improvement in force gradient $\iota$ through mass shape optimization. For the case of two cylinders, the integration boundaries become

$$\begin{aligned} z_{m1} &= -h_{\mathrm{cyl}}, & z_{m2} &= 0, & r(z_m) &= m^{1/2}(\pi\rho_m h_{\mathrm{cyl}})^{-1/2}, \\ z_{M1} &= 0, & z_{M2} &= h_{\mathrm{cyl}}, & r_{\mathrm{S}}(z_M) &= M^{1/2}(\pi\rho_M h_{\mathrm{cyl}})^{-1/2}, \end{aligned}$$

and for the case of two cones we have

$$\begin{aligned} z_{m1} &= -h_{\mathrm{con}}, & z_{m2} &= 0, & r(z_m) &= (3m)^{1/2}(\pi\rho_m h_{\mathrm{con}}^3)^{-1/2}(z_m + h_{\mathrm{con}}), \\ z_{M1} &= 0, & z_{M2} &= h_{\mathrm{con}}, & r_{\mathrm{S}}(z_M) &= -(3M)^{1/2}(\pi\rho_M h_{\mathrm{con}}^3)^{-1/2}(z_M - h_{\mathrm{con}}). \end{aligned}$$

We may normalize $\iota$ to units of $G\rho_m\rho_M$, which will then only depend on geometry (without densities), and compare it to the case of two spheres, eq. (5.43) on p. 53, for the given set of parameters. The results of the numeric integrations are presented in fig. 9.8 for different values of surface separation $d_0$. It becomes clear that for an optimal choice of cylinder dimensions, using cylindric masses over spheres can roughly double the force gradient $\iota$.[j]

It is safe to assume that a more thorough numerical estimation based on the formalism presented in section 5.11 will allow to find optimal mass shapes that potentially increase the gravitational effect in the driven test-mass scenario, possibly up to an order of magnitude. However, it is also important to mention

[j] Interestingly, this is significantly more than the 3 % increase that is to be expected in the scenario where the gravitational *force*, and not the *force gradient*, is optimized by variation of the source-mass shape (Alemi 2009; McDonald 2003).

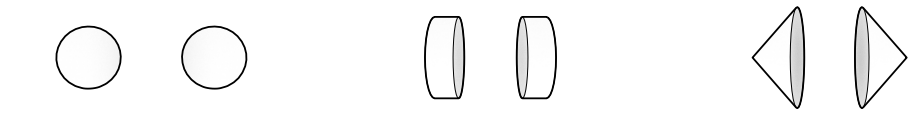

(a) Sphere-sphere geometry

(b) Cylinder-cylinder geometry with optimal radius.

(c) Cone-cone geometry with optimal inclination.

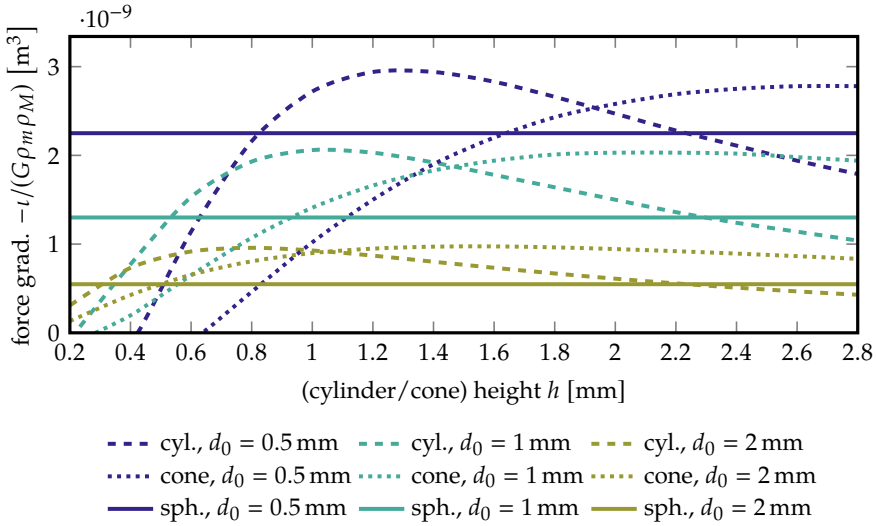


(d) Normalized force gradient as a function of mass height, where the volume is kept fixed. Continuous lines represent the scenario with spherical masses of the same volume.

**Figure 9.8:** Results of numerical force gradient estimation for three different shapes. The top-row figures are to-scale (i.e. have identical volumes in this representation) and have the optimal geometry as determined by the bottom figure.

that for optimized gravitational mass shapes, other forces, especially those with shorter interaction ranges, will potentially scale even more beneficial with the modified geometries and therefore all forces considered so far will likely have to be reevaluated.

## 9.8 Current device approaches

The goal is to establish mass-loaded micromechanical systems as possible test-mass oscillators. In this section we list a few materials that have been subject of discussion in the context of realizing a high-$Q$ 50 Hz mechanical system with a 80 mg mass load. This represents the current state of development at the time of writing this thesis.[k]

[k] The work listed in sections 9.8.2 to 9.8.4 has been carried out Richard Norte, Simon Gröblacher (Delft University of Technology) and Claus Gärtner (University of Vienna) from the

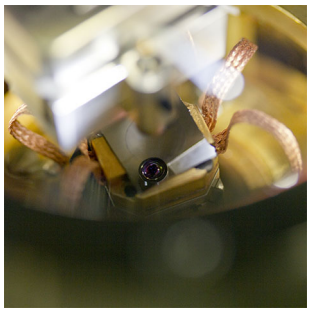

(a) InGaP membrane in a helium cryostat (Cole, Yu, et al. 2014). A reflection of the focused fiber coupler used for position readout is visible on the mirroring membrane chip (approx. 10 by 10 $mm^2$).

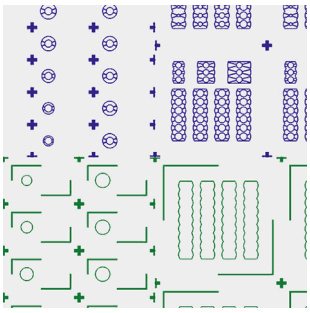

(b) Fabrication drawing (crop) for mask production of AlGaAs cantilevers. Blue parts indicate actual device structures; green parts are used for etching of the underlying support structure.

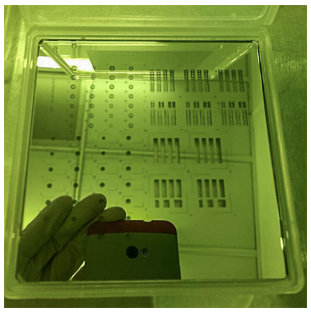

(c) Chrome mask for etching based on the fabrication drawing in (b). For the presented work, this marks the latest point in AlGaAs-based device fabrication.

**Figure 9.9:** Pictures showing current progress in the manufacturing of devices based on InGaP and AlGaAs.

### 9.8.1 Aluminium gallium arsenide and indium gallium phosphide

Aluminium gallium arsenide (AlGaAs) based Bragg mirror cantilevers have been used in multiple optomechanical applications[29] and offer reasonable quality factors of up to $5 \cdot 10^4$ at room temperature. Membranes based on gallium arsenide[30] (GaAs) and indium gallium phosphide[31] (InGaP, fig. 9.9(a)) have been reported to reach $Q$s of over $10^6$ at room temperature. All three material systems demonstrate order-of-magnitude improvements of $Q$ at cryogenic temperatures. In the ideal case, the loading the test mass will raise the effective mass of the fundamental COM oscillator mode, thereby lowering the resonance frequency while maintaining the mechanical quality. In the case of AlGaAs cantilevers, if the cantilever arms are sufficiently long and thin, geometrical losses will be completely overshadowed by internal material losses.[1] In contrast, in the case of membranes the clamping of the chip can have negative impact on the (albeit much higher) quality factors. The clear advantage of AlGaAs is that the relatively low stress (compared to e.g. typical SiN membranes) allows to reach the desired low frequencies with structures of smaller spatial dimensions. Figure 9.9 shows some pictures of current developments.

[29] Cole, Gröblacher, et al. 2008; Cole, Wilson-Rae, et al. 2011; Vanner et al. 2013

[30] Liu, Usami, et al. 2011

[31] Cole, Yu, et al. 2014

fabrication side as well as Ralf Riedinger and Hans Hepach (University of Vienna) from the testing side.

[1] For the FEM treatment of situations where this is not the case, see e.g. Cole, Wilson-Rae, et al. (2011).

(a) Welding a lead sphere onto a SiN membrane with a blowtorch. Photo by Richard Norte.

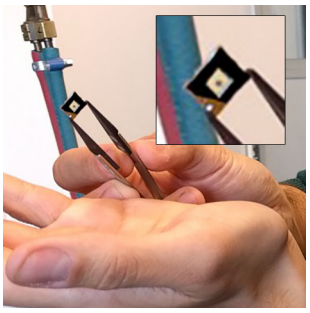

(b) Resulting mass-loaded device with a slightly off-centered mass. Photo by Claus Gärtner.

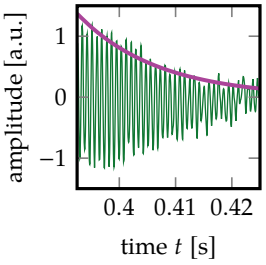


(c) Ringdown with data (green) and fitted decay envelope (purple) yielding $Q \approx 50$.

**Figure 9.10:** Pictures of the first brute-force mass-loaded SiN device and performance plot.

### 9.8.2 Silicon nitride

Silicon nitride (SiN) membranes have been successfully used in a number of optomechanical applications, being known for their high stress and quality factors exceeding $10^6$ already at room temperature.[32] A first attempt of fabricating a mass loaded SiN membrane was made using a 1 mm diameter lead ball that was welded onto the membrane using a blowtorch (figs. 9.10(a) and 9.10(b)). In addition to the contamination of the blowtorch, the chip was dropped on the floor twice and showed some wrinkling around the region where the ball was attached. Not surprisingly, a ringdown measurement confirmed a low quality factor $Q \approx 50$ for the fundamental mode at 1114 Hz (fig. 9.10(c)).

[32] Chakram et al. 2014; Purdy, Peterson, Yu, et al. 2012; Thompson et al. 2008; Wilson, Regal, et al. 2009; Zwickl et al. 2008

However, even if there are cleaner ways of attaching a gold ball to a SiN membrane without contaminating it, the tension of such a membrane is effectively too high to reach the desired frequency of around 50 Hz. This can be seen by performing a quick estimation using an expression for a circular membrane by Fletcher (1992, sec. 5.7), where the fundamental mode frequency of a circular mass-loaded membrane with radius $a$ and attachment radius $b$ is given by

$$\omega/(2\pi) = \left(\frac{T}{2\pi m \ln(a/b)}\right)^{1/2} \quad \Rightarrow \quad a = b \exp\left(\frac{2\pi T}{\omega^2 m}\right),$$

whith the surface tension $T$. For the existing system with $a \approx 4\,\mathrm{mm}$, $b \approx 100\,\mu\mathrm{m}$, a lead mass with a diameter of 500 $\mu$m and a typical SiN tension of $T \approx 400\,\mathrm{N\,m^{-1}}$, this formula yields a frequency of 1700 Hz, which reasonably agrees with the measured frequency of 1114 Hz for the fundamental mode. Since the minimum radius scales exponentially with inverse frequency, a

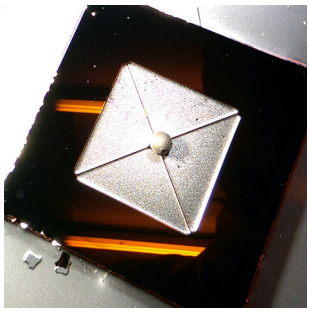

(a) SiC device, $(5\,\mathrm{mm})^2$ window with 50 $\mu$m wide tethers holding a 100 nm thick trampoline, mounting and supporting a Pb ball with 800 $\mu$m diameter.

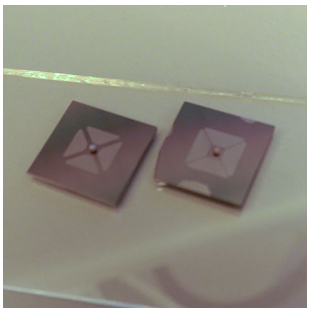

(b) $SiO_2$ devices (before etching the support layer), 5.3 $\mu$m thickness with 500 $\mu$m respective 100 $\mu$m wide tethers.

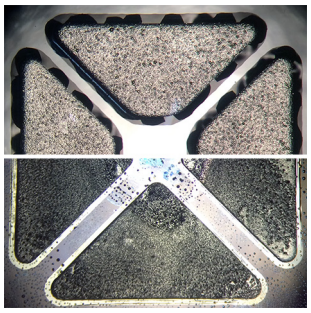

(c) Partly released SiC (top) and $SiO_2$ (bottom) trampolines after partial $XeF_2$ etching.

**Figure 9.11:** Pictures showing the current progress in the manufacturing of devices based SiC and $SiO_2$. Photos by Richard Norte and Hans Hepach.

frequency $\omega/(2\pi) \approx 50\,\mathrm{Hz}$ with a 2 mm gold ball would push the diameter of the required membrane to roughly 80 orders of magnitude above the visible universe. This suggests that the tensile strength of SiN is simply far too high for our low frequency requirement.

In order to weaken the tension of the membranes, one might think of using lower stress films – however, this will likely lower the achievable $Q$ as the high mechanical quality of SiN is mainly a product of high stress films.[33] A second approach would be to plasma etch the membrane after the mass has been attached to it and thereby make it thinner.[34] This reduces the effective spring constant while raising the mechanical quality. As a third approach one could think of tethered SiN structures, similar to the devices discussed below.

[33] Norte 2015; Schmid et al. 2011; Verbridge et al. 2006

[34] Manos and Flamm 1989

### 9.8.3 Silicon carbide

An alternative to SiN comes in the form of tethered silicon carbide[35] (SiC) trampolines. SiC has a higher hardness and ultimate yield strength than SiN[36] and is chemically inert to a significant degree. To the author's knowledge, there have been few attempts at making devices from high-stress SiC. The downside of SiC is its high optical absorption, which could be fixed by adding an additional mirror surface.

[35] Liu, Tang, et al. 2011

[36] Zerr et al. 2004

In a first attempt 100 nm of high stress SiC were deposited on a 500 $\mu$m silicon wafer (fig. 9.11(a)). Since SiC films are chemically inert, a simple hotplate can be used to cleanly melt a ball onto an unreleased trampoline. Finally, the structure can be released with a fluorinated gas, e.g. via $SF_6$ plasma release or

$XeF_2$ etch.[37]

[37] Knizikevičius and Kopustinskas 2004; SPTS Technologies 2014

Several technical hurdles still need to be overcome. It is not entirely clear if it is possible to achieve the 400 nm of thickness in SiC on Si, which are likely required to hold the test masses. The slow etch process for such thick layers poses an additional challenge. In addition, we could already observe plastic deformation through the tensile stress from an 800 $\mu$m lead sphere, painting a rather dim future for mounting 2 mm gold spheres. Alternatively to SiC, trampolines from other materials with high $XeF_2$ selectivity on silicon, such as aluminum, could be tested, but would likely have worse mechanical quality than SiC.

### 9.8.4 Silicon dioxide

Another current approach is making trampolines from thick (about 5 $\mu$m) Silicon dioxide ($SiO_2$), which again has almost infinite etch selectivity to $XeF_2$. $SiO_2$ is thermally grown[38] at 1100 °C, resulting in high mechanical quality through high density and little impurities. These properties make them useful even for mirror suspensions in gravitational wave observatories.[39] As opposed to SiN and SiC, the stress in $SiO_2$ is compressive and not tensile[40], leading to potentially much lower frequencies. First devices are currently being fabricated (see fig. 9.11(b)).

[38] Hori 1997

[39] Cumming et al. 2014

[40] Alexandrova, Szekeres, and Christova 1988

Chapter 10

# Source mass

In this chapter we cover the driving mechanism of the source mass. The challenge in actuating a millimeter-sized object in the proposed scheme arises from the fact that the combination of frequency, amplitude and effective mass lies within a parameter regime that is mostly unexplored in mechanical engineering.

This chapter is composed of a list of the various constraints for the drive engine (section 10.1), some comments on potential solutions for positioning and amplitude/phase readout (section 10.2) and some brief notes on actual technical implementations that are currently investigated (section 10.3).

## Chapter contents



## 10.1 Source-mass constraints

In this section we investigate the constraints on the source-mass driving engine. We split the discussion into amplitude- and frequency-domain constraints, residual vibrations and stray fields, and constraints for the effective moving mass as well as the minimal lifetime.

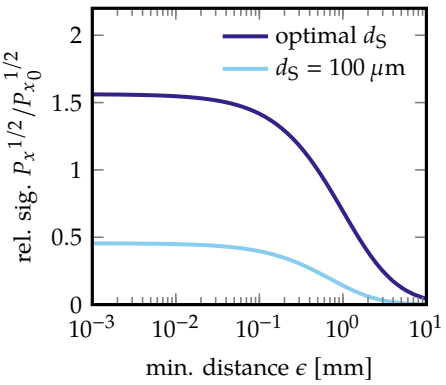


(a) Relative signal strength as a function of minimal surface distance for an optimal and a pessimistic drive amplitude.

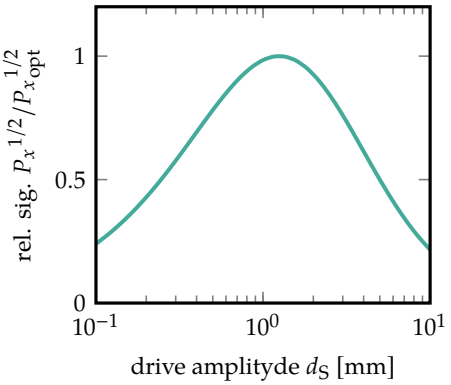


(b) Relative signal strength as a function of source-mass drive amplitude.

**Figure 10.1:** Change of the gravitationally driven signal amplitude with varied minimal surface distance and drive amplitude.

### 10.1.1 Drive amplitude and minimal distance

In section 5.9 on p. 49, eq. (5.37) we derived the optimal amplitude $d_{S_{opt}}$ of the driving motion in order to maximize the effect of the gravitational drive;

$$P_{x_G}^{1/2} \propto d_S(d_S + r_T + r_S + \epsilon)^{-3} \quad \Rightarrow \quad d_{S_{opt}} = (r_T + r_S + \epsilon)/2, \tag{10.1}$$

For the parameters discussed in chapter 8 (table 8.1 on p. 88, $\epsilon = 0.5\,\text{mm}$, $r_T = r_S = 1\,\text{mm}$) this yields optimal values of

$$\begin{aligned} d_{0_{opt}} &= 3.75\,\text{mm} \quad \text{for the COM distance} \\ \text{and} \quad d_{S_{opt}} &= 1.25\,\text{mm} \quad \text{for the actuation amplitude.} \end{aligned} \tag{10.2}$$

We can quickly check if a decrease of the minimal surface-to-surface distance $\epsilon$ yields a significant gain in the signal. Figure 10.1(a) shows the relative signal as a function of $\epsilon$, where the reference signal strength is given for our choice of $\epsilon = 0.5\,\text{mm}$, for both the case of keeping the driving amplitude optimal and a pessimistic fixed driving amplitude of $d_S = 100\,\mu\text{m}$. The gain from a decrease of the minimal surface distance is minor, topping out at around 50 %. This is also clear from the mathematical form of optimal drive amplitude, eq. (10.1), which for small values of $\epsilon$ is mainly dictated by the size of both spheres. However, we can qualitatively expect this to be different for forces with a higher-order scaling in distance. It is therefore advisable to keep the surface separation around the (rather safe) proposed value of 0.5 mm.

In a similar fashion to the above, we can analyze the decrease in relative signal strength for non-optimal drive amplitudes $d_S$, as shown in fig. 10.1(b).

While slight deviations from the optimal value of 1.25 mm yield negligible change, going significantly smaller (e.g. into the range of typical commercial Piezo stacks at $d_S \approx 100\ \mu$m) will reduce the signal to around 25 % of its optimal value. With the current parameter settings, an overall signal-to-noise ratio of 1 can be achieved with a drive amplitude of around 70 $\mu$m.

### 10.1.2 Drive bandwidth and frequency stability

With the resonance frequency of the test mass in the double-digit Hertz range, $\omega_0/(2\pi) = 50\,\text{Hz}$, and a mechanical quality of $2 \cdot 10^4$, the spectral width of the mechanical resonance lies in the range of $\gamma/(2\pi) = \omega_0/(2\pi Q) \approx 2.5\,\text{mHz}$ or even smaller for higher values of $Q$. In order to continuously drive the test mass on resonance, one therefore has to require that the spectral width $\gamma_{D,w}/(2\pi)$ of the drive should not exceed said value. However, an even stricter requirement arises from the long integration times and, in consequence, small integration bandwidth $\Gamma$ of the proposed experiment. As we ideally require that the entire driven signal contribution falls into the same integration band, we have to impose that

$$\gamma_{D,w}/(2\pi) < \Gamma/(2\pi) \approx 0.3\,\text{mHz}$$

for both the resonant and off-resonant detection cases. This should, in principle, not pose a problem as frequency references with smaller width are commonly available (e.g., Tektronix, Inc. (2017) states relative frequency drifts of less than $10^{-6}$ per year). We also note that drifts of the drive center-frequency $\omega_D$ on the scale of days or longer are currently no concern, as we expect that – at least in the case of a resonant detection scheme – it will be necessary to readjust $\omega_D$ on the scale of hours in order to account for thermally induced drifts of the test-mass frequency $\omega_0$.

### 10.1.3 Residual vibrations

As we see from the PSD of the driven harmonic oscillator (eqs. (5.15a), (5.15b) and (5.15f) on p. 36 and on p. 37), the source-mass displacement will not only act on the test mass via force gradients, but also via direct displacement of the test-mass support (*parasitic drive*). Both effects scale with the same mechanical susceptibility $\chi(\omega)$ of the test-mass device and are therefore amplified by the mechanical quality $Q$. We attenuate the drive displacement in two ways, yielding a combined transfer function $T_S$: First, the engine itself can be constructed such that the displacement of an effective combined mass is much smaller than the motion of the test mass (see below). Second, a sophisticated vibration isolation system, as we describe in chapter 12, can be deployed to reduce the force acting on the test mass that is caused by the motion of the drive engine by several orders of magnitude.

The requirement of a sinusoidal modulation of the source mass, $x_S(t) = d_S \cos(\omega_S t)$ (eq. (5.9) on p. 33), results in a sinusoidal momentum $p_S(t) = -M d_S \omega_S \sin(\omega_S t)$. In this simplified, one-dimensional model, the total momentum can be canceled by adding a displacement-modulated mass $M_{comp}$ with amplitude $d_{comp}$ and requiring that $M_{comp} d_{comp} = -M d_S$. In any practical scenario, however, this system will naturally bulge and therefore translate the initial one-dimensional problem into a multi-dimensional vibration issue. Furthermore, assuming that the drive engine is mounted on some hanging isolation platform (as described in section 12.3.4 on p. 164), non-ideal alignment could cause more complex rotation-motions of the mounting stage. The issues arise in a completely symmetric system with two identical drive engines acting in opposite directions. Ultimately, it is safe to assume that proper engineering of the drive engine can decrease the effective mass-amplitude-product and thereby the effective amplitude of the driving system, but it would be unwise to completely rely on this mechanism to cancel the parasitic drive effect. An analysis of the total performance of both source mass and isolation system should be seen as a combined engineering goal and is further investigated in section 12.3 on p. 157.

### 10.1.4 Stray field leakage

There are few methods of achieving millimeter-scale actuation or rotation without electromagnetic components, and even fewer methods to achieve such motion at a certain frequency $\omega_S$ without generating electromagnetic stray fields modulated at $\omega_S$. For example, while low-frequency loud speakers can achieve displacements of 2 mm at a frequency $\omega_S/(2\pi) = 50$ Hz, the actuation necessarily goes hand-in-hand with a powerful magnetic coil and a significant electromagnetic dipole field. The same is true for almost every electromagnetic and piezoelectric motor. Since the stray fields act at the drive frequency, which is the frequency of interest if the detection of the test-mass displacement, they can in principle drive the test mass (e.g. via dipole effects) and overshadow the effect of the gravitational interaction.

[1] Sumner, Pendlebury, and Smith 1987

To a certain extent, high-permeability materials such as Mu-metal can be used to shield such low-frequency modulated electromagnetic fields and prevent them from acting on the test mass[1], though there will necessarily be restrictions to the tolerances (as moving parts of the drive engine require some clearance) and thickness of the shielding material. A proper investigation, e.g. using finite-element methods, can only be performed once a prototype design has been established, which was not the case during the writing of this thesis.

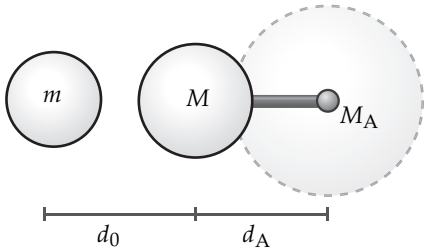


(a) Additional drive-engine mass $M_A$ that is co-moving with the source mass $M$ in some distance $d_A$ and reduced to a point-mass for convenience.

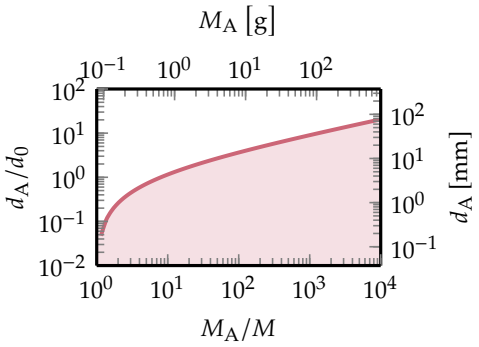


(b) Minimal additional distance $d_A$ required to suppress the effect of a co-moving motor mass $M_A$. Bottom/left scale: natural units; top/right scale: units for the given source mass $M = 80.9\,\text{mg}$ and the optimal drive $d_{0\text{opt}} = 3.75\,\text{mm}$.

**Figure 10.2:** Relevant figures for the gravitational drive effect of an additional point-like mass.

### 10.1.5 Additional moving mass

The engine driving the source mass will necessarily involve some support and motor parts that are rigidly connected to the source mass and therefore add to the effective gravitational drive. Our goal is to suppress the gravitational effect of the additional mass by bringing it sufficiently far away from the test mass.

From the processing the Newtonian signal, eq. (5.22b) on p. 41, we know that the gravitational contribution of the power signal is proportional to powers of the source mass $M$, the drive amplitude $d_S$ and the non-deflected distance $d_0$ as

$$P_{x\text{G}}(\omega_0) \propto M^2 d_S^2 d_0^{-6}.$$

We idealize the additional mass moving with the source mass as a mass point $M_A$ with a distance $d_A$ to the source mass (see fig. 10.2(a)). The requirement that the additional mass is not gravitationally driving the source mass can then be written as

$$P_{x\text{GS}}(\omega_0) \overset{!}{>} P_{x\text{GA}}(\omega_0),$$

where the indexes $T$ and $A$ denote the source mass and the additional mass contribution. This yields

$$\Leftrightarrow \quad M^2 d_S^2 d_0^{-6} > M_A^2 d_S^2 (d_0 + d_A)^{-6},$$

where the drive amplitude $d_S$ is of course identical for both masses, and therefore

$$\Leftrightarrow \qquad d_A/d_0 > (M_A/M)^{1/3} - 1.$$

This is plotted in fig. 10.2(b), both as a relation of unitless quantities $d_A/d_0$ and $M_A/M$ and for the concrete parameters (eq. (10.2) and table 8.1). For example, when modeling the bulk of the drive with a point mass $M_A \approx 50\,\mathrm{g}$, we need to require a distance of at least $d_A \gtrsim 30\,\mathrm{mm}$ between the source-mass origin and the point mass in order for the gravitational effect of the drive no to dominate the effect of the source mass.

### 10.1.6 Lifetime

We keep the previous assumption of a measurement time $\tau = 3600\,\mathrm{s}$ (table 8.1) for a single trace and, motivated by the PSD variance scaling we derive in appendix A.3.1 on p. 191, assume that up to some tens of traces will be required for a smooth spectrum. Given that some fraction of the measurements will likely by corrupted by environmental events, we believe that the collection of sufficient amounts of data will require at least a few days. For the testing phase of the system we should therefore account for around ten times the minimum requirement in lifetime, yielding around 750 h, or with $\omega_0/(2\pi) = 50\,\mathrm{Hz}$, a total of around $1.4 \cdot 10^8$ cycles.

## 10.2 Positioning and readout

In order to position the source mass, an optical scheme can be employed to read out the relative positioning of test mass and the source mass in all DOFs. This can be accomplished, for example, with quadrant diodes at the source-mass stage paired with (focused) light beams from the test-mass stage (fig. 10.3(a)). If higher precision is required, one might think of interferometric schemes (see e.g. Speake and Aston (2004)). As part of a high-precision measurement, the time-dependent displacement of the source mass could be read out in a similar fashion (fig. 10.3(b)). However, naturally the technical implementation of this will depend on the mechanism used for the source-mass drive.

In addition to the readout, a precise positioning of the source mass also requires actuation. This can be done with stable micro-positioning stages, which might have to switched off during measurement to avoid residual motion from electronic noise (e.g. by picking up stray fields through the wires and translating them into motion), as active stages could potentially cause additional vibration that interferes with the predicted signals. Suitable ultra-stable positioning systems can be found among standard components of, e.g. Smaract[2], PI[3] or attocube[4]. In addition to a precise positioning of the source

[2] SmarAct GmbH 2017
[3] Physik Instrumente (PI) GmbH & Co. KG 2017
[4] attocube systems AG 2016

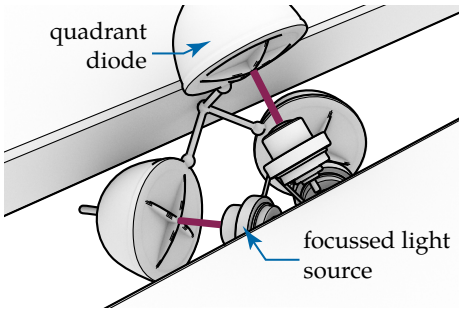


(a) 3D readout-scheme of test-mass and source-mass stage positions with quadrant diodes.

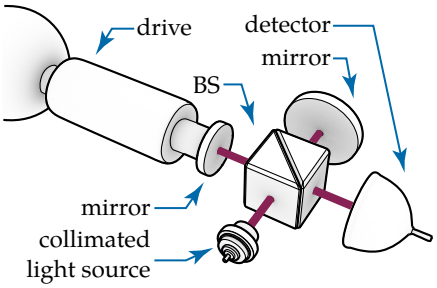


(b) Interferometric readout of source-mass position.

**Figure 10.3:** Conceptual schemes for optical stage positioning and drive-displacement readout.

mass for measurements, this should also allow to move it further away from the test mass while maintenance and calibration work is performed. This should help with keeping the source mass from crashing into the test mass due to accidental movements.

## 10.3 Possible drive-implementations

Achieving smooth driving of the source mass at around $\omega_0/(2\pi) = 50\,\mathrm{Hz}$ with a peak-to-peak amplitude of $2d_S = 2.5\,\mathrm{mm}$ with sufficiently large lifetime and not adding significant stray fields represents a substantial engineering challenge. State-of-the art piezoelectric actuators fall short of the required drive amplitude by at least one order of magnitude and available actuated positioning platforms do not achieve the desired accelerations of more than $120\,\mathrm{ms}^{-2}$.

A selection of current design approaches can be found in fig. 10.4. The development and engineering of drive implementations for the proposed experiment is performed by Mathias Dragosits[5] (University of Vienna) and is not a part of the author's work.

[5] Dragosits 2016

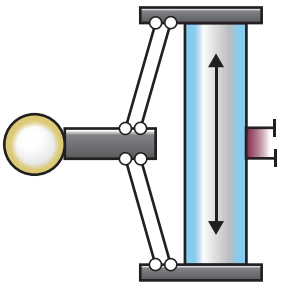

(a) Flexure guiding systems use a piezoelectric actuator that is mounted such that its contraction causes a bulge mode orthogonal to the actuators direction, which can cause displacements far beyond the piezoelectric range. Commercial systems allow for up to 1 mm peak-to-peak amplitude (Physik Instrumente (PI) GmbH & Co. KG 2017).

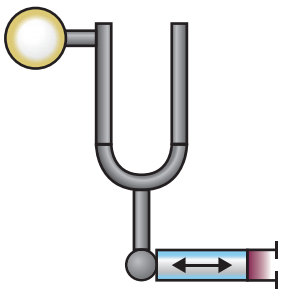

(b) A drive engine similar to a resonantly driven tuning-fork would be a comparably simple manufacturing task, but it is unclear weather the desired amplitudes can be reached and how the system can be tuned to the desired frequency.

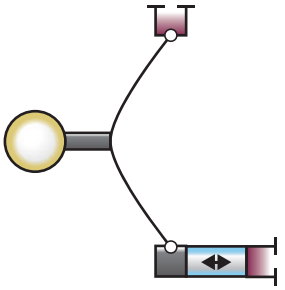

(c) A piezo stack drives one end of a thin string that is loaded with the sources mass. Resonant amplification of the piezo drive is achieved by means of excitation of the fundamental string mode. Similar to the tuning fork, this scheme is highly dependent on matched resonance frequencies of test mass and drive mechanism; however, the latter can be tuned by adjusting the string tension.

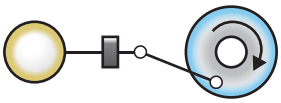

(d) In the con-rod drive the circular motion of an electric motor is converted to linear motion by a crankshaft. Given the small scale of the involved parts, we have to expect issues with imbalances and initial torque from this design, in addition to stray fields from the motor.

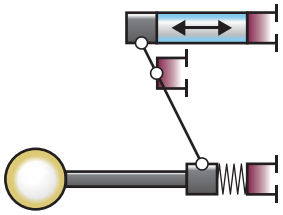

(e) Using a lever, the comparably small motion of a piezoelectric actuator (typically up to 100 $\mu$m) can be amplified. This scheme requires a stiff and lightweight lever as well as at least three bearings and a restoring spring.

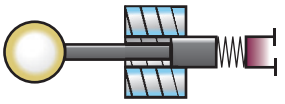

(f) Inspired by loudspeaker membrane driving, a spring-mounted electromagnetic coil allows actuation at a small input power and therefore small stray fields and heating. A similar approach is used in injection nozzles (Drummer et al. 2008).

**Figure 10.4:** Overview of current candidate designs for implementing the drive engine. The color coding is yellow for source masses, blue for the driving element and purple for fixed points.

Chapter 11

# Optical readout

The readout of the test-mass displacement plays a crucial role in the measurement scheme. Optical and/or electronic noise are always unavoidable, which can potentially overshadow the signal of the desired effect in practical scenarios. The goal of our approach is to limit the added readout noise to well below the thermal noise of the test mass.

After defining the readout requirements in section 11.1, we separately discuss the main noise sources that need to be considered. The practical realization of the readout architecture and potential noise from the implementation are discussed in section 11.2. Both classical amplitude noise and phase noise of the source need to be considered when selecting a laser (section 11.3). Lastly, suppressing quantum shot noise requires a suitable amount of optical power, that then needs to be detected without adding significant additional electronic noise (section 11.4).

## Chapter contents

## 11.1 Readout requirements

Apart from backaction noise through photon momentum (see section 5.7.2 on p. 47), no part of an optical readout (especially photon shot noise and electronic noise) is correlated with actual test-mass motion.[a] Neither do these noise sources have any impact on the test-mass dynamics nor do they depend on its mechanical susceptibility. In particular, when defining the requirement for the optical readout to be "thermal-noise limited" (as given by eq. (5.34) on p. 46), one needs to specify if only the thermal resonance peak of the relevant test-mass mode needs to be resolved (resonant readout),

$$S_{\mathrm{th}}(\omega_0) = 2Q(\omega_0^3 m\beta)^{-1} \approx (2.6 \cdot 10^{-10}\,\mathrm{m\,Hz^{-1/2}})^2,$$

or if the noise added by the readout needs to be below off-resonant thermal noise (off-resonant readout),

$$S_{\mathrm{th}}(\omega < \omega_0) \approx S_{\mathrm{th}}(0) = 2(Q\omega_0^3 m\beta)^{-1} \approx (1.3 \cdot 10^{-14}\,\mathrm{m\,Hz^{-1/2}})^2,$$

which is much tougher to achieve (i.e. by a factor of $Q$). For a measurement on resonance in an ideal scenario without any unforeseeable noise peaks, suppression of readout noise just below thermal noise on resonance would be sufficient, as in this case identification of a high-$Q$ peak by visual inspection should be straight-forward. However, a typical spectrum, even if averaged, can be full of sharp, delta-like noise peaks. With the proposed parameters (table 8.1 on p. 88), the width of the thermal mechanical peak is on the order of a few mHz, so in practical scenarios it will be indistinguishable from these delta-like noise-peaks.[b] Ideally, the optical readout should be designed such that becoming thermal-noise limited even off-resonance is feasible in order to simplify the identification of the relevant mechanical peak. A second reason to aim for readout noise below off-resonance thermal noise is the possibility of off-resonant driving and detection, which would allow to circumvent the problems associated with thermal frequency-drifts when driving the small mechanical bandwidth on resonance (section 9.4.3 on p. 107), stability (section 10.1.2 on p. 121) and ring-in (section 9.6 on p. 111).

A significant and rather untypical challenge in the proposed experiment is posed by the comparably low eigenfrequency of the test mass.[c] Systems with mechanical eigenmodes up to a few hundred Hertz are very susceptible to acoustic vibrations.[1] For a practical interferometer, these vibrations (combined with thermal drifts) cause relative phase shifts that move the interferometer away from a set point. In most experiments, this is compensated by *locking*[2]

[1] Abbott, Abbott, Adhikari, et al. 2009

[2] Bachor and Ralph 2004, sec. 8.4

[a] Note that in general, once cavities (with decay times) are incorporated, shot noise and the test-mass motion are not necessarily uncorrelated (Clerk et al. 2010).

[b] While in principle the test-mass support could be mechanically driven to excite mechanical modes, this would require an actuator directly at the test-mass stage, which should be avoided

the interferometer, where one feeds back a correction derived from an error signal to induce an additional phase shift, which counters the shift caused by disturbances. This is a convenient method if the aimed signals are located at higher frequencies than the disturbances. However, in our case we are interested in a frequency that is located somewhere in the low-frequency acoustic band. If active locking during data acquisition is required, one has to be careful to completely suppress noise from the lock into the frequency range of interest (in this case, a small band around the drive frequency). Hence, ideally the interferometer is stable enough to not require locking during measurement.

## 11.2 A homodyne interferometric readout proposal

In the typical interferometric displacement readout scheme, a moving cantilever (or other mechanical transducer) introduces a phase modulation on the probing light beam. This phase shift is proportional to the displacement as $\mathrm{d}\phi = 2k\,\mathrm{d}x$.[d] The phase of the signal beam (SI) can be read out by overlapping it with a phase-stable reference beam called local oscillator[3] (LO). In the following we motivate our choice for a specific interferometer implementation and investigate the individual optical components.

[3)] Bachor and Ralph 2004, sec. 8.1.4

### 11.2.1 Established schemes for interferometric readout in the acoustic band

Naturally, a simple interferometer that probes a phase will still be susceptible to frequency noise and amplitude noise of the laser source. In order to reduce the effect of frequency noise, one can minimize the optical path length difference of the interferometer arms. For amplitude noise, there are mainly two different ways of amplitude-fluctuation compensation that can be found in the literature.

due to the reasoning given in section 9.6 on p. 111.

[c)] At first glance it may seem fair to compare the proposed experiment to second generation gravitational wave detectors, where a much lower effective displacement-noise than the $10^{-14}\,\mathrm{m\,Hz^{-1/2}}$ required here is measured over a larger bandwidth and even down to frequencies lower than 50 Hz. However, we need to take into account how this low noise background is achieved. First, both interferometer arms use cavities to enhance the effective amplitude change $\Delta P$ per mirror strain $\Delta x$ at the detector by the finesse. Second, an *optical DC* readout scheme (Ward et al. 2008) allows to reach high sensitivity while only detecting a fraction of the power that is circulated inside the interferometer, also allowing to pump significantly more power into the system than would otherwise be possible. An implementation of a similar scheme in the proposed experiment would require a number of auxiliary optics and also lead to a high amount of incident power at the test mass. As we are confident that the required performance levels can be reached with significantly less effort, we do not consider such a scheme at this stage of development. However, for future iterations of our proposed experiment that exhibit stronger noise requirements, this will likely have to be reconsidered.

[d)] This only holds in the case of vertical reflection. For a non-zero incident angle $\alpha$, the relation changes as $\mathrm{d}\phi = 2k\,\mathrm{d}x/\cos\alpha$.

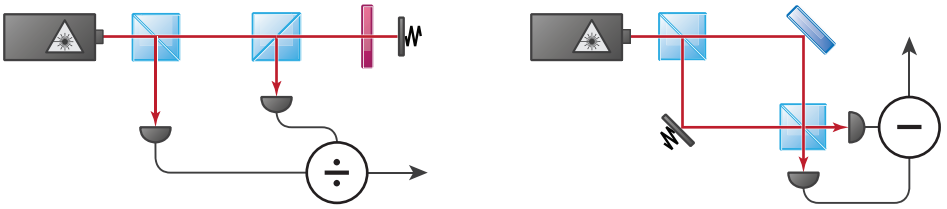

(a) Conceptual fiber interferometer. A semi-reflective mirror forms a cavity with the mechanical mirror. The light is circularized through a beam splitter and detected on a single diode. Optionally, a fraction of the initial light can be used for normalization.

(b) Conceptual free-space Mach-Zehner interferomter. The light is split into different pathways and later recombined. By taking the difference signal of both output ports, amplitude fluctuations can be reduced when similar powers are sensed at both ports (balanced homodyning).

**Figure 11.1:** Schematic drawings of the two basic homodyne interferomter types described in section 11.2

The first approach resembles a Fabry-Pérot interferometer with a low-finesse cavity. Here, a semi-reflecting surface close to the cantilever is used to generate the local oscillator. The part of the light that is transmitted enters a cavity that is formed by the semi-reflecting surface and a second mirror on the cantilever. The light inside the cavity accumulates a phase shift and is hence called signal beam. When leaving the cavity it interferes with the local oscillator (fig. 11.1(a)).[e] This first method in combination with a coherence-controlled laser (see section 11.3.2), coated evanescent wave couplers and rigidly clamped bend-insensitive fibers was used by Smith, Pratt, and Howard (2009) to reach displacement noise PSDs of $10^{-13}\,\mathrm{m\,Hz^{-1/2}}$ at 10 Hz.[f]

The second commonly found approach to compensate amplitude fluctuations is to use a Mach-Zehnder type interferometer where SI and LO are split into separate pathways and later recombined at a second beam splitter (fig. 11.1(b)). The advantage of this approach is that both interferometer output

[e] Note that for the overall power to be conserved in this scheme, there has to exist a second output port for the cavity, as otherwise no amplitude modulation would be possible at the first output. Typically, the second output is formed by a partially reflecting second cavity mirror and through photons scattered out of the cavity.

[f] In order to get an estimate of the potential noise performance, we replicated the scheme (fig. 11.1(a)) with available components. Specifically, we used a 1064 nm *Mephisto*-laser by Coherent, rigidly clamped standard fibers and simple custom detectors (Böhm 2007) on a small honeycomb breadboard (300 mm by 400 mm) placed on a passive vibration isolation stage (Platus 1996). This yielded a noise performance of $5 \cdot 10^{-12}\,\mathrm{m\,Hz^{1/2}}$ above 50 Hz and $10^{-13}\,\mathrm{m\,Hz^{1/2}}$ above 1 kHz, which falls short of the performance demonstrated by Smith, Pratt, and Howard (2009) by one to two orders of magnitude. We can therefore state that this scheme is promising, but certainly requires careful selection of components to yield the best possible performance.

ports can be accessed easily, which allows to subtract the measured powers and to significantly reduce the sensitivity to laser amplitude noise (*balanced* optical homodyning, chapter 6). The disadvantage is that due to the separation of SI and LO, it is easier to introduce additional phase noise between the two arms. Also it requires two closely matched detectors (i.e. with equal detection-efficiency).

As an optional extension to both methods, one can split off a fraction of the input power (i.e. before entering the interferometer) and divide the output signal by this quantity, as demonstrated by Rugar, Mamin, and Guethner (1989). This normalizes the outgoing amplitude to the incoming amplitude and therefore compensates for classical fluctuations of the laser power. Naturally, it cannot compensate for amplitude noise that is generated within the interferometer, e.g. by parasitic cavities. Interestingly, Smith, Pratt, and Howard (2009) report that with their stable coherence-controlled laser, this technique did not yield any noteworthy improvement of noise performance.

### 11.2.2 Choosing a suitable readout scheme

In our specific case, we require interferometric stability in the low frequency acoustic band. The readout is employed to measure the displacement of a test mass that is isolated from environmental vibrations by an isolation chain with multiple stages (see chapter 12) inside of a large vacuum system. As commercial laser sources are typically not compatible with high vacuum, the source will have to be installed outside of the vacuum, with the power fed into the system either free-space through a suitable viewport or by the means of an optical fiber feedthrough.[g]

The first of the approaches presented in the previous section (fig. 11.1(a)) does in principle allow displacement readout at low acoustic frequencies. Here it is crucial to rigidly mount all optical fibers, so that classical amplitude fluctuations from mechanical excitations of the fibers are at a minimum.[4] This impedes the requirements for vibration isolation, according to which a fiber would have to hang loosely between stages in order to keep the transmissibility low. Such a fiber, however, would oscillate at acoustic frequencies and introduce both amplitude noise and phase noise due to stress-induced birefringence and thermal effects.

[4] Smith, Pratt, and Howard 2009

Given the obvious obstacles of the fiber interferometric approach, we choose a balanced optical Mach-Zehnder type interferomter based on (polarization-selective) beam displacers. This scheme is similar to but more compact than

[g] Alternatively, one could house the laser source in a vacuum can (Coyne et al. 2007) that has atmospheric pressure within the UHV system. However, the additional payload through the can would significantly toughen the payload requirements for the last stage of seismic isolation (and in consequence all previous stages, due to the hanging nature of the isolation system).

the scheme presented by Paolino, Sandoval, and Bellon (2013), who managed to achieve long-term drifts between the interferometer arms of less than 3 nm at room temperature and without locking. Hence, it should yield high interferometric stability through a small separation of SI and LO, while allowing the usage of both output ports to measure a power difference signal.

We note that in principle both approaches can be combined with (better) optical cavities to massively enhance readout precision for a given amount of power.[5] As we will see below (section 11.3.1), our power requirements are sufficiently low that the gain of an optical cavity would not outweigh the substantial hurdles added in practicality. Still, as an optical cavity can yield much better noise performance given a maximum input- or detection-power, it is a worthy consideration for future iterations of this scheme.

[5] Bachor and Ralph 2004

### 11.2.3 A polarization-based interferometer

In order to achieve maximum stability of an interferometer the first obvious step is to limit the effect of acoustics by transferring the system into vacuum. In our case this means that all crucial components, especially those involved in the beam separation and recombination, need to be installed inside the vacuum tank. However, this will not shield them from the acoustic vibrations transfered via the mechanical parts. The obvious solution is to transfer the interferometer part entirely onto the test-mass stage, which naturally needs to have high vibration-isolation. The last step towards a low mechanical susceptibility for acoustic frequencies is to push all relevant mechanical modes of the interferometric setup beyond the detection band frequencies in order to prevent the resonant enhancement of previously suppressed vibrations. This can be achieved by making the system compact, i.e. of small spatial dimensions, as examined in section 11.2.6.

Typically an optical Mach-Zehnder interferometer requires the ability to separate and recombine different (spatial, temporal or polarization) modes of the electromagnetic field. Our approach is to encode SI and LO into orthogonal polarizations of the same geometric mode, which by the use of optical beam displacers are separated into parallel beams over a small spatial region. Depending on the design of the test-mass device, the SI beam can be reflected off the point of maximal deflection, while the LO beam is reflected off the substrate (see fig. 11.2). The spatial recombination of SI and LO can be achieved in two ways – either with a second beam displacer when not reflecting under normal incidence off the test-mass device, or with the first beam displacer used in the opposite direction. The latter approach requires an optical circulator to separate the outgoing from the incoming beam. At this point SI and LO are still stored in orthogonal polarizations. In order to split both contributions and allow for interference, a combination of half-wave plate and polarizer performs a

distribution of the horizontal/vertical modes into diagonal polarization modes that equally mix the LO and SI components.

As the first beam displacer splits the incoming beam into its horizontal and vertical polarization components, it is possible to tune the fraction of light in the SI and LO beams by rotating a linearly polarized incoming beam with a half-wave plate. In order to reach the set-point of the interferometer, i.e. the setting of average relative phase between SI and LO that yields a balanced output and optimal common mode rejection for laser intensity noise, an optical element is required that introduces a relative phase between horizontal and vertical polarization. A differential phase shift can be achieved with a birefringent material, which can serve as an arbitrary phase retarder if it is rotated around its optical axis.[6] This element could also be used to stabilize the interferometer to its set point actively. However, the achievable locking frequencies are quite limited due to the fact that a physical element has to be rotated. Furthermore, care must be taken not to introduce additional noise into the actuation band.

[6] Trojek 2007

In section 6.3 on p. 57 we demonstrated that this interferometric scheme can be fitted with all necessary degrees of freedom to tune the distribution of power into both interferometer arms as well as into the output ports. In the following we discuss the practical implementation of two variants of the scheme described above. First, we investigate an implementation with two different beam displacers, and second we repeat the analysis for an implementation with a single displacer and a beamsplitter acting as a circulating element.

### 11.2.4 Implementation with two displacers and non-normal reflection

We briefly summarize the current selection of optical elements used in the proposed scheme. A detailed derivation of the signal yielded by this design can be found in section 6.3. A conceptual representation is presented in fig. 11.2(a).

Initial fiber coupler. For coupling out of the incoming fiber we use a "60SMS" laser beam coupler (Schäfter + Kirchhoff 2017) that has titan mechanics and is HV compatible (and upon request can be made UHV compatible by omitting viton parts). Lenses for this coupler are available in a range of coatings and focal lenghts/apertures and offer tilt as well as longitudinal translation functions. Transverse adjustment can be achieved with an additional "48MB-19.5-SXY-1" adjustment clamp, though it might be advisable to perform a thermal noise analysis (cf. section 11.2.6) of this specific clamp before progressing with the design. Preliminary experiments showed that the five degrees of freedom offered by the coupler are sufficient to align the entire optical system given sufficient manufacturing precision of the mounting hardware.

Polarization filter. The polarization purification is done with a *Glan-Taylor polarizer*[7], which is has a much higher extinction ratio than a regular polarizing

[7] Archard and Taylor 1948

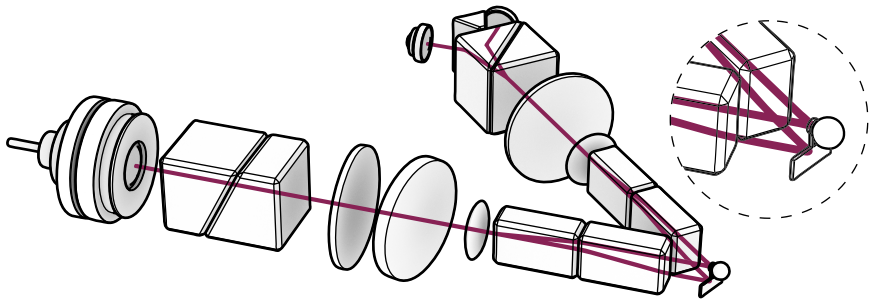

(a) Polarization based double displacer interferometer with (in order of beam transmission) $x/y/z/\phi_x/\phi_y$ fiber coupler, Glan-Taylor polarizer, half-wave plate, $YVO_4$ phase retarder, focusing lens, first set of beam displacers, test mass on chip, second set of beam displacers, colimating lens, half-wave plate, Wollaston prism, wedge mirror and detector diodes.

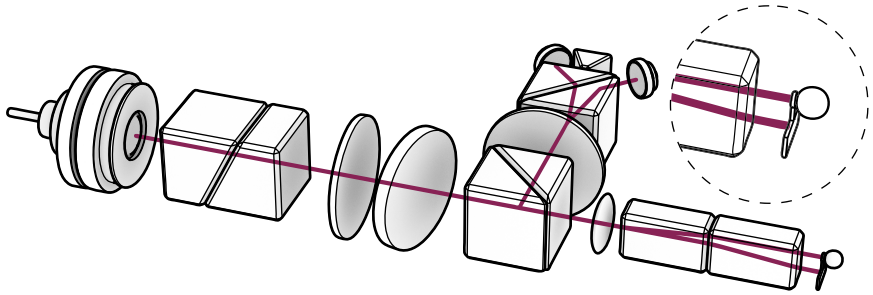

(b) Polarization based single displacer interferometer with (in order of beam transmission) $x/y/z/\phi_x/\phi_y$ fiber coupler, Glan-Taylor polarizer, half-wave plate, $YVO_4$ phase retarder, focusing lens, set of beam displacers, test mass on chip, 50/50 beam splitter (circulator), half-wave plate, Wollaston prism, wedge mirror and detector diodes.

**Figure 11.2:** Roughly to-scale models of both possible implementations of the interferometer described in sections 11.2.4 and 11.2.5 on p. 133 and on p. 137 and conceptually analyzed in sections 6.3 and 6.3.6 on p. 57 and on p. 65. In order to compactify the setup, one might consider to remove the need for wave plates by either rotating the components accordingly around the beam axis, or by directly coating/depositing the wave plates onto other components (the first onto the Glan-Taylor polarizer output, the second onto the second beam displacer output).

beam splitter.

First wave plate. Following the analysis in section 6.3.4 on p. 62, we use a standard $\lambda/2$ wave plate to rotate the light by 45° in order to achieve a 50/50 splitting ratio of the orthogonally polarized SI and LO signal. Ideally, a zero-order waveplate is used as the path lengths for horizontal and vertical polarization must not deviate by more than a few hundred micron. This is required by the small coherence length of the employed laser source (see section 11.3.2) and it

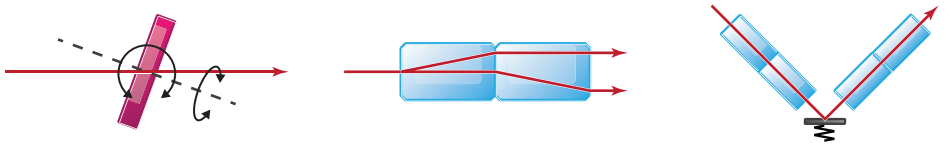

(a) An optical element that shifts the phase between horizontal and vertical polarization can be realized with a birefringent material in the correct orientation.

(b) Chaining two beam displacers allows to separate horizontal and vertical polarizations while keeping them parallel and with identical optical path lengths.

(c) Off-angled reflection of the SI and LO beams in a scheme with optimal power efficiency and minimal parasitic stray effects.

**Figure 11.3:** Conceptual principles for a polarization-determined beam-displacer implementation of a Mach-Zehnder interferometer.

also keeps the effect of laser frequency noise at a minimum.

Arbitrary phase retarder. In order to achieve an arbitrary relative phase shift between horizontal and vertical polarizations, we employ an $YVO_4$ crystal.[8] If the optical axis is aligned with one of the polarizations, it will maintain both polarizations and leave the amplitudes unaffected as well. However, their relative phase can be tuned by adjusting the rotation of the crystal around its optical axis (fig. 11.3(a)). As this adjustment has to be performed in order to set the interferometer to the optimal operation point (highest phase sensitivity and optimal laser-intensity-noise suppression), a remote actuation is required. With the "SR-2013" the company Smaract[9] offers an UHV-compatible low-footprint rotation stage which retains its position and remains noise-free when the power supply is cut. As this is another crucially sensitive part of the optical readout, mode analysis is advisable.

[8] Trojek 2007

[9] SmarAct GmbH 2017

Focusing. The spatial beam-separation will not exceed a few millimeters at any point, which is on the order of the width of a collimated beam. Therefore, focusing of the beam should be done prior to the splitting (as lenses smaller than 1 mm are rare, apart from the obvious problems of positioning). Figure 11.4 shows the Gaussian beam profile[10]

[10] Bachor and Ralph 2004

$$w(z) = w_0\sqrt{1 + (z/z_R)^2} \quad \text{with} \quad z_R = \pi w_0^2/\lambda \tag{11.1}$$

for this scenario. A smaller beam waist $w_0$ (i.e. focal spot size) implies larger beam diameters $w(z)$ at a distance $z$ from the waist position. Requiring a beam diameter $w(z) < 2\,\text{mm}$ up to 40 mm away from the test mass (e.g. because of the beam displacer's clear aperture), we are limited to a spot size $w_0 \gtrsim 10\,\mu\text{m}$, which sets an effective minimum area for the test-mass mirror.[h]

[h] We point out that since both lens positions and spot positions are fixed, it is not clear if focusing can always be achieved with the available degrees of freedom in the interferometer.

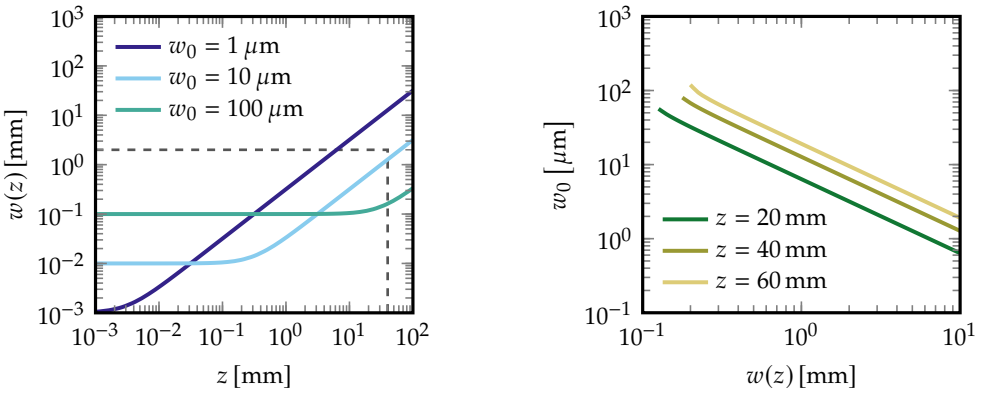


(a) Gaussian beam width $w(z)$ for different focal waist sizes $w_0$.

(b) Waist size $w_0$ depending on beam width $w(z)$ at different distances $z$.

**Figure 11.4:** Gaussian beam profile (eq. (11.1)) for a wavelength $\lambda = 1064\,\text{nm}$. Limiting the width of the beam at a distance $z = 40\,\text{mm}$ to $w(40\,\text{mm}) < 2\,\text{mm}$ implies a minimum waist size of $w_0 \gtrsim 10\,\mu$m.

**Polarization-dependent beam separation.** The spatial separation of beams is done with two beam displacers rotated by 90° with respect to each other (fig. 11.3(b)), similar to the scheme used by Paolino, Sandoval, and Bellon (2013). In this configuration the optical path length of SI and LO can in principle be kept exactly equal. Typical calcite or $YVO_4$ displacers yield around 1 mm of beam separation per 10 mm of length, so in order to reach a design goal of 2 mm, the length of the displacement block will be about 20 mm. Due to their fragility, stable mounting of the displacers in this HV application could pose a significant challenge as temperature-induced stress might cause birefringence or even breaking. This could be achieved for example by rigidly mounting the displacers to a metal with an expansion coefficient similar to calcite or YVO4, which then can be loosely mounted in a scheme that allows deterministic relative motion of the mechanical parts.

**Probing of test-mass displacement.** Both SI and LO beam will be reflected off the chip (see figs. 11.3(b) and 11.3(c)). The beams are reflected under an angle, so the outgoing light can be directed towards the detection part without the need for (lossy) circulation. The SI beam hits the backside of the cantilever or the part of the membrane where the test mass is mounted, while the LO beam is reflected off the substrate. This scheme cancels a phase shift between SI and LO through most modes of the test-mass chip, especially translation in the direction of the beam. Naturally, reflection under an angle requires that

We are currently investigating this question in a realization of the discussed scheme based on standard components (see also section 14.1.4 on p. 183).

some (prism-shaped) space above the reflective part of the test-mass device is kept clear. Therefore, this space can not be used for additional chip mass or mounting structures.

Recombination. Here we use the same configuration of two beam displacers in order to recombine the beams.

Second wave plate. Similar to the first wave plate, a second zero-order half wave plate rotates both polarizations by 45°. The horizontal and vertical component of the outgoing beam each entail half of the power of each ingoing horizontal and vertical polarizations (i.e. SI and LO).

Final interference and beam separation. Again, we do not use a regular (i.e. Glan-Taylor) PBS but a symmetric optical element with a much higher extinction ratio, a so-called Wollaston prism. Typically, horizontally and vertically polarized beams leave the prism with an angle of roughly 20°. To simplify the placement of detector diodes, it might be advantageous to split the beams further by using small mirrors or a total reflection of a wedge-shaped prism.

### 11.2.5 Implementation with a double pass of a single beam-displacer

This approach deviates from the one presented above by the usage of a beam splitter to circulate the light. It allows to use the first displacer in both directions by reflecting the readout beam vertically off the test-mass chip (fig. 11.2(b)). The derivation of the signal in this configuration is presented in section 6.3.6 on p. 65. Apart from the output power being reduced by 75 % and the signal to shot-noise by 50 %, this approach is equivalent to the case with two displacers. Overall this scheme has reduced power and thereby higher shot noise, but is potentially much easier to align. As opposed to the scheme above, this scheme has been successfully demonstrated by Paolino, Sandoval, and Bellon (2013). Compared to the scheme treated in the previous section, there are two major differences in the optical elements.

Beam splitter. A regular 50/50 beamsplitter between the arbitrary phase retarder and the beam displacer is used to circulate (a part of) the optical power.[i]

Polarization-dependent beam separation. Here, just one beam displacer is deployed, and the beam passes it in both forward and backwards direction. Therefore, the same optical element serves for both beam separation and recombination.

[i] Note that this requires a splitting ratio of 50/50 for both polarizations, which might be challenging with standard components.

### 11.2.6 Eigenmodes and thermal spectrum

Interferometers are typically susceptible to thermal drifts of their supporting structure, which affects the phases and the alignment of the interferometer arms. Thermal drifts are a low-frequency effect caused by environmental temperature changes. In the case of the proposed experiment the interferometer is supported by an alternating cascade of thin wires and heavy masses (chapter 12), which effectively acts as a *thermal low-pass* filter. We therefore assume that the effects caused by thermal drifts are small.

In addition, thermal mechanical excitations can cause phase noise within the interferometer, i.e. Brownian noise of the interferometer. While thermal drifts and external vibrations can be shielded to a large degree, mechanical excitations due to thermal noise are always present. Due to the typical $1/f$ to $1/f^2$ falloff in the susceptibility of harmonic oscillators above resonance (see section 7.1 on p. 68), mechanical modes of interferometers do not play a huge role in high frequency experiments. However, as the proposed experiment necessarily has to be performed at comparably low frequencies, Brownian noise can cause a large noise floor or excite even mechanical resonances within the detection band. Hence, if low noise performance is crucial, one has to optimize the mechanical design of the interferometer with respect to its eigenfrequencies and mode shapes.

At the time of writing of this thesis, there is no finished design of the entire interferometer. Therefore we propose a method based on the model presented in section 6.4 on p. 66 that should in principal allow to estimate the Brownian noise of a given design using finite elements. Here, we use the method exemplary to analyze the properties of a basic toy model.

Figure 11.5(a) shows a basic model of a large-area Mach-Zehnder interferometer with SI and LO beam path colored differently for simplicity. As the interferometer will be supported by soft springs in all spatial directions (chapter 12), we can treat it as being in free fall without additional boundary conditions. Computing the first 150 eigenmodes allows us to estimate the effective mass per mode via eq. (6.11) on p. 66, where $\Delta z$ is the difference of path length changes of SI and LO due to the mechanical mode.[j] As seen in section 9.2.1 on p. 97, we may then calculate and sum up the individual thermal PSDs to a total thermal PSD $S_{x\,\mathrm{th,tot}}$ (eq. (9.1)). The resulting PSD for our toy model is shown in fig. 11.5(b) for three different sizes of the interferometer and a fixed $Q = \omega_{0i}/\gamma_i$ of 50 for all modes. It immediately becomes clear that a reduction of interferometer size is advantageous for noise performance. Lastly,

[j] As described in detail by Gillespie and Raab (1995), one always has to check if the thermal PSD at the given frequency of interest is actually converging for the amount of eigenmodes that is incorporated. Here, the spectra were effectively converging after adding around 100 eigenmodes.

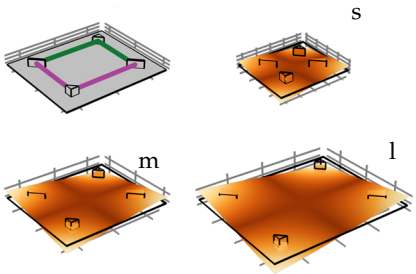


(a) Basic geometry with two beam splitters, two mirrors and two light paths (grey); fundamental mode and size comparison of the geometries used in fig. 11.5(b). The interferometer area is 0.12 m$^2$ for (s)mall, 0.48 m$^2$ for (m)edium, 1.08 m$^2$ for (l)arge.

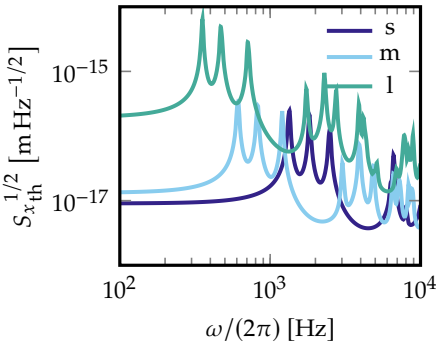


(b) Thermal displacement noise PSD for the first 150 modes as a function of frequency $\omega/(2\pi)$. Reducing the overall size of the interferometer and the physical separation of SI and LO greatly helps with reducing thermal noise.

**Figure 11.5:** Demonstration of interferometer thermal noise estimation for the case of a simple toy model.

we point out that given the very narrow bandwidth of the proposed testmass, $\gamma/(2\pi) = \omega/(2\pi Q) \approx 2.5\,\mathrm{mHz}$, we would actually have to be rather unlucky to accidentally "catch" a high-$Q$ mechanical mode of the interferometer. In that case, one could slightly shift the interferometer's eigenmode frequencies via small geometric modifications.

## 11.3 Laser source

Here we estimate the requirements for the light source in terms of power and stability.

### 11.3.1 Power requirements

In order to become limited by thermal noise $S_{x\mathrm{th}}$, it is necessary to suppress the photon shot noise $S_{x\mathrm{sh}}$ well below the thermal noise limit by increasing the power of the light source. From eqs. (5.34) and (6.1) on p. 46 and on p. 56 we have

$$S_{x\mathrm{th}} = |\chi(\omega)|^2 \frac{2\gamma}{m\beta} \quad \text{and} \quad S_{x\mathrm{sh}} = \frac{\hbar}{32\pi}\frac{\lambda c}{P}.$$

As explained in section 11.1, while reaching the thermal noise limit on resonance ($\omega = \omega_0$) is in principle sufficient for a resonant measurement of gravity, for practical reasons it will likely be necessary to resolve thermal noise

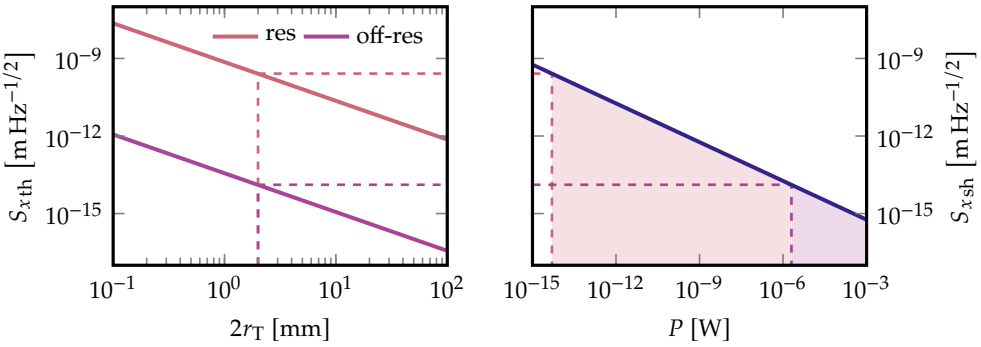


(a) Thermal displacement PSD as a function of test-mass diameter $2r_\mathrm{T}$.

(b) Shot noise displacement PSD as a function of light power.

**Figure 11.6:** Comparison of thermal noise and photon shot noise. For a given test-mass diameter $2r_\mathrm{T}$ a value of the thermal PSD is found in the left-hand figure. One can then use the right-hand figure to see the minimal power needed to suppress photon shot noise below the thermal PSD.

off-resonance ($\omega < \omega_0$). In fig. 11.6 we compare the noise PSD generated by both $S_{x\mathrm{th}}$ on- and off-resonance as a function of test-mass size as well as $S_{x\mathrm{sh}}$ as a function of power.

In order to become thermal-noise limited, we require $S_{x\mathrm{sh}} \ll S_{x\mathrm{th}}$. For the on-resonance case this yields a minimum power requirement

$$P_{\mathrm{min,res}} \gg \frac{\hbar\lambda c m\beta}{64\pi} Q^{-1}\omega_0^3,$$

while being shot noise limited off-resonance requires

$$P_{\mathrm{min,offres}} \gg \frac{\hbar\lambda c m\beta}{64\pi} Q\omega_0^3.$$

For our usual parameters, this is

$$P_{\mathrm{min,res}} \gg 5\,\mathrm{fW} \quad \text{and} \quad P_{\mathrm{min,offres}} \gg 2\,\mu\mathrm{W}.$$

So far we have not factored in photon back-action (section 5.7.2 on p. 47). Back-action becomes relevant starting in the power regime around the lowest point of the SQL (eq. (6.3) on p. 56). For our parameters, this is

$$P_{\mathrm{SQL}} = (256\pi)^{-1/2}\frac{\lambda c m}{|\chi(\omega)|} \approx \begin{cases} (256\pi)^{-1/2}\lambda c m\omega_0\gamma \approx 4\,\mathrm{mW}, & \omega = \omega_0 \\ (256\pi)^{-1/2}\lambda c m\omega_0^2 \approx 90\,\mathrm{W}, & \omega \approx 0 \end{cases}. \quad (11.2)$$

It becomes clear that due to our comparably large test mass and the lack of an optical cavity, the chosen parameters yield an experiment far away from the lowest point of the SQL. Neglecting the effect of backaction is therefore justified.

### 11.3.2 Suppression of parasitic scattering

A major source of noise in interferometric setups is *parasitic* interference[11], where scattered light from multiple backreflections between optical components reinterferes with the main signal path. In the worst case, light scattered this way picks up acoustic vibrations and therefore gets phase-shifted around the frequency of interest. This effect can be drastically reduced if the light source has a very short coherence length (on the order of a few hundred microns). Then, light scattered multiple times can not interfere with the main signal beam due to the difference in optical path lengths. This approach of low frequency noise suppression has been successfully demonstrated in atomic force microscopy applications by Rugar, Mamin, and Guethner (1989). In recent years commercial laser systems became available that have specific modes to achieve broad linewidth while maintaining sub-nanometer central peak stability, such as the 51nano-series (Schaefter + Kirchhoff) with built-in permanent linewidth broadening[12] and the 8160x-series (Agilent) that features a user controllable "coherence control". The latter has been reported to drastically reduce noise up to 1 kHz while introducing a huge amount of artifacts at higher frequencies.[13] This method requires that the difference of optical paths of SI and LO is much shorter than the coherence length. For this reason, the design proposed above has identical optical path lengths for both beams.

[11] Smith, Pratt, and Howard 2009; Vahlbruch 2008

[12] Oechsner et al. 2009

[13] Smith, Pratt, and Howard 2009

### 11.3.3 Amplitude stability

As we have seen in eqs. (6.8b) and (6.10) on p. 61 and on p. 63, an optimal choice of waveplate angles $\varphi_1$, $\varphi_2$ and compensation phase $\theta$ yields a photon count difference

$$\langle \hat{c}_H^\dagger \hat{c}_H - \hat{d}_V^\dagger \hat{d}_V \rangle \approx \frac{1}{2} \phi_{\mathrm{mod}} |\alpha|^2,$$

where $\phi_{\mathrm{mod}}$ is the phase modulation and $|\alpha|^2$ is proportional to the power of the light source. As $\alpha$ denotes a quantum-mechanical expectation value for a steady-state, this expression remains unchanged by photon shot noise. It does, however, include classical variations of $\alpha$, which can be caused by drifts or instabilities of the laser source. Therefore, ideally, one would divide the difference signal $\langle \hat{c}_H^\dagger \hat{c}_H - \hat{d}_V^\dagger \hat{d}_V \rangle$ by a signal that is proportional to the laser power before entering the interferometer, e.g. by splitting and detecting a small fraction off the main beam. As mentioned before, Rugar, Mamin, and Guethner (1989) saw a significant improvement in a single-output fiber interferometer using this technique. However, Smith, Pratt, and Howard (2009), who used a similar setup but focused on thorough fixation of all involved (custom bend-insensitive) fibers, mention that such a scheme did not yield further improvements in their noise performance.

### 11.3.4 Frequency stability

Assuming that the integrated homodyne setup is well-isolated, thermalized and mechanically stable, low-frequency noise and drifts should mainly be caused by wavelength instability of the laser source. We perform a rough estimation on how stable the wavelength needs to be in order to

1. not cause additional low-frequency noise above the desired signal and
2. allow us to chose the homodyne phase $\phi_0$ once before every measurement trace and then leave it at the set point for the remainder of that measurement without the need for real-time active locking.

To answer the first question, we start by defining $\Delta L$ as the difference in optical path lengths of SI and LO beam. The number $m$ of waves that will fit into this path length is then $m = \Delta L/\lambda$. An infinitesimal change of wavelength $\mathrm{d}\lambda$ will cause a signal equivalent to a change of position $\mathrm{d}x$ as

$$\mathrm{d}x = m\,\mathrm{d}\lambda = \Delta L\frac{\mathrm{d}\lambda}{\lambda} = \Delta L\frac{\mathrm{d}\nu}{\nu},$$

where $\nu$ is the optical frequency. This allows us to compare RMS values, or, which is more natural when relating laser frequency noise to thermal noise, PSDs. With the above the frequency PSD can be written as $S_{x\nu} = (\Delta L/\nu)^2 S_\nu$, and we should require

$$S_{x\nu}^{1/2} \ll \nu S_{x\,\mathrm{th}}^{1/2}/\Delta L \approx 3.7\cdot 10^3\,\mathrm{Hz\,Hz^{-1/2}}\cdot(\Delta L/\mathrm{mm})^{-1}$$

in order to reach frequency noise well below the thermal noise $S_{x\,\mathrm{th}}$ off-resonance.

Moving on to the second point above, we now start with an initial wavelength $\lambda_1$, fitting a number of waves $m_1 = \Delta L/\lambda_1$ in the arm length difference. After some drifting, the new wavelength yields $m_2 = \Delta L/\lambda_2$. A small difference of those two numbers is then equivalent to having tolerable drifts in the system. We demand $\Delta m \overset{!}{\ll} 1$ with $\Delta m = |m_1 - m_2|$. We can rewrite this as $\Delta L\Delta\lambda/\lambda^2 \overset{!}{\ll} 1$, where we approximated $\lambda_1\lambda_2 \approx \lambda^2$. Since the difference of two frequencies can be expressed as $\Delta\nu \approx c\Delta\lambda/\lambda^2$, we have

$$\Delta\nu \overset{!}{\ll} \frac{c}{\Delta L},$$

Taking the employment of a short coherence length (< 1 mm) laser as given limits the mechanical design to a few hundred micron of tolerable SI-LO path length difference, thus allowing laser frequency drifts $\Delta f$ as

$$\Delta\nu \ll 300\,\mathrm{GHz}.$$

This is not to be confused with the linewidth. It is the maximum drift of the central frequency (and independent of the width) that can be tolerated over a span of multiple hours.

## 11.4 Detector electronics

For the detection part of the optical readout, we require that an upper limit for the noise PSD is given by the optical shot noise, which is usually referred to as being *shot-noise limited*. Becoming shot-noise limited at high frequencies is comparably easy as the typical $1/f$ (flicker) noise[14] of many electronic components becomes negligible.[15] However, in the proposed low-frequency experiment, we have to be more careful about proper circuit design and selection of low-noise components.

[14] Hobbs 2009; Horowitz and Hill 1994

[15] Guzmán Cervantes et al. 2014; Hoogenboom et al. 2005

Following Stefszky (2012), there are in principle two ways to electronically implement the two diodes used for a balanced homodyne detection. The first one is the *variable gain* method where both photo currents are converted and amplified individually and then subtracted, either electronically or in post-processing (see e.g. McKenzie (2002)). The advantage is that the gain of both amplification circuits can be tuned individually to account for mismatched photo diodes (i.e. diodes with unequal efficiency). In this scheme it is possible to directly measure both individual diode signals so they can be used for, e.g., normalization as explained in section 11.3.3. This comes at the cost of additional noise through the amplification, since the added noise of both amplification circuits contributes to the difference signal, and through the need to resolve a small power modulation over a comparably large offset. The second method, *current subtraction*, allows to reduce the additional electronic noise by directly subtracting the current of both diodes before the amplification (see e.g. Vahlbruch (2008) and Vahlbruch et al. (2007)). The advantage here is that the added electronic noise is much lower compared to the variable gain scenario, as just one common amplification stage is employed. At the set point for maximum phase sensitivity the difference current has zero-mean, which means that this scheme also allows for higher total amplification. The disadvantage is that the balancing of both diodes has to be achieved optically (e.g. by tuning optical elements as analyzed in section 6.3.5 on p. 64 or by using neutral-density filters), which reduces the contrast. Also it is not easily possible to measure the sum of both ports, making it harder to detect total power fluctuations.

A technical detail to consider for the practical implementation is that achieving sufficiently stable coupling of the two ports of the interferometer into optical fibers will potentially be challenging, as it might introduce jitter noise[16] (with coupling efficiency into optical fibers being highly depended on beam position and direction) and amplitude noise through typical effects in long fibers (section 11.2). Therefore, it is advisable to perform the detection directly at the optics stage, as the cross section of photodiodes is much higher than that of optical fibers. As most electronic components are not vacuum compatible, having the detector circuit board directly next to the optics would

[16] McKenzie et al. 2007

| source | method | $S_x^{1/2}(50\,\mathrm{Hz})\ [\mathrm{m\,Hz^{-1/2}}]$ |
|---|---|---|
| Rugar, Mamin, and Guethner (1989) | fiber interferometer | $1.0 \cdot 10^{-13}$ |
| Smith, Pratt, and Howard (2009) | fiber interferometer | $1.6 \cdot 10^{-14}$ |
| Paolino, Sandoval, and Bellon (2013) | balanced homodyne interferometer | $1.4 \cdot 10^{-14}$ |

**Table 11.1:** Benchmark noise levels for low frequency detector electronics.

require a *vacuum can* (a can which shields the vacuum on the outside from non-vacuum compatible materials inside) housing the electronics. It turns out[17] that for low-frequency applications, it is actually quite feasible to run long well-shielded wires from the diodes through vacuum feedthroughs outside before performing the electronic conversion.

[17] Westphal 2016

We require that, for the proposed parameters, photon shot noise should be far below off-resonant thermal noise, and that electronic noise $S_{x\mathrm{el}}$ should be below the photon shot noise:

$$\sqrt{S_{x\mathrm{el}}} < \sqrt{S_{x\mathrm{sh}}} \ll \sqrt{S_{x\mathrm{th}}} = \sqrt{\frac{2\gamma}{m\beta\omega_0^4}} \approx 1.3 \cdot 10^{-14}\,\mathrm{m\,Hz^{-1/2}}.$$

Unfortunately the literature on low frequency detector electronics outside of the gravitational wave detector community (which works in an entirely different power regime) is quite sparse. A few relevant publications that explicitly focus on low frequency *displacement* performance *without optical cavities* are listed in table 11.1. However, comparing these numbers to recent publications that did not explicitly convert the detection noise to displacement indicates that much better performance should in principle be possible. For example, Stefszky et al. (2012) report shot-noise-limited measurements at 1 mW of power, which for our parameters puts the equivalent displacement PSD of the electronic noise into the regime of $10^{-16}\,\mathrm{m\,Hz^{-1/2}}$. Therefore, combining an ultra-stable interferometer with low-noise electronics and a sufficiently powerful and stable laser source to set a new benchmark for the measurement of displacement noise at audio-band frequencies poses a feasible side-goal in the development of the proposed experiment.

The investigation and development of detector circuits for the proposed experiment is currently performed by Hans Hepach[18] (University of Vienna) and is not a part of the author's work.

[18] Hepach 2015

Chapter 12

# Vibration isolation

The test mass is subject to additional external noise sources, in particular seismic noise of the environment, and mechanical backaction of the source-mass displacement. Therefore, there are two major requirements for the vibration isolation system of the proposed experiment. The first requirement is to sufficiently isolate the test mass against seismic and acoustic vibrations of the laboratory environment (and from other external sources). In this regard, the required isolation system is qualitatively very similar to typical isolation systems used for example in gravitational wave detection. However, the second requirement is conceptually different, as we also require vibration isolation of the test mass against a nearby modulated source mass. As we explained in section 7.4 on p. 78, if masses within vibration isolation chains are of similar magnitude, e.g. a suspended stage with a moving source mass and a suspended stage with a supposedly vibration-isolated test mass, the energy transfer between stages is close to maximal and therefore needs to be properly modeled.

In this chapter we start with the isolation requirements for the detection of gravity in a micromechanical system in section 12.1. We then give give an overview of the relevant elements and techniques for passive (section 12.2) and active (section 12.4) vibration isolation, where we dive into the details whenever relevant for the scheme that is proposed in section 12.3.

## Chapter contents

## 12.1 Isolation requirements

The vibration noise of the environment, $S_{x_\mathrm{E}}$, and the source-mass backaction, $S_{x_\mathrm{S}}$, are coupled through the mechanical support structure via the transfer functions $T_\mathrm{E}(\omega)$ and $T_\mathrm{S}(\omega)$, respectively. Specifically, from eqs. (5.15d) and (5.15g) on p. 36 and on p. 37 we have

$$S_{x\mathrm{E}}(\omega) = |\chi(\omega)|^2 \left|\left(\omega_0'^2 - \mathrm{i}\gamma'_\mathrm{sup}\omega\right) T_\mathrm{E}(\omega)\right|^2 S_{x_\mathrm{E}}(\omega).$$

Inserting eq. (5.15f) into eq. (5.15b), splitting the contributions of direct drive and gravity, eq. (5.21), and ignoring the other contributions yields

$$S_{x\mathrm{P}}(\omega) = d_\mathrm{S}^2 \frac{\pi}{2} |\chi(\omega_\mathrm{S})|^2 \left|\left(\omega_0'^2 - \mathrm{i}\gamma'_\mathrm{sup}\omega\right) T_\mathrm{S}(\omega)\right|^2 [\delta(\omega-\omega_\mathrm{S}) + \delta(\omega+\omega_\mathrm{S})],$$

$$S_{x\mathrm{G}}(\omega) = d_\mathrm{S}^2 \frac{\pi}{2} |\chi(\omega_\mathrm{S})|^2 \left(\frac{2GM}{d_0^3}\right)^2 [\delta(\omega-\omega_\mathrm{S}) + \delta(\omega+\omega_\mathrm{S})],$$

where the subscript $P$ now denotes the effect of a *parasitic* drive excitation. As we require to reach the thermal noise limit of the test mass, we need to compare these expressions to the test-mass thermal noise given in eq. (5.34) on p. 46,

$$S_{x\mathrm{th}}(\omega) = |\chi(\omega)|^2 \frac{2\gamma}{m\beta}.$$

In the original article (Schmöle et al. 2016) we compared both the drive backaction contribution $S_{x\mathrm{P}}$ as well as the environmental contribution $S_{x\mathrm{E}}$ to the thermal noise $S_{x\mathrm{th}}$. Here, we follow a different approach. We realize that the contributions of environmental noise and thermal noise scale with the integration time, while the contribution of the drive does not. Hence, the comparison we performed in the paper required the assumption of a specific integration bandwidth. In this thesis, we instead compare the contributions that naturally fall together: Both environmental noise and thermal noise have

continuous PSDs and can therefore be compared independent of integration time. The same is true for the gravitational drive and the parasitic backaction drive, which are both deterministic and possess delta-peaks at the same frequencies. In order to state general requirements that are independent of the integration time, we can therefore demand

$$S_{x\mathrm{E}}(\omega) \ll S_{x\mathrm{th}}(\omega) \quad \text{and} \quad S_{x\mathrm{P}}(\omega) \ll S_{xG}(\omega),$$

i.e. the environmental noise should be below the thermal noise and the parisitic drive should be below the gravitational drive. This yields

$$T_{\mathrm{E}}(\omega) \ll \left|\omega_0'^2 - \mathrm{i}\gamma'_{\mathrm{sup}}\omega\right|^{-1} \left(\frac{2\gamma}{m\beta}\right)^{1/2} S_{x_{\mathrm{E}}}^{-1/2}(\omega)$$

for the required environmental suppression and

$$T_{\mathrm{S}}(\omega) \ll \left|\omega_0'^2 - \mathrm{i}\gamma'_{\mathrm{sup}}\omega\right|^{-1} \frac{2GM}{d_0^3}$$

for the required source-mass motion suppression. A benefit to this approach is that the second requirement is now independent of the drive amplitude $d_{\mathrm{S}}$ and can be made independent of the mechanical quality $Q$ by a straightforward approximation: as seen before, in the regime of small forces we can approximate $\omega_0' \approx \omega_0$, and for a test-mass device that is limited by support losses, $\gamma'_{\mathrm{sup}} \approx \gamma$. This yields

$$\left|\omega_0'^2 - \mathrm{i}\gamma'_{\mathrm{sup}}\omega\right| \approx \omega_0 \left(\omega_0^2 + \omega^2/Q^2\right)^{1/2} \approx \omega_0^2,$$

where the second approximation holds as long as $Q \gg 1$ and the frequencies $\omega$ of interest are much smaller than $Q\omega_0$, which is trivially the case in the proposed experiment. Therefore the requirements read

$$T_{\mathrm{E}}(\omega) \ll \left(\frac{2\gamma}{\omega_0^4 m\beta}\right)^{1/2} S_{x_{\mathrm{E}}}^{-1/2}(\omega) \quad \text{and} \quad T_{\mathrm{S}} \ll \frac{2GM}{\omega_0^2 d_0^3}.$$

Of course, in a measurement scheme where technically only a single driving frequency $\omega_{\mathrm{S}}$ is of interest, these requirements only need to be fulfilled at said frequency and not for all $\omega$. We also note that by the above relation we can estimate the maximum tolerable residual environmental displacement noise directly at the test-mass stage, $S_{x_{\mathrm{E,T}}}^{1/2}(\omega)$, by setting $T_{\mathrm{E}}(\omega) := 1$:

$$S_{x_{\mathrm{E,T}}}^{1/2}(\omega) \ll \left(\frac{2\gamma}{\omega_0^4 m\beta}\right)^{1/2}.$$

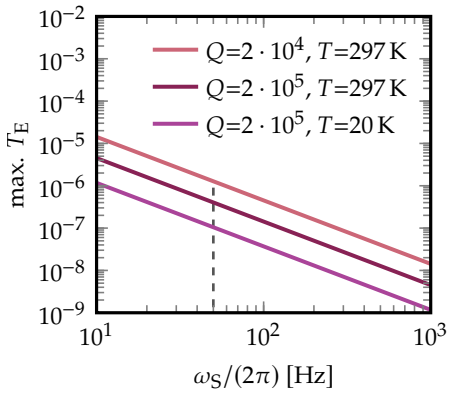


(a) Upper limit of environmental attenuation function $T_E$.

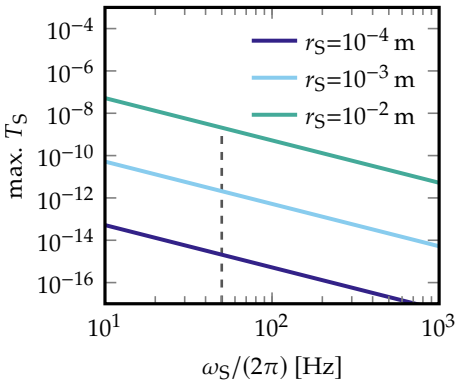


(b) Upper limit of source amplitude attenuation function $T_S$.

**Figure 12.1:** Upper boundaries for the transfer functions as a function of frequency-of-interest $\omega_S$.

From preliminary acceleration measurements we extracted a conservative value of $S_{x_E}^{1/2} \approx 10^{-8}\,\mathrm{m\,Hz^{-1/2}}$ in the relevant frequency band around 50 Hz (see fig. 12.5). For our chosen parameters (table 8.1 on p. 88) the upper boundaries for both transfer functions are shown in fig. 12.1. A measurement at 50 Hz and room temperature requires

$$T_E \ll 1.3 \cdot 10^{-6}, \quad T_S \ll 2.1 \cdot 10^{-12} \quad \text{and} \quad S_{x_{E,T}}^{1/2} \ll 1.3 \cdot 10^{-14}\,\mathrm{m\,Hz^{-1/2}}. \tag{12.1}$$

An isolation of the test-mass cantilever platform from the seismic noise even by more than six orders of magnitude is clearly within current state of the art. For example, a combination of multiple passive and actively controlled suspension stages in gravitational wave detectors routinely achieve a seismic isolation of $10^{-11}$ and better, even at lower frequencies. For our case, already a dual-stage passive spring-pendulum system should be sufficient to achieve the required levels of isolation at 50 Hz.[1] The second requirement seems to impose a more significant challenge, but one should bear in mind that we consider here the contribution of the source-mass displacement that is due to mechanical backaction on the support structure of the experiment. There are several strategies to minimize this. First, mechanical unbalance of the source-mass drive can be compensated for by having a second mass counter-moving against the first (see also section 10.1.3 on p. 121). Second, the source-mass drive platform can be physically separated from the test-mass cantilever platform. This requires a separate vibration-isolation (spring/pendulum) system, which couples to the test-mass cantilever platform only via the large mass of the vacuum tank that hosts the experiment. Finally, one can even envision a

[1] Matichard et al. 2015

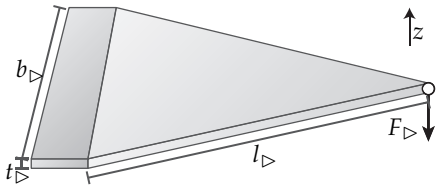


(a) Basic geometry of a triangular blade spring as considered in section 12.2.1.

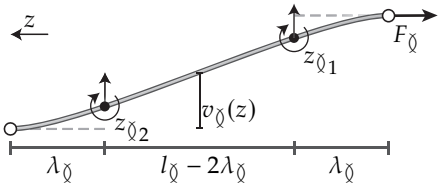


(b) Geometry and location of zero-moment points $z_0$ for the wire pendulum considered in section 12.2.2.

**Figure 12.2:** Illustrations showing the geometry and dimensions of blade springs (section 12.2.1) and wire pendulums (section 12.2.2).

complete mechanical isolation of the source mass by levitating and driving it in external fields.[2]

[2] Goodkind 1999

## 12.2 Passive vibration isolation elements

In this section we explain the passive vibration isolation elements that will be used in the proposed experiment and potential future iterations.

### 12.2.1 Blades

Intuitively, coil springs are the obvious candidate for realizing vertical springs, as they come in a huge variety of stiffnesses and materials and are linear over a large region of deflection.[3] Furthermore, they can serve as pendulums at the same time, thereby providing isolation in all spatial directions in a single element. However, due to their nature of being wound thin wires, coil springs typically possess a huge number of resonances directly above the fundamental mode frequency, which almost certainly lie within the relevant detection band. Instead, many high-performance isolation systems rely on triangular *blades*, which are solid pieces of metal and therefore have much higher eigenfrequencies above the fundamental modes than coil springs. The main problem with using solid springs, despite the requirement for a high yield strength material, is *creep noise*, a type of mechanical noise due to sudden microscopic stress release in the stressed material. This effect can be reduced significantly by artificially aging (i.e. annealing) the blade material.[4] One commonly found blade material in gravitational wave detector mirror suspensions is maraging steel (Marvel18).

[3] Winterflood, Blair, and Slagmolen 2002

[4] Beccaria et al. 1998

According to Coyne et al. (2007), "simplified bending" equations can be

used to calculate the vertical stiffness of a triangular blade as

$$k_{\triangleright} = \frac{E b_{\triangleright} t_{\triangleright}^3}{6 l_{\triangleright}^3} = \frac{F_{\triangleright}}{\alpha_{\triangleright} l_{\triangleright}^2} \quad \text{with} \quad \alpha_{\triangleright} := \frac{6 F_{\triangleright} l_{\triangleright}}{E_{\triangleright} b_{\triangleright} t_{\triangleright}^3},$$

where $l_{\triangleright}$, $b_{\triangleright}$ and $t_{\triangleright}$ denote the length, width and thickness of the blades (see fig. 12.2(a)), $E_{\triangleright}$ is the elastic modulus and $F_{\triangleright}$ is the force resulting from the weight of the payload (i.e. $F_{\triangleright} = m_{\triangleright} g$ where $m_{\triangleright}$ is the mass that is attached to the blade). Assuming a homogeneous stress distribution, the stress $\sigma_{\triangleright}$ on the loaded blade is given by

$$\sigma_{\triangleright} = \frac{6 F_{\triangleright} l_{\triangleright}}{b_{\triangleright} t_{\triangleright}^2} = \alpha_{\triangleright} E_{\triangleright} t_{\triangleright}.$$

As the spring constant scales in third order with the blade thickness $t_{\triangleright}$, we strive to make it as thin as possible to obtain a low eigenfrequency, yet large enough to avoid plastic deformation of the loaded blade. To this end we require that the stress $\sigma_{\triangleright}$ is a "safe" fraction $\xi_\sigma$ of the material yield strength $\sigma_{\max}$, $\sigma_{\triangleright} = \xi_\sigma \sigma_{\max}$, and hence

$$t_{\triangleright} \approx \left( \frac{6 F_{\triangleright} l_{\triangleright}}{b_{\triangleright} \xi_\sigma \sigma_{\max}} \right)^{1/2}.$$

From the above relations it is clear that a higher payload requires a larger width or thickness in order to keep the stress low, which again requires longer blades in order to retain a low stiffness $k_{\triangleright}$.

Treating the blades as a pure spring in the out-of-plane direction is a valid simplification, but neglects the possibility for additional mode-coupling due to the finite stiffness of the blades against transverse forces. An expression for the blade spring constant in the transverse direction was derived by Greenhalgh (2005) to be

$$k_{\trianglerighteq} = \frac{E_{\triangleright} b_{\triangleright}^3 t_{\triangleright}}{12 l_{\triangleright}^3} \epsilon_{\triangleright} \quad \text{with} \quad \epsilon_{\triangleright} = \ln(l_{\triangleright} / x_{\trianglerighteq}) + x_{\trianglerighteq} / l_{\triangleright} - 1,$$

where $x_{\trianglerighteq}$ denotes the distance of the displacement point from the blade tip, which is usually chosen on the order of a few millimeters to centimeters.

In order to maximize the in-plane stiffness of the loaded blade, one usually chooses to have a completely flat profile in the loaded state. With this requirement, there is a simple argument as to why the optimal unloaded blade shape has to be circular. We assume that the blades, modeled as triangular cantilevers of constant thickness, become flat under load. We know that the mechanical moment on every point in the blade has to be proportional to the distance from the blade tip. Since the width of a triangular blade is proportional to the

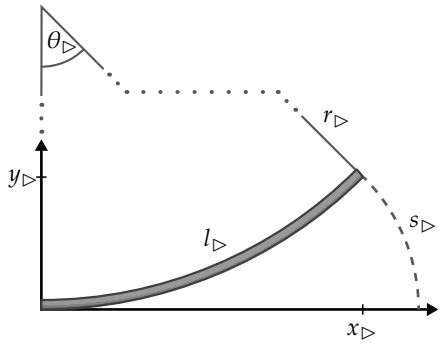


(a) Blade bent along an arc with radius $r_\triangleright$ and angle $\theta_\triangleright$. The origin is located in the root of the blade and the blade tip has coordinates $x_\triangleright$ and $y_\triangleright$.

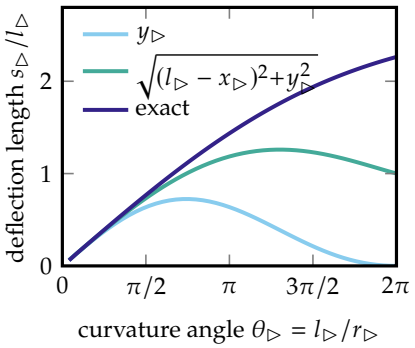


(b) Numeric solution for the deflection length integral and two approximations. Both approximations are applicable for angles below $\pi/2$ but fail for stronger curvatures.

**Figure 12.3:** Determination of the blade curvature parameters $\theta_\triangleright$ and $r_\triangleright$ from a given blade deflection path length $s_\triangleright$. The function shown in the right-hand plot has to be used inversely for this purpose, which can only be achieved numerically.

distance from the blade tip as well, it follows that the stress is homogeneous over the entire blade. Therefore the relative change in length of every volume element has to be constant over the blade, which naturally leads to a circular load-free blade-shape. Note that this argument is subject to debate and for very thick blades, parabolic shapes appear to be the more accurate model.[5]

[5] Coyne et al. 2007

The path length of the blade deflection is uniquely given by the spring constant and the attached payload via Hooke's law. However, the curvature of the blade required to yield a certain deflection towards the flat state is not directly clear, as the blade has to be deflected radially (with respect to its radius of curvature) at every point of the process. As shown in fig. 12.3(a), we start deriving the relation between deflection $s$ and radius of curvature $r_\triangleright$ by observing that

$$\theta_\triangleright = \frac{l_\triangleright}{r_\triangleright}, \quad \cos\theta_\triangleright = \frac{r_\triangleright - y_\triangleright}{r_\triangleright} \quad \text{and} \quad \tan\frac{\theta_\triangleright}{2} = \frac{y_\triangleright}{x_\triangleright},$$
$$\Leftrightarrow \quad r_\triangleright = l_\triangleright/\theta_\triangleright, \quad y_\triangleright = l_\triangleright(1-\cos\theta_\triangleright)/\theta_\triangleright \quad \text{and} \quad x_\triangleright = l_\triangleright \sin\theta_\triangleright/\theta_\triangleright,$$

for the horizontal ($x_\triangleright$) and vertical ($y_\triangleright$) coordinates of the spring blade relative to the origin of the blade. This allows us to express the differential elements of

both coordinates as

$$\mathrm{d}x_{\triangleright} = \frac{\partial x_{\triangleright}}{\partial \theta_{\triangleright}}\,\mathrm{d}\theta_{\triangleright} = \frac{l_{\triangleright}}{\theta_{\triangleright}^2}\left(\theta_{\triangleright}\cos\theta_{\triangleright} - \sin\theta_{\triangleright}\right)\,\mathrm{d}\theta_{\triangleright},$$
$$\mathrm{d}y_{\triangleright} = \frac{\partial y_{\triangleright}}{\partial \theta_{\triangleright}}\,\mathrm{d}\theta_{\triangleright} = \frac{l_{\triangleright}}{\theta_{\triangleright}^2}\left(\cos\theta_{\triangleright} + \theta_{\triangleright}\sin\theta_{\triangleright} - 1\right)\,\mathrm{d}\theta_{\triangleright}.$$

We can therefore rewrite the differential length element $\mathrm{d}s_{\triangleright}$ as

$$\mathrm{d}s_{\triangleright}^2 = \mathrm{d}x_{\triangleright}^2 + \mathrm{d}y_{\triangleright}^2 = l_{\triangleright}^2\,\theta_{\triangleright}^{-4}\left(\theta_{\triangleright}^2 - 2\cos\theta_{\triangleright} - 2\theta_{\triangleright}\sin\theta_{\triangleright} + 2\right)\,\mathrm{d}\theta_{\triangleright}^2,$$

and find the length $s_{\triangleright}$ of the curve that is described by the blade tip when loading radially as

$$s_{\triangleright} = \int_0^{s_{\triangleright}} \mathrm{d}s_{\triangleright} = l_{\triangleright}\int_0^{l_{\triangleright}/r_{\triangleright}} \theta_{\triangleright}^{-2}\left(\theta_{\triangleright}^2 - 2\cos\theta_{\triangleright} - 2\theta_{\triangleright}\sin\theta_{\triangleright} + 2\right)^{1/2}\,\mathrm{d}\theta_{\triangleright}.$$

The solution of this integral is plotted in fig. 12.3(b) along with two approximations. This allows to numerically find the required blade radius of curvature $r_{\triangleright}$ for a given deflection $s_{\triangleright}$ and hence for a given eigenfrequency (due to the direct relation between displacement under load and frequency, cf. eq. (9.2) on p. 98).

### 12.2.2 Wire pendulums

The common choice for springs in the horizontal plane are wire pendulums with a payload-dependent wire thickness. For payloads of several hundred kilograms, these pendulums need to have diameters up to centimeters and effectively become *flexure rods*, but are in principle still governed by the same equations as silica wires of a few hundred micron diameter.

We roughly outline the derivation of the restoring force of a flexure rod spring; for a complete derivation of the forces associated with flexure rods, see Smith (2004). Starting with the beam equation

$$\left(E_{\langle\rangle} I_{\langle\rangle}\frac{\mathrm{d}^2}{\mathrm{d}z_{\langle\rangle}^2} - F_{\langle\rangle}\right) - \frac{\mathrm{d}^2 v_{\langle\rangle}}{\mathrm{d}z_{\langle\rangle}^2} = 0,$$

where $v_{\langle\rangle}(z_{\langle\rangle})$ is the orthogonal beam deflection as a function of the axial coordinate $z_{\langle\rangle}$ (see fig. 12.2(b)), $E_{\langle\rangle}$ is the Young's modulus, $I_{\langle\rangle}$ is the area moment of inertia and $F_{\langle\rangle}$ is the axial load, one finds a general solution

$$v_{\langle\rangle}(z_{\langle\rangle}) = c_{\langle\rangle_1} + c_{\langle\rangle_2} z + c_{\langle\rangle_3}\cosh\kappa_{\langle\rangle} z + c_{\langle\rangle_4}\sinh\kappa_{\langle\rangle} z, \quad \kappa_{\langle\rangle} = \sqrt{\frac{F_{\langle\rangle}}{E_{\langle\rangle} I_{\langle\rangle}}}.$$

The constants $c_{\langle}$ are then determined by setting the boundary constraints in form of the displacements and rotation angles of the beam at the end points. This allows computation of the forces and moments acting on the end points for a given deflection and rotation. Interestingly, one finds that a shear and moment at each end is equivalent to a pure shear load at the distance

$$\lambda_{\langle} = \frac{1}{\kappa_{\langle}} \tanh(\kappa_{\langle} l_{\langle}/2)$$

from the end points, where $l_{\langle}$ is the length of the pendulum. This allows to treat the flexure rod analogously to a pin-ended pendulum[a] connecting the virtual *zero-moment* points $z_{\langle 1} = \lambda_{\langle}$ and $z_{\langle 2} = l_{\langle} - \lambda_{\langle}$. The according lateral stiffness is

$$k_{\langle} = \frac{F_{\langle}}{l_{\langle} - 2\lambda_{\langle}}.$$

Additionally, the wire yields a fundamental spring in the axial direction creating a restoring force against axial compression and expansion. Its stiffness $k_{\asymp}$ is simply given by the ratio of wire cross-section $A_{\langle} = \pi(d_{\langle}/2)^2$ (with diameter $d_{\langle}$) to length $l_{\langle}$,

$$k_{\asymp} = E_{\langle} \frac{\pi(d_{\langle}/2)^2}{l_{\langle}}.$$

When choosing the diameter of a wire, it should be as small as possible to minimize the restoring force due to deformation and the effective wire-shortening through larger values of $\lambda_{\langle}$. On the other hand it should be as large as necessary to ensure that the payload is securely supported and no plastic deformation occurs as part of the regular swinging motion. As seen above, we require that the stress is a fraction $\xi_\sigma$ of the maximum tensile strength $\sigma_{\max}$ of the wire material, $\sigma = \xi_\sigma \sigma_{\max}$. The stress of a wire under load is simply given by $\sigma = F_{\langle}/A_{\langle}$, and therefore choosing

$$d_{\langle} \approx 2 \left( \frac{F_{\langle}}{\pi \xi_\sigma \sigma_{\max}} \right)^{1/2},$$

ensures that the wires will not plastically deform or rip under load.

What we did not account for here are violin modes, which behave similar to the strings of musical instruments and are typically located at several hundred Hertz[6]. Their presence imposes the restriction to make the wires neither several meters long nor too thick, as this would cause lower frequency resonances.

[6] Crooks 2002

[a] The equivalence holds up to rotational stiffness terms (Smith 2004), which we did not consider in the current model.

### 12.2.3 Advanced isolation concepts

There are currently a number of approaches to increase the performance of passive vibration isolation systems even further. Several of these approaches have already been successfully demonstrated in experimental applications and even commercial systems.

A breakthrough concept of passive vibration isolation came with the deployment of *negative stiffness* or *anti-spring* mechanisms acting parallel to regular springs. The effective spring constants (and therefore eigenfrequencies) can be much lower in these systems. Implementations of anti-springs can be found, e.g., in geometric anti-spring (GAS) filters[7] for vertical isolation and inverted pendulums[8] for horizontal isolation. GAS filters consist of sets of buckled blade springs and can be tuned to low frequencies by adjusting the mounting angles and positions of the blades. In inverted pendulums, a mass that is supported by vertical rods provides an unstable quadratic potential (which is tunable via adjustment of the payload), while the restoring force of the deflected rods accounts for the regular spring. Isolation systems based on GAS filters and inverted pendulums have been demonstrated in the AEI prototype, where natural frequencies of 0.25 Hz and 0.05 Hz respectively were achieved.[9] They are also planned for the cryogenic gravitational wave detector KAGRA[10]. Passive isolation systems that rely on anti-spring effects are available commercially.[11]

7) Cella et al. 2002

8) Takamori et al. 2007

9) Wanner 2013; Westphal et al. 2012

10) Fujii et al. 2016

11) Platus 1996, 1999

While commercial systems lack the desired performance for our proposed experiment, custom anti-spring isolation systems require careful planning and adjustment. A system that yields a positive effective spring constant as a result of poor adjustment would naturally move away from the set point, posing an immediate threat to the mechanical components. We therefore chose not to incorporate custom anti-spring systems into the proposed isolation scheme. From our analysis presented in section 12.3, we are confident that we can reach the required levels with conventional spring systems.

Another passive vibration isolation concept of increasing interest is based on *nonlinear* springs. Every passive isolation system will yield a mechanical amplification when driven on resonance. The novel approach there is to deploy springs with non-proportional amplitude responses in order to counteract potentially dangerous resonant excitations. For an overview of this topic, see e.g. Ibrahim (2008). Finally, linear state-of-the art springs still undergo development. Examples include *Euler springs* and *self-damped pendulums*[12], which yield stiffness values competing with anti-spring systems, though naturally lower eigenfrequencies usually come at the expense of convenience.[13]

12) Dumas et al. 2004

13) Blair et al. 2012, sec. 11.4

### 12.2.4 Suspension thermal noise

We have touched upon the vibrational noise caused by thermal excitation of mechanical eigenmodes in the context of the test-mass device background noise and the geometric readout noise in sections 5.7.1 and 11.2.6 on p. 45 and on p. 138. Naturally, similar effects occur in the mirror suspensions of gravitational wave detectors[14] as well as in the mirror material[15]. In fact, the most significant classical noise contributions in current gravitational wave detectors stem from thermal noise in both mirror suspension and in mirror coatings and substrates.[16] Thermal effects also pose the main hurdle for other optical precision measurements involving large mirrors on soft springs, e.g. the detection of photon backaction.[17] For this reason, extensive research is focusing on the development of new coatings with extremely high mechanical qualities[18] and cryogenic vibration isolation systems[19]. A rough estimate on the magnitude of suspension thermal noise in the proposed experiment is performed in section 12.3.3 as part of the test-mass isolation proposal.

[14] Gillespie and Raab 1993, 1994, 1995

[15] Reid and Martin 2016

[16] Blair et al. 2012

[17] Neben et al. 2012

[18] Cole, Zhang, et al. 2016; Reid and Martin 2016

[19] Flaminio and KAGRA collaboration 2016

### 12.2.5 Damping

As seen in section 7.1 on p. 68, the transmissibility of an isolation stage that is damped relative to its support[b] follows a $\omega_0^2/\omega^2$-falloff between the resonance frequency and a transition frequency $\omega_0^2/\gamma = Q\omega_0$, i.e. for $\omega_0 < \omega < Q\omega_0$. Above this transition frequency it follows a $\gamma/\omega = \omega_0/(Q\omega)$ curve, which is linked to the so-called "damping shortcut" effect. In that case the relative damping rate $\gamma$ between the isolation stage and its support creates a coupling that dominates the otherwise (i.e. in the non-damped case) steeper falloff of the transmissibility at higher frequencies.

Naturally, a $\omega^{-2}$-falloff is more efficient than a $\omega^{-1}$-falloff for isolation performance. One would therefore expect that high mechanical qualities are desired when designing a vibration-isolation system. However, high values of $Q$ for isolation stages come with practical downsides. Most importantly, the amplification of environmental displacement around the mechanical resonance frequency $\omega_0$ can cause significant RMS movement for high values of $Q$. In most practical cases, one artificially *lowers* the mechanical quality, thereby trading in a steeper falloff (i.e. a more superior isolation at higher frequencies) for improved practicality.

To a certain extent, when designing multi-stage isolation systems it is still possible to retain the isolation performance of high-$Q$ springs, while at the same time avoiding low-frequency resonances. This is possible if eigenmodes

[b] Note that while inertial damping, i.e. damping with respect to an inertial frame, would be highly desirable, it is somewhat impractical as this requires the existence of a heavy *inertial* object. In the context of vibration isolation, this could only be an object that is isolated to *a similar or higher degree* than the system of interest.

of the system can be fully damped by applying direct damping exclusively at the first (i.e. topmost) stage.[20] This way, one sacrifices just one order of inverse power of frequency, while effectively damping all resonances.

[20] Aston et al. 2012

A second reason for designing a multi-stage isolation system in a way that damping only needs to be applied at the topmost stage is the inherent noise of external damping. For passive eddy-current damping, typically arrays of coated neodymium or samarium-cobalt magnets on the stage are used in conjunction with aluminum or copper blocks on the supporting structure. These magnets are prone to 50 Hz electric grid noise and exhibit thermal noise as well as Barkhausen noise.[21] In the case of active damping (see also section 12.4), feedback has to be applied based on a noisy error signal. However, as long as there are further undamped elements down the isolation chain, the additional noise from passive or active damping can usually be sufficiently suppressed.

[21] Plissi, Torrie, Barton, et al. 2004

### 12.2.6 Effect of a large intermediate mass

In the actual experimental setup, both the source-mass isolation chain as well as the one for the test mass will be supported by a common suspension point, a heavy vacuum tank (see also fig. 7.6 on p. 79). As long as its eigenmodes have frequencies far above the frequency of interest $\omega_0/(2\pi) \approx 50\,\mathrm{Hz}$, the intermediate mass can be considered as a rigid body that is coupled to the outside environment by an additional spring with stiffness $k_{\mathrm{ex}}$. We may now ask how this additional mass is affecting the total transmissibility. We build a toy-model by following eq. (7.3) on p. 71 for the case of three masses and add an additional spring $k_{\mathrm{ex}}$ connecting $m_2$ to a fixed environment. The transmissibility of this system is then computed to be

$$\begin{aligned}\tilde{x}_3/\tilde{x}_0 = k_{01}k_{12}k_{23}\Big\{&\left(k_{23}-m_3\omega^2\right)\\ &\cdot\left[\left(k_{01}+k_{12}-m_1\omega^2\right)\left(k_{12}+k_{23}+k_{\mathrm{ex}}-m_2\omega^2\right)-k_{12}^2\right]\\ &+k_{23}^2\left(-k_{01}-k_{12}+m_1\omega^2\right)\Big\}^{-1},\end{aligned}$$

where we neglected the damping terms for simplicity. This function is plotted in fig. 12.4 for multiple values of spring constants and masses. We directly see that above a certain frequency (roughly the resonance of the external spring) the transmissibility from source mass to test mass is independent of the external spring stiffness. As long is this frequency is lower than the frequency of interest, there is no gain from having a softer coupling from the intermediate mass to the environment (while, of course, there will be an advantage for the environmental isolation of the test mass from having a softer coupling to the environment). What does have a significant impact though is the size of the intermediate mass, which should be chosen as high as possible to

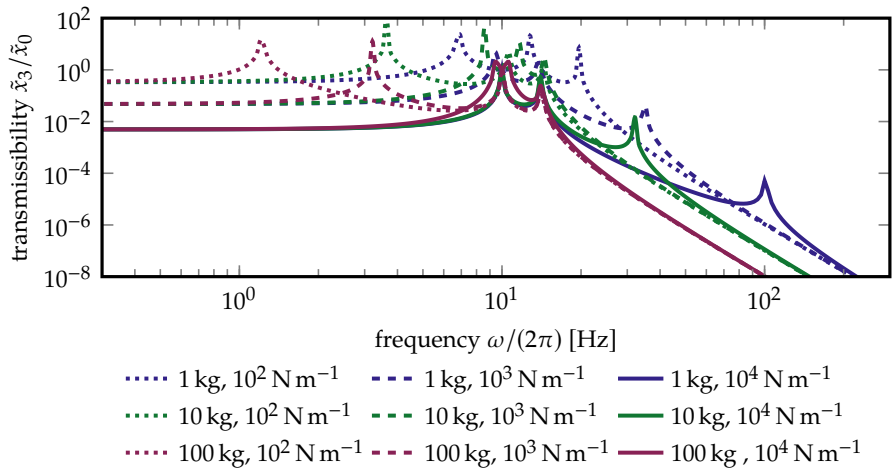


**Figure 12.4:** Transmissibility from a source mass ($x_0$) to a test mass ($x_3$) in a three-mass-chain, where the central mass $m_2$ is large and coupled to the outside with an additional spring $k_{ex}$. The values for $m_2$ and $k_{ex}$ are given in the plot legend. Further, we chose $k_{01} = k_{12} = k_{23} = 100\,\mathrm{N\,m^{-1}}$ and $m_1 = m_3 = 1\,\mathrm{kg}$. Increasing the central mass shifts its resonance to lower frequencies and decreases the effect of the stiffness $k_{ex}$ at higher frequencies.

minimize the transmissibility in the relevant frequency band. We also note that above the various additional resonances caused by an intermediate large mass, neglecting the mass will effectively lead to overestimating the transmissibility. It therefore does not compromise our conservative performance estimations.

## 12.3 Proposed vibration-isolation chain

In this section we propose a scheme that should allow to reach the vibration isolation requirements stated in section 12.1. The system is supposed to operate in an environment we describe in section 12.3.1. It is composed of a pre-isolation system (section 12.3.2) that supports the entire vacuum system (section 12.3.6). Inside of the vacuum system, separate isolation chains are in place for the test (section 12.3.3) and the source mass (section 12.3.4).

The concept of the proposed setup is inspired by the systems used in advanced LIGO.[22] The requirements for our experiment differ in two major aspects. First, not only the environment, but also the source mass act as input for vibration noise, and the latter needs to be accounted for with an individual isolation subchain. Second, our main experimental interest is focused on a small frequency band around the drive frequency, and our environmental noise isolation requirements are less stringent. Therefore, compared to the highly sophisticated systems used in aLIGO, a simpler system both in terms of development and operation should fulfill our requirements.

[22] Aston et al. 2012

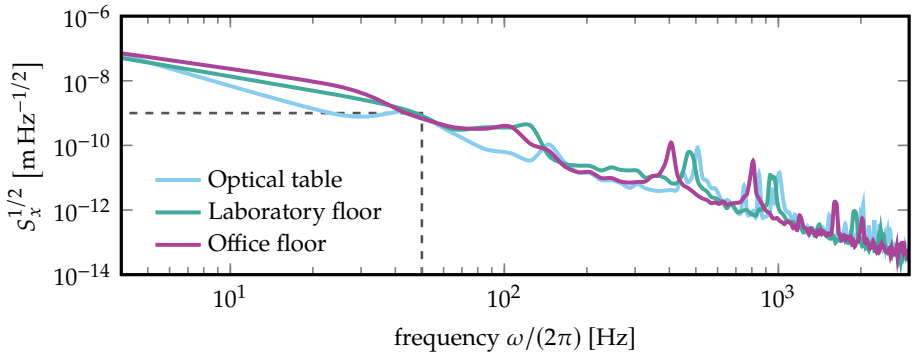


**Figure 12.5:** Laboratory background displacement PSDs extracted from acceleration sensor data, converted using eq. (12.2). Each line is the square root of the mean of ten successively measured PSDs. The first and second peaks likely correspond to internal sensor resonances that were shifted by ambient temperature or the mechanical properties of the mounting surface.

As we are currently planning to run the experiment with the gravitational drive in horizontal direction, horizontal isolation should be the main concern. Due to coupling between modes, in particular tilt coupling, vertical isolation is being considered as well.

### 12.3.1 Laboratory background noise

Typically, experiments with low-noise requirements in the single- to triple-digit Hertz range are placed on concrete slabs (often called *technical slab*) which are separated from the slab for the laboratory building.[23] In addition, facilities housing sensitive experiments are often placed at remote locations, sufficiently far away from areas of high population density. For example, the measurement of $G$ by Gundlach and Merkowitz (2000) was performed in a former cyclotron cave at the University of Washington. We design the vibration isolation system in a way that can cope with the "standard" environment of a typical laboratory (in our case an early 20th century building located adjacent to a heavy-traffic road and several tram lines).

[23] Blair et al. 2012; Fritschel et al. 2001

We performed some preliminary noise measurements at multiple points within the building (fig. 12.5). The used acceleration sensor has a bandwidth from single digit to two-thousand Hertz. We obtain a typical displacement noise on the level of $10^{-9}\,\mathrm{m\,Hz^{-1/2}}$ at 50 Hz, although the measurement was likely limited by sensor noise. While these values certainly compatible with our design goals for vibration isolation, we note that typically not high average displacement noise PSDs are the main concern in precision experiments, as achieving one or two additional orders of vibration isolation is a comparably minor effort. Instead, due to the long integration time, single transient events,

as they often occur in this type of environment, can potentially render hours of data unusable. In addition, as both test and source mass are suspended on long pendulums, sub-Hertz drifts, e.g. due to rocking of the building, can cause relative positioning drifts that may cause systematic errors in measurements. Further experimental investigation will show how severe these issues are and if the proposed measurement is feasible in the given environment, or otherwise identify another, more suited location.

### 12.3.2 Pre-Isolation

We are currently planning to install one initial isolation stage outside of the vacuum system. As seen in section 12.2.6, a heavy vacuum tank that is connected to the environment with an effective soft spring can add low-frequency resonances, but will largely reduce the transmissibility above resonance. From our experience, standard optical tables typically have tilt modes around 1 Hz that are underdamped, which could cause alignment issues with the test and source-mass pendulums described below. We therefore choose an active vibration isolation system by Herzan[24]. According to the specifications, this system should yield similar performance as heavy optical tables with stiffer springs, since the active feedback artificially increases the effective mass. It reaches a transmissibility of below 0.02 above 10 Hz and is less susceptible to changes in payload than passive systems. With the option to continuously monitor the sensor data one gains the possibility to detect significant vibrational disturbances already at the first isolation stage. The performance can in principle even be improved by the deployment of an additional sensor on the laboratory floor close to the platform in a feed-forward scheme.

[24] Herzan LLC 2016

### 12.3.3 Test-mass isolation

Motivated by eq. (12.1), we require around seven to eight orders of magnitude in horizontal isolation in the direction of interaction at 50 Hz. A similar number will be required in the transmissibility of vertical motion to horizontal motion, which are coupled via tilt degrees of freedom.[25] Following basic insights from previous experience, the suspension system should be designed with roughly similar masses of the individual stages and similar pendulum wire lengths to ensure that all modes are well observable (i.e. dampable) at the top stage. In the direction of the horizontal isolation requirement, the attachment points of the wires should be kept close to the center of mass of the respective stages, yielding low tilt frequencies and small horizontal-tilt coupling.

[25] Lantz et al. 2009

**Basic design.** We base the test-mass suspension design (fig. 12.6(a)) on the triple suspensions used in GEO 600[26] and advanced LIGO[27] (which are conceptually very similar). Between the topmost stage $T_0$ and the first suspended

[26] Plissi, Torrie, Husman, et al. 2000; Torrie 2001

[27] Robertson, Barton, et al. 2013

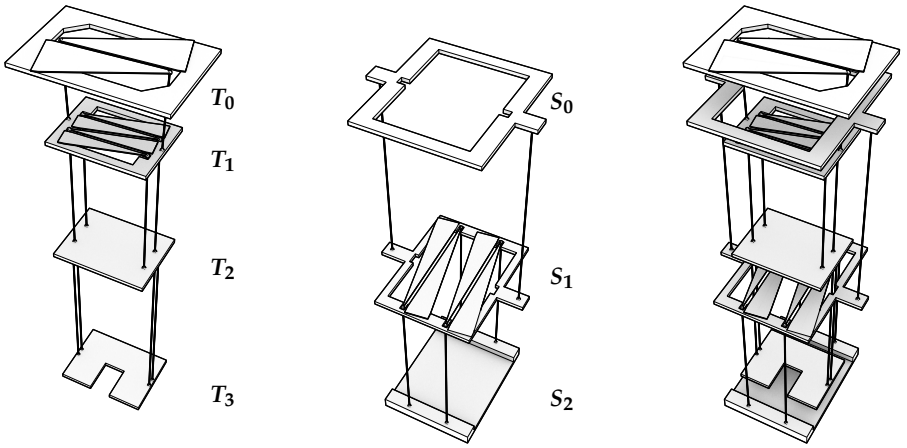


(a) Test-mass vibration isolation chain.

(b) Source-mass vibration isolation chain.

(c) Combined vibration isolation chains.

**Figure 12.6:** Proposed vibration isolation chain described in detail in section 12.3. The individual stages are designed such that a test and source-mass isolation chain share a vertical axis and the entire system fits into a vertically oriented cylinder of 500 mm diameter.

stage $T_1$ two blades and two pendulums provide an initial isolation that is quite insensitive to pitch (tilt) motion due to the small restoring force. A set of four blades and wires connects the first and the second suspended stage $T_2$, and a set of four wires connects the second and third stage $T_3$. The reason for choosing four wires instead of two is that active control as well as passive damping can be applied at $T_1$. At low frequencies the wires affect the lower stages similar to a marionette, so that alignment drifts can be compensated.[28]

[28] Robertson, Cagnoli, et al. 2002

Ideally, the blades are rotated such that a stage rotation caused by thermal drifts of the blade lengths is compensated, though naturally there is always a trade-off associated with the space taken by the blade arrangements. The electrical cabling and optical fibers required for the actual experiment can be run alongside the stages. They should be rigidly clamped at every individual stage while hanging loosely between stages to avoid mechanical shortcuts. The parameters for all stages of the test-mass suspension are listed in table 12.1.

The last stage of the test-mass isolation chain houses the interferometer and the test mass. One crucial aspect for the design of this stage is to place the test mass as close to the stage COM as possible. This will minimize coupling of stage tilt-motion into test-mass motion in the crucial DOF.

Positioning and control. For the first iteration of the experiment we estimate that the passive isolation performance will be sufficient (see below) and therefore no active control and isolation has to be deployed for the test-mass stage.

| | | $T_1$ | $T_2$ | $T_3$ | $S_1$ | $S_2$ |
|---|---|---|---|---|---|---|
| $m$ | [kg] | 6 | 4 | 4 | 6 | 10 |
| $\vec{j}$ | [g m$^2$] | ( 20 20 40 ) | ( 13 13 27 ) | ( 13 13 27 ) | ( 20 20 40 ) | ( 34 34 67 ) |

| | | $T_0 \to T_1$ | $T_1 \to T_2$ | $T_2 \to T_3$ | $S_2 \to S_1$ | $S_1 \to S_0$ |
|---|---|---|---|---|---|---|
| # | | 2 | 4 | 4 | 4 | 2 |
| $h_{\wr}$ | [mm] | 200 | 350 | 500 | 450 | 550 |
| $\vec{p}_{\mathrm{up}}$ | [mm] | ( 0 ±122 −2 ) | ( ±30 ±95 −2 ) | ( ±10 ±114 −2 ) | ( ±155 ±59 −2 ) | ( 0 ±180 −2 ) |
| $\vec{p}_{\mathrm{lo}}$ | [mm] | ( 0 ±114 2 ) | ( ±30 ±114 2 ) | ( ±10 ±114 2 ) | ( ±155 ±59 2 ) | ( 0 ±180 2 ) |
| $d_{\wr}$ | [$\mu$m] | 920 | 490 | 260 | 700 | 800 |
| $l_{\triangleright}$ | [mm] | 250 | 180 | | 302 | |
| $b_{\triangleright}$ | [mm] | 110 | 40 | | 60 | |
| $t_{\triangleright}$ | [$\mu$m] | 1250 | 940 | | 1400 | |
| $\lambda_{\wr}$ | [mm] | 9.9 | 5.0 | 3.8 | 7.5 | 8.4 |
| $l_{\wr}$ | [mm] | 220 | 361 | 508 | 515 | 517 |
| $k_{\wr}$ | [N m$^{-1}$] | 343 | 55.9 | 19.6 | 78.4 | 98.1 |
| $k_{\asymp}$ | [kN m$^{-1}$] | 583 | 101 | 36.5 | 144 | 187 |
| $k_{\triangleright}$ | [N m$^{-1}$] | 430.8 | 178.5 | | 190 | |
| $k_{\trianglerighteq}$ | [kN m$^{-1}$] | 739 | 83.1 | | 70.5 | |

**Table 12.1:** Parameters of the test and source-mass isolation stages. The upper table lists the masses and inertial moments of the stages, while the properties of the springs are shown in the lower table. # denotes the number of elements, $h_{\wr}$ denotes the height of the wire projected onto the vertical axis and the $\vec{p}$-vectors refer to the locations of the zero-moment points. The values listed in the last block are derived from the given parameters. We assumed annealed steel as the blade material with $E_{\triangleright} = 188\,\mathrm{GPa}$ (Matichard et al. 2015) and steel (Fort Wayne 2017) for the wire material with $E_{\wr} = 193\,\mathrm{GPa}$, and a maximal stress fraction $\xi_\sigma = 1/3$.

However, we plan to account for sufficient space so that we can upgrade the system with the small-footprint integrated optical motion sensors and actuators currently used at the AEI 10 m prototype facility.[29] For the time being, the set point of the suspension can be indicated with mechanical pointers and targets or with light pointers and quadrant diodes as shown in section 10.2 on p. 124.

[29] Westphal 2016

Performance of test-mass isolation. We implemented the vibration isolation model derived in section 7.3 on p. 71 in a Mathematica notebook and derived

the transmissibility curves shown in fig. 12.7.[c] As we gained access to the MatLab "state space" model for the advanced LIGO triple suspension[30], we compare both models for the parameters listed in table 12.1. In horizontal direction ($x \to x$), the results agree to a reasonable qualitative extend, though it is not entirely clear how the small modal frequency deviation between both models can be explained. For the vertical direction ($z \to z$), the models agree strikingly well at lower frequencies and follow a very similar fall-off curve for higher frequencies. It is not yet clear how the deviations between both models can be explained, or which of the two models is more accurate. The model presented here might include conceptual errors, but at the same time, the LIGO model had to be heavily modified to fit our geometry and can not be considered experimentally justified anymore. While this dissonance is subject to current investigations, it is safe to assume that the presented geometry will suffice to reach the desired seven to eight orders of magnitude in horizontal transmissibility attenuation around 50 Hz.

[30] Robertson, Barton, et al. 2013

**Thermal noise of test-mass suspension.** We perform a rough estimate of the test-mass suspension thermal noise. The basic concept of this noise source is explained in section 12.2.4. Here, instead of analyzing all effective modes of the entire isolation chain, we focus on the last pendulum of the chain and apply the for the PSD of a single pendulum, $S_{x\wr}$, which is given by González (2000) as

$$S_{x\wr}(\omega) \approx \frac{4}{\beta\omega^2}\,\Re\left[\mathrm{i}\omega\,\frac{1 - j_x/(F_{\wr\!\wr} p_{\mathrm{lo}z})}{F_{\wr\!\wr}(1-\omega^2/\omega_+^2)(1-\omega^2/\omega_-^2)/l_{\wr\!\wr}}\right],$$

with the thermodynamic beta $\beta$ and the complex eigenfrequencies

$$\omega_+ \approx F_{\wr\!\wr} p_{\mathrm{lo}z}/j_x(1+\mathrm{i}/Q_+) \quad \text{and} \quad \omega_- \approx F_{\wr\!\wr}/(m l_{\wr\!\wr})(1+\mathrm{i}/Q_-),$$

[c] Originally it was planned to realize the simulations in COMSOL with finite elements, using the **Multibody Dynamics** module, which allows to model compound systems of bodies connected with springs and joints of different types. However, it turned out that achieving convergence of such models is by no means trivial due to the close-to-zero stiffness in some degrees of freedom (e.g. pitch stiffness in the $T_1$ stage). Another problematic point is the huge difference in displacement amplitudes, corresponding to the more than ten orders of magnitude in required suppression between source and test mass. One approach is to increase the numerical working precision to a degree where the simulation of even simple models consumes many hours of computation time. Alternatively, one can make simplifications to the simulation which essentially make the results less precise than the outcome of a simplified analytical model, such as the one presented in section 7.3. In consequence, we abandoned the initial plan of a full vibration isolation model with finite element simulation.

[d] Some commercial active pre-isolation systems can not properly act against motion *on the isolated plattform*, depending on the configuration of the feedback circuit. Here, we design our passive isolation system such that we can in principle perform the experiment without additional pre-isolation.

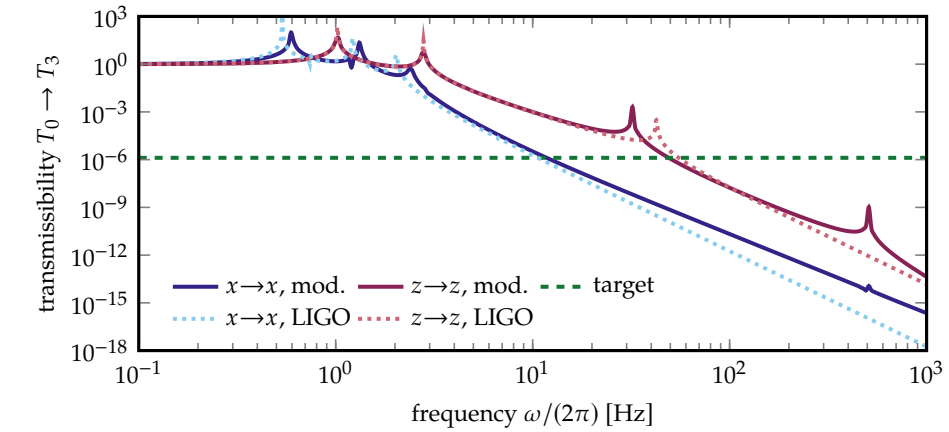


(a) Spectral range from 0.1 Hz to 1000 Hz.

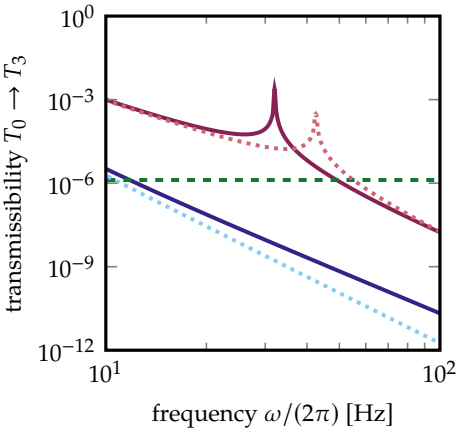


(b) Spectral range from 10 Hz to 100 Hz.

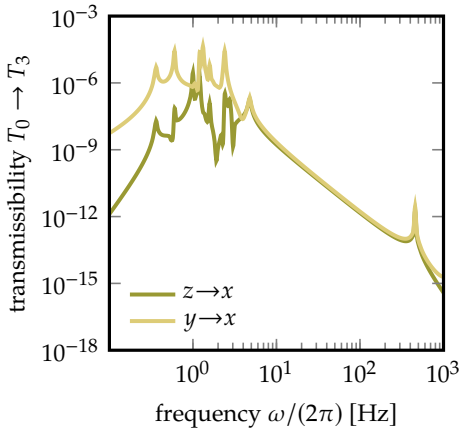


(c) Estimation of tilt-coupling.

**Figure 12.7:** Simulated performance of test-mass isolation chain $T_0 \to T_1 \to T_2 \to T_3$ using both the model described in section 7.3 on p. 71 (*mod.*) as well as the advanced LIGO state space model. The target transmissibility is shown for the combined system of preisolation and test-mass isolation, while the former has not been included into the transmissibility curves.[d]

which incorporates different quality factors $Q_\pm$ for both eigenfrequencies. Assuming a suspension quality $Q_\pm = 10^5$, this puts the thermal noise around $\omega/(2\pi) = 50\,\mathrm{Hz}$ at $S_{x_i}^{1/2} \approx 8 \cdot 10^{-16}\,\mathrm{m\,Hz^{-1/2}}$. Even though our assumptions are rather conservative (the mechanical quality of wire suspensions is typically higher than $10^5$ (Goßler 2004)), this is well below the crucial level of $1.3 \cdot 10^{-14}\,\mathrm{m\,Hz^{-1/2}}$ (see eq. (12.1)).

### 12.3.4 Source-mass isolation

Given the expected performance of the test-mass platform (section 12.3.3) and the effect of the vacuum tank acting as a large intermediate mass (section 12.2.6), an attenuation in transmissibility of five to six orders of magnitude should suffice to comfortably reach the total target transmissibility of twelve orders of well below $10^{-12}$ given in eq. (12.1).

Basic design. Compared to the test-mass isolation chain, we chose a simpler design with just two platforms, one of them with blades for vertical isolation (fig. 12.6(b)). For the drive motion the isolation scheme has to work "backwards". We hence deploy two wires (for improved tilt isolation) between the topmost and the intermediate suspended stage ($S_0$ and $S_1$) and a set of four blade-wire pairs between the intermediate suspended and the bottommost stage ($S_1$ and $S_2$).

The critical design aspect is the requirement that the moving COM of the source-mass drive should be located as closely as possible to the COM of the source-mass stage in order to prevent excessive excitation of tilt motion due to the drive. In consequence, the effect of the source-mass suspension needs to be convoluted with the test-mass suspension, as both share the same vertical axis (with a small horizontal offset as the test mass and the source mass are separated by a few millimeters). In addition, achieving the same COM height of the penultimate test mass and source-mass stages will require additional "offset"-masses.

The current selection of parameters is listed in table 12.1. The total pendulum length and fixation height of the source-mass pendulum chain should be similar to that of the test-mass chain. In that way a change of separation of the masses due to tilt of the entire experimental apparatus is avoided. Further, as demonstrated in section 12.2.6, a comparably heavy drive platform might lead to a smaller effective amplitude of the motion induced by the drive due to reduced recoil. A heavier stage implies the need for thicker and thereby stiffer blades for vertical isolation, which implies a trade-off, leading (potentially) to the existence of an optimal stage mass. We currently investigate this effect.

If we want to suppress the effect of the drive amplitude even further, two additional measures come into mind: First, one might think of an active compensation scheme for the drive motion in order to reduce the drive recoil. However, such a scheme would require compensation against another mass (i.e. the vacuum tank), which in consequence would itself be subject to an mechanical excitation. From this short argument, an active compensation scheme would, if anything, worsen the situation. Second, one might deploy *resonant dampers* or *differential dampers*.[31] These are systems composed of a mass and a (tunable) well-damped spring, supposed to absorb the vibration

[31] Gras et al. 2015

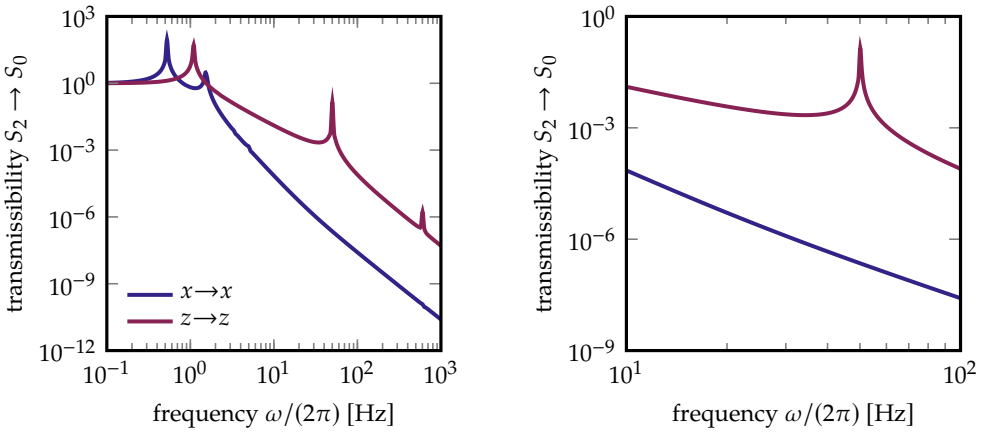


(a) Spectral range from 0.1 Hz to 1000 Hz

(b) Spectral range from 10 Hz to 100 Hz

**Figure 12.8:** Simulated performance of the source-mass isolation chain $S_2 \to S_1 \to S_0$.

energy of excitations in certain frequency bands when strategically mounted at specific locations in the isolation chain, preferably antinodes. Due to the added complexity to the overall vibration isolation scheme we decided against the addition of resonant dampers in the current design, but keep it as an (relatively easy applicable) option for the future.

An outstanding question is whether the heat generated by the drive engine will necessitate an additional dissipation scheme. In this case, one might think of thermoelectric cooling or sufficiently decoupled cryogenic cold fingers that provide a cold bath.

Performance of source mass isolation. In order to properly estimate the performance of the source-mass chain and the amplitude that is fed into the test-mass suspension, one would have to calculate the *compliance* of the source-mass chain, where the force is generated at the lowest element. This can in principle be done with the method presented in section 7.3, but increases the complexity of the computational implementation. Instead, as a rough estimate, we calculate the transmissibility of the source-mass chain in the same way we estimated the one of the test-mass isolation chain (fig. 12.8). With the proposed geometry we reach a comforting six orders of magnitude in horizontal attenuation, well within the design goal.

### 12.3.5 Total vibration-isolation performance

In order to derive an estimate for the total transmissibility from source mass to test mass, we consider two different estimation methods. First, we multiply the $6 \times 6$ matrices of both individual transmissibility functions of the source and

test-mass isolation chains presented in sections 12.3.3 and 12.3.4, including all cross-terms, as shown in section 7.4 on p. 78. By doing this we ignore all effects of coupling and backaction between both individual systems, as well as the effect of the large intermediate mass (the vacuum tank), which itself is situated on an active isolation stage (section 12.3.2). We can roughly account for the effect of the tank and the active stages by a broadband attenuation factor that we conservatively set to 0.1.

The second method is to combine the source mass and test-mass chain into a single chain by flipping the source-mass stage "upside-down". We may then treat the active platform as a heavy intermediate stage that is coupled to the (rigid) environment by a spring with an effective frequency that we set to be at 1 Hz. This model neglects the active attenuation and obviously does not properly incorporate the static offset of equilibrium coordinates due to the Earth's gravitational field, but it includes backaction effects.

Both models are compared in fig. 12.9 and confirm that the requirements posed in section 12.1 can be met. However, if it should turn out that the experiment can only be performed vertically, the proposed isolation system can not produce the required transmissibility of $10^{-12}$ between source and test mass. Nevertheless, there is still reason to be optimistic, as both approaches do not properly account for the effective performance of the active pre-isolation. Depending on the implementation, the assumed attenuation factor of 0.1 could be a severe underestimation. Further, the mass of 300 kg that we assumed for the actively damped vacuum tank stage could effectively be increased by the active gain, depending on the feedback loop.

### 12.3.6 Vacuum system

In this last section we give a brief overview of the currently planned vacuum system.

Geometry. The geometry of the proposed isolation system requires the volume of a vertical cylinder of roughly 500 mm in diameter and 1200 mm in length, with sufficient additional space to fit tools and with the possibility for visual inspection during the assembly. One method to achieve this would be the deployment of a "walkable" UHV system, similar to most gravitational wave detectors where the vacuum chambers fit entire people in sterile suits. Due to their size and stable mounting, these systems are typically quite versatile and can be used for several generations of experiments. However, because of the cost and the facilities required to operate such a massive tank, we instead opt for a much smaller, cylindric system. The advantage of such a system is that its shell can be removed to completely expose the vibration isolation system, thereby making it accessible for assembly and adjustments.

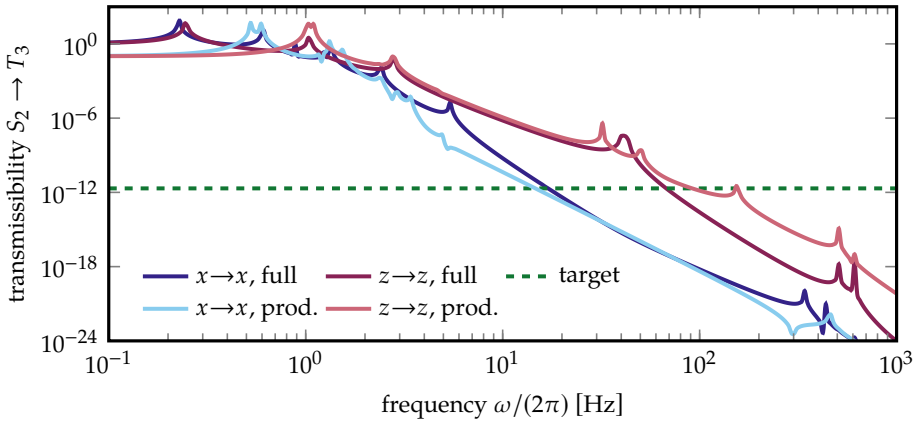


(a) Spectral range 0.1 Hz to 1000 Hz

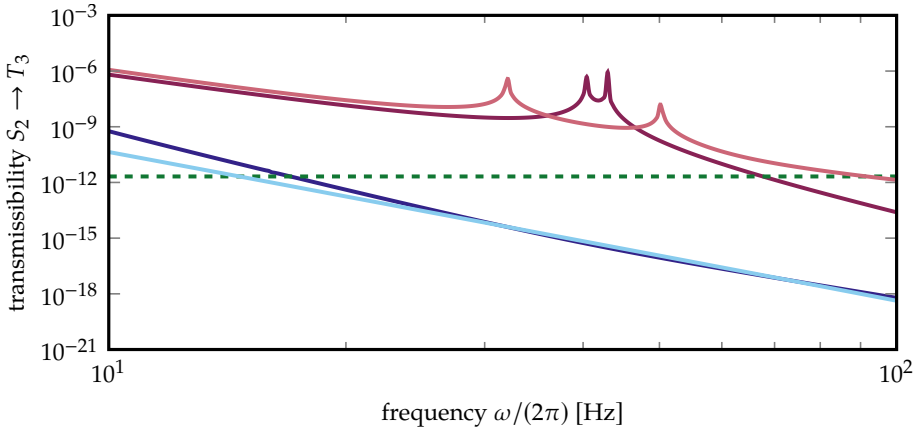


(b) Crop, spectral range 10 Hz to 100 Hz

**Figure 12.9:** Performance of full isolation chain $S_2 \to S_1 \to (S_0 = T_0) \to T_1 \to T_2 \to T_3$ estimated in two ways: By roughly combining both systems as if they were a single chain ("full") and by matrix multiplication of the individual transmissibilities ("prod.").

Given the "hanging" nature of the vibration isolation, it needs to be suspended at its highest point. It therefore makes sense to construct the tank around a relatively high base plate that provides all the necessary attachment points for the vibration isolation pendulums. The vessel can then by extended downwards with a cylindric piece. This makes it possible to open the chamber by lowering the cylinder, thereby completely exposing the suspension system and allowing to work at a convenient height. If the total height of the experiment is limited, e.g. by a low ceiling, one might even imagine dividing the cylindric part into two pieces which can be attached and detached successively. The majority of feedthroughs as well as the pumps can then be mounted at

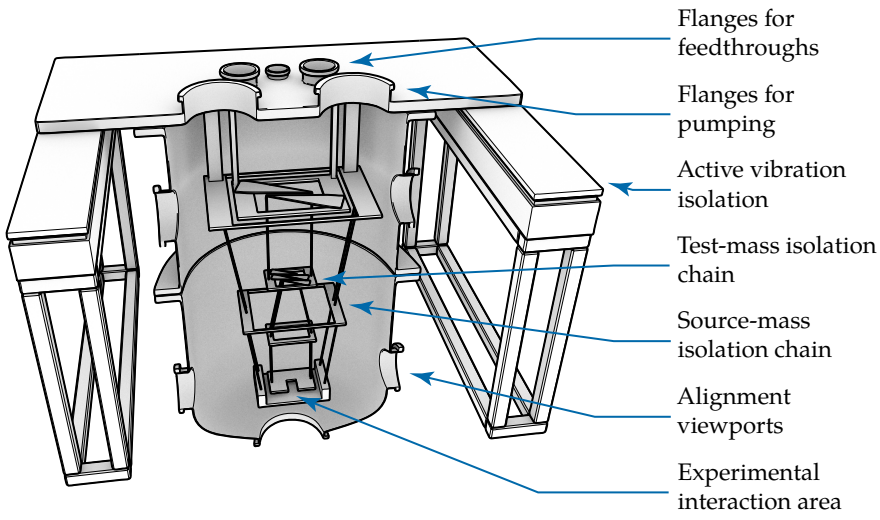


**Figure 12.10:** Currently planned vacuum system (not to scale). The base plate and chamber cylinder have been halved vertically for illustrative purposes.

the non-moving base plate.

Acces and viewports. In addition the the flanges on top, a number of large flanges should be provided on the circumference of the cylinder. These can act as viewports or provide access to work on the suspension system without the need to strip the entire (heavy) cylinder part. One large flange at the bottom of the cylinder could be fitted with a window to provide an additional vertical line of sight. Generally it is advantageous to add additional versatility flanges for unforeseeable modifications that become necessary during the commissioning phase.

Vacuum gaskets. The required background pressure is set by two factors: first, the mechanical quality of the test-mass device (see section 9.3.1 on p. 100), and second, the coupling between source mass and test mass by gas molecule scattering (see section 8.4 on p. 87). For the current geometry, we can avoid a degradation of the mechanical quality through background gas already with pressures below $10^{-2}$ hPa, which in our experience is trivial to achieve with standard high-vacuum components. From our estimation for the effect of force transfer by gas molecules, we require around $10^{-8}$ hPa to assure that this effect is smaller than the gravitational drive. Reaching such pressures generally requires ultra-high-vacuum components and heating of the vacuum system when pumping from ambient pressure.

The main difference between HV and UHV components is the type of sealing used and the flanges that connect the individual pieces of the vacuum

system. With high pressure gradients, water molecules can diffuse through the elastomer orings that are typically used in HV vacuum seals, which limits the ultimate pressure. UHV systems therefore use metal seals (typically copper) instead of rubber. The main disadvantage of UHV metal seals is that they get permanently deformed under the pressure of the flanges and therefore can be only reused a few times. While flanges with small diameters sealings are relatively cheap, large sizes (above 400 mm) usually have to be custom-made and easily go up to hundreds of Euros for a single seal. Alternatively, for large diameters one can use differential elastomer seals[32], where two concentric seals per flange are used. When the volume between the seals is held at rough vacuum by a separate pumping system the pressure gradient over the inner seal is small, leading to minimal diffusion. While this system requires wide flanges with two grooves, the seals are reusable, making it more suitable for a vacuum system that needs to be opened on a regular basis. In this design, an optional metal wire loop can be used to create a seal that allows to reach the UHV regime of $10^{-10}$ hPa and below.

[32] Westphal et al. 2012

**Pumps.** A roughing pump and, at lower pressures, a turbo pump are used to evacuate the large volume. If the optical readout system is compatible with higher temperatures, the evacuation process could be sped up significantly by baking out the tank. An alternative to remove residual water molecules from the metal walls is illumination with strong UV light.[33] This could yield several advantages over baking as it does not expose crucial components to potentially damaging amounts of heat, and would significantly reduce the time until the isolation system reaches thermal equilibrium after pumping.[e]

[33] Berman 1996

As both the roughing pumps and turbo pumps are based on mechanical gas-transportation and hence cause added vibrations in the tens to several hundreds of Hertz range, they must not run while measurements are performed. To maintain the ultra-high vacuum during measurements, an additional, non-mechanical pump has to be deployed. One possibility is to use ion pumps or titanium-sublimation pumps. They have no lubricants or moving parts, but involve strong magnetic fields and currents[34] (around 40 A). Alternatively, a non-evaporable getter pump can be used, which is an entirely passive pump that works by metallic surface sorption of gas molecules.[35] In addition to a large pump with an inlet in a wall of the vacuum tank, one might also consider a trap close to the test mass that would locally reduce the background pressure. Such a local pump could be formed by either a much smaller sorption element, or a cryogenic cold-trap.

[34] Hablanian 1997

[35] Benvenuti and Chiggiato 1993; Li, Hess, et al. 1998

[e] We are currently investigating if strong UV lighting could cause threatening effects in the proposed setup, e.g. by creating additional charges or causing excessive heating in the birefringent optical elements such as calcite and $YVO_4$.

We note that even if the mechanical pumps are switched off during measurements, they could still impose additional challenges for the experimental setup. While spinning up to their working frequency turbo pumps sweep the entire lower frequency range starting from DC, which might trigger crucial resonances and cause misalignment. Similar issues could be caused by the sheer amplitude of typical roughing pumps, which for this reason in vibration-sensitive experiments are commonly decoupled from the laboratory environment, e.g. by means of stacked layers of granite plates and rubber feet.

## 12.4 Active isolation

We expect that the presented passive isolation chain will demonstrate sufficient performance for the proposed experiment. However, if the isolation requirements become stronger in future iterations of the experiment, e.g. for significantly smaller source masses, one will likely have to add active vibration isolation in addition to a passive system. Here, we briefly touch upon some solutions to read out residual motion of isolation platforms and to compensate this via active feedback.

From the sensing side, we note that we can roughly convert acceleration spectral densities $S_{\ddot{x}}$ to displacement spectral densities $S_x$ and vice-versa via

$$S_x^{1/2}(\omega) \approx S_{\ddot{x}}^{1/2}(\omega)/\omega^2, \tag{12.2}$$

given that we neglect the effects of damping. Due to the inverse square frequency falloff, at high frequencies accelerometer sensors become quite potent displacement measurement devices, even if the acceleration measurement is limited by (relatively flat) electronic noise. Accordingly, at lower frequencies direct measurements of velocity or displacement can yield much better noise performance.

Surprisingly, most off-the-shelf accelerometers are not even sufficient to resolve the vibrational background noise in a regular laboratory. Specialized piezoelectric accelerometers can reach sensitivities of $10\,\mathrm{ng\,Hz^{-1/2}}$ at 10 Hz, corresponding to $2.5 \cdot 10^{-11}\,\mathrm{m\,Hz^{-1/2}}$.[36] The bandwidth of such devices is then typically limited to below 100 Hz, whereas less sensitive accelerometers are available up to tens of kilohertz. Another method of measuring acceleration in these acoustic low-frequency bands is through induction, specifically by sensing the motion of a permanent magnet (that is attached to a relatively heavy test mass) by the voltage that it induces in an electric coil. This is a common approach in commercial seismometers as these voltages can typically be generated and determined with comparably low noise. Converting spectral densities of typical seismometers and geophones, e.g. the Nanometric Trillium T240 and Geotech GS-13 used in the advanced LIGO intermediate isolation

[36] Meggitt Sensing Systems 2009

plattforms, yields noise levels between $10^{-12}\,\mathrm{m\,Hz^{-1/2}}$ and $10^{-13}\,\mathrm{m\,Hz^{-1/2}}$ at 10 Hz.[37] The disadvantage of these devices is that they can hardly be made high-vacuum compatible and therefore need to be housed in specially made air tanks (*vacuum cans*) if they have to be placed inside of vacuum systems.[38]

[37] Abbott, Adhikari, et al. 2002; Matichard et al. 2015

[38] Coyne et al. 2007

Specifically in the case of gravitational wave detectors, several types of active elements are used in combination. To understand the working principle based on actuation on multi-stage isolation pendulums, we have to recall two major effects. First, at comparatively low frequencies, noise typically comes with higher amplitudes, which requires less sensor performance to resolve but higher feedback powers to compensate, thereby causing more feedback noise. Second, due to the characteristic high-frequency falloff of passive vibration isolation, actuations at early stages in the chain can compensate for low-frequency vibrations in later stages, while high-frequency actuations are strongly attenuated. As an example, we consider the quadruple pendulum mirror suspensions used in advanced LIGO,[39] an isolation system with a target noise of $10^{-19}\,\mathrm{m\,Hz^{-1/2}}$ at 10 Hz. Here the topmost stage motion is sensed by shadow flag sensors integrated with electromagnetic actuation coils[40] (*BOSEM*) that reach sensing noise levels around $10^{-10}\,\mathrm{m\,Hz^{-1/2}}$.[f] Intermediate stages are actuated with smaller coils in the 1 Hz to 10 Hz range and not directly sensed, while the bottommost stage is sensed by the main optical interferometric readout in the high frequency regime and actuated by electrostatic drives, both of which obviously have to yield noise less than the target sensitivity of $10^{-19}\,\mathrm{m\,Hz^{-1/2}}$ in the higher frequency regimes (> 10 Hz). As actuation forces applied between the well isolated test mass and the seismically noisy environment potentially couple noise and hence reduce the isolation performance, each quadruple pendulum is accompanied by a nearly identical *reaction chain*. The masses in the reaction chain then serve as an inertially quiet recoil masses for the actuation and the respective actuation elements can be placed between the according stages of main chain and reaction chain without increased environmental noise coupling. Of course, a substantial effort in low-noise control electronics is necessary to collect the signals of more than ten input sensors and combine them into a vibration model that is then fed back onto more than twenty actuators each limited with specific band pass filters to its respective frequency regime.[41]

[39] Robertson, Cagnoli, et al. 2002

[40] Aston 2011; Carbone et al. 2012

[41] Matichard et al. 2015

[f] Interferometric sensors have been proposed to replace shadow sensors in the next generation of vibration isolation suspensions, as they could reduce the readout noise by more than an order of magnitude (Aston 2011; Speake and Aston 2005).

Part IV

# Discussion and outlook

A brief outlook on future possible applications of the discussed apparatus as both a precision measurement device for the gravitational constant $G$ as well as an experiment interfacing quantum mechanics and gravity is presented in chapter 13. The last chapter, chapter 14, concludes with the current status of the technical development and open problems.

"If that statement starts to chill you after a couple of moments' consideration, then don't be alarmed. A feeling of intense and crushing religious terror at the concept indicates only that you are still sane."

---

Watchmen
Alan Moore

Chapter 13

# Further developments

Demonstrations of a gravitationally driven displacement of a micromechanical system through a millimeter-scale source mass serve as a major milestone for small-force sensing. There are several ways to improve the sensitivity of the currently planned test-mass device even further. As the ratio between the Newtonian signal and the Brownian force noise scales favorably with mechanical quality $Q$ (eq. (13.1)), the most promising one is to transition to a cryogenic scheme in order to both decrease the thermal noise and to increase $Q$. Schemes based on magnetic levitation could yield drastically higher mechanical quality through their strongly suppressed environmental coupling.[1] These improvements could open up interesting application areas for our scheme.

[1] Cirio, Brennen, and Twamley 2012; Romero-Isart, Clemente, et al. 2012

On the one hand, high-precision measurements of the gravitational field of small source masses offer a completely different approach to determine Newton's constant, possibly less sensitive to systematic errors present in experiments with macroscopic source masses, which we analyze in section 13.1. On the other hand, combining the sensitivity to gravitational coupling between microsopic source masses with the ever growing ability to achieve quantum control over their center-of-mass motion might eventually lead to a completely new generation of experiments at the interface between quantum physics and gravity, which is discussed in section 13.2.

## Chapter contents



## 13.1 Measurement of the gravitational constant

As we pointed out in section 3.2.2 on p. 10, the uncertainty in the measurements of the gravitational constant is high and spans multiple standard deviations

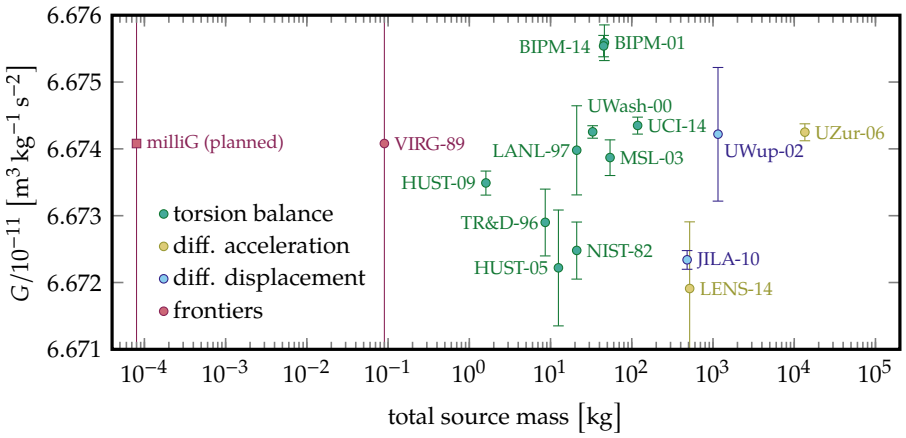


**Figure 13.1:** Experimental values of $G$ incorporated into the latest CODATA value (Mohr, Newell, and Taylor 2016) and sorted by the respective method, as well as the current and potentially new frontier for the smallest source masses. From left to right: milliG (Schmöle et al. 2016), VIRG-89 (Ritter et al. 1990) and with the CODATA identifiers HUST-09 (Luo et al. 2009; Tu et al. 2010), TR&D-96 (Karagioz and Izmailov 1996), HUST-05 (Hu, Guo, and Luo 2005), LANL-97 (Bagley and Luther 1997), NIST-82 (Luther and Towler 1982), UWash-00 (Gundlach and Merkowitz 2000), BIPM-14 (Quinn, Parks, et al. 2013), BIPM-01 (Quinn, Speake, et al. 2001), MSL-03 (Armstrong and Fitzgerald 2003), UCI-14 (Newman et al. 2014), JILA-10 (Parks and Faller 2010), LENS-14 (Rosi et al. 2014), UWup-02 (Kleinevoß 2002), UZur-06 (Schlamminger et al. 2006).

of individual experiments. Many potential systematic flaws arise from the large spatial dimensions of the experiments, including inhomogeneities in the macroscopic source masses due to manufacturing limitations, inaccuracies in the determination of the effective distance between test and source masses due to, for example, temperature fluctuations, and nonlinear effects as well as suspension noise in the typical pendulum fiber suspensions. In addition, long integration times require a detailed understanding of all long-term systematics in these experiments. Figure 13.1 shows an overview over all measurements of $G$ that have been incorporated into the latest determination of the CODATA recommended value[2],

[2] Mohr, Newell, and Taylor 2016

$$G = 6.674\,08(31) \cdot 10^{-11}\,\mathrm{m^3\,kg^{-1}\,s^{-2}}, \quad \Delta G/G = 4.7 \cdot 10^{-5},$$

as a function of the source mass size. The figure also shows the current record for the measurement of a gravitational field from a small source mass (VIRG-89) as well as the *milliG* experiment proposed in this thesis. According to Gillies and Unnikrishnan (2014), when the dependence of the measured value for $G$ is plotted against the total source mass for a selection of higher-precision experiments, one might even think of interpreting a power-law dependency

into the data. Clearly, despite gravitational forces being much weaker in a microscopic system than in decimeter to meter-scale setups with much larger masses, the prospect of entering a hitherto unexplored regime of source masses for gravitational measurements is very attractive, even if it may not reach competitive precision.

Our approach involves a centimeter-scale experimental architecture, a microscopic source mass and short integration times of only hours. When compared with the common measurements of $G$, this combination yields a very small overlap of systematic effects, since the small volumes enable a better control of positioning and density inhomogeneities of the masses as well as of temperature fluctuations. All components can be defined in a clean microfabrication process and are in principle small enough to even perform tomography and identify inhomogeneities and cavities in the substrates and materials. Also, the scheme does not rely on long fibers twisted in nonlinear regimes. In addition, short integration times may allow for a systematic study of the influence of fluctuations of other spurious external forces that give rise to systematic errors in long-term experiments.

A remaining challenge is to achieve a measurement precision that is competitive with experiments involving macroscopic source masses, as new potential systematic errors arise from the determination of the effective modal and gravitational mass and nonlinear effects due to the gravitational pull on the test mass (see section 9.2.2 on p. 98). In addition, due to the comparably high frequencies and small masses, the gravitational effects in the proposed system are much weaker. We may briefly estimate the performance of the milliG proposal if thermal noise limits the signal-to-noise performance. This comparison is not necessarily fair, as thermal noise in conventional measurements is always overshadowed by other sources of uncertainty. However, it provides an insight for the ultimate precision limit. Comparing the effect of the Newtonian contribution (eq. (5.22a) on p. 41) to the thermal noise (eq. (5.34) on p. 46) yields

$$\left(\frac{P_{x\mathrm{G}}(\omega)}{P_{x\mathrm{th}}(\omega)}\right)^{1/2} = GM\left(\frac{\pi m\beta}{\gamma\Gamma}\right)^{1/2}\frac{d_\mathrm{S}}{d_0^3} = GM\left(\frac{mQT\beta}{2\omega_0}\right)^{1/2}\frac{d_\mathrm{S}}{d_0^3}, \tag{13.1}$$

which is independent of the drive frequency $\omega_\mathrm{S}$. We keep our previous parameters of 2 mm-diameter gold spheres for both the source and the test mass and an optimal drive amplitude $d_\mathrm{S} = 1.25\,\mathrm{mm}$, but assume cryogenic temperatures in a system with good vibration isolation ($\Theta = 20\,\mathrm{K}$). The latter has been studied and judged feasible for cryogenic third-generation gravitational wave detector designs.[3] We estimate a conservative value of $Q = 10^6$ and choose a reasonable test-mass frequency of $\omega_0/(2\pi) = 100\,\mathrm{Hz}$ to make the system less susceptible to systematic errors associated with lower frequencies, yielding a

[3] Punturo et al. 2010; Somiya 2012

hypothetical signal-to-noise optimum of

$$\left(\frac{P_{x\mathrm{G}}}{P_{x\mathrm{th}}}\right)^{1/2} \approx 2\,\mathrm{s}^{-1/2} \cdot T^{1/2}.$$

This is around 120 for an integration time of $T = 1\,\mathrm{hour}$, and 1500 for $T = 1\,\mathrm{week}$, slowly approaching a regime that is competitive with existing high-precision experiments to measure $G$. One straight-forward way to improve these numbers is to increase the size of the masses, which will both boost the gravitational signal and decrease the thermal cantilever noise. For example, using 10 mm radius spheres instead of 1 mm would push the signal-to-noise ratio to $(P_{x\mathrm{G}}/P_{x\mathrm{th}})^{1/2} \approx 55 \cdot 10^3$ after 1 hour of integration. We need to point out that in this scenario, achieving the optimal drive amplitude of over 10 mm at 100 Hz might be unfeasible, as analyzed in chapter 10 on p. 119, and all residual noise, such as readout noise and vibrational noise, need to be constrained to a considerably lower thermal noise level than before as well. In summary, even though a micromechanical system will likely not be able to compete with current measurements of $G$ in the near future, it is still a worthwhile investigation as it opens up a mass regime that has been completely unaccessible to previous setups.

## 13.2 Towards quantum source-masses

The two main fundamental theories of modern physics, quantum theory and gravity, individually withstood a huge number of tests. Specifically, quantum superposition has been demonstrated, for example, using orbital angular momentum of photons up to hundred quantum numbers[4], microampere current states carrying up to $10^6$ electrons[5], collective spin degrees of freedom of $10^{12}$ rubidium atoms[6], large organic molecules[7] and vibrational degrees of freedom of mechanical resonators composed of up to $10^{15}$ atoms[8]. In general relativity, we find, next to the variety of lab-based experiments discussed in section 3.2 on p. 9, the measurement of gravitational waves from binary pulsars[9] and in gravitational wave observatories[10] or tests of the Lense-Thirring effect using satellites[11] and laser ranging[12].[a] However, today, physics finds itself in a peculiar situation. Despite the fact that the predictions of both quantum theory and general relativity are extremely well confirmed by experiment, interfacing these two theories still belongs to one of the outstanding big challenges of modern science. Notwithstanding the conceptual and mathematical hurdles in writing down a full quantum theory of gravity, the number of available experiments that probe the interface between quantum physics and gravity is also extremely sparse – thus far, all of the laboratory scale experiments above

4) Fickler et al. 2012

5) Friedman et al. 2000; Wal 2000

6) Julsgaard, Kozhekin, and Polzik 2001

7) Arndt, Nairz, et al. 1999; Gerlich et al. 2011

8) O'Connell et al. 2010; Palomaki et al. 2013

9) Hulse and Taylor 1975; Taylor and Weisberg 1982

10) Abbott, Abbott, Abbott, et al. 2016

11) Everitt et al. 2011

12) Ciufolini and Pavlis 2004

a) For a more complete overview of tests of general relativity, see e.g. Will (2006).

have, at most, been using quantum systems as test masses in external gravitational fields, with source masses ranging from several-kilo heavy objects to the entire earth. Therefore, we may legitimately ask: What happens if we put a gravitational source mass in a quantum superposition state and what would be the gravitational field of such a state?

The question about the gravitational field of a quantum spatial superposition was discusssed already by Feynmann at the 1957 Chapel Hill conference[13]. He suggested a Gedankenexperiment in which such a mass configuration would attract a second mass, thereby generating entanglement through gravitational interaction. Estimating the practicality of an experiment to test gravitational entanglement, we may ask for the time that it would take to generate such entanglement in a configuration with two masses, one of them being in a spatial superposition. Using a straight-forward calculation[14], the entanglement rate $\Gamma_{\text{ent}}$, which in this scenario is equivalent to a decoherence rate, can be estimated as

[13] DeWitt and Rickles 2011, p. 250

[14] Aspelmeyer 2017

$$\Gamma_{\text{ent}} = \frac{GM^2}{\hbar d^3} d_\psi \Delta x_\psi .$$

Here, $d_\psi$ is the superposition displacement of the source masses, $\Delta x_\psi$ is the width of the test-mass wave packet, and $d$ is the COM separation. Both masses $M$ are chosen to be identical. We set the material to be gold, the masses to be spheres with a diameter of 2 mm located at a surface distance of 100 $\mu$m, the superposition size to $d_\psi = 100\,\text{nm}$ and the test mass to be in the COM ground-state of a harmonic trap with $\omega = 50\,\text{Hz}$, i.e. $\Delta x_\psi = \hbar^{1/2}(M\omega)^{-1/2}$. This yields an entanglement rate $\Gamma_{\text{ent}} \approx 3\,\text{Hz}$, so entanglement would be generated on a scale of less than a second. Unfortunately, today's experiments are still far away from reaching comparable numbers of spatial superpositions for such massive objects. Similar coherence times have only been achieved for spatial superpositions of large organic molecules[15] or BECs[16] up to a few thousand amu, while experiments approaching the relevant mass regime have much shorter coherence times, such as 120 $\mu$s for a micromechanical resonator with an effective mass of 48 pg[17] or 7 ps for the collective motion of $10^{16}$ diamond atoms. Obviously, achieving quantum control over the motion of sufficiently massive objects while at the same time keeping the experimental sensitivity to their gravitational forces – which is needed for establishing quantum systems as gravitational source mass – is not within reach at this point in time. However, in this context, our micromechanics platform presented in this thesis can be seen as a top-down approach towards designing such future experiments. The lowest masses and shortest timescales over which gravitational coupling can be observed will be an important benchmark for both mass and coherence time of future quantum experiments. In the most optimistic scenario, the combination

[15] Juffmann et al. 2012

[16] Müntinga et al. 2013

[17] Palomaki et al. 2013

of force sensitivity and coherence time will eventually enable the quantum regime of gravitational source masses.

Chapter 14

# Conclusion

We have introduced a micromechanical method to measure gravitational coupling between small masses. Current state-of-the-art technology should allow for a proof-of-concept demonstration for objects on the scale of millimeters and tens of milligrams, which already improves the current limit for sensing the gravitational field of a small source mass by three orders of magnitude.

We divide this chapter into two parts: A brief summary of the current state of the project and the outstanding challenges (section 14.1), and an outlook for the near future of the experiment (section 14.2).

## Chapter contents



## 14.1 Current status

At the time of writing, the proposed experiment undergoes heavy development. The theoretical model of the detection scheme, which is at the heart of this thesis, leaves few open questions of direct relevance for the near future. Our work is now mainly focused on the four main components – test mass, source-mass drive, optical readout and vibration isolation – of the experimental implementation.

### 14.1.1 Status of the relevant theory

In this thesis we have developed a scheme to calculate the contributions of all foreseeable forces and fundamental noise-sources in a driven harmonic oscillator measurement. The estimation of the effect of nonlinear force contributions and the proper inclusion of distance-dependent statistical noise components are ongoing efforts.

Further, we have presented a new framework to estimate the transmissibility of passive vibration-isolation chains. Due to its generality, this method can in principle be applied to arbitrary systems with few modifications. We currently extend the framework to account for additional effects of thin suspension wires, i.e. restoring forces on rotational degrees of freedom and higher-order violin modes.

### 14.1.2 Test-mass status

Throughout this thesis we have established routines to characterize and tune the frequencies and modes of test-mass devices using finite-element simulations. These simulations can account for a range of additional effects, such as the local absorption of incident readout power and stress due to the gravitational background field. Further, we have investigated the effects of damping by residual gas molecules and by soft clamping materials, which allows us to formulate geometric requirements for the experimental assembly in order to achieve an optimal mechanical quality of the test mass.

There are a few promising candidates for test-mass substrates and first working devices are expected by mid-2017. A few open questions still require further investigation. Compensating the displacement magnitude of the gravitational pull could require slight redesigns of the interferometer, and it is not entirely clear if more complex device geometries will be needed in order to counteract the potential degradation of mechanical quality through the attachment of larges masses.

### 14.1.3 Source-mass status

Our investigations lead to a set of requirements for the source-mass drive engine. The most promising system that meets our needs is an actuator based on a flexure-guiding system (fig. 10.4(a) on p. 126). At the time of this writing, first prototypes are tested (fig. 14.1(a)) and iterated (fig. 14.1(b)). Preliminary simulations give enough reason to be optimistic that this system will be able to achieve a reasonable amplitude (i.e. at least 1 mm peak-to-peak) at 50 Hz.

Open questions primarily concern the dissipation of heat generated by the drive engine (as the drive itself needs to be vibrationally decoupled) and the life times that can be achieved. Both can be tested and optimized once

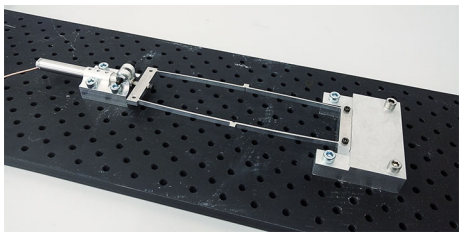

(a) Current source-mass drive design with a length of 200 mm, driven with a piezo-actuator. This design already yields an actuation of 1 mm (peak-to-peak) at 50 Hz.

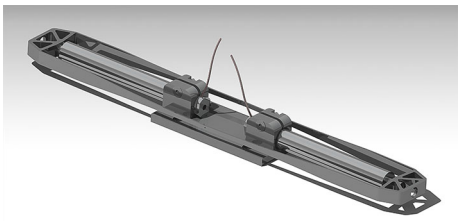

(b) Design-drawing of the next iteration with a length of 270 mm and two piezo-actuators. The design is expected to yield more than 2 mm of peak-to-peak actuation at 50 Hz

**Figure 14.1:** Status of the source-mass drive engine realized as a flexure-guiding system. The force applied by the piezo actuators causes the structures to bulge, which effectively amplifies the piezo amplitude by (roughly) the aspect ratio of the steel frame. The design and manufacturing was performed by Mathias Dragosits.

first running drives are established. Further current work is concerned with finite-element simulations for the estimation of electromagnetic stray-fields generated by the drive.

### 14.1.4 Readout status

We have proposed a polarization-based Mach-Zehnder homodyne interferometer that can be implemented with a small geometric footprint. This scheme has been tested with standard components (fig. 14.2(a)) and yields promising performance and stability. The components for a fully-integrated realization of this scheme have already been selected and, as the next step, need to be arranged on the test-mass platform. Selecting an appropriate laser source should be feasible as there are a few commercial short-coherence length laser systems available that likely meet our requirements.

The remaining challenge for the optical readout comes down to the noise performance of the detection and electronic signal conversion. If the electronic noise can be suppressed far enough, an off-resonant detection scheme becomes feasible, which circumvents the challenges associated with test-mass frequency drifts and ring-ins/downs. The electronic circuit is undergoing active development and is currently in its fourth iteration (fig. 14.2(b)).

### 14.1.5 Vibration isolation status

The good agreement between the vibration isolation model we built from scratch and a similar model used for advanced LIGO leads us to believe in the credibility of our performance estimation results. A complete model of

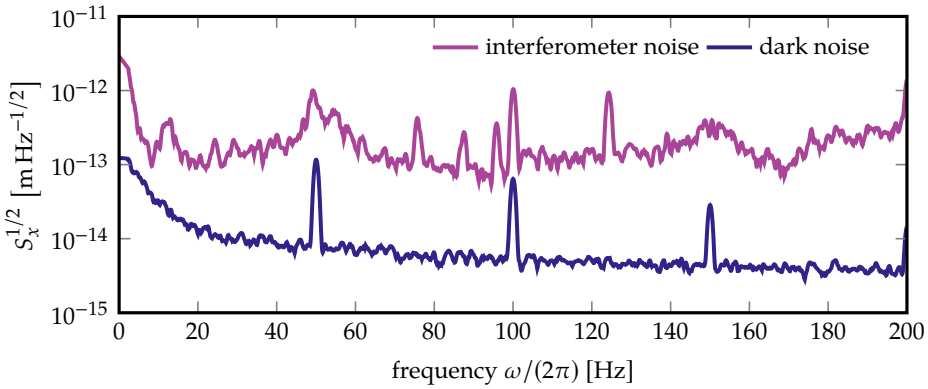


(a) Noise performance of a polarization-based interferometer built with standard components. For the experimental scheme, see fig. 11.2(a) on p. 134. The detection was realized with a commercial "Nirvana" auto-balanced photoreceiver by Newport Corporation (2017).

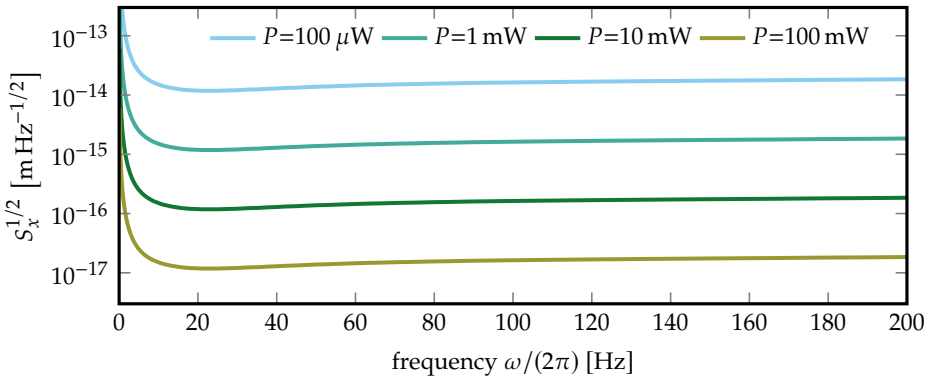


(b) Simulated performance of analogue detector electronics for a range of light powers $P$ incident on the detector diodes. The results were achieved with a program based on the open software *LISO* (Heinzel 1999).

**Figure 14.2:** Status of readout optics and electronics. The measurements and simulations were performed by Hans Hepach and Tobias Westphal.

the entire system including both the test- and source-mass chains as well as the active pre-isolation is being set up. This is mainly a programming effort and does not impose new principle challenges. The design of a blade-pendulum system yielding the desired performance is straightforward as our requirements are far looser than those typically encountered in gravitational wave detectors, which can be considered established technology. A commercial pre-isolation system has been selected, and while the available laboratory space is far from ideal, we are optimistic that our design allows us to complete the experiment.

The remaining challenge is of engineering nature; namely designing the

test-mass and source-mass stages in a way that both have their center-of-total-mass in the respective masses, while test and source mass are separated by a few hundred microns. This is absolutely feasible, but still requires careful planning and execution.

## 14.2 Outlook

As of early 2017, we are confident that the proposed experiment is feasible with current technology. We expect to be able to fabricate and characterize test-mass devices meeting the requirements by the end of the year. The off-resonant thermal-noise limited readout of such devices will certainly be a first major technical milestone, as it is only possible if the test mass, the optical readout and the test-mass vibration isolation meet our requirements. Once this is established, demonstrating gravitational interaction between the source and the test mass comes down to the engineering of the drive and the drive vibration-isolation. As the development of the drive engine is already in the stage of prototype testing and revision, we expect that by the time a thermal-noise limited readout of the test mass has been established, the driving side of the proposed experiment will be finalized. Without major setbacks, this should render the achievement of measuring gravitational interaction between milligram-masses feasible by 2018.

As we lay out in chapter 13, future directions of this experiment could lead to an alternative high-precision measurement of the gravitational constant, which might be less susceptible to conventional source-mass related disturbances of other approaches. Further, in the long run, the ability to extend the control over gravitational coupling into the microscopic domain may enable a new generation of quantum experiments, in which the source-mass character of the quantum systems start to play a role. However, while the former can be seen as a straight-forward extension of current state-of-the-art technology, the latter poses technical hurdles for environmental isolation and mechanical quality factors so demanding that it is not quite clear if they can ever be achieved. Nevertheless, these steps will ultimately accumulate to significant progress and even its early stages, the proposed experiment may act as a driving motor for the technical developments necessary to ultimately achieve gravitating quantum systems in the far future.

Part V

# Supplement

---

We lay out the definitions used throughout this thesis and perform some technical calculations in appendix A. In appendix B we appeal to some of the comments that are regularly brought up in the context of this work. We conclude with acknowledgments and the relevant indexes.

"I know my apprehensions might
never be allayed, and so I close,
realizing that perhaps the ending has not yet been written."

---

Myst
Rand Miller, Robyn Miller

"This was a triumph.
I'm making a note here: huge success.
It's hard to overstate my satisfaction."

---

Portal
Erik Wolpaw, Chet Faliszek

Appendix A

# Mathematics

## Chapter contents



## A.1 Conventions

We define the Fourier transform as

$$\mathcal{F}[x(t)](\omega) = \tilde{x}(\omega) := \int_{-\infty}^{+\infty} x(t) \mathrm{e}^{+\mathrm{i}\omega t}\,\mathrm{d}t,$$

which means that the inverse transform has to be

$$\mathcal{F}^{-1}[\tilde{x}(\omega)](t) = x(t) = \frac{1}{2\pi}\int_{-\infty}^{+\infty} \tilde{x}(\omega) \mathrm{e}^{-\mathrm{i}\omega t}\,\mathrm{d}\omega,$$

with the Dirac delta function

$$\delta(\omega) := \frac{1}{2\pi}\int_{-\infty}^{+\infty} \mathrm{e}^{+\mathrm{i}\omega t}\,\mathrm{d}t.$$

With these definitions, we see that

$$\mathcal{F}[\dot{x}(t)](\omega) = -\mathrm{i}\omega\tilde{x}(\omega) \quad \text{and} \quad \mathcal{F}[\ddot{x}(t)](\omega) = -\omega^2\,\tilde{x}(\omega).$$

Further, for real valued $x(t)$,

$$x(t) \in \mathbb{R} \quad \Rightarrow \quad \bar{\tilde{x}}(\omega) = \tilde{x}(-\omega) \quad \Rightarrow \quad |\tilde{x}(\omega)|^2 = \tilde{x}(\omega)\tilde{x}(-\omega). \tag{A.1}$$

The chosen conventions imply the following convolution identities:

$$\begin{aligned} \mathcal{F}[x(t)\, y(t)](\omega) &= \frac{1}{2\pi}\left[\tilde{x} \cdot \tilde{y}\right](\omega), \\ \mathcal{F}^{-1}[\tilde{x}(\omega)\, \tilde{y}(\omega)](t) &= \left[x \cdot y\right](t), \end{aligned} \tag{A.2}$$

as well as the Parseval identity for real, square-integrable $x(t)$,

$$\int_{-\infty}^{+\infty} x(t)^2 \,\mathrm{d}t = \frac{1}{2\pi}\int_{-\infty}^{+\infty} |\tilde{x}(\omega)|^2 \,\mathrm{d}\omega. \tag{A.3}$$

As another important identity we find that

$$\int_{-\infty}^{+\infty} S_x \,\mathrm{d}\omega = 2\pi \lim_{T\to\infty} \frac{1}{2T}\int_{-T}^{+T} \langle x(t)^2 \rangle \,\mathrm{d}t. \tag{A.4}$$

## A.2 Formulae

[1] Zwillinger 2011

We need the following trigonometric identities[1]:

$$\begin{aligned} \sin^n x &= \frac{1}{2^n}\binom{n}{\frac{n}{2}} + \frac{2}{2^n}\sum_{k=0}^{\frac{n}{2}-1}(-1)^{(\frac{n}{2}-k)}\binom{n}{k}\cos\left((n-2k)x\right), \quad n \text{ even}, \\ \sin^n x &= \frac{2}{2^n}\sum_{k=0}^{\frac{n-1}{2}}(-1)^{(\frac{n-1}{2}-k)}\binom{n}{k}\sin\left((n-2k)x\right), \quad n \text{ odd}, \\ \cos^n x &= \frac{1}{2^n}\binom{n}{\frac{n}{2}} + \frac{2}{2^n}\sum_{k=0}^{\frac{n}{2}-1}\binom{n}{k}\cos\left((n-2k)x\right), \quad n \text{ even}, \\ \cos^n x &= \frac{2}{2^n}\sum_{k=0}^{\frac{n-1}{2}}\binom{n}{k}\cos\left((n-2k)x\right), \quad n \text{ odd}, \end{aligned} \tag{A.5}$$

as well as

$$\begin{aligned} \sin x \sin y &= \frac{1}{2}\Big(\cos(x-y) - \cos(x+y)\Big), \\ \cos x \cos y &= \frac{1}{2}\Big(\cos(x-y) + \cos(x+y)\Big), \\ \sin x \cos y &= \frac{1}{2}\Big(\sin(x-y) + \sin(x+y)\Big). \end{aligned} \tag{A.6}$$

## A.3 Calculcations

### A.3.1 Variance of variance for Gaussian white noise

We closely follow the derivation given by Smith (2010) with modified notation. First, we define an expectation estimation function $\langle y \rangle_M$ of a quantity $y$, which is the expectation value of $y$ for a finite number $M$ of systems in an ensemble or of repetitions of a measurement on a single system:

$$\langle y \rangle_M := \frac{1}{M} \sum_{m=0}^{M-1} y_m,$$

where $m$ is an ensemble index and so $y$ can be any quantity that is accessible in a repeatable fashion, e.g. the value of a Fourier transform at a specific frequency $\omega^*$, $y = \tilde{x}(\omega^*)$. We directly see that the expectation value of this quantity is the expectation value of $y$, as $\langle \langle y \rangle_M \rangle = M^{-1} \sum_{m=0}^{M-1} \langle y \rangle = \langle y \rangle$. Now, taking the variance $\sigma_y^2$ of $y$ as $\sigma_y^2 := \langle \big(y - \langle y \rangle\big)^2 \rangle$, we may ask about the variance of the estimation function of $y^2$, or more specifically in the case of white noise with $\langle y \rangle = 0$, about the variance of a variance:

$$\sigma^2_{\langle y^2 \rangle_M} = \langle \big( \langle y^2 \rangle_M - \langle \langle y^2 \rangle_M \rangle \big)^2 \rangle \,.$$

We use that $\langle \langle y^2 \rangle_M \rangle = \langle y^2 \rangle$, and that for a zero-mean quantity ($\langle y \rangle = 0$) $\sigma_y^2 = \langle (y - \langle y \rangle)^2 \rangle = \langle y^2 \rangle$, so

$$\begin{aligned} \ldots &= \langle \Big( \langle y^2 \rangle_M - \sigma_y^2 \Big)^2 \rangle = \langle \langle y^2 \rangle_M^2 \rangle - \sigma_y^4 \\ &= \frac{1}{M^2} \sum_{m_1=0}^{M-1} \sum_{m_2=0}^{M-1} \langle y_{m_1}^2 y_{m_2}^2 \rangle - \sigma_y^4. \end{aligned}$$

In the case of Gaussian white noise, the fourth moment is given by

$$\langle y_{m_1}^2 y_{m_2}^2 \rangle = \begin{cases} 3\sigma_y^4, & m_1 = m_2 \\ \sigma_y^4, & m_1 \neq m_2 \end{cases},$$

and therefore

$$\sigma^2_{\langle y^2 \rangle_M} = \frac{1}{M^2} \Big( (M^2 - M)\sigma_y^4 + 3M\sigma_y^4 \Big) - \sigma_y^4 = \frac{2}{M} \sigma_y^4.$$

For example, when considering the power spectral density $S$ of white noise (or a PSD that is deterministically derived of white noise, such as the displacement PSD of a thermally driven oscillator), we can now write

$$S(\omega) = \langle S(\omega) \rangle_M \pm \sqrt{\frac{2}{M}} S(\omega) \approx \left( 1 \pm \sqrt{\frac{2}{M}} \right) \langle S(\omega) \rangle_M \,.$$

This means that for a non-averaged spectral density of a Gaussian white-noise signal, i.e. $M = 1$, the error at each measured frequency will be larger than the power-spectrum expectation value (by a factor of $\sqrt{2}$).

### A.3.2 Proof of the Wiener-Khinchin theorem

In order to proof the Wiener-Khinchin theorem (see section 4.6 on p. 23) we consider

$$\begin{aligned}\langle|\tilde{x}_T(\omega)|^2\rangle &= \frac{1}{2T}\int_{-T}^{+T} \mathrm{d}t_2 \int_{-T}^{+T} \mathrm{d}t_1 \ \langle x(t_2)x(t_1)\rangle \, \mathrm{e}^{\mathrm{i}\omega(t_2-t_1)} \\ &= \frac{1}{2T}\int_{-T}^{+T} \mathrm{d}t_2 \int_{-T}^{+T} \mathrm{d}t_1 \, r_x(t_2-t_1)\mathrm{e}^{\mathrm{i}\omega(t_2-t_1)},\end{aligned}$$

where we assumed that the autocorrelation function does not depend on the individual times $t_1$, $t_2$ but only on their difference. This kind of process is often referred to as *weakly stationary* or *wide-sense stationary*. Using the following identity,

$$\int_{-T}^{+T} \mathrm{d}t_2 \int_{-T}^{+T} \mathrm{d}t_1 \, f(t_2-t_1) = \int_{-2T}^{+2T} \mathrm{d}\tau \, g(\tau)(2T-|\tau|),$$

we can process the above as

$$\begin{aligned}\langle|\tilde{x}_T(\omega)|^2\rangle &= \frac{1}{2T}\int_{-2T}^{+2T} \mathrm{d}\tau \, r_{xx}(\tau)\mathrm{e}^{\mathrm{i}\omega\tau}(2T-|\tau|) \\ &= \int_{-2T}^{+2T} \mathrm{d}\tau \, r_{xx}(\tau)\mathrm{e}^{\mathrm{i}\omega\tau}\left(1-\frac{|\tau|}{2T}\right).\end{aligned}$$

Therefore,

$$S_{P,x} = \lim_{T\to\infty}\langle|\tilde{x}_T(\omega)|^2\rangle = \int_{-\infty}^{+\infty} \mathrm{d}\tau r_{xx}(\tau)\,\mathrm{e}^{\mathrm{i}\omega\tau} = \mathcal{F}[r_{xx}(\tau)](\omega).$$

### A.3.3 Limit of $T\,\mathrm{sinc}^2(\omega T)$

The limit of $T\,\mathrm{sinc}^2(\omega T)$ for $T \to \infty$ is of relevance for the spectra-related calculations. To derive this limit, we first consider the expression

$$\eta(\omega) := \frac{\tau}{\pi}\,\mathrm{sinc}^2(\omega\tau),$$

which is continuous, absolutely integrable and fulfills $\int_{-\infty}^{+\infty}\eta(\omega)\,\mathrm{d}\omega = 1$. Therefore, a *nascent delta function* $\eta_\epsilon(x) := \epsilon^{-1}\eta(x/\epsilon)$ can be constructed[2] which will weakly converge[3] to the Dirac delta function in the limit of $\epsilon \to 0$:

[2] Stein and Weiss 1971, Theorem 1.18

[3] Rudin 1991, sec. 6.31

$$\lim_{\epsilon\to 0} \eta_\epsilon(x) = \lim_{\epsilon\to 0} \frac{\tau}{\pi\,\epsilon} \operatorname{sinc}^2\left(\omega\frac{\tau}{\epsilon}\right) = \delta(\omega).$$

If we substitute $T := \tau/\epsilon$, the limit $\epsilon \to 0$ becomes $T \to \infty$ and the equation above can be rewritten as

$$\lim_{T\to\infty} T\ \operatorname{sinc}^2(\omega\, T) = \pi\,\delta(\omega).$$

### A.3.4 Integrated susceptibility

For the susceptibility $\chi(\omega) = (\omega_0^2 - \omega^2 - \mathrm{i}\gamma\omega)^{-1}$, we find that the integral is

$$\int_{-\infty}^{\infty} |\chi(\omega)|^2\ \mathrm{d}\omega = \frac{\pi}{\gamma\omega_0^2}. \tag{A.7}$$

### A.3.5 Splitting of Fourier contributions for the PSD calculation

Suppose we split the position coordinate into a sum of multiple contributions, $x(t) = \sum_i x_i(t)$. Naturally, the Fourier transform of the position can be split up in the same way,

$$\tilde{x}(\omega) = \sum_i \tilde{x}_i(\omega),$$

and due to the linearity of the convolution, we may apply eq. (4.2) on p. 21 and write the windowed Fourier transform as

$${}_T\tilde{x}(\omega) = \sum_i {}_T\tilde{x}_i(\omega)$$

$$\text{with}\quad {}_T\tilde{x}_i(\omega) = \frac{1}{\sqrt{2T}}\frac{1}{2\pi}\left[{}_T\tilde{h}\cdot\tilde{x}_i\right](\omega),\quad {}_T\tilde{h}(\omega) = 2T\operatorname{sinc}(\omega T).$$

The power spectral density, eq. (4.4) on p. 23, is then given by

$$S_x = \lim_{T\to\infty} \langle |{}_T\tilde{x}(\omega)|^2\rangle = \lim_{T\to\infty} \sum_{i,j} \langle {}_T\tilde{x}_i(\omega)\, {}_T\bar{\tilde{x}}_j(\omega)\rangle\,.$$

If we now assume that we split $x(t)$ in such a way that at most one of the $x_i(t)$ is deterministic and all other $x_i(t)$ are statistic with zero-mean, and we further assume that all statistic $x_i(t)$ are uncorrelated[a], we have that

$$\lim_{T\to\infty} \langle {}_T\tilde{x}_i(\omega)\, {}_T\bar{\tilde{x}}_j(\omega)\rangle = \delta_{ij} S_{x_i},$$

and therefore

$$S_x = \lim_{T\to\infty} \sum_i S_{x_i}.$$

[a] As is pointed out by Clerk et al. (2010), this is not always trivially the case. E.g. in opto-mechanical cavities mixed terms between shot noise and backaction can occur, as they are effects of the same underlying photon rate fluctuations.

### A.3.6 Nonlinear source-contributions

Here, we will briefly investigate the nonlinear terms in eq. (5.8e) on p. 32, namely

$$\tilde{x}_\Xi(\omega) = \chi(\omega) \sum_{n_1,n_2=1}^{\infty} \Xi(n_1,n_2)\mathcal{F}[x_S^{n_1}\dot{x}_S^{n_2}]$$
$$\text{with} \quad \Xi(n_1,n_2) = \sum_i \frac{1}{n_1!n_2!} \frac{\partial^{n_1+n_2}}{\partial x_S^{n_1}\partial \dot{x}_S^{n_2}} F_i(x_S,\dot{x}_S)\bigg|_{0,0}.$$

Similar to section 5.2 on p. 33, we assume a sinusoidal drive motion $x_S(t) := d_S\cos(\omega_S t)$. With this, we can break down the Fourier transform of $x_S^{n_1}\dot{x}_S^{n_2}$ as

$$\mathcal{F}[x_S^{n_1}\dot{x}_S^{n_2}] = d_S^{n_1+n_2}(-\omega_S)^{n_2}\mathcal{F}[\cos^{n_1}(\omega_S t)\sin^{n_2}(\omega_S t)].$$

Without actually processing this expression much further, we can look at the trigonometric power expansion theorems, eq. (A.5), and see that for all $n_1$, $n_2$ we can reduce both the cos and the sin power expressions to sums of single trigonometric functions oscillating with frequencies $\omega = (n-2k)\omega_S$ with integer-valued $k$s. Using the trigonometric multiplication theorems, eq. (A.6), it becomes clear that all terms of the total sum oscillate at frequencies

$$\omega = ((n_1-2k_1) \pm (n_2-2k_2))\omega_S.$$

Thinking in terms of spectra, the meaning of this expression is obvious: On top of additional contributions at the drive frequency, the nonlinear drive terms generate a spectrum of higher order frequency contributions, which are positioned at integer multiples of the original source frequency $\omega_S$.

Appendix B

# Comments

## Chapter contents



## B.1 Making sense of spectrum analyzers

Here, we account for some of the confusion that can arise when trying to put a spectrum analyzer in the context of PSD estimation. A general issue is that the default units of a spectrum analyzer, e.g. dbm, are not valuable for much more than an "arbitrary units" figure and require more work if quantitative amplitude information is desired. Let us assume that the spectrum analyzer is set to a *power mode*, so in principle it should show the square of the voltage spectral density of the signal integrated of some frequency band, times an unknown conversion constant. We call this the spectrum analyzer power spectrum $P_{\mathrm{SA}}$ (SAPS). The SAPS can then be related to the actual PSD of the relevant quantity by deterministic modulation. We call the desired quantity $x$, which could be position, phase, voltage or any quantity that is part of the physical detection chain and can be modulated, and vary it as

$$x(t) = B_{\mathrm{mod}} \cos(\omega_{\mathrm{mod}} t),$$

where the amplitude $B_{\mathrm{mod}}$ *has* to be known. For example, in a position measurement with interference where some diode voltage is measured, one can

cause a half wave phase shift $\pi$ and from that measurement extract the phase shift that corresponds to a certain voltage difference. We can then calculate the theoretical power spectral density of $x$ to be

$$S_x = B_{\text{mod}}^2 \pi/2 \left(\delta(\omega + \omega_{\text{mod}}) + \delta(\omega - \omega_{\text{mod}})\right),$$

repeating the calculation we performed in section 5.2 on p. 33. The signal of the spectrum analyzer will be the integral of this expression with a certain bandwidth $\Gamma$ and multiplication with an unknown factor $\alpha$, i.e. $P_{\text{SA}}(\omega) = \alpha \int_{\omega-\Gamma/2}^{\omega+\Gamma/2} S_x \, \mathrm{d}\omega$.[a] Referring to the height of the modulation peak in the SAPS with $B_{\text{SA}}$, at $\omega = \omega_{\text{mod}}$ the condition reads $B_{\text{SA}} = \alpha B_{\text{mod}}^2 \pi/2$, and therefore

$$S_x(\omega) \approx \frac{\pi B_{\text{mod}}^2}{2\Gamma B_{\text{SA}}} P_{\text{SA}}(\omega) = \frac{T B_{\text{mod}}^2}{4 B_{\text{SA}}} P_{\text{SA}}(\omega)$$

with the integration time $T$. This conversion should, in principle, hold true for any spectrum analyzer in power mode and does not change for different modes of conversion between symmetrized and non-symmetrized spectra or different settings of input resisance (as long as the amplitude $B_{\text{SA}}$ and the integration time $T$ are used correctly).

## B.2 Fourier transform: From continuous to discrete

In this section we lay out how a spectral density from an actual, finite and discrete measurement differs from the idealized value. The definition we introduced in section 4.2 on p. 20,

$$S_x = \lim_{T\to\infty} \langle |{}_T\tilde{x}(\omega)|^2 \rangle ,$$

has little to do with the experimental reality, as from a physical point of view there are no continuous measurements (every measurement yields a discrete series of data points) and no infinitely long measurements.

First, we have to assume that the deterministic part of the system is periodic and that there is a $T'$ which is the longest period, which allows us to effectively treat a trace as being infinite if we chose $T \gg T'$ and drop the limit. We also have to comply with the fact that usually there is no ensemble of systems, but just a single system available. This means that we have to drop the ensemble average and replace it with a time average, where we evaluate the same system at different periods in time:

$$S_x \approx \langle S_{x,\text{single}} \rangle_{\text{time}} \quad \text{with} \quad S_{x,\text{single}} = |{}_T\tilde{x}(\omega)|^2.$$

[a] Technically, we also need to account for the window function that is caused by the finite measurement time as discussed in appendix B.2.2, which here we skip for clarity.

We previously used ${}_T\tilde{x}(\omega) = (2T)^{-1/2}\int_{-T}^{+T} x(t)\mathrm{e}^{\mathrm{i}\omega t}\,\mathrm{d}t$, but for convenience here we redefine it as

$$ {}_T\tilde{x}(\omega) := \frac{1}{\sqrt{T}}\int_{0}^{+T} x(t)\mathrm{e}^{\mathrm{i}\omega t}\,\mathrm{d}t. $$

An actual measurement will not yield a continuous trace $x(t)$, but instead a serious of points $x_n = x(n\Delta t)$, corresponding to snapshots (or weighted averages) of the actual trace in time steps $\Delta t$. We therefore replace the integral with a sum as

$$ {}_T\tilde{x}(\omega) \approx \frac{1}{\sqrt{T}}\sum_{n=0}^{N-1} x_n \mathrm{e}^{\mathrm{i}\omega n\Delta t}\Delta t \tag{B.1} $$

where $N\Delta t = T$ with the total number of points $N$ and the total measurement time $T$.

### B.2.1 Software implementation of spectral densities

Computationally it is convenient to also treat the transformed function (and not only the original data) as a series of points. Starting from eq. (B.1) we write

$$ \tilde{x}_m :=_T \tilde{x}(m\Delta\omega) =_T \tilde{x}(m2\pi\Delta f) \approx \frac{\Delta t}{\sqrt{T}}\sum_{n=0}^{N-1} x_n \mathrm{e}^{\mathrm{i}2\pi nm\Delta t\Delta f} \tag{B.2} $$

It seems like one can choose $\Delta f$ freely, but there is just one choice that actually makes sense. For the smallest step in frequency $\Delta f$, we require that the exponent is periodic in $n$ with period $N$, which leads to

$$ 1 = \mathrm{e}^{\mathrm{i}2\pi N\Delta t\Delta f} \quad \Rightarrow \quad N\Delta t\Delta f = 1 $$

Inserting this into eq. (B.2), we get

$$ \tilde{x}_m = \sqrt{\frac{\Delta t}{N}}\sum_{n=0}^{N-1} x_n \mathrm{e}^{\mathrm{i}2\pi nm/N}, $$

and coming back to the single spectral density, we have

$$ S_{x,\mathrm{single},m} \approx \frac{\Delta t}{N}\left|\sum_{n=0}^{N-1} x_n \mathrm{e}^{\mathrm{i}2\pi nm/N}\right|^2. $$

The implementation of the above depends on the definition of the discrete fourier transform in the respective programming language. For example, in Mathematica the default Fourier transform is defined as

```
Fourier[list_]:=Table[
        1/Sqrt[nMax] Sum[
                list[[n]] Exp[I 2 Pi (n-1)(m-1)/nMax],
                {n,1,nMax}],
        {m,1,nMax}]
```

where one should note that in Mathematica lists start at the first and not at the zeroth entry. As can be seen from this definition, in order the extract the spectral density we have to multiply the absolute square of the Mathematica Fourier series by the time step size $\Delta t$. The single spectral density in Mathematica code is therefore given by

```
spectralDensity = timeStep Abs[ Fourier[ trace ] ]^2
```

where the timestep can be extracted from the difference between the first and the last timestamp of the trace divided by the number of points in the trace, which equals the time difference between two successive points in the trace.

### B.2.2 Finite sampling of a continuous signal

As seen in eq. (4.2) on p. 21 we may write

$$ {}_T\tilde{x}(\omega) = \frac{1}{\sqrt{2T}} \frac{1}{2\pi} \left[ {}_T\tilde{h} \cdot \tilde{x} \right](\omega) $$

where ${}_Th(t)$ represents a step-window function in the simplest case, but can be any appropriate $L^2$ function. While a window step-window function corresponds to the case where the measurement is switched on and off at certain points in time, one might also think of taking snippets of longer traces by "fading" the values of the outside of the range in and out, e.g. by using a Gauss function instead of a discrete window function, and having some amount of overlap between traces

If we now introduce a finite sampling rate $1/\Delta t$, the expression above will slightly change. Generalizing eq. (B.1) to arbitrary window functions $h(t)$, we have

$$\begin{aligned} {}_T\tilde{x}(\omega) &\approx \frac{1}{\sqrt{2T}} \sum_{n=-\infty}^{\infty} h(n\Delta t) x(n\Delta t) \mathrm{e}^{\mathrm{i}\omega n\Delta t} \Delta t \\ &= \frac{1}{\sqrt{2T}} \frac{1}{2\pi} \sum_{n=-\infty}^{\infty} h(n\Delta t) \left( \int_{-\infty}^{+\infty} \tilde{x}(\omega') \mathrm{e}^{-\mathrm{i}\omega' n\Delta t} \, \mathrm{d}\omega' \right) \mathrm{e}^{\mathrm{i}\omega n\Delta t} \Delta t \\ &= \frac{1}{\sqrt{2T}} \frac{1}{2\pi} \int_{-\infty}^{+\infty} \left( \sum_{n=-\infty}^{\infty} h(n\Delta t) \mathrm{e}^{\mathrm{i}(\omega-\omega')n\Delta t} \Delta t \right) \tilde{x}(\omega') \, \mathrm{d}\omega', \end{aligned}$$

thereby allowing us to write

$$ {}_T\tilde{x}(\omega) = \frac{1}{\sqrt{2T}} \frac{1}{2\pi} \left[ \tilde{h}_f \cdot \tilde{x} \right](\omega) \quad \text{with} \quad \tilde{h}_f(\omega) := \sum_{n=-\infty}^{\infty} {}_Th(n\Delta t) \mathrm{e}^{\mathrm{i}\omega n\Delta t} \Delta t, \quad \text{(B.3)} $$

meaning that we now use a finitely sampled Fourier transform $\tilde{h}_f(\omega)$ instead of the continuous one.

We may briefly check the impact of the finite sampling for the easiest case of a step-window ${}_T h(t)$,

$$ {}_T h(t) := \begin{cases} 1 & \text{for } t \in [-T;T) \\ 0 & \text{else} \end{cases}, $$

which can be inserted into eq. (B.3) to compute the finitely sampled Fourier transform $\tilde{h}_f(\omega)$ as

$$ \begin{aligned} \tilde{h}_f(\omega) &= \Delta t \sum_{n=-N}^{N-1} \mathrm{e}^{\mathrm{i}\omega n \Delta t} = \frac{\Delta t}{\sqrt{2T}} \sum_{n=0}^{N-1} \left( \mathrm{e}^{\mathrm{i}\omega n \Delta t} + \mathrm{e}^{-\mathrm{i}\omega \Delta t} \mathrm{e}^{-\mathrm{i}\omega n \Delta t} \right) \\ &= \Delta t \left( \frac{1 - \exp(\mathrm{i}\omega T)}{1 - \exp(\mathrm{i}\omega \Delta t)} + \mathrm{e}^{-\mathrm{i}\omega \Delta t} \frac{1 - \exp(-\mathrm{i}\omega T)}{1 - \exp(-\mathrm{i}\omega \Delta t)} \right) \\ &= 2T \operatorname{sinc}(\omega T) \frac{\exp(-\mathrm{i}\omega \Delta t/2)}{\operatorname{sinc}(\omega \Delta t/2)}, \end{aligned} $$

where in the second line we identified a geometric series and the third line is basic calculus. To re-iterate, the continuous Fourier transform of ${}_T h(t)$, which was used for the idealized power spectral densities throughout this thesis, is

$$ {}_T\tilde{h}(\omega) = \int_{-T}^{T} \mathrm{e}^{\mathrm{i}\omega t} \mathrm{d}t = \left( \mathrm{e}^{\mathrm{i}\omega T} - \mathrm{e}^{-\mathrm{i}\omega T} \right) (\mathrm{i}\omega)^{-1} = 2T \operatorname{sinc}(\omega T). $$

The consistency of these results is quickly verified as $\tilde{h}_f(\omega) \xrightarrow{\Delta t \to 0} {}_T\tilde{h}(\omega)$, which is required as the continuous case should be recovered from the discrete for infinitely small time steps $\Delta t \to 0$. Both functions are compared in fig. 4.1 on p. 25. It becomes evident that the actual values of $x$ will be sampled into smooth bins, the width of which depend on the time span of the trace – the longer the time, the smaller the bins become as $\tilde{h}_f(\omega)$ is modulated with period $\omega_m = 2\pi/(N\Delta t) = 2\pi/T$, which is the frequency resolution of the trace. But we also note that due to the finite sampling, the higher frequency contributions of $\tilde{x}(\omega)$ will be convoluted, or shifted, onto the lower ones. This effectively adds to their amplitudes as $\tilde{h}_f(\omega)$ is periodic in $\omega$ with period $\omega_p = 2\pi/\Delta t$, which is the bandwidth of the trace. In essence, this is the sampling theorem.[1] In signal processing, when signals at specific frequencies cause spectral contributions at different frequencies due to the nature of the sampling, one speaks of *leakage*, and in general there is a variety of window functions ${}_T h(t)$, some of which are more and and some of which are less suitable for specific signals. A detailed analysis of windows for discrete Fourier transforms was first published by Harris (1978), and a more recent overview of the topic can be found in Heinzel et al. (2002).

[1] Luke 1999

## B.3 Relation between power spectral density and RMS

It is very typical to find root mean square, or RMS, noise characteristics in technical data sheets of devices – usually without any frequency dependence, sometimes given at a specific frequency and in rare cases given as a spectral plot. Here, we analyze when this actually makes sense (and when it does not). Generally, the mean square at a certain frequency $\omega_0$ is proportional to the integrated power spectrum $P_x$,

$$\mathrm{RMS}^2 \propto P_x(\omega_0) = \int_{\omega_0-\Gamma/2}^{\omega_0+\Gamma/2} S_x(\omega)\,\mathrm{d}\omega \tag{B.4}$$

where $\Gamma$ is the integration bandwidth and the proportionality comes down to factors of $\pi$ and 2, depending on the convention. As this definition depends on $\Gamma$, it generally does not make sense to specify RMS without naming the integration bandwidth. The only relevant exception to this is the case where a single sharp peak dominates the power spectral density, which we explain below. Nevertheless, one often finds RMS values given without any reference to bandwidth. Sometimes, they implicitly refer to conventions, such as the 1/3 *octave standard*[2] which does not use a fixed integration bandwidth $\Gamma$ for all frequencies $\omega_0$, but an octave-based scaling.

[2] Veggeberg 2008

In the cases where a single sharp peak dominates an otherwise broad spectrum, the power-spectral density is not the ideal tool in the proximity of the peak. As we demonstrated in section 5.2 on p. 33, sinusoidal signals become delta-peaks in the PSD, meaning they diverge at a single frequency. It is clear that a finite measurement bandwidth will always yield a finite peak height; however, if we deduce the PSD from the integrated power via $S_x(\omega) \approx P_x(\omega)/\Gamma$, the height of a deterministic peak in the PSD will now depend on the integration bandwidth $\Gamma$. This becomes clear if we insert $S_x \propto \delta(\omega - \omega')$ into eq. (B.4), which means that the *estimated* PSD will be a step function with amplitude proportional to $1/\Gamma$ around $\omega'$ and zero elsewhere. As in this case $P_x$ is *independent* of $\Gamma$, it makes sense to specify an RMS value instead of a PSD. Note though that this information will only be relevant for measurements of signals around the frequency of the dominating noise peak and is not a valid figure for the overall noise performance of a technical device.

## B.4 Phase information in power spectral densities

It is clear from the definition of the power spectral density, eq. (4.4) on p. 23, that due to the absolute square, the phase information of the time trace can not be recovered from the PSD. However, as a measure against noise, this information might actually be useful.

### B.4.1 Phase-coherent power spectral density

Suppose the signal $x(t)$ is composed of a deterministic part $x_\mathrm{D}(t)$ and a zero-mean statistic part $x_\mathrm{N}(t)$,

$$x(t) = x_\mathrm{D}(t) + x_\mathrm{N}(t).$$

Then, by eq. (4.4), the PSD is given by

$$\begin{aligned} S_x &= \lim_{T\to\infty} \langle |{}_T\tilde{x}(\omega)|^2 \rangle = \lim_{T\to\infty} \left\langle \left| \int_{-T}^{+T} [x_\mathrm{D}(t) + x_\mathrm{N}(t)][\cos(\omega t) + \mathrm{i}\sin(\omega t)] \right|^2 \right\rangle \\ &= \lim_{T\to\infty} \frac{1}{2T} \left\{ \left( \int_{-T}^{+T} x_\mathrm{D}(t)\cos(\omega t)\,\mathrm{d}t \right)^2 + \left( \int_{-T}^{+T} x_\mathrm{D}(t)\sin(\omega t)\,\mathrm{d}t \right)^2 \right\} \\ &\quad + \lim_{T\to\infty} \frac{1}{2T} \left\{ \left\langle \left( \int_{-T}^{+T} x_\mathrm{N}(t)\cos(\omega t)\,\mathrm{d}t \right)^2 \right\rangle + \left\langle \left( \int_{-T}^{+T} x_\mathrm{N}(t)\sin(\omega t)\,\mathrm{d}t \right)^2 \right\rangle \right\}, \end{aligned} \tag{B.5}$$

where we used that $\langle x_\mathrm{D}(t) x_\mathrm{N}(t) \rangle = x_\mathrm{D}(t) \langle x_\mathrm{N}(t) \rangle = 0$. As $x_\mathrm{D}(t)$ and $x_\mathrm{N}(t)$ are naturally uncorrelated, we expect that the individual PSDs add as

$$S_x = S_{x_\mathrm{D}} + S_{x_\mathrm{N}}. \tag{B.6}$$

Therefore, we can identify

$$\lim_{T\to\infty} \frac{1}{2T} \left( \int_{-T}^{+T} x_\mathrm{N}(t)\cos(\omega t)\,\mathrm{d}t \right)^2 = \lim_{T\to\infty} \frac{1}{2T} \left( \int_{-T}^{+T} x_\mathrm{N}(t)\sin(\omega t)\,\mathrm{d}t \right)^2 = \frac{1}{2} S_{x_\mathrm{N}}$$

Further, setting a sinusoidal signal

$$x_\mathrm{D} := d_\mathrm{D}\cos(\omega_\mathrm{D} t)$$

we see that[b]

$$\lim_{T\to\infty} \frac{1}{2T} \left( \int_{-T}^{+T} x_\mathrm{D}(t)\sin(\omega t)\,\mathrm{d}t \right)^2 = 0$$

and therefore the first term of eq. (B.5) contains the full deterministic PSD contribution, i.e.

$$\lim_{T\to\infty} \frac{1}{2T} \left( \int_{-T}^{+T} x_\mathrm{D}(t)\cos(\omega t)\,\mathrm{d}t \right)^2 = S_{x_\mathrm{D}}(\omega).$$

[b] Note that, while the nature of the solution remains unchanged, this derivation becomes more complicated for the choice of a non-symmetric time window.

Now, realizing that $S_x = \lim_{T\to\infty} \langle \Re^2 [{}_T\tilde{x}(\omega)] + \Im^2 [{}_T\tilde{x}(\omega)] \rangle$, instead of the PSD, we consider a new quantity

$$S'_x := \lim_{T\to\infty} \langle \Re^2 [{}_T\tilde{x}(\omega)] \rangle$$

and call it the *phase-coherent power spectral density*. By identifying the appropriate terms in the above calculation, we immediately see that

$$S'_x = S_{x_\mathrm{D}} + \frac{1}{2} S_{x_\mathrm{N}}.$$

Interestingly, in comparison to the regular PSD (eq. (B.6)), this quantity halves the contribution of statistic noise. The intuition behind this result is that by ignoring the imaginary part of the windowed Fourier transform ${}_T\tilde{x}(\omega)$, we can keep the entire deterministic signal information, while erasing the statistic contributions that are not in phase with the signal. Of course, this simple example works because we set the deterministic motion to be an non-shifted cosine function. More generally, we have to define the phase-coherent PSD as

$${}^{\phi}S'_x := \lim_{T\to\infty} \langle \Re^2 \left[ \mathrm{e}^{\mathrm{i}\phi} {}_T\tilde{x}(\omega) \right] \rangle \,, \tag{B.7}$$

where the phase $\phi$ has to be tuned to match the deterministic signal. With this choice, the quantity can be seen as a PSD that is optimized with respect to the measurement of a sinusoidal signal.

### B.4.2 Optimal measurement of a sinusoidal signal

Above, we showed that we can define a quantity that is in phase with a deterministic sinusoidal signal $x_\mathrm{D}(t)$ to improve the ratio of signal to noise. Being motivated by these results, we now ask in general for the *optimal* solution of the problem at hand.

Suppose, again, that a signal is composed of a deterministic part and a statistic part, $x(t) = x_\mathrm{D}(t) + x_\mathrm{N}(t)$. The goal is to find a filter $h(t)$ that generates a filtered signal $x'(t)$ via a convolution

$$x'(t) = [h \cdot x](t).$$

Now, by comparing the contributions of signal and noise power in $x'(t)$, one can show[3] that the optimal choice of $h(t)$ is a *matched filter*, i.e. the time-reverse of the expected signal $x_\mathrm{D}(t)$,

[3] Turin 1960

$$h_\mathrm{opt}(t) = x_\mathrm{D}(-t).$$

Due to the symmetry of the cosine, the optimally filtered signal is then

$$x'(t)_\mathrm{opt} = [x_\mathrm{D} \cdot x](t) = d_\mathrm{D} \int_{-\infty}^{+\infty} [x_\mathrm{D}(\tau) + x_\mathrm{N}(\tau)] \cos(\omega_\mathrm{D}\tau - \omega_\mathrm{D} t) \,\mathrm{d}\tau. \tag{B.8}$$

We can compare this to the phase-coherent PSD, eq. (B.7), at a specific frequency $\omega = \omega_D$,

$$ {}^{\phi}S'_x(\omega_D) = \lim_{T\to\infty} \langle \left( \int_{-T}^{+T} [x_D(\tau) + x_N(\tau)] \cos(\omega_D \tau + \phi)\, \mathrm{d}\tau \right)^2 \rangle . \tag{B.9} $$

It becomes clear that the expressions are closely related. Knowing that in eq. (B.8) the ratio of contributions of the $x_D$-term and the $x_N$-term of is optimized, the same is likely true for eq. (B.9). Indeed, this is an indicator that for a sinusoidal signal, the phase-coherent part of the Fourier transform acts as an optimized filter. Therefore, we have reason to believe that the choice of the phase-coherent PSD, eq. (B.7), as the signal evaluation method is optimal.

## B.5 Two-dimensional driving mass pattern

A common technical suggestion to the presented work is to modify the drive such that it moves in a circular fashion instead of back and forth on a line. Here, we analyze if the dynamics of the test mass will change significantly due to a two-dimensional driving pattern. We may quickly check this by looking at eqs. (5.2) and (5.3) on p. 29 and on p. 30. For convenience, we focus on a single force $\vec{F}(\vec{d}_{tot})$ with $\vec{d}_{tot} = \left(\begin{smallmatrix} d_0 \\ 0 \end{smallmatrix}\right) + \left(\begin{smallmatrix} x_S \\ y_S \end{smallmatrix}\right) - \left(\begin{smallmatrix} x \\ 0 \end{smallmatrix}\right)$ and drop the dependence on velocity. Since the oscillator with position $x$ can only move in one direction, we may restrict the relevant force term to the same direction by defining

$$ F_x := \vec{F} \cdot \vec{e}_x . $$

Now, similar to eq. (5.2), we write

$$ F_x(\left(\begin{smallmatrix} d_0 \\ 0 \end{smallmatrix}\right) + \left(\begin{smallmatrix} x_S \\ y_S \end{smallmatrix}\right) - \left(\begin{smallmatrix} x \\ 0 \end{smallmatrix}\right)) \approx F_x(\left(\begin{smallmatrix} d_0 \\ 0 \end{smallmatrix}\right) + \left(\begin{smallmatrix} x_S \\ y_S \end{smallmatrix}\right)) + \partial_x F_x\big|_{\left(\begin{smallmatrix} d_0 \\ 0 \end{smallmatrix}\right)} x + \ldots , $$

and similar to eq. (5.3)

$$ F_x(\left(\begin{smallmatrix} d_0 \\ 0 \end{smallmatrix}\right) + \left(\begin{smallmatrix} x_S \\ y_S \end{smallmatrix}\right)) \approx F_x(\left(\begin{smallmatrix} d_0 \\ 0 \end{smallmatrix}\right)) + \partial_{x_S} F_x\big|_{\left(\begin{smallmatrix} d_0 \\ 0 \end{smallmatrix}\right)} x_S + \partial_{y_S} F_x\big|_{\left(\begin{smallmatrix} d_0 \\ 0 \end{smallmatrix}\right)} y_S + \ldots . \tag{B.10} $$

If we now assume a isotropic force, i.e. one that only depends on the distance $|\vec{d}_{tot}|$, of the form

$$ F_x(\vec{d}_{tot}) = c|\vec{d}_{tot}|^n , $$

and insert this into eq. (B.10), we realize that there is no contribution of $y_S$ in first order, while the contributions of $x_S$ remain unchanged:

$$\partial_{x_S} F_x\Big|_{\binom{d_0}{0}} x_S = cnd_0^{n-1} x_S, \qquad \frac{1}{2}\partial_{x_S}^2 F_x\Big|_{\binom{d_0}{0}} x_S^2 = \frac{1}{2}cn(n-1)d_0^{n-2}x_S^2,$$

$$\partial_{y_S} F_x\Big|_{\binom{d_0}{0}} y_S = 0, \qquad \frac{1}{2}\partial_{y_S}^2 F_x\Big|_{\binom{d_0}{0}} y_S^2 = \frac{1}{2}cnd_0^{n-2}y_S^2,$$

$$\frac{1}{2}\partial_{x_S}\partial_{y_S} F_x\Big|_{\binom{d_0}{0}} x_S y_S = 0.$$

This means that as long as our implicit assumption $x_S$, $y_S < d_0$ remains correct, a circular, or any two-dimensional drive motion, will only cause a deviation in the second order of the motion orthogonal to the test-mass direction. Therefore, in first order we recover the equation of motion for the 1-dimensional case, eq. (5.4) on p. 30.

We can also see from the equations above that adding additional masses to a circular drive can only decrease the signal: The first order contribution in $x_S$ would then become

$$cnd_0^{n-1}x_S \to cnd_0^{n-1}\sum_{m=0}^{M-1} x_{Sm},$$

with $M$ being the total number of masses on the circular support. If we now assume an explicit drive $x_{Sm} = d_S\cos(\omega_S t + 2\pi m/M)$, i.e. source masses that are equally spaced on a circle, we find that

$$\sum_{m=0}^{M-1} x_{Sm} = 0,$$

so surprisingly, in first order gravity vanishes *completely* for the multi-mass disk drive, and therefore this configuration provides a terribly inefficient source drive. Even more so, by the generalization of this argument any drive configuration that has a constant center of mass will not cause a gravitational drive in first order, as the dipole moment of the source mass is the main cause of the discussed effect.

# Personal acknowledgements

I want to wholeheartedly thank my colleagues who also became good friends during what has been a more than six-year journey towards this thesis. Michael, for the astonishing amount of weirdly specific memes and my first and everlasting bromance. Uros, for joyfully shared emotional destructiveness and his top-tier friendship skills. David, for owning my favorite cat and always being the last-standing sparring partner in entirely pointless but beautifully engaging discussions. Mathias, for continuous fruitful exchange of video game related themes and references and his occasional assistance in well-being. And Josh for being Josh, especially regarding (but not limited to) his ultimate pursuit of ridiculous awesomeness. The list goes on with Amir, Claus, Florian, Garrett, Hans, Igor, Jason, Karoline, Lorenzo, Nikolai, Philipp, Ralf, Ramon, Sebastian, Tobias and Witlef, who became integral parts of my Vienna experience.

Of the valuable people outside of my typical office habitat, obligatory acknowledgments go to Andrea, Anna, Bruno, Chiara, Heiko, Ina, Jan, Marlene, Stefan and Welm. In addition, I especially want to mention the individuals with whom I share some of the best memories of recent times. Dreamboy Andre, inventor of the "finger dance move" and the "sneaky Dre", cultural beacon and spiritual companion. Dreamboy Botho, ultimate provider of good vibes, whitest bro alive and the best reason to go to airports with no intention of flying anywhere. Christoph, preferred receiver of aubergine emojies and the proof that friendship can overcome time, distance and world views. Gilbert, my partner in crime, bringer of genuine abfak and appreciably brutal truth. Julia, who gave me a new perspective on Vienna at the right time and one of the very few people I was ever truly happy to have shared a WG with. And Marcus, for 19 years of friendship, nuanced in such unexpected things as a nearly identical musical taste including both death metal and early-2000s poprock.

I could not conclude without mentioning Klaus-Peter Haupt, who created a phenomenal opportunity for me to intensify my passion for physics and selflessly continues to do so for countless generations of students.

With the last words of this thesis, I want to deeply thank my parents, Gilla and Hans, for their unconditional and wholehearted support.

# Full contents

# Lists of tables and figures

## List of tables



## List of figures

# Bibliography


Abbott B. P., Abbott R., Abbott T. D., et al. (2016). "Observation of Gravitational Waves from a Binary Black Hole Merger". *Physical Review Letters* 116.6, p. 61102. DOI: 10.1103/PhysRevLett.116.061102 (cit. on pp. 10, 178).

Abbott B. P., Abbott R., Adhikari R., et al. (2009). "LIGO: the Laser Interferometer Gravitational-Wave Observatory". *Reports on Progress in Physics* 72.7, p. 076901. DOI: 10.1088/0034-4885/72/7/076901 (cit. on p. 128).

Abbott R., Adhikari R., et al. (2002). "Seismic isolation for Advanced LIGO". *Classical and Quantum Gravity* 19.7, pp. 1591–1597. DOI: 10.1088/0264-9381/19/7/349 (cit. on p. 171).

Acernese F. et al. (2015). "Advanced Virgo: a second-generation interferometric gravitational wave detector". *Classical and Quantum Gravity* 32.2, p. 024001. DOI: 10.1088/0264-9381/32/2/024001 (cit. on p. 10).

Adelberger E. et al. (2009). "Torsion balance experiments: A low-energy frontier of particle physics". *Progress in Particle and Nuclear Physics* 62.1, pp. 102–134. DOI: 10.1016/j.ppnp.2008.08.002 (cit. on p. 13).

Aguilera D. N. et al. (2014). "STE-QUEST – test of the universality of free fall using cold atom interferometry". *Classical and Quantum Gravity* 31.11, p. 115010. DOI: 10.1088/0264-9381/31/11/115010 (cit. on p. 13).

Albrecht T. R. et al. (1991). "Frequency modulation detection using high-Q cantilevers for enhanced force microscope sensitivity". *Journal of Applied Physics* 69.2, pp. 668–673. DOI: 10.1063/1.347347 (cit. on p. 112).

Alemi A. (2009). *Building Planets*. URL: http://pages.physics.cornell.edu/~aalemi/random/planet.pdf (visited on Sept. 21, 2016) (cit. on p. 113).

Alexandrova S., Szekeres A., and Christova K. (1988). "Stress in silicon dioxide films". *Philosophical Magazine Letters* 58.1, pp. 33–36. DOI: 10.1080/09500838808214727 (cit. on p. 118).

Amaro-Seoane P. et al. (2012). "Low-frequency gravitational-wave science with eLISA/NGO". *Classical and Quantum Gravity* 29.12, p. 124016. DOI: 10.1088/0264-9381/29/12/124016 (cit. on pp. 10, 67).

Anastopoulos C. and Hu B. L. (2015). "Probing a gravitational cat state". *Classical and Quantum Gravity* 32.16, p. 165022. DOI: 10.1088/0264-9381/32/16/165022 (cit. on p. 15).

Ang X. et al. (2006). "Pressure dependence in peripheral bonding in gold-gold thermocompression". *8th Electronics Packaging Technology Conference*. IEEE, pp. 318–323. DOI: 10.1109/EPTC.2006.342736 (cit. on p. 95).

Antoniadis I., Dimopoulos S., and Dvali G. (1998). "Millimetre-range forces in superstring theories with weak-scale compactification". *Nuclear Physics B* 516.1, pp. 70–82. DOI: 10.1016/S0550-3213(97)00808-0 (cit. on p. 12).

Antoniadis I. (2005). "Extra dimensions and possible modifications of Newton's law". *Journal of Physics: Conference Series* 8.1, pp. 112–121. DOI: 10.1088/1742-6596/8/1/015 (cit. on p. 12).

Archard J. F. and Taylor A. M. (1948). "Improved Glan-Foucault Prism". *Journal of Scientific Instruments* 25.12, pp. 407–409. DOI: 10.1088/0950-7671/25/12/304 (cit. on p. 133).

Arcizet O. et al. (2006). "High-Sensitivity Optical Monitoring of a Micromechanical Resonator with a Quantum-Limited Optomechanical Sensor". *Physical Review Letters* 97.13, p. 133601. DOI: 10.1103/PhysRevLett.97.133601 (cit. on p. 112).

Arkani-Hamed N., Dimopoulos S., and Dvali G. (1999). "Phenomenology, astrophysics, and cosmology of theories with submillimeter dimensions and TeV scale quantum gravity". *Physical Review D* 59.8, p. 086004. DOI: 10.1103/PhysRevD.59.086004 (cit. on p. 12).

Armstrong T. R. and Fitzgerald M. P. (2003). "New Measurements of *G* Using the Measurement Standards Laboratory Torsion Balance". *Physical Review Letters* 91.20, p. 201101. DOI: 10.1103/PhysRevLett.91.201101 (cit. on pp. 11, 176).

Arndt M. and Hornberger K. (2014). "Testing the limits of quantum mechanical superpositions". *Nature Physics* 10.4, pp. 271–277. DOI: 10.1038/nphys2863 (cit. on p. 15).

Arndt M., Nairz O., et al. (1999). "Wave-particle duality of $C_{60}$ molecules". *Nature* 401.6754, pp. 680–682. DOI: 10.1038/44348 (cit. on p. 178).

Asenbaum P. et al. (2013). "Cavity cooling of free silicon nanoparticles in high vacuum". *Nature Communications* 4, p. 2743. DOI: 10.1038/ncomms3743 (cit. on p. 8).

Aspelmeyer M. (2017). "Entanglement through Gravity". Private communication (cit. on p. 179).

Aspelmeyer M., Kippenberg T. J., and Marquardt F. (2014). "Cavity optomechanics". *Reviews of Modern Physics* 86.4, pp. 1391–1452. DOI: 10.1103/RevModPhys.86.1391 (cit. on p. 7).

Aspelmeyer M., Meystre P., and Schwab K. (2012). "Quantum optomechanics". *Physics Today* 65.7, pp. 29–35. DOI: 10.1063/PT.3.1640 (cit. on p. 7).

Aston S. M. et al. (2012). "Update on quadruple suspension design for Advanced LIGO". *Classical and Quantum Gravity* 29.23, p. 235004. DOI: 10.1088/0264-9381/29/23/235004 (cit. on pp. 73, 156, 157).

Aston S. M. (2011). "Optical Read-out Techniques for the Control of Test-masses in Gravitational Wave Observatories". PhD thesis. University of Birmingham (cit. on p. 171).

attocube systems AG (2016). *attocube | pioneers of precision*. URL: http://www.attocube.com/ (visited on Jan. 5, 2017) (cit. on p. 124).

Bachor H.-A. and Ralph T. C. (2004). *A Guide to Experiments in Quantum Optics*. Second. Hoboken: Wiley (cit. on pp. 128, 129, 132, 135).

Bagley C. and Luther G. (1997). "Preliminary Results of a Determination of the Newtonian Constant of Gravitation: A Test of the Kuroda Hypothesis". *Physical Review Letters* 78.16, pp. 3047–3050. DOI: 10.1103/PhysRevLett.78.3047 (cit. on p. 176).

Bah T. et al. (2003). *Inkscape*. URL: https://inkscape.org/ (visited on Sept. 28, 2016) (cit. on p. iv).

Bahrami M., Bassi A., et al. (2015). *Is Gravity Quantum?* arXiv: 1507.05733 [quant-ph] (cit. on p. 15).

Bahrami M., Smirne A., and Bassi A. (2014). "Role of gravity in the collapse of a wave function: A probe into the Diósi-Penrose model". *Physical Review A* 90.6, p. 062105. DOI: 10.1103/PhysRevA.90.062105 (cit. on p. 14).

Bak P. and Sneppen K. (1993). "Punctuated equilibrium and criticality in a simple model of evolution". *Physical Review Letters* 71.24, pp. 4083–4086. DOI: 10.1103/PhysRevLett.71.4083 (cit. on p. 48).

Barton M. (2004). *Advanced LIGO Quad Pendulum Model*. URL: https://labcit.ligo.caltech.edu/~e2e/SUSmodels/ (visited on Sept. 22, 2016) (cit. on pp. 71, 74).

Bawaj M. et al. (2015). "Probing deformed commutators with macroscopic harmonic oscillators". *Nature Communications* 6, p. 7503. DOI: 10.1038/ncomms8503 (cit. on p. 13).

Beccaria M. et al. (1998). "The creep problem in the VIRGO suspensions: a possible solution using Maraging steel". *Nuclear Instruments and Methods in Physics Research Section A: Accelerators, Spectrometers, Detectors and Associated Equipment* 404.2, pp. 455–469. DOI: 10.1016/S0168-9002(97)01123-6 (cit. on p. 149).

Behunin R. O. et al. (2014). "Limits on the accuracy of force sensing at short separations due to patch potentials". *Physical Review D* 89.5, p. 051301. DOI: 10.1103/PhysRevD.89.051301 (cit. on pp. 24, 85).

Belenchia A. et al. (2016). "Testing Quantum Gravity Induced Nonlocality via Optomechanical Quantum Oscillators". *Physical Review Letters* 116.16, p. 161303. DOI: 10.1103/PhysRevLett.116.161303 (cit. on p. 15).

Benvenuti C. and Chiggiato P. (1993). "Obtention of pressures in the $10^{-14}$ torr range by means of a ZrVFe non evaporable getter". *Vacuum* 44.5, pp. 511–513. DOI: 10.1016/0042-207X(93)90084-N (cit. on p. 169).

Berman A. (1996). "Water vapor in vacuum systems". *Vacuum* 47.4, pp. 327–332. DOI: 10.1016/0042-207X(95)00246-4 (cit. on p. 169).

Bern Z. (2002). "Perturbative Quantum Gravity and its Relation to Gauge Theory". *Living Reviews in Relativity* 5. DOI: 10.12942/lrr-2002-5 (cit. on p. 14).

Biedermann G. W. et al. (2015). "Testing gravity with cold-atom interferometers". *Physical Review A* 91.3, p. 033629. DOI: 10.1103/PhysRevA.91.033629 (cit. on p. 9).

Biercuk M. J. et al. (2010). "Ultrasensitive detection of force and displacement using trapped ions." *Nature nanotechnology* 5.9, pp. 646–50. DOI: 10.1038/nnano.2010.165 (cit. on p. 6).

Billingsley P. (2012). *Probability and measure*. Fourth. Wiley (cit. on p. 45).
Blair D. G. et al. (2012). *Advanced Gravitational Wave Detectors*. Ed. by D. G. Blair et al. First. Cambridge University Press (cit. on pp. 10, 154, 155, 158).
Blencowe M. P. (2013). "Effective Field Theory Approach to Gravitationally Induced Decoherence". *Physical Review Letters* 111.2, p. 021302. DOI: 10.1103/PhysRevLett.111.021302 (cit. on p. 14).
Blender Foundation (1995). *The Blender project*. URL: https://www.blender.org/ (visited on Sept. 28, 2016) (cit. on p. iv).
Bleszynski-Jayich A. C. et al. (2009). "Persistent currents in normal metal rings." *Science* 326.5950, pp. 272–5. DOI: 10.1126/science.1178139 (cit. on p. 5).
Boashash B. (2015). *Time frequency signal analysis and processing : a comprehensive reference*. Second. Academic Press (cit. on p. 25).
Böhm H. R. (2007). "Radiation-Pressure Cooling of a Mechanical Oscillator". PhD thesis. University of Vienna (cit. on p. 130).
Braginsky V., Ryazhskaya O., and Vyatchanin S. (2006). "Notes about noise in gravitational wave antennas created by cosmic rays". *Physics Letters A* 350.1-2, pp. 1–4. DOI: 10.1016/j.physleta.2005.09.073 (cit. on p. 109).
Braginsky V. B., Khalili F. Y., et al. (1995). *Quantum Measurement*. First. Cambridge University Press (cit. on p. 56).
Brax P. et al. (2008). "$f(R)$ gravity and chameleon theories". *Physical Review D* 78.10, p. 104021. DOI: 10.1103/PhysRevD.78.104021 (cit. on p. 12).
Brown R. G. and Hwang P. Y. C. (2012). *Introduction to random signals and applied Kalman filtering with MATLAB exercises*. Fourth. Wiley (cit. on p. 25).
Buchman S. et al. (1995). "Charge measurement and control for the Gravity Probe B gyroscopes". *Review of Scientific Instruments* 66.1, p. 120. DOI: 10.1063/1.1145276 (cit. on p. 109).
Burnham N., Colton R., and Pollock H. (1992). "Work-function anisotropies as an origin of long-range surface forces." *Physical review letters* 69.1, pp. 144–147. DOI: 10.1103/PhysRevLett.69.144 (cit. on p. 43).
Bushev P. et al. (2013). "Shot-Noise-Limited Monitoring and Phase Locking of the Motion of a Single Trapped Ion". *Physical Review Letters* 110.13, p. 133602. DOI: 10.1103/PhysRevLett.110.133602 (cit. on p. 112).
Butt H. J. and Jaschke M. (1995). "Calculation of thermal noise in atomic force microscopy". *Nanotechnology* 6.1, p. 1. DOI: 10.1088/0957-4484/6/1/001 (cit. on p. 45).
Butt H.-J., Cappella B., and Kappl M. (2005). "Force measurements with the atomic force microscope: Technique, interpretation and applications". *Surface Science Reports* 59.1-6, pp. 1–152. DOI: 10.1016/j.surfrep.2005.08.003 (cit. on p. 94).
Carbone L. et al. (2012). "Sensors and actuators for the Advanced LIGO mirror suspensions". *Classical and Quantum Gravity* 29.11, p. 115005. DOI: 10.1088/0264-9381/29/11/115005 (cit. on p. 171).
Cavalleri A., Ciani G., Dolesi R., Heptonstall A., et al. (2009). "Increased Brownian Force Noise from Molecular Impacts in a Constrained Volume". *Physical Review Letters* 103.14, p. 140601. DOI: 10.1103/PhysRevLett.103.140601 (cit. on p. 101).
Cavalleri A., Ciani G., Dolesi R., Hueller M., et al. (2010). "Gas damping force noise on a macroscopic test body in an infinite gas reservoir". *Physics Letters A* 374.34, pp. 3365–3369. DOI: 10.1016/j.physleta.2010.06.041 (cit. on p. 100).
Cavendish H. (1798). "Experiments to Determine the Density of the Earth. By Henry Cavendish, Esq. F. R. S. and A. S." *Philosophical Transactions of the Royal Society of London* 88, pp. 469–526. DOI: 10.1098/rstl.1798.0022 (cit. on pp. 9, 10).
Caves C. M. (1980). "Quantum-Mechanical Radiation-Pressure Fluctuations in an Interferometer". *Physical Review Letters* 45.2, pp. 75–79. DOI: 10.1103/PhysRevLett.45.75 (cit. on p. 56).
Cella G. et al. (2002). "Seismic attenuation performance of the first prototype of a geometric anti-spring filter". *Nuclear Instruments and Methods in Physics Research Section A: Accelerators, Spectrometers, Detectors and Associated Equipment* 487.3, pp. 652–660. DOI: 10.1016/S0168-9002(01)02193-3 (cit. on p. 154).
Chakram S. et al. (2014). "Dissipation in Ultrahigh Quality Factor SiN Membrane Resonators". *Physical Review Letters* 112.12, p. 127201. DOI: 10.1103/PhysRevLett.112.127201 (cit. on p. 116).
Chan H. B., Aksyuk V. A., et al. (2001). "Quantum mechanical actuation of microelectromechanical systems by the Casimir force." *Science* 291.5510, pp. 1941–4. DOI: 10.1126/science.1057984 (cit. on p. 94).
Chan J., Alegre T. P. M., et al. (2011). "Laser cooling of a nanomechanical oscillator into its quantum ground state." *Nature* 478.7367, pp. 89–92. DOI: 10.1038/nature10461 (cit. on p. 8).

Chang D. E. et al. (2010). "Cavity opto-mechanics using an optically levitated nanosphere." *Proceedings of the National Academy of Sciences of the United States of America* 107.3, pp. 1005–10. DOI: 10.1073/pnas.0912969107 (cit. on p. 44).

Chou C. W. et al. (2010). "Optical clocks and relativity." *Science* 329.5999, pp. 1630–3. DOI: 10.1126/science.1192720 (cit. on p. 9).

Churnside A. B. et al. (2012). "Routine and timely sub-picoNewton force stability and precision for biological applications of atomic force microscopy." *Nano letters* 12.7, pp. 3557–61. DOI: 10.1021/nl301166w (cit. on p. 95).

Cirio M., Brennen G. K., and Twamley J. (2012). "Quantum magnetomechanics: ultrahigh-$Q$-levitated mechanical oscillators." *Physical review letters* 109.14, p. 147206. DOI: 10.1103/PhysRevLett.109.147206 (cit. on pp. 8, 175).

Ciufolini I. and Pavlis E. C. (2004). "A confirmation of the general relativistic prediction of the Lense-Thirring effect". *Nature* 431.7011, pp. 958–960. DOI: 10.1038/nature03007 (cit. on p. 178).

Clerk A. A. et al. (2010). "Introduction to quantum noise, measurement, and amplification". *Reviews of Modern Physics* 82.2, pp. 1155–1208. DOI: 10.1103/RevModPhys.82.1155 (cit. on pp. 23, 45–48, 56, 128, 193).

Cole G. D. (2012). "Cavity optomechanics with low-noise crystalline mirrors". *Proc. SPIE 8458, Optical Trapping and Optical Micromanipulation IX*, p. 845807. DOI: 10.1117/12.931226 (cit. on p. 105).

Cole G. D., Gröblacher S., et al. (2008). "Monocrystalline $Al_xGa_{1-x}As$ heterostructures for high-reflectivity high-$Q$ micromechanical resonators in the megahertz regime". *Applied Physics Letters* 92.26, p. 261108. DOI: 10.1063/1.2952512 (cit. on p. 115).

Cole G. D., Wilson-Rae I., et al. (2011). "Phonon-tunnelling dissipation in mechanical resonators." *Nature communications* 2, p. 231. DOI: 10.1038/ncomms1212 (cit. on p. 115).

Cole G. D., Yu P. L., et al. (2014). "Tensile-strained InGaP membranes for cavity optomechanics". *Applied Physics Letters* 104.20, p. 201908. DOI: 10.1063/1.4879755 (cit. on p. 115).

Cole G. D., Zhang W., et al. (2016). "High-performance near- and mid-infrared crystalline coatings". *Optica* 3.6, p. 647. DOI: 10.1364/OPTICA.3.000647 (cit. on pp. 107, 155).

Colella R., Overhauser A. W., and Werner S. A. (1975). "Observation of Gravitationally Induced Quantum Interference". *Physical Review Letters* 34.23, pp. 1472–1474. DOI: 10.1103/PhysRevLett.34.1472 (cit. on p. 9).

Corinthios M. (2009). *Signals, systems, transforms, and digital signal processing with MATLAB*. First. CRC Press (cit. on p. 22).

Corti C., Holliday R., and World Gold Council (2010). *Gold: Science and Applications*. First. CRC Press (cit. on p. 95).

Coyne D. et al. (2007). *Advanced LIGO Single Stage HAM Vibration Isolation Table*. LIGO viewgraph G-0701156-00-R (cit. on pp. 72, 131, 149, 151, 171).

Crooks D. R. M. (2002). "Mechanical loss and its significance in the test mass mirrors of gravitational wave detectors". PhD thesis. University of Glasgow (cit. on p. 153).

Cumming A. V. et al. (2014). "Silicon mirror suspensions for gravitational wave detectors". *Classical and Quantum Gravity* 31.2, p. 025017. DOI: 10.1088/0264-9381/31/2/025017 (cit. on p. 118).

Cutler C. and Thorne K. S. (2002). "An Overview of Gravitational-Wave Sources". *World Scientific*, pp. 1–40. DOI: 10.1142/9789812776556_0004 (cit. on p. 9).

Davenport W. B. and Root W. L. (1987). *An introduction to the theory of random signals and noise*. First. IEEE Press (cit. on p. 19).

Derakhshani M., Anastopoulos C., and Hu B. L. (2016). "Probing a Gravitational Cat State: Experimental Possibilities". *Journal of Physics: Conference Series* 701.1, p. 012015. DOI: 10.1088/1742-6596/701/1/012015 (cit. on p. 15).

DeWitt C. M. and Rickles D. (2011). *The Role of Gravitation in Physics: Report from the 1957 Chapel Hill Conference*. First. Edition Open Access (cit. on p. 179).

Diggory I. S. et al. (1974). "The momentum spectra of nuclear active particles in the cosmic radiation at sea level. I. Experimental data". *Journal of Physics A: Mathematical, Nuclear and General* 7.6, pp. 741–764. DOI: 10.1088/0305-4470/7/6/010 (cit. on pp. 110, 111).

Dimopoulos S. and Giudice G. (1996). "Macroscopic forces from supersymmetry". *Physics Letters B* 379.1, pp. 105–114. DOI: 10.1016/0370-2693(96)00390-5 (cit. on p. 12).

Diósi L. (1989). "Models for universal reduction of macroscopic quantum fluctuations". *Physical Review A* 40.3, pp. 1165–1174. DOI: 10.1103/PhysRevA.40.1165 (cit. on p. 14).

Dolesi R. et al. (2011). "Brownian force noise from molecular collisions and the sensitivity of advanced gravitational wave observatories". *Physical Review D* 84.6, p. 063007. DOI: 10.1103/PhysRevD.84.063007 (cit. on p. 101).

Donoghue J. F. (1994). "General relativity as an effective field theory: The leading quantum corrections". *Physical Review D* 50.6, pp. 3874–3888. DOI: 10.1103/PhysRevD.50.3874 (cit. on p. 14).
Dragosits M. (2016). "An approach to a high frequency linear movement engine with millimetre displacement for a micro-mechanical proof of principle experiment for measuring the forces of milligram masses". Bachelor's thesis. University of Vienna (cit. on p. 125).
Drummer E. et al. (2008). "Magnetventilgesteuerte Einspritzdüse". Pat. DE 10235240 B4 (cit. on p. 126).
Dumas J. C. et al. (2004). "Testing of a multi-stage low-frequency isolator using Euler spring and self-damped pendulums". *Classical and Quantum Gravity* 21.5, S965–S971. DOI: 10.1088/0264-9381/21/5/087 (cit. on p. 154).
Einstein A. and Rosen N. (1937). "On gravitational waves". *Journal of the Franklin Institute* 223.1, pp. 43–54. DOI: 10.1016/S0016-0032(37)90583-0 (cit. on p. 9).
Everitt C. W. F. et al. (2011). "Gravity Probe B: Final Results of a Space Experiment to Test General Relativity". *Physical Review Letters* 106.22, p. 221101. DOI: 10.1103/PhysRevLett.106.221101 (cit. on p. 178).
Feldman M. R. et al. (2016). "Deep space experiment to measure G". *Classical and Quantum Gravity* 33.12, p. 125013. DOI: 10.1088/0264-9381/33/12/125013 (cit. on p. 12).
Feuersänger C. (2008). *CTAN: Package pgfplots*. URL: https://www.ctan.org/pkg/pgfplots (visited on Sept. 28, 2016) (cit. on p. iv).
Fickler R. et al. (2012). "Quantum Entanglement of High Angular Momenta". *Science* 338.6107, pp. 640–643. DOI: 10.1126/science.1227193 (cit. on p. 178).
Flaminio R. and KAGRA collaboration the (2016). "The cryogenic challenge: status of the KAGRA project". *Journal of Physics: Conference Series* 716.1, p. 012034. DOI: 10.1088/1742-6596/716/1/012034 (cit. on pp. 10, 155).
Fletcher N. H. (1992). *Acoustic systems in biology*. First. Oxford University Press (cit. on p. 116).
Fort Wayne (2017). *Fort Wayne Metals*. URL: http://fwmetals.com/ (visited on Jan. 6, 2017) (cit. on p. 161).
Friedman J. R. et al. (2000). "Quantum superposition of distinct macroscopic states". *Nature* 406.6791, pp. 43–46. DOI: 10.1038/35017505 (cit. on p. 178).
Fritschel P. et al. (2001). *Seismic Isolation Subsystem Design Requirements Document*. LIGO engineering documentation E990303-03-D (cit. on p. 158).
Fujii Y. et al. (2016). "Active damping performance of the KAGRA seismic attenuation system prototype". *Journal of Physics: Conference Series* 716.1, p. 012022. DOI: 10.1088/1742-6596/716/1/012022 (cit. on p. 154).
Gatscher J. A. and Kawiecki G. (1996). "Comparison of Mechanical Impedance Methods for Vibration Simulation". *Shock and Vibration* 3.3, pp. 223–232. DOI: 10.3233/SAV-1996-3308 (cit. on pp. 50, 68, 79).
Genet C. et al. (2003). "Electromagnetic vacuum fluctuations, Casimir and Van der Waals forces". *Annales de la Fondation Louis de Broglie* 29.1-2, pp. 331–348 (cit. on p. 42).
Geraci A. A., Papp S. B., and Kitching J. (2010). "Short-Range Force Detection Using Optically Cooled Levitated Microspheres". *Physical Review Letters* 105.10, p. 101101. DOI: 10.1103/PhysRevLett.105.101101 (cit. on p. 13).
Geraci A. A., Smullin S. J., et al. (2008). "Improved constraints on non-Newtonian forces at 10 microns". *Physical Review D* 78.2, p. 022002. DOI: 10.1103/PhysRevD.78.022002 (cit. on pp. 6, 12, 13).
Gerlich S. et al. (2011). "Quantum interference of large organic molecules". *Nature Communications* 2, p. 263. DOI: 10.1038/ncomms1263 (cit. on p. 178).
Gerry C. C. and Knight P. L. (2005). *Introductory quantum optics*. First. Cambridge University Press (cit. on p. 58).
Ghirardi G. C., Rimini A., and Weber T. (1985). "A model for a unified quantum description of macroscopic and microscopic systems". *Quantum Probability and Applications II: Proceedings of a Workshop held in Heidelberg, West Germany, October 1–5, 1984*. Ed. by L. Accardi and W. von Waldenfels. Springer Berlin Heidelberg, pp. 223–232. DOI: 10.1007/BFb0074474 (cit. on p. 14).
Ghirardi G. C., Rimini A., and Weber T. (1986). "Unified dynamics for microscopic and macroscopic systems". *Physical Review D* 34.2, pp. 470–491. DOI: 10.1103/PhysRevD.34.470 (cit. on p. 14).
Ghirardi G. C., Pearle P., and Rimini A. (1990). "Markov processes in Hilbert space and continuous spontaneous localization of systems of identical particles". *Physical Review A* 42.1, pp. 78–89. DOI: 10.1103/PhysRevA.42.78 (cit. on p. 14).
Giessibl F. J. (2003). "Advances in atomic force microscopy". *Reviews of Modern Physics* 75.3, pp. 949–983. DOI: 10.1103/RevModPhys.75.949 (cit. on p. 112).

Gillespie A. and Raab F. (1993). "Thermal noise in the test mass suspensions of a laser interferometer gravitational-wave detector prototype". *Physics Letters A* 178.5, pp. 357–363. DOI: 10.1016/0375-9601(93)90861-S (cit. on p. 155).
Gillespie A. and Raab F. (1994). "Suspension losses in the pendula of laser interferometer gravitational-wave detectors". *Physics Letters A* 190.3, pp. 213–220. DOI: 10.1016/0375-9601(94)90744-7 (cit. on p. 155).
Gillespie A. and Raab F. (1995). "Thermally excited vibrations of the mirrors of laser interferometer gravitational-wave detectors". *Physical Review D* 52.2, pp. 577–585. DOI: 10.1103/PhysRevD.52.577 (cit. on pp. 97, 138, 155).
Gillies G. T. and Unnikrishnan C. S. (2014). "The attracting masses in measurements of *G*: an overview of physical characteristics and performance." *Philosophical transactions. Series A, Mathematical, physical, and engineering sciences* 372.2026, pp. 20140022–. DOI: 10.1098/rsta.2014.0022 (cit. on pp. 5, 12, 84, 89, 176).
Gillies G. T. (1997). "The Newtonian gravitational constant: recent measurements and related studies". *Reports on Progress in Physics* 60.2, pp. 151–225. DOI: 10.1088/0034-4885/60/2/001 (cit. on p. 12).
González G. (2000). "Suspensions thermal noise in the LIGO gravitational wave detector". *Classical and Quantum Gravity* 17.21, pp. 4409–4435. DOI: 10.1088/0264-9381/17/21/305 (cit. on p. 162).
Goodkind J. M. (1999). "The superconducting gravimeter". *Review of Scientific Instruments* 70.11, p. 4131. DOI: 10.1063/1.1150092 (cit. on p. 149).
Goßler S. (2004). "The suspension systems of the interferometric gravitational-wave detector GEO 600". PhD thesis. University of Hannover (cit. on p. 163).
Goulielmakis E. et al. (2004). "Direct Measurement of Light Waves". *Science* 305.5688. DOI: 10.1126/science.1100866 (cit. on p. 20).
Gras S. et al. (2015). "Resonant dampers for parametric instabilities in gravitational wave detectors". *Physical Review D* 92.8, p. 082001. DOI: 10.1103/PhysRevD.92.082001 (cit. on p. 164).
Greenhalgh J. (2005). *Blade springs with a point bending moment at the tip, and lateral stiffness of blade*. LIGO technical note T050253-00-K (cit. on p. 150).
Grieder P. K. (2001). *Cosmic Rays at Earth*. First. Elsevier (cit. on p. 110).
Gröblacher S. et al. (2009). "Observation of strong coupling between a micromechanical resonator and an optical cavity field." *Nature* 460.7256, pp. 724–7. DOI: 10.1038/nature08171 (cit. on p. 8).
Gundlach J. and Merkowitz S. (2000). "Measurement of Newton's Constant Using a Torsion Balance with Angular Acceleration Feedback". *Physical Review Letters* 85.14, pp. 2869–2872. DOI: 10.1103/PhysRevLett.85.2869 (cit. on pp. 11, 158, 176).
Guzmán Cervantes F. et al. (2014). "High sensitivity optomechanical reference accelerometer over 10 kHz". *Applied Physics Letters* 104.22, p. 221111. DOI: 10.1063/1.4881936 (cit. on pp. 8, 143).
Hablanian M. H. (1997). *High-vacuum technology: a practical guide*. Second. CRC Press (cit. on p. 169).
Hamaker H. (1937). "The London-van der Waals attraction between spherical particles". *Physica* 4.10, pp. 1058–1072. DOI: 10.1016/S0031-8914(37)80203-7 (cit. on pp. 42, 85).
Hamilton P. et al. (2015). "Atom-interferometry constraints on dark energy". *Science* 349.6250, pp. 849–51. DOI: 10.1126/science.aaa8883 (cit. on pp. 6, 13).
Harris F. (1978). "On the use of windows for harmonic analysis with the discrete Fourier transform". *Proceedings of the IEEE* 66.1, pp. 51–83. DOI: 10.1109/PROC.1978.10837 (cit. on p. 199).
Harry G. M. et al. (2002). "Thermal noise in interferometric gravitational wave detectors due to dielectric optical coatings". *Classical and Quantum Gravity* 19.5, pp. 897–917. DOI: 10.1088/0264-9381/19/5/305 (cit. on p. 105).
Haynes W. M. (2014). *CRC Handbook of Chemistry and Physics*. Ninety-fifth. CRC Press (cit. on p. 95).
Heinzel G. (1999). *LISO – Program for Linear Simulation and Optimization of analog electronic circuits*. URL: http://www2.mpq.mpg.de/~ros/geo600_docu/soft/liso/manual.pdf (visited on Feb. 26, 2017) (cit. on p. 184).
Heinzel G. et al. (2002). *Spectrum and spectral density estimation by the Discrete Fourier transform (DFT), including a comprehensive list of window functions and some new flat-top windows*. URL: https://holometer.fnal.gov/GH_FFT.pdf (visited on Nov. 4, 2016) (cit. on p. 199).
Heisenberg W. (1930). *The Physical Principles of the Quantum Theory*. First. Dover Publications (cit. on p. 47).
Hepach H. (2015). "Design and Characterisation of a Low-Noise Audio-Band Photodetector at 100 mW Optical Power". Master's thesis. University of Vienna (cit. on p. 144).
Herzan LLC (2016). *Acoustic and Vibration Isolation Specialists*. URL: http://www.herzan.com/ (visited on Jan. 6, 2017) (cit. on p. 159).

Hewitson M. et al. (2007). "Charge measurement and mitigation for the main test masses of the GEO 600 gravitational wave observatory". *Classical and Quantum Gravity* 24.24, pp. 6379–6391. DOI: 10.1088/0264-9381/24/24/013 (cit. on p. 109).
Hobbs P. C. D. (2009). *Building electro-optical systems: making it all work*. Second. Wiley (cit. on p. 143).
Hoogenboom B. W. et al. (2005). "A Fabry-Perot interferometer for micrometer-sized cantilevers". *Applied Physics Letters* 86.7, pp. 1–3. DOI: 10.1063/1.1866229 (cit. on p. 143).
Hori T. (1997). "Thermally Grown Silicon Oxide". *Gate Dielectrics and MOS ULSIs: Principles, Technologies and Applications*. Springer Berlin Heidelberg, pp. 149–207. DOI: 10.1007/978-3-642-60856-8_4 (cit. on p. 118).
Horowitz P. and Hill W. (1994). *The art of electronics*. Third. Cambridge University Press (cit. on p. 143).
Hoskins J. K. et al. (1985). "Experimental tests of the gravitational inverse-square law for mass separations from 2 to 105 cm". *Physical Review D* 32.12, pp. 3084–3095. DOI: 10.1103/PhysRevD.32.3084 (cit. on p. 90).
Howl R. et al. (2016). *Gravity in the Quantum Lab*. arXiv: 1607.06666 [quant-ph] (cit. on p. 15).
Hu Z.-K., Guo J.-Q., and Luo J. (2005). "Correction of source mass effects in the HUST-99 measurement of G". *Physical Review D* 71.12. DOI: 10.1103/PhysRevD.71.127505 (cit. on pp. 11, 176).
Hua W. (2005). "Low frequency vibration isolation and alignment system for advanced ligo". PhD thesis. Stanford University (cit. on p. 71).
Hulse R. A. and Taylor J. H. (1975). "Discovery of a pulsar in a binary system". *The Astrophysical Journal* 195, p. L51. DOI: 10.1086/181708 (cit. on pp. 9, 178).
Husman M. E. et al. (2000). "Modeling of multistage pendulums: Triple pendulum suspension for GEO 600". *Review of Scientific Instruments* 71.6, p. 2546. DOI: 10.1063/1.1150646 (cit. on p. 71).
Ibrahim R. (2008). "Recent advances in nonlinear passive vibration isolators". *Journal of Sound and Vibration* 314.3, pp. 371–452. DOI: 10.1016/j.jsv.2008.01.014 (cit. on p. 154).
Imboden M. and Mohanty P. (2014). "Dissipation in nanoelectromechanical systems". *Physics Reports* 534.3, pp. 89–146. DOI: 10.1016/j.physrep.2013.09.003 (cit. on p. 93).
Inguscio M., Stringari S., and Wieman C. E. (1999). *Bose-Einstein Condensation in Atomic Gases (Proceedings of the International School of Physics)*. First. Amsterdam: IOS Press (cit. on p. 87).
Issler L., Ruoß H., and Häfele P. (2003). *Festigkeitslehre – Grundlagen*. Second. Springer-Lehrbuch. Springer. DOI: 10.1007/978-3-540-73485-7 (cit. on p. 95).
Jackson J. D. (1998). *Classical Electrodynamics*. Third. Wiley (cit. on p. 111).
Jenke T., Cronenberg G., et al. (2014). "Gravity Resonance Spectroscopy Constrains Dark Energy and Dark Matter Scenarios". *Physical Review Letters* 112.15, p. 151105. DOI: 10.1103/PhysRevLett.112.151105 (cit. on p. 13).
Jenke T., Geltenbort P., et al. (2011). "Realization of a gravity-resonance-spectroscopy technique". *Nature Physics* 7.6, pp. 468–472. DOI: 10.1038/nphys1970 (cit. on pp. 9, 13).
Juffmann T. et al. (2012). "Real-time single-molecule imaging of quantum interference". *Nature Nanotechnology* 7.5, pp. 297–300. DOI: 10.1038/nnano.2012.34 (cit. on p. 179).
Julsgaard B., Kozhekin A., and Polzik E. S. (2001). "Experimental long-lived entanglement of two macroscopic objects". *Nature* 413.6854, pp. 400–403. DOI: 10.1038/35096524 (cit. on p. 178).
Kafri D., Taylor J. M., and Milburn G. J. (2014). "A classical channel model for gravitational decoherence". *New Journal of Physics* 16.6, p. 065020. DOI: 10.1088/1367-2630/16/6/065020 (cit. on p. 14).
Kapner D. J. et al. (2007). "Tests of the Gravitational Inverse-Square Law below the Dark-Energy Length Scale". *Physical Review Letters* 98.2, p. 021101. DOI: 10.1103/PhysRevLett.98.021101 (cit. on pp. 13, 90).
Karagioz O. V. and Izmailov V. P. (1996). "Measurement of the gravitational constant with a torsion balance". *Measurement Techniques* 39.10, pp. 979–987. DOI: 10.1007/BF02377461 (cit. on p. 176).
Kasevich M. and Chu S. (1991). "Atomic interferometry using stimulated Raman transitions." *Physical review letters* 67.2, pp. 181–184. DOI: 10.1103/PhysRevLett.67.181 (cit. on p. 9).
Keane A. (1995). "Passive vibration control via unusual geometries: the application of genetic algorithm optimization to structural design". *Journal of Sound and Vibration* 185.3, pp. 441–453. DOI: 10.1006/jsvi.1995.0391 (cit. on p. 67).
Kehagias A. and Sfetsos K. (2000). "Deviations from the $1/r^2$ Newton law due to extra dimensions". *Physics Letters B* 472.1-2, pp. 39–44. DOI: 10.1016/S0370-2693(99)01421-5 (cit. on p. 12).
Keith J. T. (2015). "Recent astronomical tests of general relativity". *International Journal of Physical Sciences* 10.2, pp. 90–105. DOI: 10.5897/IJPS2014.4236 (cit. on p. 9).
Kiefer C. (2007). "Why Quantum Gravity?" *Approaches to Fundamental Physics: An Assessment of Current Theoretical Ideas*. Berlin, Heidelberg: Springer Berlin Heidelberg, pp. 123–130. DOI: 10.1007/978-3-540-71117-9_7 (cit. on p. 13).

Kiefer C. (2012). *Quantum Gravity*. Third. Oxford University Press. DOI: 10.1093/acprof:oso/9780199585205.001.0001 (cit. on p. 13).
Kiesel N. et al. (2013). "Cavity cooling of an optically levitated submicron particle." *Proceedings of the National Academy of Sciences of the United States of America* 110.35, pp. 14180–5. DOI: 10.1073/pnas.1309167110 (cit. on p. 8).
Kim W. J. et al. (2010). "Surface contact potential patches and Casimir force measurements". *Physical Review A* 81.2, p. 022505. DOI: 10.1103/PhysRevA.81.022505 (cit. on p. 43).
Kippenberg T. J. and Vahala K. J. (2008). "Cavity optomechanics: back-action at the mesoscale." *Science* 321.5893, pp. 1172–6. DOI: 10.1126/science.1156032 (cit. on p. 7).
Kleinevoß U. (2002). "Bestimmung der Newtonschen Gravitationskonstanten *G*". PhD thesis. Gesamthochschule Wuppertal (cit. on pp. 11, 176).
Klimenko S. et al. (2011). "Localization of gravitational wave sources with networks of advanced detectors". DOI: 10.1103/PhysRevD.83.102001 (cit. on p. 10).
Knizikevičius R. and Kopustinskas V. (2004). "Anisotropic etching of silicon in $SF_6$ plasma". *Vacuum* 77.1, pp. 1–4. DOI: 10.1016/j.vacuum.2004.07.063 (cit. on p. 118).
Kolkowitz S. et al. (2012). "Coherent sensing of a mechanical resonator with a single-spin qubit." *Science* 335.6076, pp. 1603–6. DOI: 10.1126/science.1216821 (cit. on p. 5).
Kub M. (2017). *Goldschmiede Michael Kub*. URL: http://www.goldschmiede-kub.at/ (visited on Feb. 16, 2017) (cit. on p. 95).
Kwon O. and Hogan C. J. (2016). "Interferometric tests of Planckian quantum geometry models". *Classical and Quantum Gravity* 33.10, p. 105004. DOI: 10.1088/0264-9381/33/10/105004 (cit. on p. 13).
LaHaye M. D. (2004). "Approaching the Quantum Limit of a Nanomechanical Resonator". *Science* 304.5667, pp. 74–77. DOI: 10.1126/science.1094419 (cit. on p. 57).
Lantz B. et al. (2009). "Review: Requirements for a Ground Rotation Sensor to Improve Advanced LIGO". *Bulletin of the Seismological Society of America* 99.2B, pp. 980–989. DOI: 10.1785/0120080199 (cit. on p. 159).
Lecocq F. et al. (2015). "Quantum Nondemolition Measurement of a Nonclassical State of a Massive Object". *Physical Review X* 5.4, p. 041037. DOI: 10.1103/PhysRevX.5.041037 (cit. on p. 8).
Lee K. C. et al. (2011). "Entangling Macroscopic Diamonds at Room Temperature". *Science* 334.6060, pp. 1253–1256. DOI: 10.1126/science.1211914 (cit. on p. 8).
Leggett A. J. (2002). "Testing the limits of quantum mechanics: motivation, state of play, prospects". *Journal of Physics: Condensed Matter* 14.15, R415–R451. DOI: 10.1088/0953-8984/14/15/201 (cit. on p. 15).
Lekner J. (2012a). "Electrostatic calibration of sphere-sphere forces". *Measurement Science and Technology* 23.8, p. 085007. DOI: 10.1088/0957-0233/23/8/085007 (cit. on p. 41).
Lekner J. (2012b). "Electrostatic force between two conducting spheres at constant potential difference". *Journal of Applied Physics* 111.7, p. 076102. DOI: 10.1063/1.3702438 (cit. on p. 41).
Leonhardt U. and Paul H. (1995). "Measuring the quantum state of light". *Progress in Quantum Electronics* 19.2, pp. 89–130. DOI: 10.1016/0079-6727(94)00007-L (cit. on p. 64).
Levin Y. (1998). "Internal thermal noise in the LIGO test masses: A direct approach". *Physical Review D* 57.2, pp. 659–663. DOI: 10.1103/PhysRevD.57.659 (cit. on pp. 97, 98).
Li T., Kheifets S., and Raizen M. G. (2011). "Millikelvin cooling of an optically trapped microsphere in vacuum". *Nature Physics* 7.7, pp. 527–530. DOI: 10.1038/nphys1952 (cit. on p. 100).
Li Y., Hess D., et al. (1998). "Design and pumping characteristics of a compact titanium–vanadium non-evaporable getter pump". *Journal of Vacuum Science & Technology A: Vacuum, Surfaces, and Films* 16.3, p. 1139. DOI: 10.1116/1.581248 (cit. on p. 169).
Lienhard J. H. I. and Lienhard J. H. V. (2011). *A Heat Transfer Textbook*. Fourth. Dover Publications (cit. on p. 106).
Liu J., Usami K., et al. (2011). "High-*Q* optomechanical GaAs nanomembranes". *Applied Physics Letters* 99.24, p. 243102. DOI: 10.1063/1.3668092 (cit. on p. 115).
Liu L., Tang W., et al. (2011). "Fabrication and characterization of SiC thin films". *6th IEEE International Conference on Nano/Micro Engineered and Molecular Systems*, pp. 146–149. DOI: 10.1109/NEMS.2011.6017316 (cit. on p. 117).
Long J. C. et al. (2003). "Upper limits to submillimetre-range forces from extra space-time dimensions." *Nature* 421.6926, pp. 922–5. DOI: 10.1038/nature01432 (cit. on p. 13).
Loudon R. (2000). *The quantum theory of light*. First. Oxford University Press (cit. on p. 58).
Luke H. (1999). "The origins of the sampling theorem". *IEEE Communications Magazine* 37.4, pp. 106–108. DOI: 10.1109/35.755459 (cit. on pp. 25, 199).

Luo J. et al. (2009). "Determination of the Newtonian Gravitational Constant $G$ with Time-of-Swing Method". *Physical Review Letters* 102.24. DOI: 10.1103/PhysRevLett.102.240801 (cit. on pp. 11, 176).
Luther G. and Towler W. (1982). "Redetermination of the Newtonian Gravitational Constant $G$". *Physical Review Letters* 48.3, pp. 121–123. DOI: 10.1103/PhysRevLett.48.121 (cit. on p. 176).
Mamin H. J. and Rugar D. (2001). "Sub-attonewton force detection at millikelvin temperatures". *Applied Physics Letters* 79.20, p. 3358. DOI: 10.1063/1.1418256 (cit. on pp. 6, 8).
Mandelbrot B. B. (1999). *Multifractals and* $1/f$ *Noise*. First. Springer-Verlag (cit. on p. 48).
Manos D. M. and Flamm D. L. (1989). *Plasma etching: an introduction*. First. Academic Press (cit. on p. 117).
Manoukian E. B. (2016). *Quantum Field Theory II*. First. Springer International Publishing. DOI: 10.1007/978-3-319-33852-1 (cit. on p. 14).
Maskelyne N. (1775). "An Account of Observations Made on the Mountain Schehallien for Finding Its Attraction. By the Rev." *Philosophical Transactions of the Royal Society of London* 65.0, pp. 500–542. DOI: 10.1098/rstl.1775.0050 (cit. on p. 9).
Matichard F. et al. (2015). "Seismic isolation of Advanced LIGO: Review of strategy, instrumentation and performance". *Classical and Quantum Gravity* 32.18, p. 185003. DOI: 10.1088/0264-9381/32/18/185003 (cit. on pp. 10, 68, 78, 80, 148, 161, 171).
McDonald K. T. (2003). *Maximal Gravity at the Surface of an Asteroid*. arXiv: physics/0312029 [physics] (cit. on p. 113).
McKenzie K. (2002). "Squeezing in the Audio Gravitational Wave Detection Band". PhD thesis. Australian National University (cit. on pp. 57, 143).
McKenzie K. et al. (2007). "Technical limitations to homodyne detection at audio frequencies". *Applied Optics* 46.17, p. 3389. DOI: 10.1364/AO.46.003389 (cit. on p. 143).
Meggitt Sensing Systems (2009). *Model 86 Seismic accelerometer*. URL: https://www.endevco.com/86/ (visited on Nov. 9, 2016) (cit. on p. 170).
Miao H., Srinivasan K., and Aksyuk V. (2012). "A microelectromechanically controlled cavity optomechanical sensing system". *New Journal of Physics* 14.7, p. 075015. DOI: 10.1088/1367-2630/14/7/075015 (cit. on p. 8).
Milgrom M. (1983). "A modification of the Newtonian dynamics as a possible alternative to the hidden mass hypothesis". *The Astrophysical Journal* 270, p. 365. DOI: 10.1086/161130 (cit. on pp. 49, 90).
Miller S. L. and Childers D. G. (2004). *Probability and random processes*. First. Elsevier Academic Press (cit. on p. 20).
Milotti E. (2002). $1/f$ *noise: a pedagogical review*. arXiv: physics/0204033 [abs] (cit. on p. 48).
Mitrofanov V., Prokhorov L., and Tokmakov K. (2002). "Variation of electric charge on prototype of fused silica test mass of gravitational wave antenna". *Physics Letters A* 300.4-5, pp. 370–374. DOI: 10.1016/S0375-9601(02)00857-5 (cit. on pp. 109, 110).
Mohideen U. and Roy A. (1998). "Precision Measurement of the Casimir Force from 0.1 to 0.9 $\mu$m". *Physical Review Letters* 81.21, pp. 4549–4552. DOI: 10.1103/PhysRevLett.81.4549 (cit. on p. 94).
Mohr P. J., Newell D. B., and Taylor B. N. (2016). "CODATA recommended values of the fundamental physical constants: 2014". *Reviews of Modern Physics* 88.3, p. 035009. DOI: 10.1103/RevModPhys.88.035009 (cit. on pp. 12, 176).
Mohr P. J., Taylor B. N., and Newell D. B. (2012). "CODATA recommended values of the fundamental physical constants: 1998". *Reviews of Modern Physics* 77.2, pp. 633–730. DOI: 10.1103/RevModPhys.84.1527 (cit. on p. 11).
Montgomery R. (2011). *SRM NIST Standard Reference Materials Catalog 2012*. Standard reference material SRM 685r (cit. on p. 95).
Moser J. et al. (2013). "Ultrasensitive force detection with a nanotube mechanical resonator". *Nature Nanotechnology* 8.7, pp. 493–496. DOI: 10.1038/nnano.2013.97 (cit. on pp. 6, 8).
Mueller C. L. et al. (2016). "The advanced LIGO input optics". *Review of Scientific Instruments* 87.1, p. 014502. DOI: 10.1063/1.4936974 (cit. on p. 10).
Müller-Ebhardt H. et al. (2008). "Entanglement of Macroscopic Test Masses and the Standard Quantum Limit in Laser Interferometry". *Physical Review Letters* 100.1, p. 013601. DOI: 10.1103/PhysRevLett.100.013601 (cit. on p. 8).
Müntinga H. et al. (2013). "Interferometry with Bose-Einstein Condensates in Microgravity". *Physical Review Letters* 110.9, p. 093602. DOI: 10.1103/PhysRevLett.110.093602 (cit. on p. 179).
Murch K. W. et al. (2008). "Observation of quantum-measurement backaction with an ultracold atomic gas". *Nature Physics* 4.7, pp. 561–564. DOI: 10.1038/nphys965 (cit. on p. 48).
Neben A. R. et al. (2012). "Structural thermal noise in gram-scale mirror oscillators". *New Journal of Physics* 14.11, p. 115008. DOI: 10.1088/1367-2630/14/11/115008 (cit. on pp. 98, 155).

Nesvizhevsky V. V. et al. (2002). "Quantum states of neutrons in the Earth's gravitational field." *Nature* 415.6869, pp. 297–9. DOI: 10.1038/415297a (cit. on p. 9).
Newman R. et al. (2014). "A measurement of G with a cryogenic torsion pendulum". *Philosophical Transactions of the Royal Society A: Mathematical, Physical and Engineering Sciences* 372.2026, pp. 20140025–20140025. DOI: 10.1098/rsta.2014.0025 (cit. on pp. 11, 12, 176).
Newport Corporation (2017). *Newport Corporation*. URL: https://www.newport.com/ (visited on Jan. 25, 2017) (cit. on p. 184).
Newton I. (1726). *Isaac Newton's Philosophiae Naturalis Principia Mathematica*. Third. Harvard University Press (cit. on p. 40).
Norte R. A. (2015). "Nanofabrication for On-Chip Optical Levitation, Atom-Trapping, and Superconducting Quantum Circuits". PhD thesis. California Institute of Technology (cit. on p. 117).
O'Connell A. D. et al. (2010). "Quantum ground state and single-phonon control of a mechanical resonator." *Nature* 464.7289, pp. 697–703. DOI: 10.1038/nature08967 (cit. on pp. 8, 178).
Oechsner U. et al. (2009). "Rauscharme Laserdioden-Strahlquellen mit reduzierter Kohärenz". *Photonik* 06, pp. 25–28 (cit. on p. 141).
Olive K. (2014). "Review of Particle Physics". *Chinese Physics C* 38.9, p. 090001. DOI: 10.1088/1674-1137/38/9/090001 (cit. on p. 111).
Orfanidis S. (2016). *Electromagnetic Waves and Antennas, vol.1*. First. Piscataway: Self-published (cit. on p. 104).
Owen R. and Müller T. (2014). *Attaching microspheres to cantilevers using the NanoWizard Life Science stage and AFM head*. Tech. rep. JPK Instruments AG (cit. on p. 94).
Palomaki T. A. et al. (2013). "Entangling Mechanical Motion with Microwave Fields". *Science* 342.6159, pp. 710–713. DOI: 10.1126/science.1244563 (cit. on pp. 8, 178, 179).
Paolino P., Sandoval F. A. A., and Bellon L. (2013). "Quadrature phase interferometer for high resolution force spectroscopy." *The Review of scientific instruments* 84.9, p. 095001. DOI: 10.1063/1.4819743 (cit. on pp. 96, 132, 136, 137, 144).
Parks H. and Faller J. (2010). "Simple Pendulum Determination of the Gravitational Constant". *Physical Review Letters* 105.11. DOI: 10.1103/PhysRevLett.105.110801 (cit. on pp. 11, 176).
Pathria R. K. and Beale P. D. (2011). *Statistical mechanics*. Third. Academic Press (cit. on p. 46).
Pearle P. (2015). "Relativistic dynamical collapse model". *Physical Review D* 91.10, p. 105012. DOI: 10.1103/PhysRevD.91.105012 (cit. on p. 14).
Penrose R. (1996). "On Gravity's role in Quantum State Reduction". *General Relativity and Gravitation* 28.5, pp. 581–600. DOI: 10.1007/BF02105068 (cit. on p. 14).
Physik Instrumente (PI) GmbH & Co. KG (2017). *Physik Instrumente*. URL: https://www.physikinstrumente.com/ (visited on Jan. 5, 2017) (cit. on pp. 124, 126).
Pikovski I., Vanner M. R., et al. (2012). "Probing Planck-scale physics with quantum optics". *Nature Physics* 8.5, pp. 393–397. DOI: 10.1038/nphys2262 (cit. on p. 13).
Pikovski I., Zych M., et al. (2015). "Universal decoherence due to gravitational time dilation". *Nature Physics* 11.8, pp. 668–672. DOI: 10.1038/nphys3366 (cit. on p. 14).
Pinard M., Hadjar Y., and Heidmann A. (1999). "Effective mass in quantum effects of radiation pressure". *The European Physical Journal D – Atomic, Molecular, Optical and Plasma Physics* 7.1, pp. 107–116. DOI: 10.1007/s100530050354 (cit. on p. 50).
Pino H. et al. (2016). *Magnetic Skatepark for Quantum Interference of a Superconducting Microsphere*. arXiv: 1603.01553 [quant-ph] (cit. on p. 15).
Pirkkalainen J.-M. et al. (2015). "Squeezing of Quantum Noise of Motion in a Micromechanical Resonator". *Physical Review Letters* 115.24, p. 243601. DOI: 10.1103/PhysRevLett.115.243601 (cit. on p. 8).
Platus D. L. (1996). *Minus K Technology*. URL: http://www.minusk.com/ (visited on Nov. 8, 2016) (cit. on pp. 130, 154).
Platus D. L. (1999). "Negative-stiffness-mechanism vibration isolation systems". *Proc. SPIE 3786, Optomechanical Engineering and Vibration Control*, pp. 98–105. DOI: 10.1117/12.363841 (cit. on p. 154).
Plissi M. V., Torrie C. I., Barton M., et al. (2004). "An investigation of eddy-current damping of multistage pendulum suspensions for use in interferometric gravitational wave detectors". *Review of Scientific Instruments* 75.11, p. 4516. DOI: 10.1063/1.1795192 (cit. on p. 156).
Plissi M. V., Torrie C. I., Husman M. E., et al. (2000). "GEO 600 triple pendulum suspension system: Seismic isolation and control". *Review of Scientific Instruments* 71.6, p. 2539. DOI: 10.1063/1.1150645 (cit. on pp. 71, 159).
Plodinec M., Loparic M., and Aebi U. (2010). "Preparation of microsphere tips for atomic force microscopy (AFM)." *Cold Spring Harbor protocols* 2010.10. DOI: 10.1101/pdb.prot5502 (cit. on p. 94).

Poggio M. and Degen C. L. (2010). "Force-detected nuclear magnetic resonance: recent advances and future challenges". *Nanotechnology* 21.34, p. 342001. DOI: 10.1088/0957-4484/21/34/342001 (cit. on p. 112).
Pound R. V. and Rebka G. A. (1959). "Gravitational Red-Shift in Nuclear Resonance". *Physical Review Letters* 3.9, pp. 439–441. DOI: 10.1103/PhysRevLett.3.439 (cit. on p. 9).
Pound R. V. and Rebka G. A. (1960). "Apparent Weight of Photons". *Physical Review Letters* 4.7, pp. 337–341. DOI: 10.1103/PhysRevLett.4.337 (cit. on p. 9).
Punturo M. et al. (2010). "The Einstein Telescope: a third-generation gravitational wave observatory". *Classical and Quantum Gravity* 27.19, p. 194002. DOI: 10.1088/0264-9381/27/19/194002 (cit. on pp. 10, 177).
Purdy T. P., Peterson R. W., and Regal C. A. (2013). "Observation of Radiation Pressure Shot Noise on a Macroscopic Object". *Science* 339.6121, pp. 801–804. DOI: 10.1126/science.1231282 (cit. on pp. 5, 48).
Purdy T. P., Peterson R. W., Yu P.-L., et al. (2012). "Cavity optomechanics with $Si_3N_4$ membranes at cryogenic temperatures". *New Journal of Physics* 14.11, p. 115021. DOI: 10.1088/1367-2630/14/11/115021 (cit. on p. 116).
Quinn T., Speake C., et al. (2001). "A New Determination of $G$ Using Two Methods". *Physical Review Letters* 87.11. DOI: 10.1103/PhysRevLett.87.111101 (cit. on p. 176).
Quinn T. (2000). "Fundamental constants: Measuring big $G$". *Nature* 408.6815, pp. 919–921. DOI: 10.1038/35050187 (cit. on p. 11).
Quinn T. (2016). "Gravity on the balance". *Nature Physics* 12.2, pp. 196–196. DOI: 10.1038/nphys3651 (cit. on p. 12).
Quinn T., Parks H., et al. (2013). "Improved Determination of $G$ Using Two Methods". *Physical Review Letters* 111.10, p. 101102. DOI: 10.1103/PhysRevLett.111.101102 (cit. on pp. 11, 176).
Ranjit G. et al. (2016). "Zeptonewton force sensing with nanospheres in an optical lattice". *Physical Review A* 93.5, p. 053801. DOI: 10.1103/PhysRevA.93.053801 (cit. on p. 8).
Reid S. and Martin I. (2016). "Development of Mirror Coatings for Gravitational Wave Detectors". *Coatings* 6.4, p. 61. DOI: 10.3390/coatings6040061 (cit. on p. 155).
Rider A. D. et al. (2016). "Search for Screened Interactions Associated with Dark Energy below the 100 $\mu$m Length Scale". *Physical Review Letters* 117.10, p. 101101. DOI: 10.1103/PhysRevLett.117.101101 (cit. on p. 13).
Riedinger R. et al. (2016). "Non-classical correlations between single photons and phonons from a mechanical oscillator". *Nature* 530.7590, pp. 313–316. DOI: 10.1038/nature16536 (cit. on p. 8).
Ritter R. C. et al. (1990). "Experimental test of equivalence principle with polarized masses". *Physical Review D* 42.4, pp. 977–991. DOI: 10.1103/PhysRevD.42.977 (cit. on pp. 5, 13, 89, 176).
Robertson N. A., Barton M., et al. (2013). *HAM Small Triple Suspension (HSTS) Final Design Document*. LIGO technical note T0900435-v9 (cit. on pp. 159, 162).
Robertson N., Cagnoli G., et al. (2002). "Quadruple suspension design for Advanced LIGO". *Classical and Quantum Gravity* 19.15, pp. 4043–4058. DOI: 10.1088/0264-9381/19/15/311 (cit. on pp. 71, 80, 160, 171).
Rodriguez A. W., Capasso F., and Johnson S. G. (2011). "The Casimir effect in microstructured geometries". *Nature Photonics* 5.4, pp. 211–221. DOI: 10.1038/nphoton.2011.39 (cit. on p. 42).
Romero-Isart O., Clemente L., et al. (2012). "Quantum magnetomechanics with levitating superconducting microspheres." *Physical review letters* 109.14, p. 147205. DOI: 10.1103/PhysRevLett.109.147205 (cit. on pp. 8, 175).
Romero-Isart O., Pflanzer A., et al. (2011). "Optically levitating dielectrics in the quantum regime: Theory and protocols". *Physical Review A* 83.1. DOI: 10.1103/PhysRevA.83.013803 (cit. on p. 8).
Romero-Isart O. (2011). "Quantum superposition of massive objects and collapse models". *Physical Review A* 84.5, p. 052121. DOI: 10.1103/PhysRevA.84.052121 (cit. on p. 15).
Rosi G. et al. (2014). "Precision measurement of the Newtonian gravitational constant using cold atoms." *Nature* 510.7506, pp. 518–21. DOI: 10.1038/nature13433 (cit. on pp. 12, 176).
Rothleitner C. and Schlamminger S. (2015). "Schwere Experimente". *Physik Journal* 14.11, pp. 37–42 (cit. on p. 11).
Rovelli C. (2007). *Quantum Gravity*. First. Cambridge University Press (cit. on p. 13).
Rudin W. (1991). *Functional Analysis*. Second. McGraw-Hill Inc. (cit. on p. 192).
Rugar D., Budakian R., et al. (2004). "Single spin detection by magnetic resonance force microscopy." *Nature* 430.6997, pp. 329–32. DOI: 10.1038/nature02658 (cit. on p. 5).
Rugar D., Mamin H. J., and Guethner P. (1989). "Improved fiber-optic interferometer for atomic force microscopy". *Applied Physics Letters* 55.25, p. 2588. DOI: 10.1063/1.101987 (cit. on pp. 131, 141, 144).

Safavi-Naeini A. et al. (2012). "Observation of Quantum Motion of a Nanomechanical Resonator". *Physical Review Letters* 108.3. DOI: 10.1103/PhysRevLett.108.033602 (cit. on p. 8).
Saulson P. R. (1990). "Thermal noise in mechanical experiments". *Physical Review D* 42.8, pp. 2437–2445. DOI: 10.1103/PhysRevD.42.2437 (cit. on pp. 97, 103).
Schäfter + Kirchhoff (2017). *Optics, Metrology, and Photonics*. URL: http://www.sukhamburg.com/ (visited on Jan. 27, 2017) (cit. on p. 133).
Schediwy S. W. et al. (2005). "High $Q$ factor bonding using natural resin for reduced thermal noise of test masses". *Review of Scientific Instruments* 76.2, p. 026117. DOI: 10.1063/1.1847654 (cit. on p. 105).
Schenk C. (2006). *MiKTeX Project Page*. URL: http://miktex.org/ (visited on Sept. 28, 2016) (cit. on p. iv).
Schlamminger S. et al. (2006). "Measurement of Newton's gravitational constant". *Physical Review D* 74.8. DOI: 10.1103/PhysRevD.74.082001 (cit. on pp. 12, 176).
Schmid S. et al. (2011). "Damping mechanisms in high-$Q$ micro and nanomechanical string resonators". *Physical Review B* 84.16, p. 165307. DOI: 10.1103/PhysRevB.84.165307 (cit. on p. 117).
Schmöle J. (2011). "Towards magnetic levitation in opto-mechanics". Master's thesis. University of Vienna (cit. on p. 8).
Schmöle J. et al. (2016). "A micromechanical proof-of-principle experiment for measuring the gravitational force of milligram masses". *Classical and Quantum Gravity* 33.12, p. 125031. DOI: 10.1088/0264-9381/33/12/125031 (cit. on pp. 4, 146, 176).
Schreppler S. et al. (2014). "Optically measuring force near the standard quantum limit." *Science* 344.6191, pp. 1486–9. DOI: 10.1126/science.1249850 (cit. on pp. 6, 8, 57).
Shaul D. N. A. et al. (2008). "Charge Management for LISA and LISA Pathfinder". *International Journal of Modern Physics D* 17.07, pp. 993–1003. DOI: 10.1142/S0218271808012656 (cit. on p. 109).
Singh-Miller N. E. and Marzari N. (2009). "Surface energies, work functions, and surface relaxations of low-index metallic surfaces from first principles". *Physical Review B* 80.23, p. 235407. DOI: 10.1103/PhysRevB.80.235407 (cit. on p. 85).
SmarAct GmbH (2017). *SmarAct GmbH - Perfect Motion*. URL: https://www.smaract.com/ (visited on Jan. 5, 2017) (cit. on pp. 124, 135).
Smith D. T., Pratt J. R., and Howard L. P. (2009). "A fiber-optic interferometer with subpicometer resolution for dc and low-frequency displacement measurement." *The Review of scientific instruments* 80.3, p. 035105. DOI: 10.1063/1.3097187 (cit. on pp. 130, 131, 141, 144).
Smith J. O. (2010). *Spectral Audio Signal Processing*. First. W3K Publishing (cit. on pp. 23, 191).
Smith K. (2004). *Analysis of LIGO Flexure Rods*. Tech. rep. 20007235–C. Alliance Space Systems, Inc. (cit. on pp. 152, 153).
Somiya K. (2012). "Detector configuration of KAGRA – the Japanese cryogenic gravitational-wave detector". *Classical and Quantum Gravity* 29.12, p. 124007. DOI: 10.1088/0264-9381/29/12/124007 (cit. on p. 177).
Sorrentino F. et al. (2014). "Sensitivity limits of a Raman atom interferometer as a gravity gradiometer". *Physical Review A* 89.2, p. 023607. DOI: 10.1103/PhysRevA.89.023607 (cit. on pp. 8, 12).
Souradeep T. (2016). "LIGO-India". *Resonance* 21.3, pp. 225–231. DOI: 10.1007/s12045-016-0316-6 (cit. on p. 10).
Speake C. C. and Aston S. M. (2005). "An interferometric sensor for satellite drag-free control". *Classical and Quantum Gravity* 22.10, S269–S277. DOI: 10.1088/0264-9381/22/10/019 (cit. on p. 171).
Speake C. C. and Trenkel C. (2003). "Forces between Conducting Surfaces due to Spatial Variations of Surface Potential". *Physical Review Letters* 90.16, p. 160403. DOI: 10.1103/PhysRevLett.90.160403 (cit. on pp. 43, 85, 86).
Speake C. and Aston S. (2004). *Interferometric OSEM Sensor Development Update*. LIGO technical note T040139-00-K (cit. on p. 124).
Speake C. and Quinn T. (2014). "The search for Newton's constant". *Physics Today* 67.7, pp. 27–33. DOI: 10.1063/PT.3.2447 (cit. on pp. 5, 12).
SPTS Technologies (2014). $XeF_2$ *Etch for MEMS Release*. URL: http://www.spts.com/uploaded_files/1193/images/XeF2-Intro-A4.pdf (visited on Jan. 5, 2017) (cit. on p. 118).
Stamp P. C. E. (2012). "Environmental decoherence versus intrinsic decoherence". *Philosophical Transactions of the Royal Society A: Mathematical, Physical and Engineering Sciences* 370.1975, pp. 4429–4453. DOI: 10.1098/rsta.2012.0162 (cit. on p. 14).
Stamp P. C. E. (2015). "Rationale for a correlated worldline theory of quantum gravity". *New Journal of Physics* 17.6, p. 065017. DOI: 10.1088/1367-2630/17/6/065017 (cit. on p. 14).
Stefszky M. S. et al. (2012). "Balanced homodyne detection of optical quantum states at audio-band frequencies and below". *Classical and Quantum Gravity* 29.14, p. 145015. DOI: 10.1088/0264-9381/29/14/145015 (cit. on p. 144).

Stefszky M. S. (2012). "Generation and Detection of Low-Frequency Squeezing for Gravitational-Wave Detection". PhD thesis. Australian National University (cit. on pp. 57, 143).
Stein E. M. and Weiss G. L. (1971). *Introduction to Fourier Analysis on Euclidean Spaces*. First. Princeton University Press (cit. on p. 192).
Stipe B. C. et al. (2001). "Noncontact friction and force fluctuations between closely spaced bodies." *Physical review letters* 87.9, p. 096801. DOI: 10.1103/PhysRevLett.87.096801 (cit. on p. 43).
Stowe T. D. et al. (1997). "Attonewton force detection using ultrathin silicon cantilevers". *Applied Physics Letters* 71.2, p. 288. DOI: 10.1063/1.119522 (cit. on pp. 8, 46).
Sumner T. J., Pendlebury J. M., and Smith K. F. (1987). "Convectional magnetic shielding". *Journal of Physics D: Applied Physics* 20.9, pp. 1095–1101. DOI: 10.1088/0022-3727/20/9/001 (cit. on p. 122).
Takamori A. et al. (2007). "Inverted pendulum as low-frequency pre-isolation for advanced gravitational wave detectors". *Nuclear Instruments and Methods in Physics Research Section A: Accelerators, Spectrometers, Detectors and Associated Equipment* 582.2, pp. 683–692. DOI: 10.1016/j.nima.2007.08.161 (cit. on p. 154).
Taylor J. H. and Weisberg J. M. (1982). "A new test of general relativity - Gravitational radiation and the binary pulsar PSR 1913+16". *The Astrophysical Journal* 253, p. 908. DOI: 10.1086/159690 (cit. on pp. 10, 178).
Tektronix, Inc. (2017). *AFG3000 arbitrary function generator datasheet*. URL: http://www.tek.com/datasheet/afg3000c-arbitrary-function-generator-datasheet (visited on Jan. 5, 2017) (cit. on p. 121).
Teo L. P. (2012). "Casimir effect between two spheres at small separations". *Physical Review D* 85.4, p. 045027. DOI: 10.1103/PhysRevD.85.045027 (cit. on p. 42).
Terrano W. A. (2015). "Torsion Pendulum Searches for Macroscopic Spin-Interactions as a Window on New Physics". PhD thesis. University of Washington (cit. on p. 13).
Teufel J. D., Donner T., et al. (2011). "Sideband cooling of micromechanical motion to the quantum ground state." *Nature* 475.7356, pp. 359–63. DOI: 10.1038/nature10261 (cit. on p. 8).
Teufel J. D., Li D., et al. (2011). "Circuit cavity electromechanics in the strong-coupling regime." *Nature* 471.7337, pp. 204–8. DOI: 10.1038/nature09898 (cit. on p. 8).
The LIGO Scientific Collaboration et al. (2015). "Advanced LIGO". *Classical and Quantum Gravity* 32.7, p. 74001. DOI: 10.1088/0264-9381/32/7/074001 (cit. on p. 10).
Thompson J. D. et al. (2008). "Strong dispersive coupling of a high-finesse cavity to a micromechanical membrane." *Nature* 452.7183, pp. 72–5. DOI: 10.1038/nature06715 (cit. on p. 116).
Tol P. (2012). *Paul Tol's Notes*. URL: https://personal.sron.nl/~pault/ (visited on June 21, 2016) (cit. on p. iv).
Torrie C. I. E. (2001). "Development of Suspensions for the Geo 600 Gravitational Wave Detector". PhD thesis. University of Glasgow (cit. on pp. 71, 73, 159).
Trojek P. (2007). "Efficient Generation of Photonic Entanglement and Multiparty Quantum Communication". PhD thesis. Ludwig-Maximilians-Universitat München (cit. on pp. 133, 135).
Tu L.-C. et al. (2010). "New determination of the gravitational constant G with time-of-swing method". *Physical Review D* 82.2. DOI: 10.1103/PhysRevD.82.022001 (cit. on pp. 11, 176).
Turin G. (1960). "An introduction to matched filters". *IEEE Transactions on Information Theory* 6.3, pp. 311–329. DOI: 10.1109/TIT.1960.1057571 (cit. on p. 202).
Vahlbruch H. (2008). "Squeezed Light for GravitationalWave Astronomy". PhD thesis. Gottfried Wilhelm Leibniz Universität Hannover (cit. on pp. 57, 141, 143).
Vahlbruch H. et al. (2007). "Quantum engineering of squeezed states for quantum communication and metrology". *New Journal of Physics* 9.10, pp. 371–371. DOI: 10.1088/1367-2630/9/10/371 (cit. on p. 143).
Vanner M. R. et al. (2013). "Cooling-by-measurement and mechanical state tomography via pulsed optomechanics". *Nature Communications* 4, pp. 697–703. DOI: 10.1038/ncomms3295 (cit. on pp. 8, 50, 102, 115).
Veggeberg K. (2008). *Octave analysis explored – A tutorial*. URL: http://www.evaluationengineering.com/octave-analysis-explored.php (visited on Nov. 4, 2016) (cit. on p. 200).
Verbridge S. S. et al. (2006). "High quality factor resonance at room temperature with nanostrings under high tensile stress". *Journal of Applied Physics* 99.12, p. 124304. DOI: 10.1063/1.2204829 (cit. on p. 117).
Verhagen E. et al. (2012). "Quantum-coherent coupling of a mechanical oscillator to an optical cavity mode." *Nature* 482.7383, pp. 63–7. DOI: 10.1038/nature10787 (cit. on p. 8).
Wagner T. A. et al. (2012). "Torsion-balance tests of the weak equivalence principle". *Classical and Quantum Gravity* 29.18, p. 184002. DOI: 10.1088/0264-9381/29/18/184002 (cit. on pp. 13, 90).

Wal C. H. van der (2000). "Quantum Superposition of Macroscopic Persistent-Current States". *Science* 290.5492, pp. 773–777. DOI: 10.1126/science.290.5492.773 (cit. on p. 178).
Wanner A. (2013). "Seismic attenuation system (AEI-SAS) for the AEI 10 m prototype". PhD thesis. Gottfried Wilhelm Leibniz Universität Hannover (cit. on p. 154).
Ward R. L. et al. (2008). "DC readout experiment at the Caltech 40m prototype interferometer". *Classical and Quantum Gravity* 25.11, p. 114030. DOI: 10.1088/0264-9381/25/11/114030 (cit. on p. 129).
Weld D. M. (2007). "Design, construction, and operation of an apparatus for detecting short-length-scale deviations from Newtonian gravity". PhD thesis. Stanford University (cit. on p. 89).
Welsch D.-G., Vogel W., and Opatrny T. (2009). *Homodyne Detection and Quantum State Reconstruction*. arXiv: 0907.1353 [quant-ph] (cit. on p. 63).
Westphal T. (2016). "A Coating Thermal Noise Interferometer for the AEI 10 m Prototype facility". PhD thesis. Universität Hannover (cit. on pp. 48, 144, 161).
Westphal T. et al. (2012). "Design of the 10 m AEI prototype facility for interferometry studies". *Applied Physics B* 106.3, pp. 551–557. DOI: 10.1007/s00340-012-4878-z (cit. on pp. 154, 169).
Will C. M. (2006). "The Confrontation between General Relativity and Experiment". *Living Reviews in Relativity* 9. DOI: 10.12942/lrr-2006-3 (cit. on pp. 5, 9, 178).
Willems P. et al. (2002). "Investigations of the dynamics and mechanical dissipation of a fused silica suspension". *Physics Letters A* 297.1, pp. 37–48. DOI: 10.1016/S0375-9601(02)00380-8 (cit. on p. 102).
Wilson D. J., Regal C. A., et al. (2009). "Cavity Optomechanics with Stoichiometric SiN Films". *Physical Review Letters* 103.20, p. 207204. DOI: 10.1103/PhysRevLett.103.207204 (cit. on p. 116).
Wilson P. R. and Madsen L. (2001). *CTAN: Package memoir*. URL: https://www.ctan.org/pkg/memoir (visited on Sept. 28, 2016) (cit. on p. iv).
Winterflood J., Blair D., and Slagmolen B. (2002). "High performance vibration isolation using springs in Euler column buckling mode". *Physics Letters A* 300.2, pp. 122–130. DOI: 10.1016/S0375-9601(02)00258-X (cit. on p. 149).
Wipf C. et al. (2008). "Route to ponderomotive entanglement of light via optically trapped mirrors". *New Journal of Physics* 10.9, p. 095017. DOI: 10.1088/1367-2630/10/9/095017 (cit. on p. 8).
Wolf R. (1977). "Electropolishing of gold and gold-rich alloys". *Micron* 8.3, pp. 171–172. DOI: 10.1016/0047-7206(77)90021-8 (cit. on p. 95).
Wollman E. E. et al. (2015). "Quantum squeezing of motion in a mechanical resonator". *Science* 349.6251, pp. 952–955. DOI: 10.1126/science.aac5138 (cit. on p. 8).
Yuan M., Cohen M. A., and Steele G. A. (2015). "Silicon nitride membrane resonators at millikelvin temperatures with quality factors exceeding $10^8$". *Applied Physics Letters* 107.26, p. 263501. DOI: 10.1063/1.4938747 (cit. on p. 102).
Zander B. van der et al. (2009). *TeXstudio*. URL: http://www.texstudio.org/ (visited on Sept. 28, 2016) (cit. on p. iv).
Zerr A. et al. (2004). "Elastic Moduli and Hardness of Cubic Silicon Nitride". *Journal of the American Ceramic Society* 85.1, pp. 86–90. DOI: 10.1111/j.1151-2916.2002.tb00044.x (cit. on p. 117).
Zhang W. et al. (2014). "Reduction of residual amplitude modulation to $1 \cdot 10^{-6}$ for frequency modulation and laser stabilization". *Optics Letters* 39.7, p. 1980. DOI: 10.1364/OL.39.001980 (cit. on p. 66).
Zwickl B. M. et al. (2008). "High quality mechanical and optical properties of commercial silicon nitride membranes". *Applied Physics Letters* 92.10, p. 103125. DOI: 10.1063/1.2884191 (cit. on pp. 93, 116).
Zwillinger D. (2011). *CRC standard mathematical tables and formulae*. Thirty-second. CRC Press (cit. on p. 190).